STUDY OF MECHANICAL PROPERTIES AND MICROSTRUCTURE OF FRICTION STIR WELDING OF DISSIMILAR ALLOY

A Thesis submitted in partial fulfillment of the requirements for the award the degree of

DOCTOR OF PHILOSOPHY

IN

(MECHANICAL ENGINEERING)

By

HUSAIN MEHDI (2K17/PhD/ME/61)

Under the Supervision of

Prof. R.S Mishra

DEPARTMENT OF MECHANICAL ENGINEERING
DELHI TECHNOLOGICAL UNIVERSITY,
NEW DELHI- 110042 (INDIA)
AUGUST, 2020

DELHI TECHNOLOGICAL UNIVERSITY, DELHI

DECLARATION

I hereby declare that the research work presented in this thesis, entitled **"STUDY OF MECHANICAL PROPERTIES AND MICROSTRUCTURE OF FRICTION STIR WELDING OF DISSIMILAR ALLOY"** is an original work carried out by me under the supervision of Prof. R.S. Mishra, Professor, Department of Mechanical Engineering, Delhi Technological University, Delhi. This thesis has been prepared in conformity with the rules and regulation of the Delhi Technological University, Delhi. The research work reported and results presented in the thesis have not been submitted either in part or full to any other university or institute for the award of any other degree or diploma.

Husain Mehdi
(2K17/Ph.D/ME/61)
Research Scholar
Department of Mechanical Engineering
Delhi Technological University, Delhi

DELHI TECHNOLOGICAL UNIVERSITY, DELHI

CERTIFICATE

This is to certify that the work embodied in this thesis entitled **"STUDY OF MECHANICAL PROPERTIES AND MICROSTRUCTURE OF FRICTION STIR WELDING OF DISSIMILAR ALLOY"** submitted by **Husain Mehdi, (Roll No. 2K17/Ph.D/ME/61)** in partial fulfillment of requirements for the award of degree of **DOCTOR OF PHILOSOPHY** in **Mechanical Engineering** is an authentic record of student own work carried by him under my supervision.

This is also certified that this work has not been submitted to any other institute or university for the award of any other diploma or degree.

Prof. (Dr.) R.S. Mishra
Professor & DRC chairman
Department of Mechanical Engineering
Delhi Technological University, Delhi

ACKNOWLEDGEMENTS

The work presented here would not have been possible without the help of many talented and learned people. First and foremost, I would like to thank my supervisor Prof. R.S. Mishra, Delhi Technological University, Delhi, for extending his full support and encouragement. I deeply value invaluable suggestions and creative freedom, he provided to me. I also greatly benefitted from his experience and skills which he shared with me with utmost generosity. I highly appreciate the personal attention and interest which he showed towards my research work. I had the privilege to learn from him not just lessons of engineering but of life. I am thankful to the supervisor to help me to get access to all the necessary facilities in DTU including welding laboratory.

I also thank the technical staff of welding laboratory, Mr. Girish Anand and Mr Tek Chand for all the help received during experimentation.

I am deeply thankful to my family for their appreciation, patience and tolerance. The encouragement I received from my father and mother laid the foundation of this Ph.D thesis. I express special thanks to my wife Fazilat, sister Nusrat Fatima, and my brother Hasan Mehdi for their valuable assistance and suggestions during research work.

Husain Mehdi

ABSTRACT

Tungsten inert gas (TIG) welding is the most commonly used joining process for aluminum alloy for AA6061 and AA7075 which are highly demanded in the aerospace engineering and automobile sector, but there are some defects occurs during TIG welding like micro-crack, coarse grain structure, and porosity. To improve these defects, the TIG welded joint is processed using friction stir processing (FSP).

In this work, the FSP tool pin rotates on an already welded joint by TIG welding to improve the lower the welding load and weld quality by adjusting the processing parameters of friction stir processing and analyzed the mechanical properties of TIG, FSW and TIG+FSP welded joint and then computational fluid dynamics based numerical model was developed to predict the temperature distribution and material flow during FSW of dissimilar aluminum alloys of AA6061 and AA7075 by ANSYS fluent software. The tensile strength, micro-hardness and residual stress of friction stir welded joint was observed 221.3 MPa, 97 HV and 29 MPa respectively at tool rotational speed of 1300 rpm, traverse speed of 30 mm/min with tilt angle 2^0 and the tensile strength of TIG welded joints with filler ER4043 and ER5356 was observed 158.6 MPa and 176.2 MPa respectively. After friction stir processing on TIG welded joint, the maximum tensile strength (255 MPa), microhardness (105 HV) and minimum residual stress (28.3 MPa) for TIG+FSP welded joints were observed at tool rotational speed of 1300 rpm, traverse speed of 45 mm/min with tilt angle 1 with filler ER4043, whereas the maximum tensile strength (281.1 MPa), microhardness (107.1 HV) and minimum residual stress (18.3 MPa) for TIG+FSP welded joints were observed at tool rotational speed of 1300 rpm, traverse speed of 30 mm/min with tilt angle 2 with filler ER5356.

The empirical relationships were developed to analyze the tensile strength, % strain, residual stress and microhardness of TIG+FSP welded joint of AA6061 and AA7075 at 95% confidence level. The optimized value of tensile stress, percentage strain, microhardness at nugget zone and residual stress at nugget zone are 218.82 MPa, 24.15, 90.21 HV and 45.19 MPa respectively, whereas the optimized processing parameters i.e. tool rotational speed, feed rate and tilt angle are 1076.24 rpm, 37.76 mm/min and 1.73^0 respectively for filler ER 4043 and the optimized value of tensile stress, percentage strain, microhardness at nugget zone and residual stress at nugget

zone are 266.66 MPa, 29.74, 103.19 HV and 21.66 MPa respectively, whereas the optimized processing parameters i.e. tool rotational speed, feed rate and tilt angle are 1278.12 rpm, 35.95 mm/min and 1.75^0 respectively for filler ER 5356. The predicted peak values of temperature at the weld region were calculated by the ANSYS software and found the maximum temperature about 515ºC at tool rotation of 1300 rpm. To increases the tool rotational speed and decrease the feed rate, leads to increases in heat input in TIG+FSP welded joint. The residual stress of TIG welded joints with filler ER4043 and ER5356 was observed 77 MPa and 63 MPa respectively. The grains in the nugget zone in TIG+FSP welded joint was observed much finer than the TIG welded joint at fusion zone. The large dimples and quasi cleavage with a sharp edge and various depths were found on the fractured tensile specimen surface of low tool rotational speed whereas fine dimples were found at high tool rotational speed of TIG+FSP welded joints.

Table of Contents

List of Tables

List of Figures

CHAPTER- 1

Introduction

1 Introduction

The joining of two similar or dissimilar material by a coalescence of the contact surface with or without melting the base material is called welding. This coalescence can be achieved by melting of the contact surface by pressure welding or fusion welding. Pressure welding also known as solid phase joining. When the welding involves melting and fusion of the base material is known as autogenous welding, but some welding processes required the filler material in the form of wire or rod and melted into the joint with the help of fusion welding, like gas welding, arc welding, metal inert gas welding (MIG) and tungsten inert gas welding (TIG) etc. There are many types of welding processes, in which some welding processes are very common to use. In welding, different types of arc welding widely used in the industries. Some arc welding as given below.

1.1 Arc welding

The term arc welding refers that an electric arc as the source of heat to melt and join the base material with or with filler rod. It is the types of welding which is uses a power supply to create an electric arc between the parent material and the electrode at the point of contact. In this welding direct current (DC) or alternating current (AC) can be used. There are flowing types of arc welding.

1.1.1 Shielded metal arc welding (SMAW)

Shielded metal arc welding is the cheapest, simplest, and most widely used arc welding process in which the arc maintained between the base material and the tip of the coated electrode generates the required heat. The shielding is provided by the decomposition of the electrodes. The main function of the shield is to protect the arc and molten metal from chemical reactions with atmospheric constituents. In this process, no pressure is required, and filler metal is obtained from the electrode. This welding process is widely used for all ferrous materials in all positions.

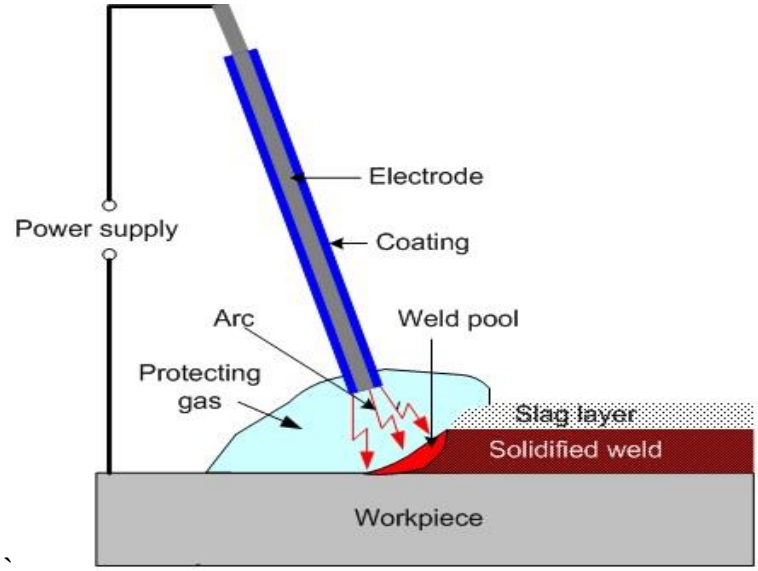

Figure 1: Shielded Metal Arc welding (SMAW)

1.1.2 Gas metal arc welding (GMAW)

Gas metal arc welding also known as metal inert gas welding is a high speed welding process. In this process, an arc created between the parent materials and continuously supply consumable electrode which provide the filler metal to weldment from the externally supplied inert gas (Helium, argon or carbon dioxide) without application of pressure. The fume generated during MIG process derived the consumption of consumable electrode not from the parent material.

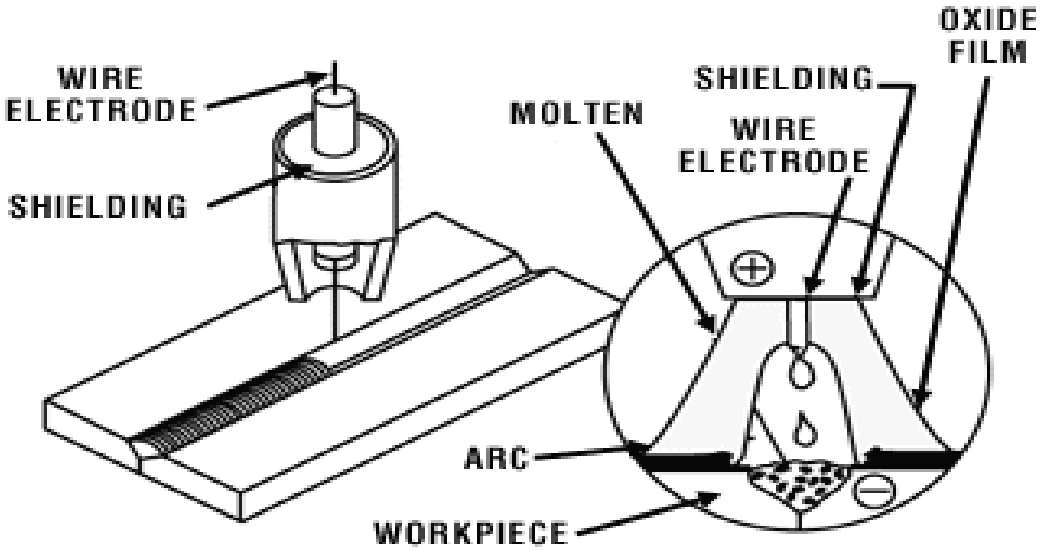

Figure 2: Gas metal arc welding (GMAW)

1.1.3 Gas tungsten arc welding (GTAW)

Gas tungsten arc welding (GTAW) or tungsten inert gas (TIG) is an arc welding process that creates an arc between a non-consumable tungsten electrode and a welded workpiece. TIG is commonly used in railway vehicle construction, automotive and chemical industries. Aluminum alloys are used as an important metal in the industries due to its excellent corrosion resistance and light weight. TIG is one of the welding processes and is commonly used to weld uniform and different aluminum alloy joints. It has been observed that most of the work is done on different aluminum alloy, which are most commonly used is automotive and aerospace industries. Key areas of research are weld characterization, dissimilar metal welding, parameter optimization, process modeling, fault analysis and automation of the TIG welding process. GTAW welding is an arc welding process in which fusion energy is generated by burning between a workpiece and a tungsten electrode by an electric arc. The electrode and the weld pool are protected from the harmful effects of the atmosphere by an inert protective gas during the welding process. The shield passes through the gas nozzle to the gas weld zone where it replaces the atmosphere. TIG welding differs from other arc welding processes in that the electrodes are not used like electrodes like other processes such as MIG / MAG.

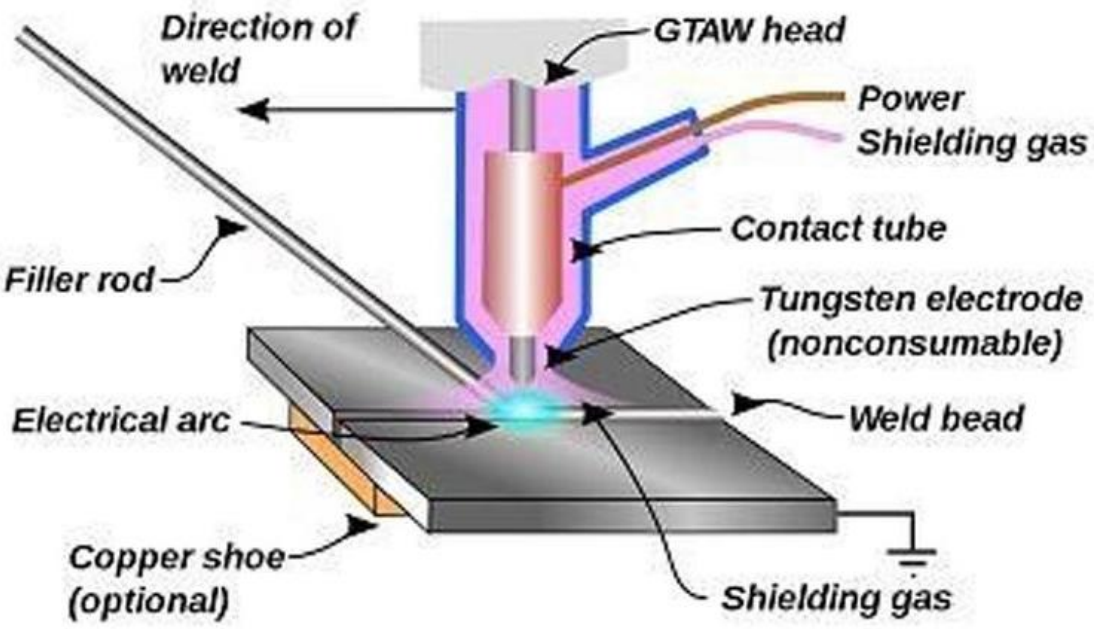

Figure 3: Gas tungsten arc welding (GTAW)

Tungsten filler rods are commonly available in the market from 0.6 mm to 6.5 mm diameter and length100-200 mm. The electrode size depends on current carrying capacity whether it is connected to positive or negative terminal of direct current (DC) power source. The power source voltage ranges from 60-80 V used in TIG welding.

1.1.4 Types of welding current used in tungsten inert gas welding (TIG)

1.1.4.1 Direct current straight polarity (DCSP)

The direct current is used in this type of tungsten inert gas welding. The electrode is connected to the negative terminal of power supply. This type of connection is widely used in DC welding process. 30% of the welding heat energy is received when tungsten electrode connected to the negative terminal.

1.1.4.2 Direct current reverse polarity (DCRP)

In Direct current reverse polarity, the tungsten electrode is connected to the positive terminal of power supply. Generally, this type of connection is not used, because the excess heat is generated in the tungsten electrode which may cause the burn away of parent material. This welding is used only for light material at very low current.

1.1.4.3 Alternating Current (AC)

Alternating current is mostly used for aluminum alloy and magnesium alloy welding. When AC current is used then the tungsten electrode continues change from plus to minus polarity. On the half cycle i.e. positive polarity, the negatively polarized electrons move from the parent material into the electrode. This will result oxide layer rupturing onto the parent material. When the next half cycle comes i.e. negative polarity, then the electron moves in to the parent material and generated heat. This is how the penetration required for the weld seam occurs.

1.1.5 Advantages of TIG welding

There are following advantages of TIG welding over the other fusion welding.

- TIG welded joint have clean and high quality weld as compare to other fusion welding.
- TIG welded joint weld a wide range of metal.
- There is no slag or spatter, sparks or smoke during welding process.
- Provide high strength compare to other welding process.
- Does not use flux or leave a slag.
- Uses a shielding gas to protect the weld pool and tungsten

1.1.6 Application

Although the aerospace and automobile industries are one of the main user of TIG welding, many industries use GTAW to weld thin work pieces, especially non-ferrous metals. It is widely used in the construction of spacecraft and is commonly used for small wire, thin walled pipes, such as those used in the bicycle industry. In addition, GTAW is commonly used for root or first welding of pipes of different sizes. In maintenance and repair work, this process is often used for repair and death of equipment, especially parts made of aluminum and magnesium. Because weld metal is not directly transferred into the arc as most open arc welding processes, welding engineers can use a wide variety of weld metals. Some application of TIG welded joints are

- Nuclear industry
- Automobile and Aircraft
- Food processing industry.
- Maintenance and repair work.
- Precision manufacturing industry

1.1.7 Processing parameters of TIG welding

There are two types of welding parameters either direct weld parameter (DWP) or indirect weld parameter (IWP). The direct weld parameter are those relating to the

weld reinforcement, fusion zone geometry, mechanical properties of the completed weld, weld microstructure and discontinuities and indirect weld parameter are those input variables that collectively control the direct weld parameter, such as current, voltage, wire feed rate, torch travel speed, travel angle etc.

The main TIG welding parameters that affect the quality and strength of weldment are as given below.

Table 1: Process parameter of TIG welding

Indirect Weld Parameters (IWP)	Welding Process	Direct Weld Parameters (DWP)
⇒ Current ⇒ Voltage ⇒ Travel Speed ⇒ Wire Feed Speed ⇒ Electrode Extension ⇒ Travel Angle ⇒ Focused Spot Zone ⇒ Depth Of Focus	Material Parameters Melting Point Thermal Conductivity Diffusivity Joint Type	⇒ Bead Width ⇒ Weld Penetration ⇒ Mechanical ⇒ Microstructure ⇒ Grain Size ⇒ Discontinuities ⇒ Porosity

1.1.7.1 Welding Current

The welding current is the effective and extremely sensitive process parameter of TIG welding process, the applied current is depending upon the thickness of welded joint. Higher current in tungsten inert gas welding can lead to splatter and welded joint become damage and lower current may lead to sticking of the filler rod. The large heat affected area may be found during low welding current. Fixed current mode may vary the voltage in order to maintain a constant arc current.

1.1.7.2 Welding voltage

Welding voltage can be adjusted according to the TIG welding equipment. For making easy arc initiation, a high initial voltage required. Too high voltage may lead to large variable in welding quality.

1.1.7.3 Inert Gases

Shielding gas can be used as per the working metals, weld temperature, arc stability and electrode life etc. Shielding gas also affect the weld quality, weld penetration depth, porosity, and mechanical properties of weldment. The most commonly used shielding gases are argon, helium and carbon dioxide. Argon gas is successfully used in tungsten inert gas welding. Generally, argon gas provides an arc which operate more smoothly than the other shielding gas and obtained less penetration during process. Pure argon may be used for low alloy steel, aluminum alloy, stainless steel and copper etc. mixture of argon and helium can be used for aluminum alloy and copper.

1.1.7.4 Welding speed

Primarily control of penetration and bead size are depend upon the welding speed. Extremely high welding speed decreases wetting action and increases the tendency of porosity, undercut and uneven bead shapes, whereas low welding speed reduces the tendency the porosity and uneven bead shapes.

1.1.8 Filler rod for tungsten inert gas welding

Selection of filler rod is very important to join the parent aluminum alloy plate. Filler metal produced in the weld pool is a combination of filler and parent metals that should have high ductility, strength and free from cracking. Good quality weld may have achieved only if the filler metal is of high quality and clean, if so not a large amount of contaminant may be introduced in to the weld pool. The filler wire diameter may choose according to the current supply, joint design and thickness of the welded plate. There are different fillers wire used in the aluminum alloy welding by TIG welded process, some fillers are as given below.

1.1.8.1 ER4043

ER4043 is silicon base aluminum alloy filler wire, in which 4.5 to 6% silicon is used. Thus filler is designed for welding of 6xxx and 7xxx series. It may also be used to weld 3xxx series. Because of silicon base alloy ER4043 has lower melting point and more fluidity than the other filler wire series and this is mostly preferred by the welders. Weld penetration of ER4043 is re than ER5356 but produce less ductility. ER4043 is not suited for high magnesium content aluminum alloy like 5xxx series except (Mg content less or equal to 2.5 %) i.e. AA5083, AA5086 or AA5456, because Mg_2Si (Magnesium silicide) may developed in the weld zone to increase the crack sensitivity and decrease ductility.

1.1.8.2 ER5356

ER5356 is magnesium base aluminum alloy filler wire, in which up to 6% magnesium is used. This filler wire is most commonly used of other aluminum filler alloy due to its good feed ability and excellent tensile strength, this filler wire I mainly designed for 5xxx and 6xxx series alloy. ER5356 is not suitable for service temperature more than 65^0. The formation of Al_2Mg at elevated temperature at the grain boundaries makes the alloy prone to stress corrosion.

1.2 Solid state welding

In solid state welding processes, no external heat source is used to joining the base metal. In this processes, no filler rods are required and this welding does not involve molten state of parent metal or filler metal. Due to intermolecular diffusion process the weld formation is takes place and the interface molecules of work pieces' flows from high concentration region to low concentration region due to applied pressure. The solid state welding is widely used in automotive and aerospace industries because these processes does not affect the mechanical properties of the base metal. There are various types of solid state welding in which friction stir welding is most popular and effective solid state welding for aluminum and magnesium alloy.

1.2.1 Friction stir welding

Friction stir welding/processing is a method of changing the properties of a metal through penetrating localized plastic deformation. This deformation is produced by non-consumable tool which is inserted into the work-piece and revolving the tool in a stirring motion pushed laterally along the length of the work-piece. This technique is used to join multiple pieces of similar or dissimilar metal without creating the heat affected zone like of fusion welding. Friction stir welding was invented by the Wayne Thomas in 1991 by the welding institute Cambridge, U.K.

Because of porosity in the fusion zone (FZ), poor solidification, coarse grain structure, and loss in mechanical properties, the welding of aluminum alloy is very difficult by the conventional process. Friction stir welding process is used to weld aluminum alloy without any defect or FSW can improve the mechanical properties, fine grain structure at the welded region.

1.2.1.1 Working Principle

In friction stir welding a non-consumable rotating tool with pin and shoulder is inserted in to parent sheet to be welded as shown in fig.4. During this process, the tool has two primary functions moment of function and heating of work piece. The heating is obtained by friction between the tool and the work piece. There are different types of tool can be used in the friction stir welding, and the tool section criterion is completely dependent on parent material [1].

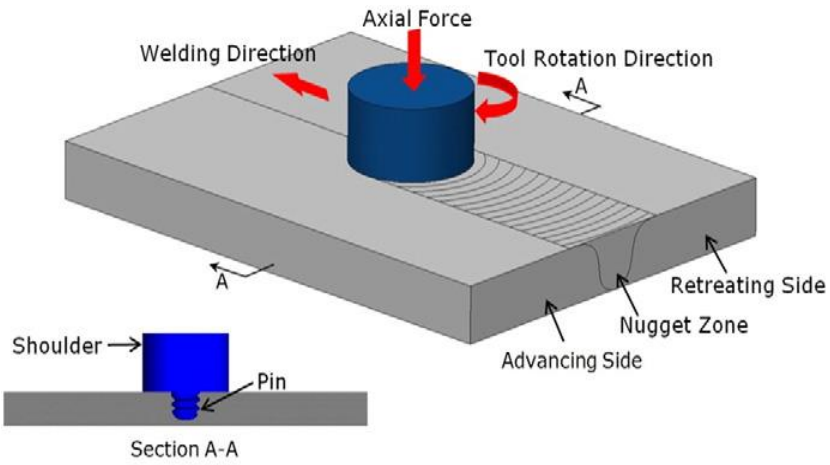

Figure 4: Friction Stir Welding

For aluminum alloy welding, tool of H13 and stainless steel generally preferred. The plastic deformation will occur at the tool contacting area in the work piece. Due to the combination of tool rotation and tool moment, the material flow from the front side of the pin to the back side of the pin.

When the direction of tool rotation is the same as the welding direction, then it is called advancing side (AS), whereas the other side is called retreating side (RS). When the tool moves with rotation speed and travel speed, then the material is moved from the edge of the tool to the rear edge and stirred by mixing of the pin rotation.

1.2.2 Advantages of friction stir welding

There are many advantages of friction stir welding over fusion welding, which are as follow.

- FSW improves the grain structure and provide excellent mechanical properties of welded joint as compared to other welding processes.
- The efficiency of welded joint can have improved up to (50-70%), depending upon the parent material.
- Similar or dissimilar welding can be done without melting or external heat source.
- Cracking, shrinking and porosity defects can be avoid/minimized.
- No filler material, spatter and shielding gas is required during friction stir welding process.
- Weld distortion and solidification defect can be eliminated completely.
- Friction stir welding is ecofriendly, it saves money and time.
- No high power source is required as compare to fusion welding.

1.2.3 Limitation of friction stir welding

There are some limitation/defect of friction stir welding, which are as follow.

- After welding process, when the tool is lifted at the end, a hole would be presented, which is main defect of friction stir welding.
- Clamping of parent material is very necessary for this process to prevent the joint from moving away.

- Welding parameter such as rotation speed, travel speed and tilt angle may change the properties of weldment.
- Same tool cannot be used for different material; tool specification may change according to the welding plate material.
- Friction stir welding is not so good for ferrous material. For welding ferrous material very hard and costly tool is required which may increase the cost of welded joint.
- If the rotating tool pin is not long enough then the interface at the bottom of the weld joint cannot be disrupted, because of this problem penetration defect may occur.
- Low rotation speed with high traverse speed cannot create sufficient weld temperature.

1.2.4 Friction stir welding tool materials

The FSW tool design including material and geometry is one of the most important parameter of welded joint. Many researchers have been studied on the tool material and their design. Welding tool geometry may have led the higher production speeds, improved joint efficiency and grain size also.

FSW tool consists of a pin and shoulder. The shoulder diameter is very large as compare to pin diameter. When the tool pin comes to contact with parent material create friction and heating and softens the parent material. Firstly, tool undergoes only rotational motion in one place until parent material goes to soften after the rotating motion the tool begins the forwarded to traverse motion along the welded joint and create a fine grain recrystallized microstructure behind the tool. The load which is produced along the welding direction is known as transverse load.

The tool material and their geometries are the scope the open literature of friction stir welding. Welding tool material development can improve the productivity and efficiency of welded joint. There are different types of tool materials are used in friction stir welding which are as given below.

1.2.4.1 Tool Steel

Tool steel like H13 is very common tool material which is used in friction stir welding for aluminum alloy, magnesium alloy and copper alloy. The advantages of tool steel include easy machinability and availability, low cost and have excellent mechanical properties. The tool steel H13 can be used for similar or dissimilar aluminum alloy. H13 tool steel have a resistance to damage from deformation and abrasion in the friction stir welding of aluminum alloy and other low melting temperature materials.

1.2.4.2 Nickel Cobalt base alloy

Nickel cobalt base alloys are developed to have high ductility, corrosion resistance and high strength. These alloys used for operating temperature must be less than the precipitation temperature range from 600-800^{0}C to prevent the dissolution and precipitate over-aging. Nickel cobalt base alloy tool is mainly designed for aircraft engine components.

1.2.4.3 Refractory Metals

The refractory metals such as molybdenum, tungsten, and tantalum are used for high temperatures and high densities parent materials for friction stir welding. These metals are the strongest alloy having melting point from 1000-1500^{0}C. The refractory metals tools are mainly design for welding of aluminum alloy, copper, steels and tungsten base alloy, but the main drawback of refractory metals are high cost, long lead time and difficult to machining.

1.2.4.4 Carbides and Metal matrix composite

Because of superior mechanical and physical properties (i.e. fracture toughness, wear resistance and ambient temperature) of carbide they are mainly used as machining tools. Friction stir welding tool such as tungsten carbide is reported to have fine and uniform welded surface with or without pin thread. Tungsten carbide is brittle in

nature and have very high strength due to bonding between tungsten and carbide atoms. Tis bonding also leads to have high melting point about 2800^0C. This tool is mainly used for copper, steel and aluminum alloy welding.

1.2.5 Friction stir welding tools design

A good tool design and correct material selection may change the weld characteristics and reduce the void size. A good quality and perfect designed tool may prevent the surface tears and reduce the flashing. The tool shoulder diameter and pin diameter design may play some significant roles in the welded joint. Additionally, tool pin can reduce tool stresses and provide better flow along the direction of welding. There are different types of tool design including shoulder design and pin design which are given below.

1.2.5.1 Shoulder design

The tool shoulder is used to produce heat between friction and material deformation to the surface region of the parent material. The tool shoulder produced frictional heat and deformation in thin sheet, whereas the pin produce heating in thick work-piece. The shoulder also produces downward forging force for weld consolidation. There are different types of shoulder used in friction stir welding, which are as given below.

1.2.5.1.1 Concave shoulder

Concave shoulder is most common and standard design for friction stir welding because they produce good quality welds, easily machined and simple design. The small angle from 6 to10^0 produced between the pin and the edge of the shoulder. The material displaced by the pin is fed into the cavity with in the tool shoulder. The friction stir welding tool shoulder can have to increase the amount of material deformation produced by the shoulder, resulting increase the proper mixing of base material and high quality weld. When the tool traverse speed increased, the concave shoulder has tendency to lift away the work piece surface, and when concave shoulder

replaces by the scrolled shoulder then they reduce the tool lift and increase the welding speed.

1.2.5.1.2 Convex Shoulder

Another type of friction stir welding tool is convex shoulder. Generally, this type of shoulder is not use because the convex shape pushed the base material away from the pin. This type of shoulder is reported successfully for very thin plate approx. 0.4 mm with tool shoulder diameter of 5 mm. The outer edge of the tool is not engaged with the work piece this is the only advantage of convex shape tool, so the tool shoulder may be engaged with the work piece at any location along the convex surface. There are two types of profile may be used of convex shoulder either tapered or curved profile.

1.2.5.2 Pin Design

The friction stir welding tool pin is designed for contacting the surfaces of the work piece and obtaining the heat through friction between tool pin and parent material. The tool travel speed and depth of deformation are governed by the pin design. In this section different types of pin design and their merit and demerit are discussed in open literature.

1.2.5.2.1 Round bottom cylindrical pin

Round bottom cylindrical pin are used to transport the material from the shoulder down to the bottom of the pin. The root diameter of the tool pin is 75-80% of the pin diameter. It means the diameter of pin root decreases up to the pin diameter as shown in fig. 5. The weld quality was observed by the various past researchers [2]. The flexibility of the round bottom cylindrical pin design is that the length of pin and diameter may be readily altered to suit the user's requirements. The tool life may increase by eliminating stress concentration at the root of the threads with the help of machining a root radius.

Figure 5: Design of round bottom cylindrical pin [3]

1.2.5.2.2 Flat bottom cylindrical pin

Flat bottom cylindrical pin is one of the most commonly used friction stir welding tool pin. The benefit of flat bottom cylindrical pin over round bottom cylindrical pin is that the velocity of rotating cylinder increases to a maximum value to the edge of the cylinder. The flat bottom cylindrical pin has a velocity 28 times the round bottom cylindrical pin, because of increased surface velocity, the throwing power of the flat pin also increases. The other advantage of flat over round is that the machining to flat pin is easier than the round pin and welding defect can be improved by the flat pin instead of round pin.

Figure 6: Design of flat bottom cylindrical pin [3]

1.2.5.2.3 Truncated cone pin

Past researchers were found that the cylindrical pin is sufficient for aluminum and magnesium alloy welding up to 13 mm thick plate, but they want faster travel speed of thick plates, so this reason truncated cone pin was introduced to increase the travel speed as well as decrease the welding time. The truncated cone pin has lower transverse load as compare to cylindrical pin. The design of truncated cone pin is design for high temperature material [4-6].

Figure 7: Design of truncated cone pin [3]

1.2.5.2.4 Thread less pin

Thread less pins are used in some specific friction stir welding application where thread pin feature could not survive without fracture. The threaded tool pin cannot retain at high temperature or high abrasive composite alloys without excessive pin wear.

Figure 8: Design of thread less pin [3]

1.2.6 Processing parameter of friction stir welding

In friction stir welding, the rotating and traverse speed of tool in contact with the parent material that initiates material flow, while at the same time the heat required to reduce the material flow stress and so allow for constant volume deformation to take place. Friction stir welding/processing involves material movements and plastic deformation, because of this the process parameters play an important role during the process. There are mainly three different types of process parameters like tool geometry, welding parameters and joint design. In tool geometry, the variable parameters are tool profile, shoulder diameter, plunge depth, pin profile and tilt angle. The welding parameters are tool rotational speed, and traverse speed. All parameters are represented in fig. 9. Past researchers have discussed about effect of process parameters during friction stir welded joint [7-10].

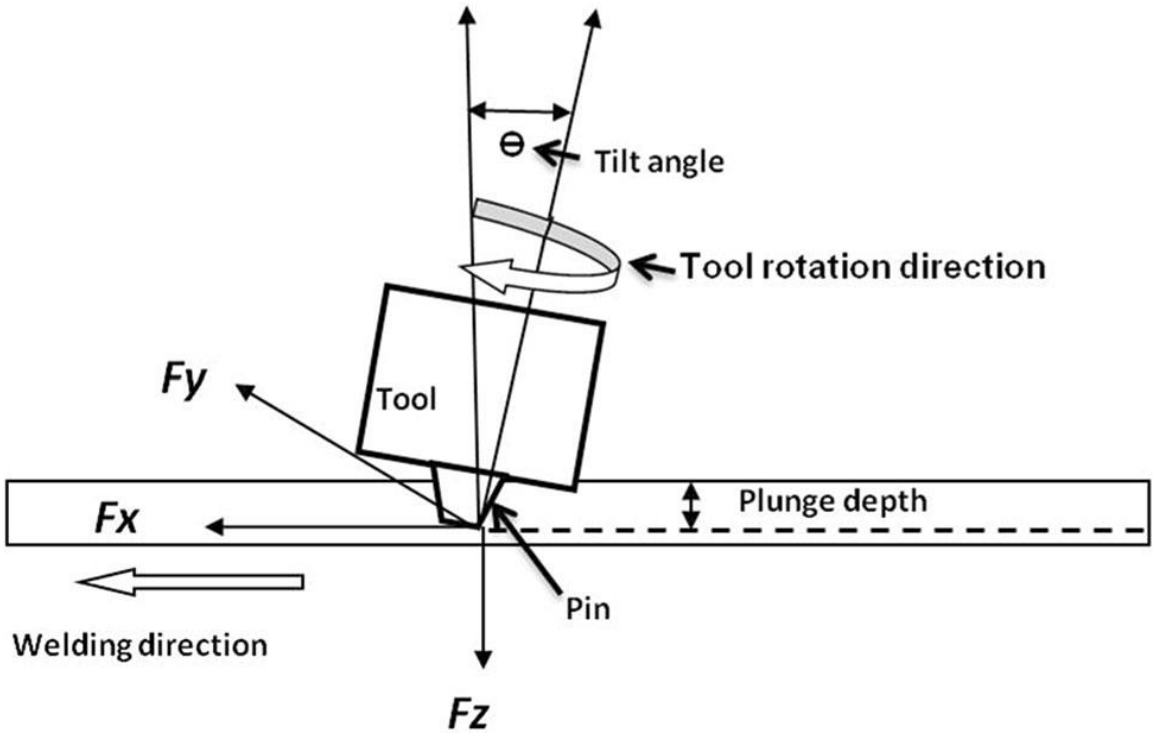

Figure 9: Schematic diagram for main process parameters of friction stir welding

Table 2: Effect of process parameters in friction stir welding

S.No	Parameters	Effect	Ref
1	Tool rotational Speed	The high tool rotation speed of FSW gives results in Friction heat, "stirring," oxide layer breaking, mixing of materials, good tensile strength of welded joint.	[11]
2	Traverse Speed	Increasing the tool traverse speeds decreased the peak temperature and hence caused to lower heat input during friction stir welding	[12]
3	Tilt angle	The tool tilt angle affects the material flow during the weld and thus the heat generation. In FSW, the heat is generated by friction and plastic dissipation	[13]

1.2.6.1 Rotational speed of tool

Tool rotational speed is one of the most important process parameter of friction stir welding. The enough heat and plasticized flow is obtained only when the tool rotation is high. The grain size and micro hardness of aluminum alloy

1.3 Aluminum alloy

In aluminum alloy, aluminum is the predominant metal. The major alloying elements which are used in different Al-alloys are copper (Cu), silicon (Si), magnesium (Mn), zinc (Zn), manganese (Mn) and tin (Sn). The most important aluminum alloy is silicon base alloy (Al-Si), where high percentage 3.5 to 12% silicon is used. Silicon base aluminum alloy have good casting characteristics. These alloys are widely used in automobile sector, aerospace engineering such as metal skinned aircraft etc. The second widely used alloy is magnesium base aluminum alloy. This alloys are lighter than the all-aluminum alloys. Aluminum alloy have an attractive appearance in its natural finish, which may be shiny, lustrous and soft. Aluminum alloy can re recycle from the scrap value and providing environmental benefits and economics. It has easily fabrication and joining ability. The physical, chemical and mechanical properties of aluminum alloys depend on composition of alloying elements (i.e. Cu, Si, Mg, Mn, Zn, Sn, and Fe), grain size and microstructure. The total amount of

alloying elements should be less than or equal to 10% and the impurity elements should be less than 0.15%. There are wide range of mechanical and physical properties of aluminum alloy over a steel which are as given below.

- The density of aluminum alloy is only 1/3rd that of steel.
- Aluminum alloys have high ultimate tensile strength, high toughness and highly ductility, and have high strength to weight ratio.
- Aluminum alloy have a high resistance to corrosion under critical service conditions and it's also used for cryogenic application
- Aluminum alloys are highly reflective material and it is an excellent conductor of electricity and heat.
- Aluminum alloys are nontoxic and non-ferromagnetic material and it can used for food and beverages containers.

1.3.1 Types of Aluminum alloys

On the basis of alloying elements, the aluminum alloy may be classified into different categories which are as given below.

1.3.1.1 1XXX series

In wrought aluminum having 1XXX series have present several elements as natural impurities in the smelter grade. Aluminum alloys 1100 and 1135 are the 1XXX series alloys. These alloys have specified minimum and maximum copper contents. Corrosion resistance, thermal conductivity and electrical conductivity of 1XXX series alloys is very high. The silicon, iron and copper are the alloying elements present in the highest percentage in 1XXX series. The high strength may be obtained by strain hardening.

1.3.1.2 2XXX series

In 2XXX series, copper (Cu) is the major alloying element and magnesium as secondary. For obtaining optimum mechanical and physical properties, these alloys required heat treatment. After heat treatment the mechanical properties of 2XXX

series are very similar or sometimes exceed the low carbon steel. The corrosion resistance properties of these alloys is not good as compare to other aluminum alloys or sometimes it shows intergranular corrosion. These alloys have high strength to weight ratio and it is commonly used to make aircraft wheels, structural parts, truck and suspension parts etc.

1.3.1.3 3XXX series

In 3XXX series, Manganese (Mn) is the major alloying element, the strength of 2XXX series alloys have 20% more than 1XXX series alloys. The alloys are not heat treatable but have high resistance to corrosion properties. The alloying element Mn is limited (up to 1.5%) present in the aluminum solid solution and form precipitates Al_6(Mn, Fe) or Al_{12} (Mn, Fe)$_3$Si phase. These alloys are widely used in cooking equipment, architectural product, chemical equipment's and resistance to corrosion.

1.3.1.4 4XXX series

In 4XXX series, silicon (Si) is the major alloying element. Silicon can be added in this series up to 12% to lowering the melting point without producing brittleness. Aluminum silicon alloys are mostly used in welding filler wire for joining similar or dissimilar aluminum alloy. Mostly these alloys are not heat treatable. ER4043 is widely used as a filler wire. Due to containing of silicon they are demanded in architectural application, production of forged engine piston etc.

1.3.1.5 5XXX series

In this series, magnesium (Mg) is the major alloying element. When it is used with manganese (Mn) give result moderate to high strength hardenable alloy. Mg is more effective than Mn as harder. 0.8% magnesium is equal to 1.25 manganese for hardened the alloys. The 5XXX series shows good resistance to corrosion in the marine atmosphere and also have excellent welding characteristics. Magnesium base aluminum alloy like ER5356 used as a filler wire to join the different aluminum alloys with TIG or MIG welding processes.

1.3.1.6 6XXX series

In 6xxx series, the principal alloying elements are magnesium and silicon, typically less than 1%each, and small amounts of copper, chromium, manganese and zinc. The magnesium silicate Mg_2Si is the hardening constituent in 6XXX series. The alloys are sensitive to weld metal cracking. The cracking may be readily prevented by the use of filler metals containing higher proportions of silicon such as ER4043 or with a slightly increased risk of hot cracking, the higher magnesium alloys such as ER5356.
The strength losses in the 6000 alloys are less in the naturally aged metal than in the artificially aged alloys. The strength of the weld and heat affected zone in the artificially aged condition generally drop to match that of the naturally aged alloy with a narrow solution treated zone either side of the weld and an over aged zone beyond this, which is weaker than the T6 condition. With controlled low-heat input welding procedures the strength of the weldment will not drop to that of an annealed structure but will be close to that of the T4 condition. These alloys are commonly used for automotive components and architectural extrusions.

1.3.1.7 7XXX series

7XXX series alloys may, from a welding point of view, be conveniently divided into two groups. The first group is the high-strength alloys containing more than 1% copper, normally used in the aerospace industry and joined by non-welding methods. The second group is the medium strength alloys which have been developed for welding. Aluminum and zinc form a eutectic containing solid solutions of 83% zinc in aluminum and 1.14% aluminum in zinc. The addition of magnesium complicates the situation with additional ternary eutectics and complex intermetallic being formed, these intermetallic providing dispersion hardening and precipitates of composition $MgZn_2$. Copper provides further precipitation hardening, forming $CuAl_2$ and an intermetallic of the copper zinc system.
One problem peculiar to the 7XXX series is that the zinc rapidly forms an oxide during welding, affecting the surface tension of the weld pool and increasing the risk of lack of fusion defects. This requires the use of welding procedures in which the welding current is some 10–15% higher than would be used for a 5XXX alloy. It has

also been found to be beneficial to use a shorter arc than normal so that metal transfer is almost in the globular range.

1.3.1.8 8XXX series

The 8XXX series is used to identify those alloys that do not fit conveniently into any of the other groups, such as 8001 (Al-Ni-Fe) and 8020 (Al-Sn). However, contained within this 8XXX group are the Al-Li alloys, a relatively new family that gives substantial weight savings of up to 15% and a higher Young's modulus compared with some of the other high-strength alloys. Each 1% of lithium added results in an approximate 3% reduction in weight. These advantages mean that significant weight savings can be achieved in the design of aerospace structures and that the very high-strength alloys, such as those in the 2XXX series, may be replaced by the weld able, lighter Al-Li alloys.

A further family of alloys that may fall into this group once they have been assigned a designation are those containing scandium. These are new alloys, still to a great extent in the development phase. Scandium is a rare earth element that has been found to be highly effective in increasing strength by age hardening and by grain refinement, the latter being particularly useful in weld metal. Scandium is likely to be used in conjunction with other alloying elements such as zirconium, magnesium, zinc or lithium where tensile strengths of over 600 N/mm^2 have been achieved in laboratory trials.

1.3.2 History of parent material

1.3.2.1 Aluminum alloy AA6061

The mechanical and physical properties of pure aluminum are fixed, when two or more metallic elements added in the pure aluminum alloy then new alloy blends the mechanical and physical properties to give better results, more flexible and more durable metal. Most of the aluminum alloy nearly as strong as steel. Aluminum alloy AA6061 was first developed in 1935 and is one of the most commonly available heat treatable Al-alloys for commercial use. This alloy is Mg and Si base alloy and it also

include Fe, Cr, Cu, Zn, Mn and Ti. Most of the aluminum alloys are difficult to weld because of their lack of conductivity and chemical composition whereas AA6061 is heat treated alloys.

The most common uses of AA6061 are manufacture of automotive components, bicycle frames, yachts, camera lenses, couplings and valves, electrical fitting etc.

1.3.2.2 Aluminum alloy AA7075

The aluminum alloys are largely used in aerospace engineering. In 19th century Count Ferinand Zeppelin used AA7075 to fabricate the frames of his iconic airships. The AA7075 was selected because it has excellent fatigue resistance, light weight, excellent mechanical properties, and high corrosion resistance and has similar strength like steel due to its high levels of zinc.

The writer Jules Verne was the first person to understand the potential of Al-alloy in the aerospace engineering. In World War I, the light weight Al-alloys became essential in aircraft design and development and in Second World War the production of aluminum alloys was increased

The aluminum alloy can be machined easily and hence it was high preferred for fighter planes in world II, including the Mitsubish A6M0 fighter used by Japanese imperial Navy on their carriers between 1940 and 1945. Now these days, the AA7075 is still used in military aircraft.

CHAPTER-2

Literature Review

2 Literature Review

Y. Wang, X.L Shi et al [14] studied the tensile properties of the as-extruded material and the welds with different FSW processing parameters was analyzed. The ductility of weld was improved to 11.6 % with slightly decrease in strength compared with base material. There was loss of yield strength from 633 MPa to 568 MPa. They find out that decreases in strength is likely to be a result of microstructure coarsening and analyzed the fine grained microstructures achieved through dynamic recrystallization during FSW.

IndrajeetCharit, R.S Mishra et al [15] fabricated of multi sheet structure via friction stir welding and analyzed with the help of diffusion bonding. The material is used for this experiment was superplastic 7475 aluminum alloy sheet having an actual composition of Al-5.69, Zn-2.42, Mg-1.47, Cu- 0.082, Si-0.095, Fe-0.026, Ti-0.21. They used single pass and six pass joint welding condition for 2.5 mm thick lap joint. The flown of material inside the nugget is evidence of substantial plastic stirring during FSW. The average grain size of the parent material is 10μm whereas microstructure of one pass & six pass nuggets are finer than the parent material and average sizes are 2.2 and 3.2 μm respectively. The value of yield strength, ultimate tensile strength and ductility of parent material are 398 MPa, 511MPa and 21.8% respectively. The corresponding value of single pass nugget are 402, 541 MPa and 31.4% and for six pass nugget are 334, 451 MPa and 31.8%. The microstructure in the weld HAZ is stable and retains superplastic properties. The high strength weld nugget, because of the high flow stress at 783K compared to parent metal.

J-Q. Su, et al [16] studied the heat affected zones of a friction stir weld of aluminum alloy 7050-T651 were investigated and compare with the unaffected base metal. Composition of 7050-T651 are 5.7-6.7 Zn, 1.9-2.6 Mg, 2.0-2.6 Cu, 0.08-0.115 Zr. He considered the DXZ consisted of re-crystallized, fine equiaxed grains on the order of 1-4 μm in diameter. Most of the DXZ grains contained a high dislocation density with various degree of recovery from grain to grain and along with rotation speed of pin was 350 rpm and travel speed was 15mm/min. Compared to parent material microstructure, the strengthening precipitates have coarsened severely and the precipitate free zone along the grain boundaries has increased by factor of five during friction stir welding, The original base metal grains structure is completely eliminated

and replaced by a very fine equiaxed grain structure in the dynamic re-crystallized zone (DXZ) and observed precipitates in the 7050-T651 base alloy are predominantly intra granular fine η less than 50nm with coarse η precipitates along grain boundaries.

Z.Y.Ma, R.S Mishra et al [17] studied that friction stir processing homogenizes and refines the cast microstructure, completely eliminated porosity and creates a microstructure with five Silicon particles distributed in a fine grain aluminum matrix in cast A356Al. The distribution of Si particles is not uniform throughout the aluminum matrix. While most Si particles exhibited a fibrous morphology. He used friction stir processing which resulted in a breakup of both the fibrous Si particles and the aluminum dendritic structure with a redistribution of Si particles in the aluminum matrix and found at the low tool rotation rate of 300rpm, the nugget zone of the sample did not exhibit an onion ring structure, as is often observed in transverse section in FSW/FSP aluminum alloys. During solid solution treatment at high temperature about 540^0C fibrous Si particles in the modified structure are fragmented and spheroidzed much more rapidly than the plate shaped Si particles in unmodified structure. FSP resulted in generated five grains of 3-4 μm in FSP A356 samples. FSP parameter did not exert a significant effect of grains size.

Patrick B. Berbon et al [18] analyzed of microstructure in hot isostatic pressing (HIP) and friction stir processing has been studied. There are three different areas are apparent, i.e. the dark areas consist of almost pure aluminum, whereas the brighter areas contain either fine or coarse Al_3Ti intermetallic. The microstructure developed due to the fast diffusion rate of aluminum at the HIP temperature compared with the difficult diffusion of the Al_3Ti intermetallic via aluminum and titanium diffusion. The aluminum rich area is here appearing as elongated dark strings. The homogeneity increased dramatically via friction stir processing. There are no traces of the pure aluminum area left and the largest intermetallic particles have a small size. The tensile properties of the material at different temperature has been studied. The strength is very high at the lower temperature. The ductility however is very poor. Improvement in ductility were due to a significantly improved homogenization of the microstructure during FSP.

Z.Y. Ma, R.S Mishra et al [19] studied the two fine grained 7075Al alloy with a grain size of 3.8 and 7.5 μm are obtained with different processing parameters in friction stir processing. The fine grain micro structure was stable at high temperature

about 490^0 for one hour. Grain size will decrease in the temperature range of 420^0-530^0 and strain rate range of $1x10^{-3}$ to 10^{-1}. For the 3.8µm 7075Al alloy, super plastic elongation of 1250% were obtained at 480^0 in the strain rate range of $3x10^{-3}$ to $3x10^{-2}$ s^{-1}, whereas the 7.5 µm 7075Al alloy exhibited a maximum ductility of 1042% at 500^0 and $3x10^{-3}$ s^{-1} and found decrease in grain size from 7.5 to 3.8 µm resulted in significantly enhanced superplastic ductility, reduced flow stress, reduced optimum temperature and a shift to higher optimum strain rates. Scanning electron microscope examination on the surface of deformed specimens revealed distinct evidence of extensive grain boundary sliding.

S.Jana, R.S Mishra et al [20], analyzed that, the influence of process parameter and FSP run configuration on the stability of nugget microstructure at elevated temperature has been evaluated. All single pass runs showed some extent of abnormal gain growth (AGG), whereas multi pass runs were more resistance to AGG. Cast Al-Alloy of F357 we used for this study. This alloy belongs to the hypoeutectic family of Al-Si system. The occurrence of abnormal grain growth increase when the tool rotation rate is reduced from 2236 rpm to 1500 rpm. The most notable feature of this investigation is the observation of change in the microstructural response of the nugget towards AGG as a function of number of passes inside the nugget. The multiple pass does not result in Si particles refined beyond a certain limit. The multi pass run of second configuration indicate that the extent of AGG can be reduced if the material is FSPed multiple times.

Jian Qing Su, T.W Nelson et al [21] studied friction stir processing is an efficient technique for grain refinement in metal and alloys using small tools and imposing rapid cooling, nanocrystalline structure were successfully produced in copper in a single step. Microstructure at the mid depth of the stir zone and various location behind the tool pin were examined in copper after FSP that had been conducted with continuous quenching to enhance cooling rate. The sub structure initially formed around pin tool consisting of very small crystallites having sizes of a few tens of nanometers. The material flow in a very thin layer around pin tool resulted in severe strain heterogeneity giving rise to highly concentrated micro plastic deformation at location with in this layer. Under such circumference a very high density of micro band structure was formed having units as small as few tens nanometer and containing no further substructure with in them.

Nilesh Kumar, R.S Mishsra [22] analyzed, that friction stir processing was used as a severe plastic deformation tool to process ultrafine grained micro structure FSP successfully produced a defect free bulk, equiaxed and homogenous ultra-fine grained microstructure by changing the process parameter, it was possible to control mean grain size and its distribution. The alloy was processed in as-received and aged (563K, 22 hours) condition and at three different tool rotation rates 800, 400 and 325 rpm. The grain size varied from 0.89 to 0.39 μm depending on the processing and initial thermos-mechanical condition of the alloy. The grain size reduction was observed with increase in Zener-Holloman parameter. Grain size analysis at different section and location on the transverse section of the dynamically recrystallized zone showed a homogenous and equiaxed microstructure the average dispersoid (Al_3(Sc,Zr)) size was ~8.0 nm in diameter obtained using high resolution transmission electron microscopy.

Z.Y Ma, S.R Sharma, R.S Mishra [23] studied, under the as-friction stir processing condition, both the strength and ductility of transitional zone were lower than those of the nugget zones. The strength of the previous FSP zones was lowered than that of the subsequent FSP zones further in the multi pass material, the strength of the previously processed zones was lower than that of the subsequent processed zones, due to over aging from the FSP thermal cycle. The strength of both nugget and transitional zone decreases with increasing distance from the 5^{th} pass processed zone, both the strength and ductility of the 5^{th} pass FSP nugget zone are similar to those achieved in the single pass FSP sample, furthermore both the tensile and yield strength of various micro-structure region in the present 5-pass FSP A356 achieved by mine tensile specimen are higher than those for large specimen.

Z.Y. Ma, R.S Mishra et al [24] analyzed, two pass friction stir processing with 50% overlap did not exert a significant effect on the resulting grains size in various zone of the second pass FSP compared to single pass FSP and two pass FSP resulted in an enhancement in superplastic elongation and a change in super plastic response. A shift to higher optimum temperature was observed in the two pass FSP 7075Al. Maximum superplastic elongation of 1220% was achieved at 480^0C and an initial strain rate of 10^{-2} s^{-1} in the center region of second pass in the two pass FSP 7075Al. In the initial strain rate range of $3x10^{-4}$ to $10^{-1}s^{-1}$ a strain rate sensitivity of 0.5 was observed for both single pass and two pass FSP 7075Al. this indicate that grain boundary (GBS) in

the main super plastic deformation mechanism which are evidenced by analyses of the superplastic data.

Jianqing Su, Jiye Wang et al [25] studied, Microstructural distribution and thickness of different region of the FSP samples strongly depended on the temperature distribution and cooling rates which is closely related to the processing parameters, compared with the base material the stir zone of FSP samples exhibit higher tensile strength and comparable ductility. The tensile strength was influenced by microstructure related to the prior β grains size and α colony size, which are controlled by processing parameters. The lower rotational rate and/or a higher traverse speed resulted in finer prior β grains and smaller α colonies, leading to a higher tensile strength. The higher yield and ultimate tensile strength of 1067 MPa and 1156MPa without any losses of ductility were achieved in 900 rpm/4IPM sample having the smallest prior β grains size of ~12μm. The development feature in the thermos mechanically affected zone (TMAZ), which usually could be marked by phase transformation in FSP Ti-6Al-4V.

Omar S. Salih et al [26], studied, the mechanical properties of aluminum matrix composite (AMCs) joined by FSW are largely dependent on the combined effect of both the composition of AMCs and the FSW processing condition, therefore the mechanical performance of FSW joints should be evaluated accordingly. Welding parameters such as tool rotation, speed, transverse speed and axial force have a significant effect on the amount of heat generation and strength of FSW joints. Microstructural evaluation showed the formation of tunnel defect due to inappropriate flow of plasticized metal. Microstructural evaluation of FSW joints clearly shows the formation of new fine grains and refinements of reinforcement particles in the weld zone with different amount of heat input by controlling the welding parameter.

S.R.Ren et al [27] analyzed that the higher tensile strength was obtained at tool transverse speed of 400 mm/min with 45^0 shear angle for Al-Mg-Si alloy, whereas lower tensile strength with nearly vertical fracture were observed at lower speed of 100 mm/sec.

Y.S. Sato et al [28], studied on friction stir welding to an accumulative roll-bonded aluminum alloy 1100 with ultrafine grained microstructure and high hardness. Friction stir welding suppressed large reduction of hardness in the accumulative roll-bonded material, although the stir zone and the thermo- mechanically affected zone

experienced small reductions of hardness due to dynamic recrystallization and recovery. Friction stir welding can effectively prevent softening in an accumulative roll-bonded Al alloy 1100 having an equivalent strain of 4.8 in the as- accumulative roll-bonded condition.

A. Barcellona et al [29], investigated two different materials namely AA2024-T4 and AA7075-T6 from a metallurgical point of view. Grain dimensions and insoluble particle densities were investigated both in the parent materials and in the joints. The percentage of insoluble particles locally decreases due to the tool pin action. The recrystallization phenomena occurring in the nugget zone contrast to material softening due to precipitates density decrease. The inhomogeneous decrease of the material mechanical characteristics is observed and in particular a reduction of the material micro-hardness values is obtained, with minimum value reached in corresponding of the thermally altered zones of the material.

T. Minton et al [30], presented methodology for determining, if a conventional milling machine is capable of being used to undertaken friction stir welding. The methodology is tested by producing same thickness welds of 6.3 mm and 4.6 mm 6082-T6 aluminum sheets. The micro hardness profiles across the tool shoulder diameter are presented in conjunction with tensile test results.

H.W. Zhang et al [31], simulated material flow in friction stir welding under different process parameter using finite element technique base on the nonlinear continuum mechanics. The material flow can be accelerated with the increase of the translational velocity and the angular velocity of the pin. The equivalent plastic strain distribution in the nugget zone can be affected by the variation of the axial load on the shoulder, but the ones in heat affected zone (HAZ) and thermos-mechanical zone (TMZ) are not affected. With the increase of the axial load, the equivalent plastic strain in the nugget zone can be increased. The flow of the material in front of the pin on the retreating side is faster, but the flow behind the pin on the retreating side is slower, and the increase of translational velocity or the angular velocity of the pin, the maximum material velocity can be increased.

Olivier Lorrain et al [32], performed experiments on two different pin profiles. Both pins are unthreaded but have or do not have flat faces. To investigate the material, flow the cross sections and longitudinal sections of weld were observed with and without the use of material marker. The material flow using classical threaded tool has

the same feature as the material flow using classical threaded tools. Material is deposited in the advancing side in the upper part of the weld and in the retreating side in the lower part of the weld. Macro section of the joints demonstrate that the zone influenced by the shoulder rotation along the thickness is thicker when increasing the product of the plunge force and the rotational speed and for the cylindrical pin than for the tapered pin with three flats.

CemalMeran et al [33], Investigated the characteristics of the structure, mechanical properties, and microstructure of friction stir welds of CuZn30. Because of not reaching the melting point of metal during welding, evaporation of zinc and copper which makes welding more difficult disappears in friction stir welding. The mechanical properties of obtained weld joints can reach to base metal strength level if suitable welding parameters are determined fractures usually occur either in the heat-affected zone or in the weld joint, however, fractures had occurred on base material under conditions of 2050 rpm and 112 mm/min. The surface of the base plate should be flat. The root joint of softened weld metal has occurred straight in this way.

HasanOkuyucu et al [34], developed an artificial neural network model for the analysis and simulation of the correlation between the friction stir welding parameters of aluminum plates and mechanical properties. It was found that the correlation between the measured and predicted values of tensile strength, the hardness of weld metal better than those of elongation and yield strength. The input parameters of the model consist of weld speed and tool rotation speed. The output of the artificial neural network model includes property parameters namely, tensile strength, yield strength, elongation, the hardness of weld metal and hardness of heat-affected zone. The good performance of the artificial neural network model was achieved.

Z. Zhang et al [35], analyzed the effect of transverse speed on friction stir welding by using a fully coupled thermos-mechanical model. The stirring effect of the welding tool becomes weaker, if transverse speed is high, which is the reason for the occurrence of weld flaw. The friction on the tool plate interface takes the main contribution to the temperature rise in friction stir welding. The material particles on the top surface at the advancing side are transported by the shoulder to the retreating side and piles up on the border of the nugget zone at the retreating side. This is a reason for the formation of weld flash in the friction stir process. When the transverse speed is increased, the contribution of the plastic deformation to the

temperature rise is increased. But the variation of the transverse speed does not significantly affect the power needed for friction stir welding.

Moataz M. Attallah, et al [36], investigated the fine weld nugget grain structure of friction stir welds undergoes abnormal grain growth in the post-weld solution heat-treated condition. Once the friction stir welding sheets are subjected to solution heat treatment, the welds experience abnormal grain growth within the surface of the sheet as within the swirl zone. The extent of abnormal grain growth depends on the welding parameters. Welds carried out at lower rotation speeds and higher feed rates are more susceptible to higher dominance for the abnormal grain growth microstructure.

Wang Kuai-she et al [37], conclude that ultrafine-grained microstructure with the mean grain size of ~0.7 μm is obtained in the weld nugget by using water cooling. However, The FSW joint exhibits softening compared with the ultrafine-grained based material and the heat-affected zone (HAZ) has the lowest hardness owing to the coarsening of the strengthening precipitates.

A. Pirondi et al [38], investigated the fracture toughness of the FSW joint is about 25% lower than the unwelded material in the case of W6A20A, while it is 10–20% higher in the case of W7A10A, the influence of FSW joining on Fatigue Crack Growth strength, in particular, at near-threshold crack growth rates, is the opposite as for the fracture toughness, i.e. crack propagation rate is lower than the in the unwelded material in the case of W6A20A, while it is higher in the case of W7A10A.

Y.G. Kim et al [39], examined that for different tool plunge down forces, the optimum FSW conditions of aluminum die casting alloy. The shape of the top part on the advancing side in the stir zone is completely different. For this type of defect, the effect of the tool plunge downforce is small, though the defect size gradually decreases with the increased downforce.

Yingchun Chen et al [40], investigate the effects of the base material conditions on the FSW characteristics. The experimental results indicated that the base material condition has a significant effect on weld morphologies, weld defects, and mechanical properties of joints. In the 2219-O welds, no discernible interface exists between the stir zones (SZ) and the thermal mechanically affected zone (TMAZ), and weld defects are liable to form in the lower part of the weld. In the 2219-T6 welds, there is a visible interface between the SZ and the TMAZ, and a weld nugget with an “onion ring”-like

morphology clearly exists. The strength efficiency of 2219-O joints is 100%, and one of the 2219-T6 joints is only up to 82%.

Yutaka S. Sato et al [41], The Al alloys 6063-T5 and T4 were friction stir welded at given rotational speeds, and then the distributions of microstructure and hardness were examined in these welds. The maximum temperature of the welding thermal cycle measured by a thermocouple rose sharply with increasing rotation speed up to 2000 rpm, beyond which it gradually rose. The grain size of the stir zone increased exponentially with increasing maximum temperature. The relationship between the grain size and the maximum temperature satisfied the static grain-growth equation. The hardness values in the as-welded condition were reduced around the weld center in the weld of Al alloy 6063-T5 and were distributed homogeneously in the weld of Al alloy 6063-T4. There was no significant difference in the hardness profile due to the different rotation speeds in these welds, except for the width of the softened region in the weld of Al alloy 6063-T5. Post weld aging led to an increase in hardness in most parts of the welds, but the overaged regions and the stir zone of the 800 rpm weld showed a small increase in hardness

Jerry Wong et al [42], conducted on 1 mm thick strips from a 6061T6 aluminum alloys that were welded together by the action of the rotating tool; the parameters that were varied in these tests were the rotating and advancing speeds. The specimens were sectioned to evaluate the joint strength. Metallographic analyses and Vickers microhardness indentations were carried out The stir zone present particularly fine equal axial grains, resulting from crystallization, and higher feed rates and intermediate rotating tool speed result in the better weld joint, the tensile test confirms those because is at this rotating speed when found better strain-stress combination. Lower advance and feed rate produce a dissolution of hardening precipitates, Mg_2Si for the present alloy, and enhanced precipitation due to the heat input.

Su et al. [43] studied the resulting microstructure of friction stir processed commercial 7075 Al alloy. The grain structure of the FSW processed area was examined by Transmission Electron Microscopy (TEM). The microstructure of the FSW area did not have a uniform grain size distribution. The average grain size slightly decreases from top to bottom. Also, diffraction rings were observed which, according to them confirm that there are large misorientations between the individual grains. Generally, the dislocation density was not uniform within the stir zone even

with similar grain size; this observation suggested that non-uniform plastic deformation was introduced in the recrystallized grains during FSP. By running multiple overlapping passes any desired sheet size can be processed to an ultrafine-grained microstructure. The investigations showed that multiple overlapping passes indicated can be used as an effective technique to fabricate large bulk ultrafine grain material with relatively uniform microstructure.

Peel et al. [44] reported the results of microstructural, mechanical property and residual stress investigations of AA5083 FSW. According to them, the weld properties were dominated by the thermal input rather than the mechanical deformation caused by the tool. Their results showed that increasing the traverse speed and hence reducing the heat input narrowed the weld zone, also that the recrystallization in the weld zone had considerably lower hardness and yield stress than the parent AA5083. It was observed that almost all the plastic flow occurred within the recrystallized weld zone and the synchrotron residual stress analysis indicated that the weld zone is in tension in both the longitudinal and transverse directions. The peak longitudinal stresses increased as the traverse speed increases. They suggested that this increase is probably due to steeper thermal gradients during welding and the reduced time for stress relaxation to occur. The tensile stresses appear to be limited to the softened weld zone resulting in a narrowing of the tensile region as the traverse speed increased.

Jata et al. [45], examined the microstructures of friction stir welds of Al-Li alloy using Optical and TEM microscopy to establish the mechanism of the evolution of microstructure in the dynamically recrystallized region of FSW welds. Using orientation imaging microscopy, many of the grain boundary misorientations created in the dynamically recrystallized region were observed to be between 15° to 35°. This suggested that the recrystallized grains in that region caused by a continuous dynamic recrystallization mechanism. It was concluded that the grain size was found to have the same dependence on the Zener-Holloman parameter as material deformed via the conventional hot working process for using reasonable estimates of the strain rate and temperature in the FSW nugget.

Bensavides et al. [46] investigated the microstructures of Al 2024 friction stir welds and compared the grain sizes of friction stir welding at room temperature (30°C) and at low temperature (-30°C). They observed that there was an increase in the weld zone

equiaxed grain size from the bottom to the top at room temperature but at low temperature, there is a smaller difference from bottom to top. Furthermore, the grain size is considerably smaller in the low-temperature weld. These observations are consistent with the grain growth relations which states that there is a direct relationship between temperature and grain growth. The average grain sizes obtained were measured to be between 3 and 0.65 μm.

Kwon et al. [47], investigated the hardness and tensile strength of the friction stir processed 1050 aluminum alloy. They observed that the hardness and tensile strength increased significantly with decreased tool rotation speed. At 560 rpm, the hardness tensile strength increased as a result of grain refinement by up to 37% and 46% respectively compared to the as-received material. The hardness was higher on the advancing side than that of the retreating side. The results demonstrate that the friction stir processing technique is highly effective for creating improved mechanical properties resulting from grain refinement.

Vijay Soundararajan et al [48], In their research thermo-mechanical simulation of friction stir welding can predict the transient temperature field, active stresses developed, forces in all the three dimensions and may be extended to determine the residual stress. The thermal stresses constitute a major portion of the total stress developed during the process. Boundary conditions in the thermal modeling of the process play a vital role in the final temperature profile.

P. Heurtier et al [49], in the present paper, a three-dimensional thermomechanical model for Friction Stir Welding (FSW) is presented. Based on the velocity fields classically used in fluid mechanics and incorporating heat input from the tool shoulder and the plastic strain of the bulk material, the semi-analytical model can be used to obtain the strains, strain rates, and estimations of the temperatures and micro-hardness in the various weld zones. The calculated results are in good agreement with experimental measurements performed on an AA2024T351 alloy friction stir welded joint.

Zhang et al. [50], represent the 3D material flows and mechanical features under different process parameters by using the finite element method based on solid mechanics. Experimental results are also given to study the effect of process parameters on joining properties of the friction stir welds. Numerical results indicate

that the tangent flow constitutes the major part of the material flow. The shoulder can accelerate the material flow on the top half of the friction stir weld.

G. Buffa et al [51], proposed a 3D numerical model, thermo-mechanical coupled for friction stir welding to use rigid visco-plastic material description and a continuum assumption for the weld seam. This model is capable of predicting the effect of process parameters on process thermos- mechanics, such as the temperature strain, strain rate as well as material flow and forces. It was found that an expansion of the heat-affected zone and an increase of the maximum temperature and maximum strain in the nugget with the decrease in advancing speed. Martial flow in the weld zone is non symmetrically side distributed about the weld line because the material flow during friction stir welding is mail y controlled by both advancing and rotating speeds.

L. Commin et al [52], analyzed that the temperature distribution is uniform along the weld length, whereas it is asymmetric between the advancing side and the retreating side, owing to the heat input generated by the plastic deformation, Stress levels observed are higher on the retreating side and Grain growth is observed with an increase in the processing parameters that promote heat generation. The grain size evolution is consistent with the models developed, taking into account the strain rate and the processing temperature.

G. Buffa et al [53], investigated the prediction of the residual stress distribution in friction stir welding of two AA6060-T4 aluminum alloy sheets of relevant dimension, based on both a rigid viscoplastic thermos mechanically coupled model and an elastoplastic thermos mechanically coupled.

C. Hamilton et al [54], developed the thermal model of friction stir welding that utilized a new slip factor based on the energy per unit length of the weld. The slip factor is derived from an empirical, linear relationship observed between the ratio of the maximum welding temperature to the solidus temperature and the welding energy. The thermal model successfully predicts the maximum welding temperature over a wide range of energy levels but supports the hypothesis that the relationship between the temperature ratio and energy level is characteristic of aluminum alloys that share similar thermal diffusivities. The thermal model can be used to generate characteristic temperature curves from which the maximum welding temperature in an alloy may be

estimated if the thermal diffusivity, welding parameters, and tool geometry are known.

C. Hamilton et al [55], proposed the Johnson-cook plasticity model in order to account for heat generation due to plastic deformation for a thermal model of friction stir welding. This proposed formulation is derived from an empirical, linear relationship observed between the ratio of the maximum welding temperature to the solidus temperature of the alloy and welding energy. The thermal model accurately predicts the maximum weld temperature and temperature profiles at the higher energy weld conditions, i.e. 300 and 400 rpm. At the lower energy welds (i.e. 225 and 250 rpm) where plastic deformation contributes a larger portion to the total heat generation, the model under-predicts the maximum weld temperatures under the tool shoulder.

Mohamed Assidi et al [56], the accurate 3D simulation software, which allows modeling the entire complexity of the friction stir welding process, makes it possible to follow a much more rigorous inverse analysis approach. A friction stir welding trial is conducted on an AL 6061 aluminum plate with an unthreaded concave tool. Force and tool temperatures are accurately recorded at a steady welding state, for different welding speeds. The numerical simulations are based on an arbitrary Lagrangian-Eulerian (ALE) formulation that has been implemented in the forge3 F.E. software. The main feature of the numerical approach is to accurately compute the contact and frictional surface between the plate and the tool. The welding forces and tool temperatures are highly sensitive to small variations of friction, which allows accurate identification of the friction coefficient.

R. Nandan et al [57], investigated theoretically and experimentally 3-D viscoplastic flow and heat transfer during friction stir welding of mild steel. Non-Newtonian viscosity for the metal flow was calculated. The computed result showed significant viscoplastic flow near the tool surface, and convection was found to be the primary mechanism of heat transfer in this region. The maximum strain rate during friction stir welding of mild steel was 40 s^{-1} and the maximum viscosity, above which no significant material flow occur was found to be $9.9x10^{6}$ Pa s.

M. Maalekian et al [58], analyzed the heat generation rate in orbital friction welding of steel bars using different methods, constant coulomb friction, sliding sticking friction. The temperature-dependent thermal conductivity, specific heat and yield

strength are considered. All approaches represented the actual heat generation rate is deduced by comparing the predicted and measured temperature data. The results show that the inverse heat conduction method is the most accurate approach, and best represents the actual heat input in the FSW.

L. Commin, M et al [59], studied the temperature advancement during friction stir welding and the resulting residual stresses of AZ31 Mg alloy. The relationship between the processing parameters, the heat, and the plastic deformation produced and the resulting microstructure and mechanical properties were investigated. The grain growth prompted when increasing the shoulder diameter or the tool rotation speed or decreasing the welding speed produced an increase in the heat generated during the process. The temperature distribution on the advancing side and on the retreating side differed and the stress levels were higher on the retreating side.

Z. Zhang et al [60], developed the thermomechanical model to predict the material deformations and temperature histories in the friction stir welding process. According to this model, the maximum temperature in the friction stir welding process can be increased with the increase of the rotating speed, and welding speed can lead to an increase of the efficient input power for friction stir welding system. The increase of the rotating speed and the decrease of the welding speed can lead to an increase in the stirring effect of the welding tool, which can modify the friction stir weld quality. When the welding speed becomes higher, the rotating speed must be increased simultaneously to avoid any possible welding defect such as void, it also increases the residual stress when rotating and the translating speeds of the welding increased.

D. Jacquin et al [61], developed a simplified thermo-mechanical model for friction stir welding, this model predicts the temperature contours in the welded zone, power dissipation, and the sliding ratio on the interface between the shoulder and the workpiece. The analysis of the result concerning the contact conditions provides interesting data about the evolution of the relative sliding between the shoulder and material to be welded. The sliding ratio increases with the tool rotational velocity and decreases with the temperature in the vicinity of the tool. The velocity fields are introduced in a steady-state thermal calculation to compute the temperature field during welding. They allow partial sliding between the shoulder and the workpiece, the amount of which is provided as an additional result of the model.

2.1 Effect of Tool pin profile

The effect of tool pin profile on mechanical and microstructure properties of similar or dissimilar friction stir welded joints of aluminum alloys were investigated by various researchers [62-70] and conclude the various outcomes which are as follows.

2.1.1 Tensile Properties

The tool pin profile plays a crucial role in the mechanical properties of the FSW welded joint. The tool pin generally has frustum tapered, threaded, cylindrical plain and flat surface. Pin profiles with flat faces (triangular and suare0 are associated with eccentricity. This eccentricity allows incompressible material to pass around the pin profile [62-63].

Table 3: Mechanical properties of FSW joint of Al7075 and Al6061 [64]

Tool Pin	Sample	Position of Plate	Tensile strength (MPa)	Yield Strength (Mpa)	Elongation (%)
Straight Cylinder	1	RS-Al6061 AS-Al7075	140.21	124.53	3.2
	2	RS-Al 7075 AS-Al 6061	196.96	174.13	8.8
Straight square	3	RS-Al6061 AS-Al7075	168.03	151.6	4.4
	4	RS-Al 7075 AS-Al 6061	181.2	163.76	9.2
Tapered Hexagon	5	RS-Al6061 AS-Al7075	184.5	164.15	6
	6	RS-Al 7075 AS-Al 6061	171.4	152.11	6.4

The tensile strength and yield strength of sample 2 are better than the other samples. In a straight tool pin profile, it is observed that the positioning of the plates of the same nature (sample 2 and 4) give better tensile strength, yield strength and %

elongation, when compared to reverse the position of the plates (Sample 1 and Sample 3) due to rapid solidification. Because of the sharp edge, the straight cylinder tool pin profile obtained higher mechanical properties than the other pin profile as shown in table 3 [64].

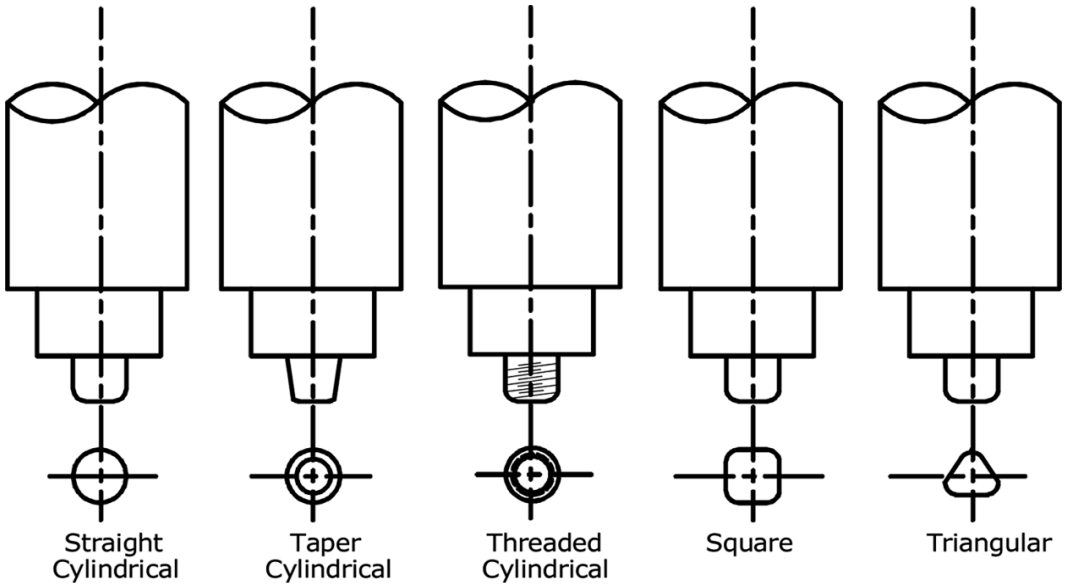

Figure 10: Five different tool profile [65]

Five different tool pin profiles (tapered cylindrical, triangular, straight cylindrical, square and threaded cylindrical) have been used to fabricate the joints at different tool rotational speed (800-1600 rpm) and observed that the joint fabricated using square pin profiled tool with a tool rotational speed 1200 rpm exhibited superior mechanical properties compared to other tool profiles [65].

The friction stir welded joint with square pin profiled has high tensile strength as compared to other joints. The least tensile strength was observed by the tapered square pin profiled tool. The other tool pin profile like tapered hexagon, hexagon, tapered octagon and octagon does not change the tensile strength significantly due to the difference in the dynamic orbit created by the eccentricity of the rotating tool of the friction stir welding process [66].

2.1.2 Micro-hardness

The effect of tool pin profile on micro-hardness of FSW welded joint was studied by different researchers. Five different tool pin profiles has chosen and found the highest

hardness value (87 HV) by using square pin profile and lowest hardness value (60 HV) was observed in straight cylindrical profile tool as shown in fig.11 [65].

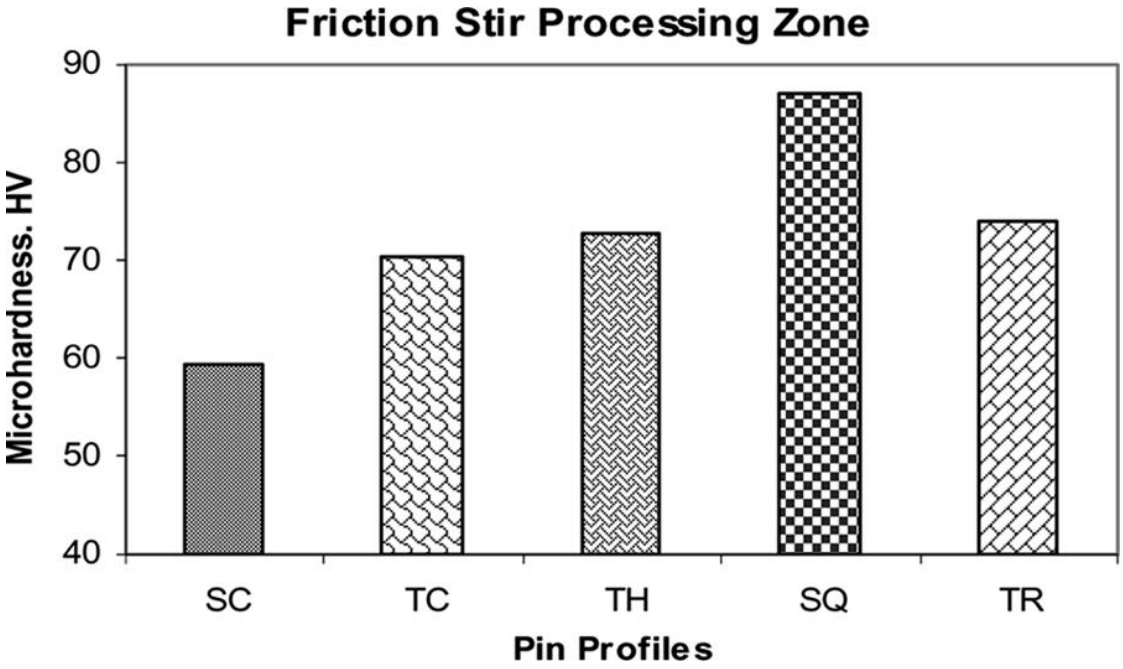

Figure 11: Effect of tool pin profiles on FSP zone hardness at rotational speed 1200 rpm [65]

Square and triangular pin profiles with flat faces are associated with eccentricity. The eccentricity allows incompressible material to pass around the pin profile. The influence of pin profile on micro-hardness of the FSW welded joint of AA6061 was investigated [67] and found maximum hardness using threaded pin profile because the joints from the threaded pin profile contain very fine equiaxed grain structure compare to other.

To investigate the material, flow the cross-sections and longitudinal sections of weld were observed with and without the use of a material marker. The material flow using the classical threaded tool has the same feature as the material flow using classical threaded tools. Material is deposited in the advancing side in the upper part of the weld and in the retreating side in the lower part of the weld. The Macro section of the joints demonstrates that the zone influenced by the shoulder rotation along the thickness is thicker when increasing the production of the plunging force and the rotational speed and for the cylindrical pin than for the tapered pin with three flats [68].

2.2 Effect of tool rotational speed

2.2.1 Tensile strength

The tensile characteristics of butt joint of friction stir welding of Al-6063 and Al 5083 have been investigated and they observed that the tensile strength and hardness increased significantly with the increase in tool rotational speed as shown in fig.12.

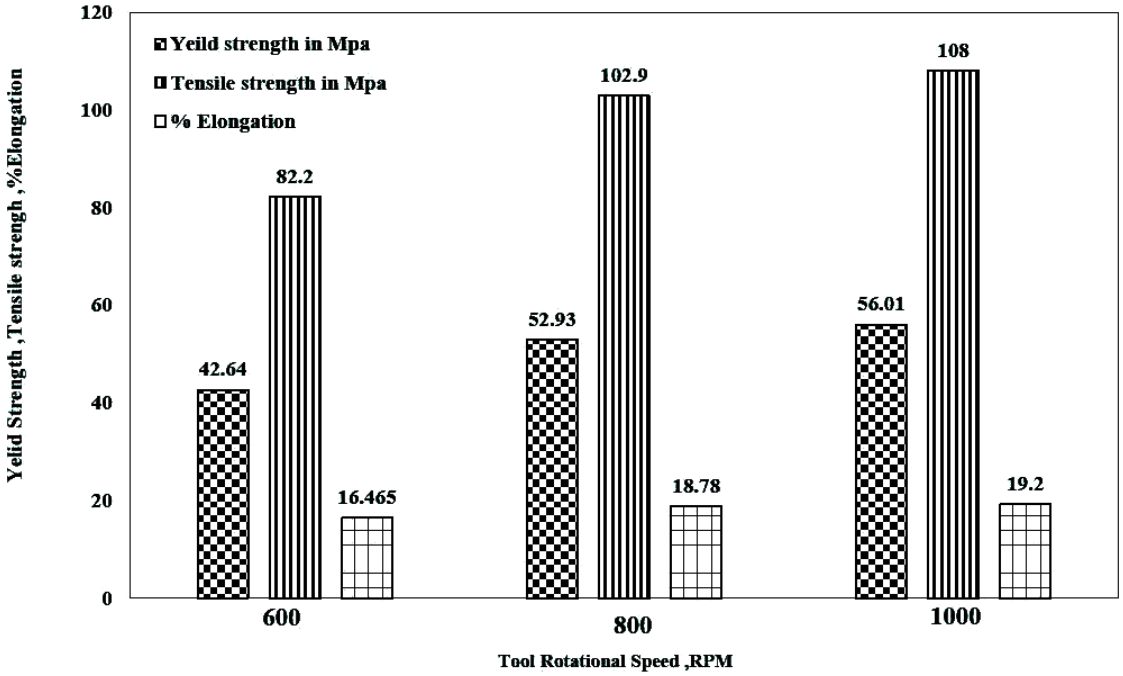

Figure 12: Effect of tool rotational speed on tensile properties [69]

The experiments were conducted for different tool rotational speeds of 600, 800 and 1000 rpm with an axial load of 4kN and a welding speed of 40 mm/min [69]. The essential nature of the use of higher rotational speed for providing good heat input thus obtained high tensile strength and reveal that the ductility of the stir zone is lower than the base material.

The highest hardness value (74.2 HB) was obtained at tool rotational speed of 1000 rpm whereas minimum hardness value (64.61 HB) was obtained at 600 rpm. The flexural strength and impact strength decreases when the tool rotational speed rises, whereas the tensile strength and hardness increase. The impact strength of FSW weld

joints has been evaluated for different tool rotational speeds. These are 0.46, 0.45 and 0.42 J/mm^2 for 600, 800 and 1000 rpm, respectively [69].

2.2.2 Micro-hardness

The friction stir welding of AA6061 has been investigated and they observed that the hardness of SZ increased with increasing tool rotational speed. The lower cooling rate was recorded in higher tool rotational speed because the SZ reached an excess temperature. At low heat input, fine grain structure was observed leads to high strength and hardness [70].

When the tool rotational speed increases the frictional heat also increases due to the increasing residing time of the tool. The hardness of the FSW of the AA5083 stir zone decreased with increasing tool rotation speed. The average grain size at the SZ (i.e. 0.23, 0.35, and 1.28 mm) with a speed of 250, 320, 800 rpm respectively, i.e., the grain size increased with the rotation speed increases. The increase in grain size led to the lower hardness value of the stir zone which was produced at the higher rotation speed [71]. The microstructure and mechanical properties as a function of rotation speed in underwater friction stir welded aluminum alloy joints were observed. A softening region having a lower hardness than the parent metal (PM) (120-130 HV) is produced in all the joints welded at different rotation speeds, which is a typical characteristic for the FSW of heat treatable aluminum alloys. The width of the softening region increases with the increase of rotation speed [72].

When the rotation speed is low (e.g. 600 rpm), the strain hardening of the low-density dislocations is insufficient to recover the strength loss induced by precipitate deterioration, and thus the lowest hardness is in the SZ. In the case of high rotation speeds, the hardness of the SZ is improved due to the increase in dislocation density, and then the lowest hardness location is shifted to the TMAZ or the HAZ.

If the rotation speed increases up to a rather high value (e.g. 1400 rpm), the heat input plays the dominant role and lowers the hardness minimum markedly. In friction stir welded AA 7010 aluminum alloy, when the spindle speed was increased, the hardness levels at the base of the weld increased more rapidly than at the top, so that the hardness values converge at high spindle speeds. This behavior corresponds to the

development of more uniform temperature distribution within the nugget zone, as the heat input was increased [73].

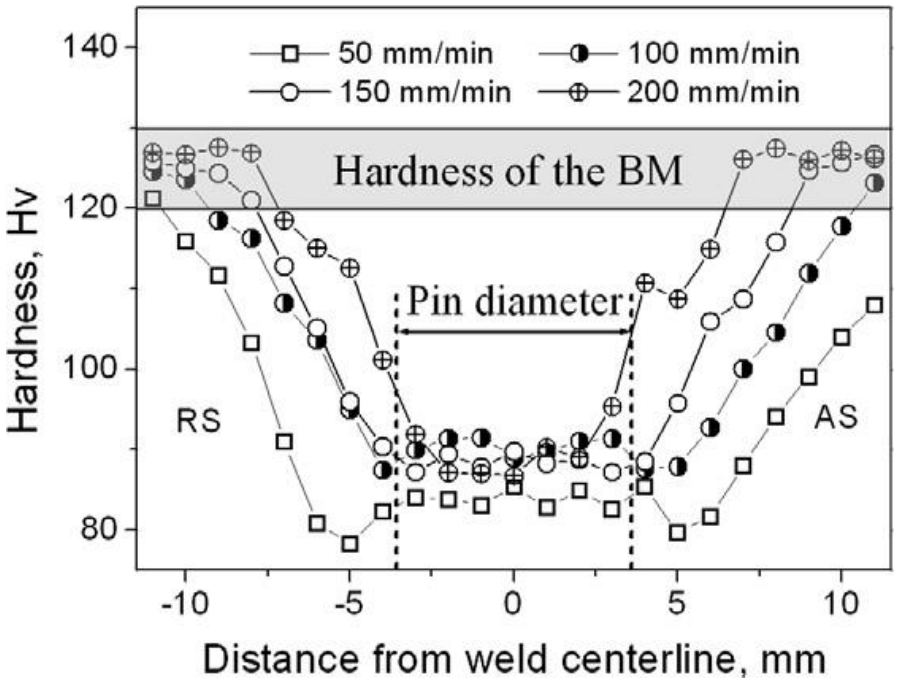

Figure 13: Micro-hardness distributions of the joints welded at different welding speeds [72]

2.2.3 Microstructure

Tool rotation speed appears to be the most significant process variable as it tends to influence the translational velocity. Higher tool rotation speed resulted in a higher temperature and slower cooling rate in the (friction stir processing) FSP zone after welding. A higher tool rotation speed makes the excessive release of stirred materials to the upper surface, which resultantly left voids in the FSP zone. But lower heat input conditions caused by lower tool rotation speed resulted in a lack of stirring. The area of the FSP zone decreased with the decrease in the tool rotation speed and influenced the temperature distribution in the FSP zone [74]. Microstructure and mechanical properties as a function of rotation speed in underwater friction stir welded aluminum alloy joints were studied. Fig. 14 shows the cross-sections of the underwater joints. In the figure (and throughout the paper), retreating and advancing sides of the joint are abbreviated as RS and AS, respectively. Three microstructural zones, i.e. SZ, TMAZ,

and HAZ are identified in the joints, as denoted in Fig. 14 c, with increasing rotation speed, the SZ presents a size increase in the lower part, implying the strengthening of the tool pin effect on material plastic flow near the bottom surface.

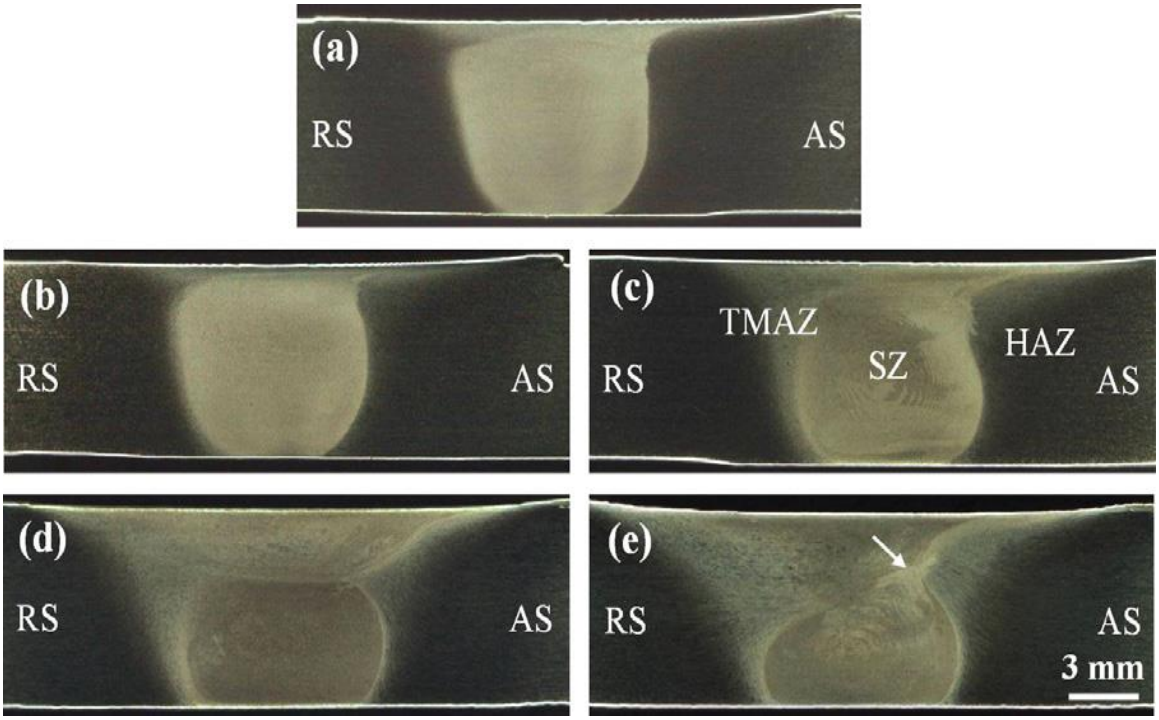

Figure 14: Cross-sections of the joints welded at different rotation speeds: (a) 600 rpm, (b) 800 rpm, (c) 1000 rpm, (d) 1200 rpm and (e) 1400 rpm [75]

At the rotation speed of 600 rpm, the TMAZ is not evident from the cross-section owing to the small size. Above 600 rpm, the TMAZ becomes discernible and its size increases progressively with the rotation speed. No welding defects are detected in the joints under the rotation speed range of 600–1200 rpm. However, at the high rotation speed of 1400 rpm, a large amount of fine voids are formed in the SZ. The exact location of the void defect is marked by an arrow in Fig. 14e [75].

The weld nugget zone (WNZ) was formed by the mixing of deformed material from both sides of the plates. The formation of this WNZ was due to the abrasion, wear and shearing of dissimilar material by tool rotating action [76], so, the tool rotational speed has a greater effect on material flow behavior and surface morphology. It is observed that the grain size decreases from the material towards the WNZ. The friction stir processing parameters, forged force and tool design impact on the size of recrystallized grains in the welded material [77]. The influences of tool rotational

speed on microstructure in the FSW process have been studied and observed that recrystallized grain size can be reduced bt decreasing the tool rotation speed and overall heat input [78].

2.3 Effect of tool traverse speed

2.3.1 Tensile Strength

The tool travel speed has greater force on the grain growth of the friction stir welded AA 2095 aluminum alloy. It was also reported that the variation in both the strength and ductility was a part of the tool travel speed [79]. The percentage of the contribution from the different FSW process parameters has been investigated. The survey concluded that the tool travel speed contribution was 33 % towards the tensile force of the FSW joints [80]. FSW was conducted at a constant rotation rate of 600 rpm together with different welding speeds of 25, 50, 100, 150 and 200 mm/min. Fig. 15 shows the tensile properties of the joints welded at various welding speeds. It can be observed that the ultimate tensile strength (UTS) and elongation have similar variation trends. Both increase at first and decrease finally with increasing welding speed. It is noted that the UTS and elongation of joints obtained at the welding speed range of 25–150 mm/min have little change, and their highest values are corresponding to the welding speeds of 50 mm/min and 100 mm/min, respectively [81].

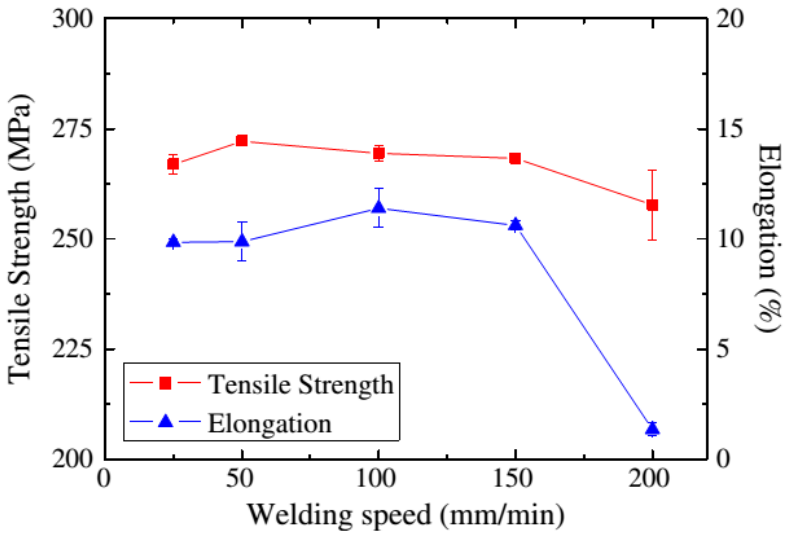

Figure 15: Effect of welding speed on tensile properties [81]

2.3.2 Micro-hardness

The effect of tool rotational speed on friction stir welded joint of Al 7075-T6 joints on hardness characteristics were investigated. The hardness profile indicates a decrease in the hardness compared to that of the base alloy. This behavior has been attributed to the dissolution of precipitates into the solution and subsequently, the weld cooling rates do not favor nucleation and growth of all the 25 precipitates.

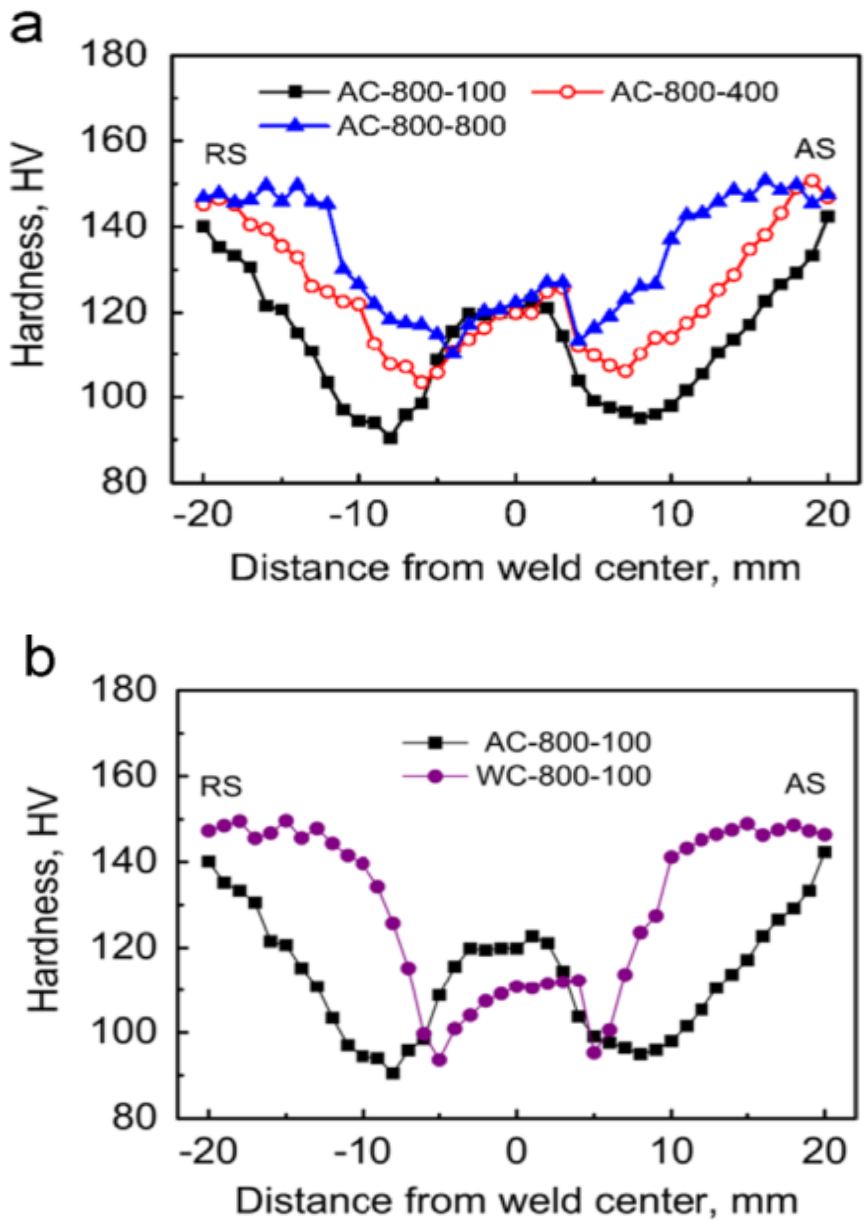

Figure 16: Micro-hardness profiles of FSW 2014Al-T6 joints showing effect of (a) welding speed under normal welding condition, and (b) water cooling [83]

The main reason for this behavior may be attributed to grain refinement in the weld zone. The material that flows around the tool undergoes intense plastic deformation at elevated temperatures, normally leading to a very fine grain structure in the center of the weld region in addition to redistribution of the precipitates to creation in inhomogeneity on the microscopic scale [82].

The effects of the welding speed and water cooling on the hardness profiles of the FSW 2014Al-T6 joints under air cooling and water cooling was studied [83]. All the hardness profiles exhibited a "W" shape with a low hardness distribution region (LHDR) on both AS and RS of the FSW joints and the hardness of the SZ was lower than that of the PM (Fig. 16). At a constant rotational rate of 800 rpm, increasing the tool travel speed from 100 to 800 mm/min enhanced the hardness values of the LHDR and moved their position towards the weld center (Fig. 16a). The water cooling exerted no noticeable influence on the hardness values of the 26 LHDR but moved the position of the LHDR towards the weld center (Fig. 16b). Furthermore, the water cooling reduced the hardness of the SZ [83].

2.3.3 Microstructure

Few researchers revealed that wormholes are formed in welds, as a result of insufficient material flow towards the bottom of the weld, and also because of inadequate heat under the tool shoulder. At a constant tool rotational speed, an increase in the tool travel speed leads to wormhole initiation near the bottom of the weld, and a high weld pitch ratio. This is the ratio of the traverse speed to the rotational speed; is also known to cause wormholes in welds. Friction stir welded AA2095 at higher welding rates resulted in shorter exposure times at higher temperatures [84].

Fig. 17a–e shows the precipitates lying on {1 0 0} planes of the matrix in the Base material, Heat affected zone (HAZ) and thermo-mechanically affected zone (TMAZ) of the welded joints. The plate-like precipitates densely distributed in the BM, 54 nm in diameter and 4 nm in thickness, is believed to be Meta stable θ' phases. The θ' precipitates can be coarsened, transformed into a stable state or dissolved into the matrix during FSW with increasing the temperature level. At a lower welding speed of 50 mm/min, the θ' precipitates in the HAZ exhibit a significant coarsening and a

dramatically decrease in density (Fig. 17b). The size of the precipitates is 114 nm in diameter and 25 nm in thickness, much larger than that of the BM. In the TMAZ, the θ' precipitates nearly disappear and have been transformed to the block-shaped equilibrium h precipitates (Fig. 17d). The considerably low density compared to the BM implies that precipitate dissolution should also occur in the region. However, when the welding speed increases (e.g. 150 mm/min), the precipitate evolution exhibits quite different features. In the HAZ, the size of the h precipitates only reaches 70 nm in diameter and 7 nm in thickness (Fig. 17c), and the precipitate density is also higher than that obtained at 50 mm/min, suggesting a remarkable lowering in precipitate coarsening level. On the other hand, a large quantity of θ' precipitates having a diameter of 90 nm and a thickness of 18 nm are still distributed in the TMAZ (Fig. 17e), indicating that the precipitate deterioration in the TMAZ is also retarded by increasing the welding speed [72].

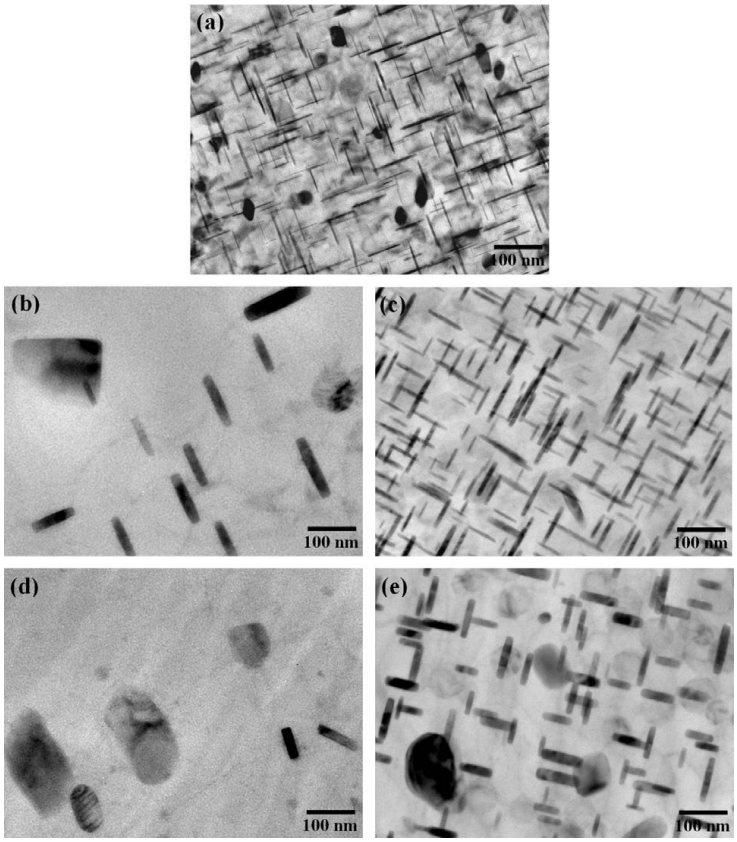

Figure 17: precipitates distributed in different zones of the joints welded at different welding speeds: (a) BM, (b) HAZ formed at 50 mm/min, (c) HAZ formed at 150 mm/min, (d) TMAZ formed at 50 mm/min and (e) TMAZ formed at 150 mm/min [84]

Welding at the higher rates resulted in a structure with a higher dislocation density because of the limited time available for recovery process. The faster the welding rate the higher was the dislocation density generated which resulted in an angled dislocation structure, indicating an early stage of dynamic recovery. The effect of tool traverse speed on microstructure and they inferred that the base material had an elongated coarse grain structure, while the stir zones consisted of equiaxed grain structures. Grain size in the stir zone increased with an increase in the heat input during FSW. Welds with lower welding speeds proved that the grains contained many sub boundaries. The sub grain size increased with the increasing heat input during FSW. It is inferred that the greater heat input resulted in larger grains with a lower density of dislocations and sub- boundaries in the stir zone [85].

2.4 Effect of tool tilt angle

2.4.1 Tensile strength

The influence of tool tilt angle on mechanical properties of FSWed joint of AA5083 have been studied. It was observed that the tool tilt angle influenced on tensile properties of welded joint. The FSW joint fabricated at tilt angle 1^0 has shown the lowest tensile strength whereas maximum tensile strength was observed at tilt angle 4^0. The tunnel defect occurred at tilt angle 1^0, 2^0, and 3^0. These defects generally occurred in advancing side of the WNZ. On the other side defect free joint produced at tilt angle 4^0 [86]. The tensile strength increases with increase the tool tilt angle. It is due to surface contact between tool shoulder and work-pieces. At lower tool tilt angle, large surface contact between tool and work-piece causes excess heat generated. Excessive heat in weld region results, pulling the plasticized material apart from welds line and produce defective joints. At higher tool tilt angle, the flow of plasticized material is sufficient due to good forging action. Good forging action leads to less porosity, fine and homogeneous grains. So, high tensile strength was achieved [87].

2.4.2 Micro-hardness

The variation of micro-hardness and different tilt angle are shown in fig. 18. It was observed that the micro-hardness value in the WNZ was increases as the tilt angle increases from 1^0 to 3^0. Minimum micro-hardness value (260 HV) was observed in the stir zone at tilt angle 1^0, whereas maximum micro-hardness value (300 HV) was observed in the stir zone at angle 1^0 for dissimilar aluminum alloy AA1100 and A441. The increase in micro-hardness is stir region can be attributed to dynamic recrystallization which has occurred during the friction stir welding process. Because of the rise in the overall heat generation and extraction of base metals in to the stir zone, formation of intermetallic compounds increases as tilt angle increases [88].

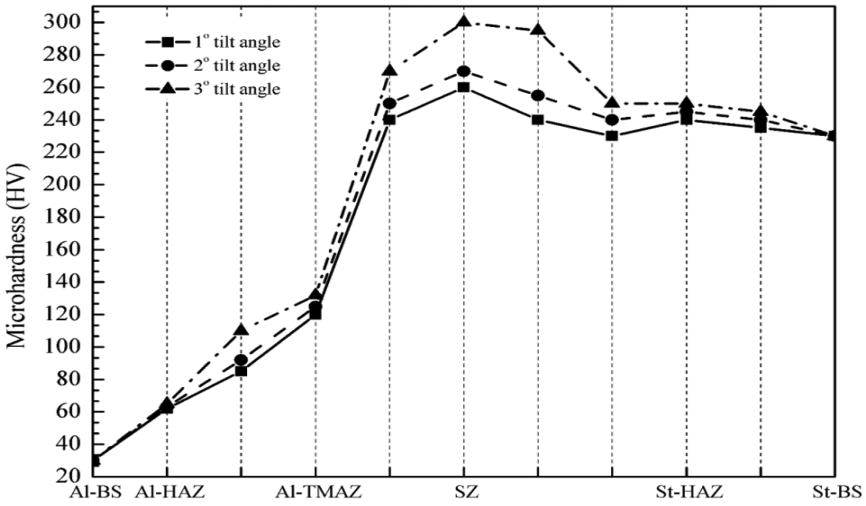

Figure 18: The micro-hardness of joint at different tool tilt angle [88]

The micro-hardness distribution of friction stir welded joint fabricated by various tilt angles (1^0-3^0) as shown in fig.18. The FSW joints experienced plastic deformation followed by dynamic recrystallization in the stir zone. The maximum micro-hardness value (132 HV) was observed at tilt angle 2^0. It is also observed that the micro-hardness in the stir zone increasing when increasing tilt angle from 1^0 to 2^0.

This is due to formation of fine and recrystallized grains and the density distribution of precipitates in the stir zone, whereas, two lowest hardness are observed at TMAZ/SZ on both advancing and retreating sides which are caused by dissolution or coarsening of strengthening precipitates due to peak temperature [89].

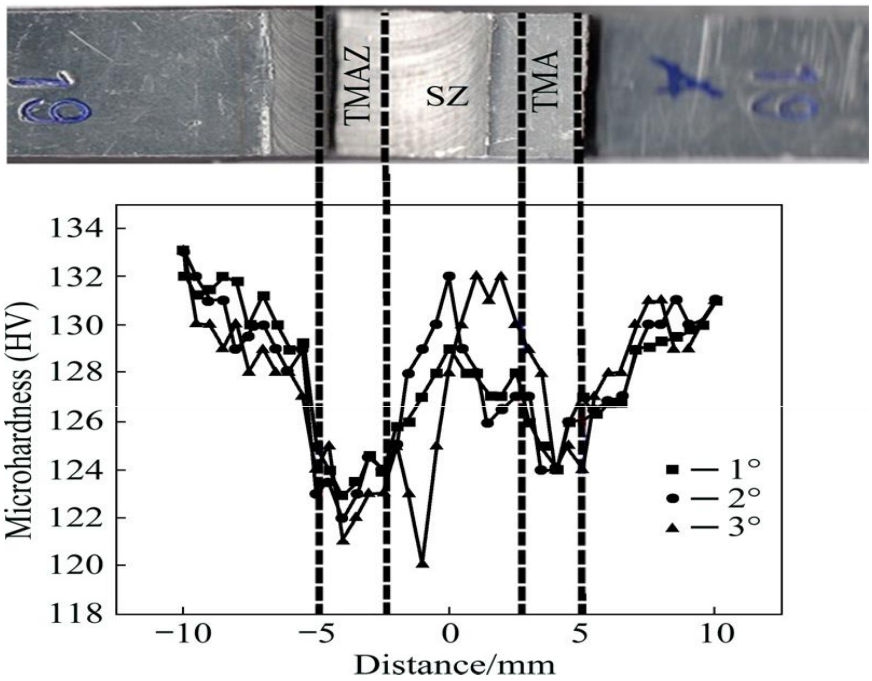

Figure 19: Micro-hardness distribution of FSLW joints [89]

2.4.3 Microstructure

The microstructure in various region of friction stir welded joint of AA2014-T6 at different tilt angles (1^0-3^0) are shown in fig. 20.

All the stir zones extensively contain equiaxed and fine grains followed by dynamic recrystallization which could be observed by thermo-mechanical action of tool and axial force during the friction stir welding. The tool tilt angle has a relationship with an axial force which gives more heat. This shows that the stir zone is subjected to severe plastic deformation. The stir zone of welded joint with tilt angle 3^0 exhibits three onion ring region and many numbers of concentric circles one over by another as shown in fig. 20c. Furthermore, the stir zone area is increased to 9.3 mm with an increase in the axial load, but the effective sheet thickness is reduced to 1.73 mm due to the partial amount of plasticized material expelled in the form of flash by the rotation of tool shoulder. The micrograph thermo-mechanically affected zone on advancing side reveals coarse and elongated grains, which are formed due to the imparted stress forms due to the rotation of tool shoulder and traverse speed of the tool during the welding process as shown in figures 20 (d-f) [89].

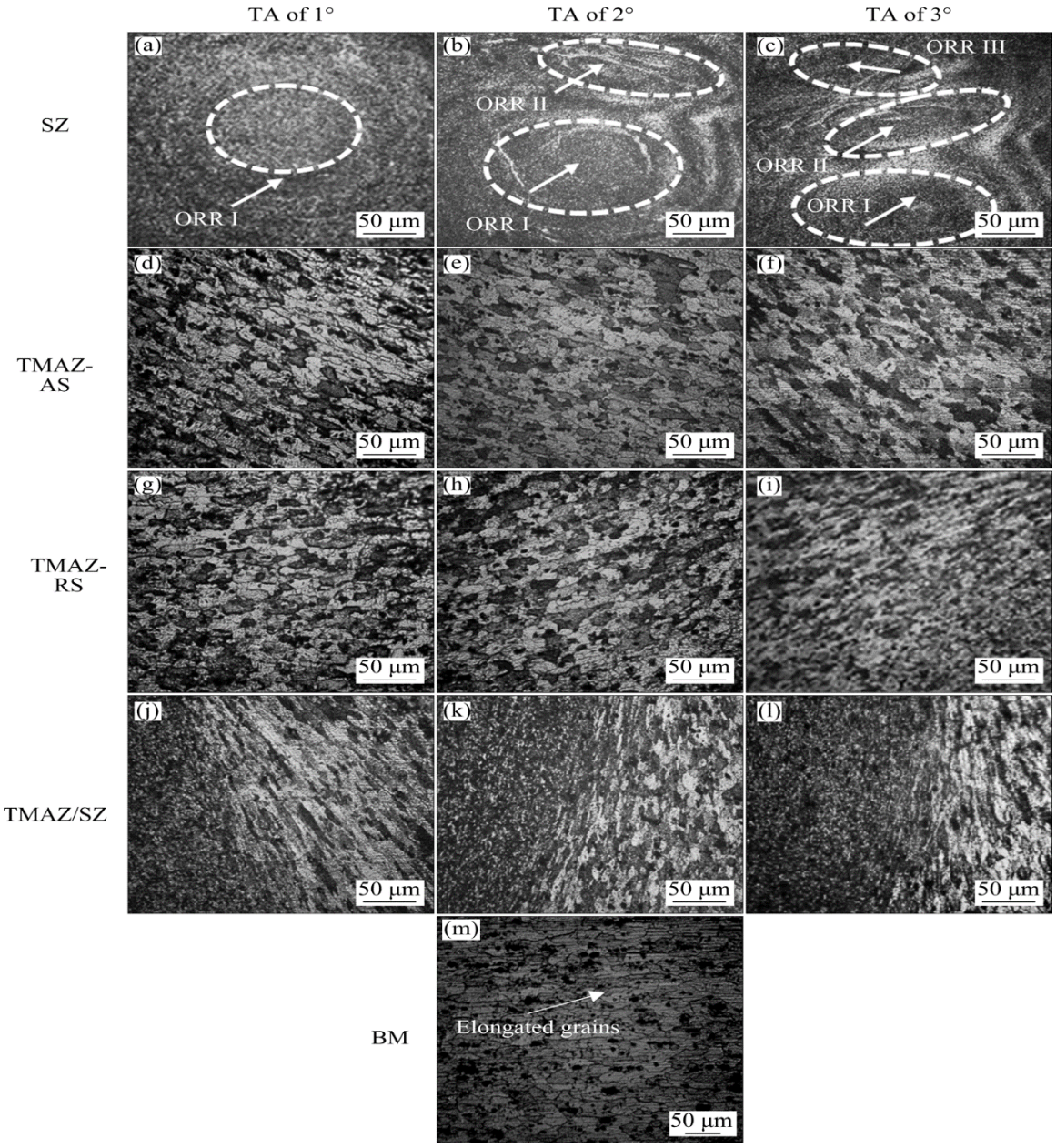

Figure 20: Micrographs of FSLW joints at different Tilt angles [89]

The effect of tool tilt angle on friction stir welded joint of AA2014-T6 have been investigated. The tool tilt angles were varied from 0^0 to 3^0 at an interval of 0.5^0. It was observed that the defect size reduced gradually from the lower tool tilt angle to a higher tool tilt angle as shown in fig. 21. Increase in tool tilt angle in the sharp increase in Z- torque, X load and Z load with a slight increase in temperature. High torque, temperature, and load indicate that term material is heated up to a wider extent and stirred adequately to fill the cavities left unfilled at a low tool tilt angle. The

increase of tool tilt angle also results in an increase of forging action on the trailing edge of the weld thereby filling the cavities which remain at lower tool tilt angle [90].

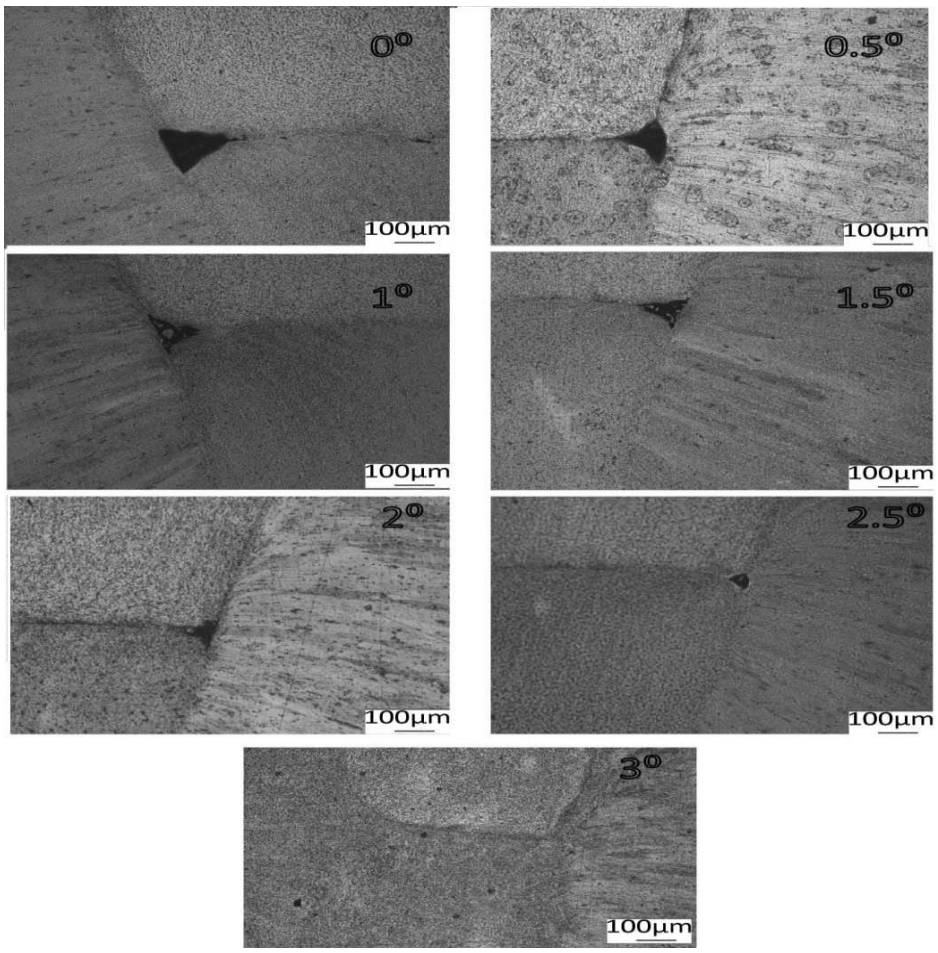

Figure 21: Defect size at different tool tilt angle [90]

2.5 Effect of post weld heat treatment (PWHT)

2.5.1 Tensile strength

Heat treatable aluminum alloys acquired their strength from hardening precipitates. After solution heat treating, the distribution of these precipitates is optimized through aging processes, i.e. controlled heating and cooling. The strengthening precipitates in heat treatable aluminum alloys are needle-like or plate-like phase structures that are finely and uniformly distributed. These precipitates hinder dislocation movement and the strength is improved. On disruption of precipitation distribution, lead to decrement in the strength [91]. The effect of post-weld heat treatment on the plastic deformation

behavior of friction stir welded 2024 - O aluminum alloy at annealing temperatures from 250 °C to 450 °C with an interval of 50 °C for 2 hours, followed by cooling to 200 °C in the furnace have been studied. The plastic deformation of as-welded joint is very heterogeneous. In contrast, the plastic deformation of PWHT joint is relatively homogeneous by both the nugget and the base material showing large deformation. The decrease in elongation of as-welded joints is completely recovered by PWHT. The high ductility of the joint is mainly attributed to the retention of the fine-equiaxed grains in the nugget during PWHT [92]. The effect of cyclic solution treatment on microstructure and mechanical properties of friction stir welded 7075 Al alloy have ben studied. The results showed that precipitate particles of the welding area before and after heat treatment are $MgZn_2$ and $MgAlCu/A_{l7}Cu_2Fe$, respectively. Cyclic solution treatment (CST) improves tensile strength and elongation while homogenizes the hardness distribution of the FSWed joint. A noteworthy enhancement in the hardness (~ 45%) and tensile strength (~33%) of the FSWed sample is achieved after CST and aging at 130 ˚C for 24 h. The tensile fracture surface of the Al alloy joint demonstrates fine dimples after CST while less developed dimples are detected after aging [93]. The post weld heat treatments increased the size of aluminum grains in all zones of friction stir weld joints. Abnormal grain growth was observed in entire zone modified by friction stir welding in case of solution treated joints with and without artificial aging. The naturally aged joints offered the highest mechanical properties while solution treated joints offered lowest mechanical properties of the joints. Naturally aged joints yielded highest tensile strength (94.9%) and elongation (174.2%) efficiencies while artificially aged joints yielded highest yield strength efficiency (96.7%). Further, post weld heat treatment also affected fracture location and mode of fracture [94].

The effects of initial temper condition and post weld heat treatment on the properties of dissimilar friction-stir-welded joints between AA7075 and AA6061 aluminum alloys. The authors concluded from their investigation PWHT generally resulted in an increase in the strength values of both O and T6 joints; thus, very high joint performance values in terms of tensile strength were obtained, i.e., higher than 85 % as shown in fig.22 [95].

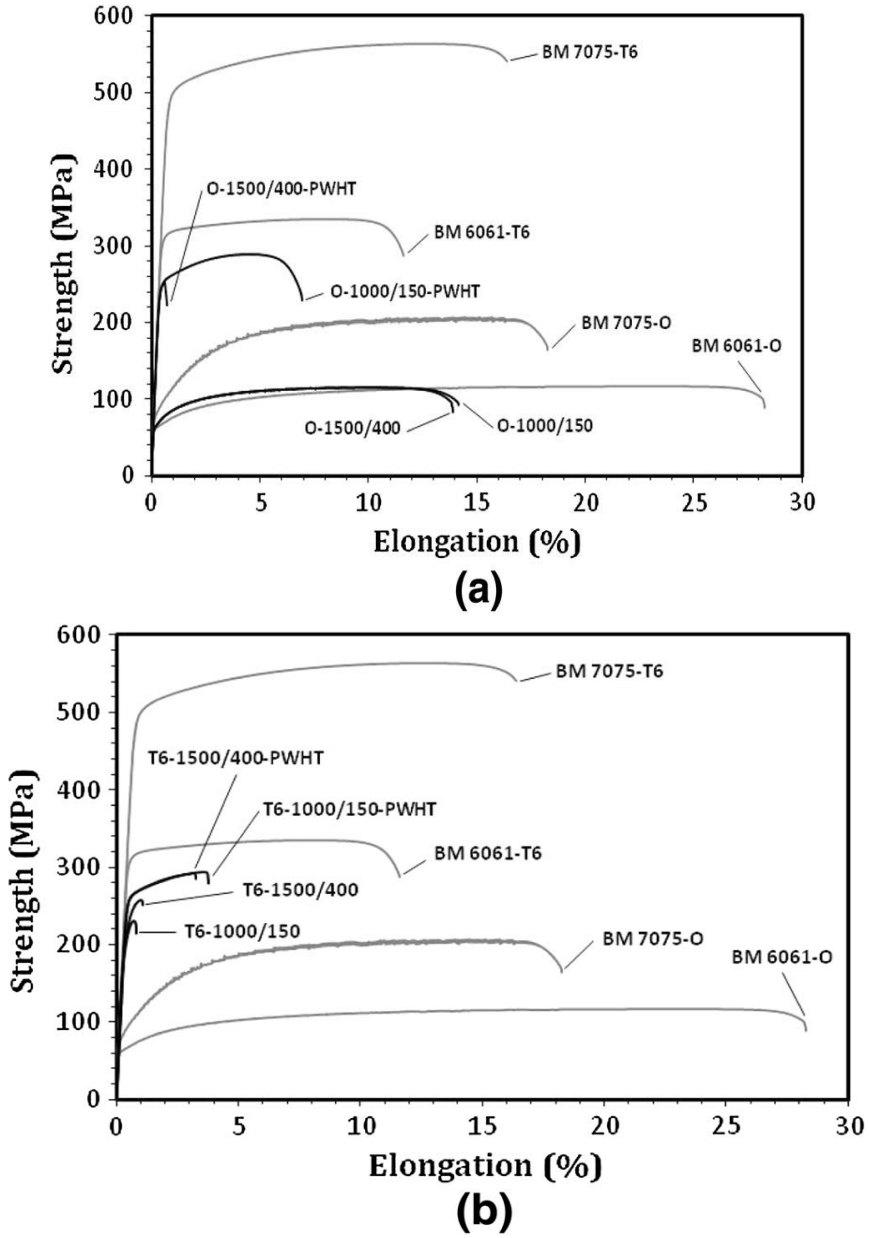

Figure 22: Stress strain diagram, (a) O joints, (b) T6 joints [95]

2.5.2 Micro-hardness

The effect of post-weld heat treatment on the mechanical properties of 2024-T4 friction stir-welded joints have been studied. Solution heat treatment and various ageing treatments were carried out to the welded joints. The PWHT procedures caused abnormal coarsening of the grains in the weld zone, which resulted in a drop in micro-hardness at the weld zone compared to the base material of the joints. T6 (190°C-10 h) ageing treatment after welding was found to be more beneficial than the other heat treatments in enhancing the mechanical properties of the 2024-T4 joints.

However, the T6 (190°C-10 h) heat treatment led to significant ductility deterioration in the joint. The micro-hardness across the weld zone of PWHT joints vary depending on the PWHT procedure as shown in fig. 23. The hardness values in the FSW zone for all PWHT joints are lower than those in base metal of the joints [96].

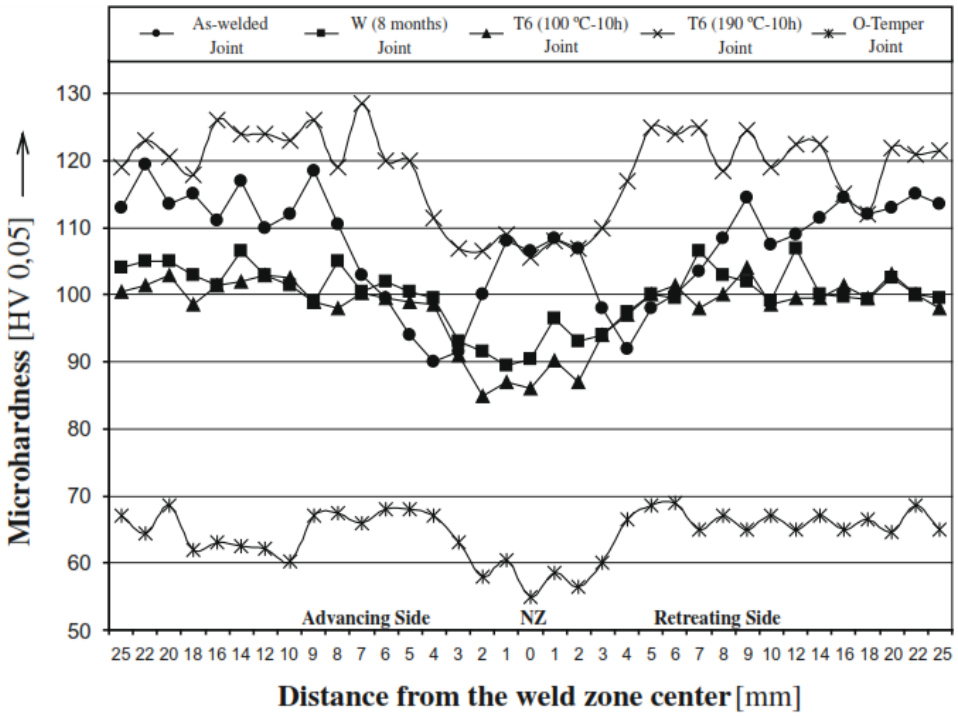

Figure 23: Micro-hardness distributions in the joints [96].

The micro-hardness of stir zone (SZ) at as-weld state and post-welding natural aging (PWNA) state under different heat input conditions were investigated for friction stir-welded joints of 2024 aluminum alloy thin-sheets. Examination of tested results reveals that welding heat input has obvious effect on the hardness of the SZ. Under the high welding heat input condition, the hardness of the SZ is lower than that of the parent metal (PM). However, under low welding heat input condition, the hardness of the SZ exhibits strong dependency on the rotational speed of the stirring tool. With increasing the rotational speed of the stirring tool, the 40 hardness of the SZ increases. The average hardness in the SZ of the joint welded at 1500 rpm and 1000 mm/min achieves the PM level. In comparison, the effect of the PWNA on the improvement of the hardness in the SZ is limited. The variation in the strengthening-phase particles plays a more important role than does grain size in the SZ for the improvement of

hardness. The minimum hardness values for the welded joint in air, cold water and hot water are 105, 114 and 115 HV respectively [97].

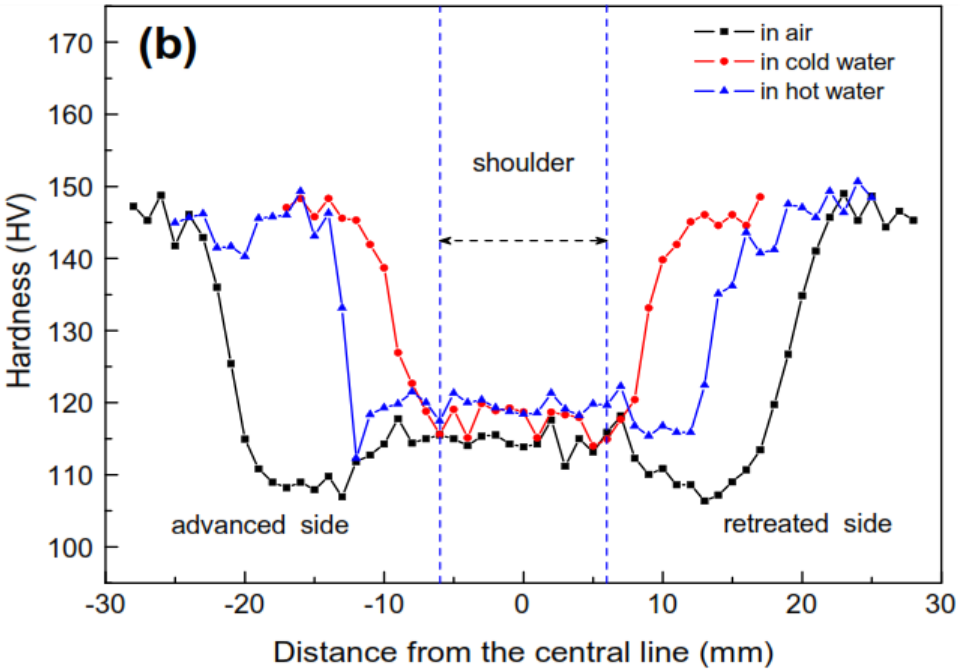

Figure 24: Distribution of micro-hardness under different welding ambient conditions [97]

2.5.3 Microstructure

The microstructural softening and the natural aging observed in the dynamic recrystallized zone and thermo mechanically affected zone are mainly caused by the frictional heating from the tool shoulder, resulting in dissolution and re-precipitation of strengthening precipitates [98].

The Precipitate evolution in friction stir welding of 2219- T6 aluminum alloys. From the study, it was found that the strengthening precipitates morphology in the WNZ is significantly different from that in the PM. The precipitates distribute on the fine grains (Fig. 25a). The precipitate is characterized by selected area diffraction (SAED). The SAED result shows that the diffraction spots are from θ phase, which indicates the presence of a high volume fraction of θ phase in this region.

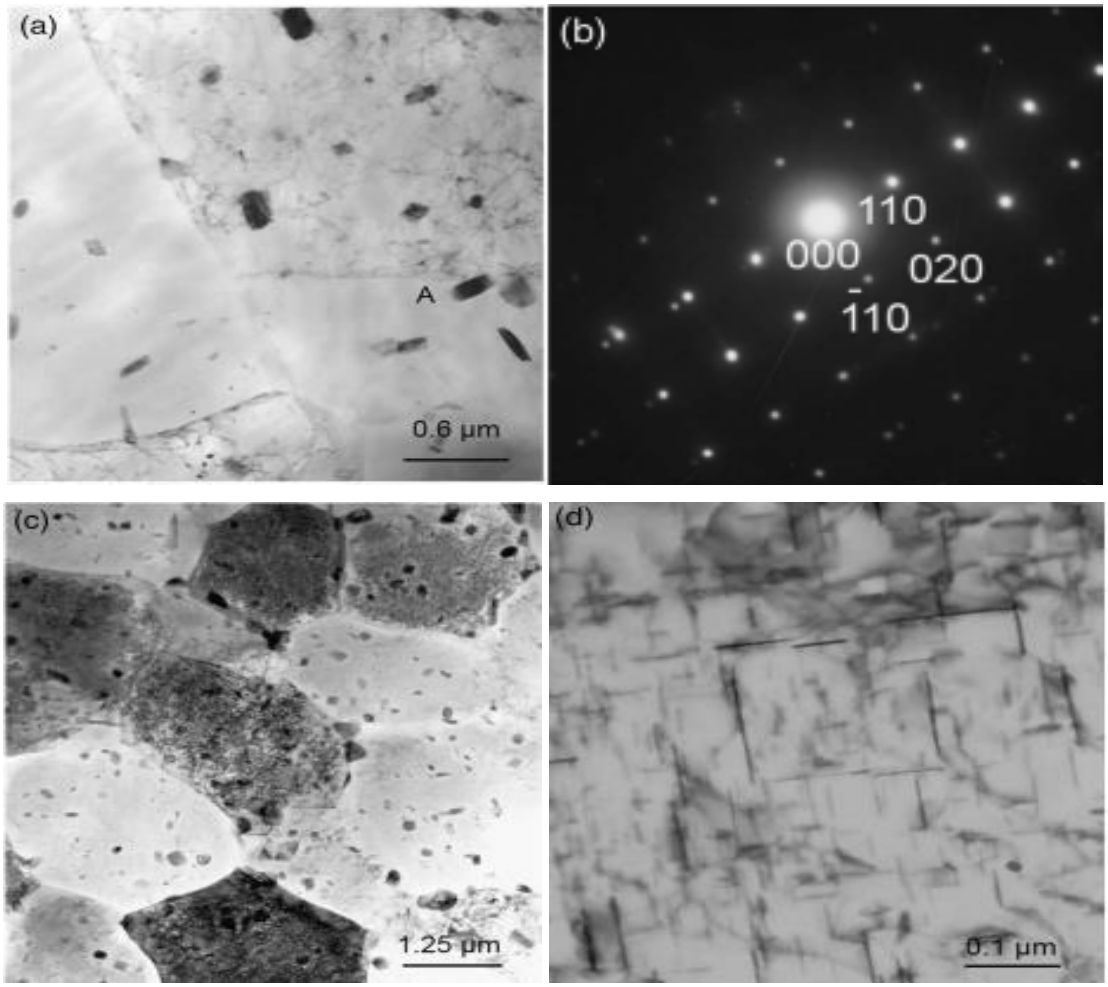

Figure 25: (a) Precipitates and grains structure in the as-welded condition (b) The SAD pattern (c) Low magnification TEM image showing θ precipitates and grains structure in the PWHT condition (d) High magnification TEM image showing the re-precipitated metastable in PWHT [99]

It implies that some metastable precipitates, present in the PM, have been transformed to stable precipitates. In order to verify the presence of solution during welding, post-weld ageing heat treatment (PWHT) was performed. After ageing heat treatment, the stable precipitates still distribute on the equiaxed grains (Fig. 25c), while a large number of plate shaped precipitates re-precipitate (Fig. 25d). This implies that a great deal of metastable precipitates solutionized into the α (Al) solid solution during welding [99]. The effects of post weld heat treatments, namely artificial ageing and solution treatment followed by artificial ageing on microstructure of friction stir welded AA7075-T651 aluminum alloy were investigated. The solutionizing process during the STA treatment caused the dissolution of precipitates in the matrix. The

artificial ageing process in the STA treatment caused the re-precipitation of finer θ' (Mg (Zn, AL, Cu) $_2$) in the stir zone. This is the reason for the higher hardness and tensile strength [100].

The as-welded weld had a softened region, which was characterized by dissolution and growth of precipitates. The precipitate-dissolved region contained a minimum hardness in the as-welded condition. Post weld aging significantly increased the density of strengthening precipitates and led to a high hardness in the precipitate-dissolved region. The density of strengthening precipitates was hardly increased in the precipitate-coarsened region, which showed a slight increase in hardness during post weld aging. Subsequent aging after solution treatment led to a high density of strengthening precipitates and brought, homogeneously, a high hardness in the overall weld [99].

2.6 Effect of TIG+FSP approach on mechanical properties of welded joint

A new welding approach of TIG + FSP was successfully applied to the AA2024 to enhance the mechanical properties of the TIG welded joints. They conclude that the defects and porosities in the TIG welded joints are completely reduced by the FSP process and modified the microstructure and mechanical properties of the TIG+FSP welded joint [101]. The application of FSP on the TIG welded joint improved the ductility and tensile strength of the FSW and TIG welded joint of AA5083-H111 and results revealed best-reduced dimple size [102].

The microstructure of Stir zone of TIG and TIG+FSP welded joints are shown in fig.26. Fig. 26(a) represent the microstructure of the BM (AA5083) containing coarse grain structures. Dark dendrites with fine precipitates of Mg_3Al_2 were noted in the micrograph of unprocessed TIG welded joint with filler ER5356 as shown in fig. 26b. The application of FSP on TIG welded joint found a very fine grain structure with distinguished boundary layers as shown in fig. 26c. The unprocessed friction stir welded micrograph (fig. 26d) shows the uniform arrangement with fine grains. Ultrafine grains with the uniform arrangement is also noticed on friction stir processed FSW [102].

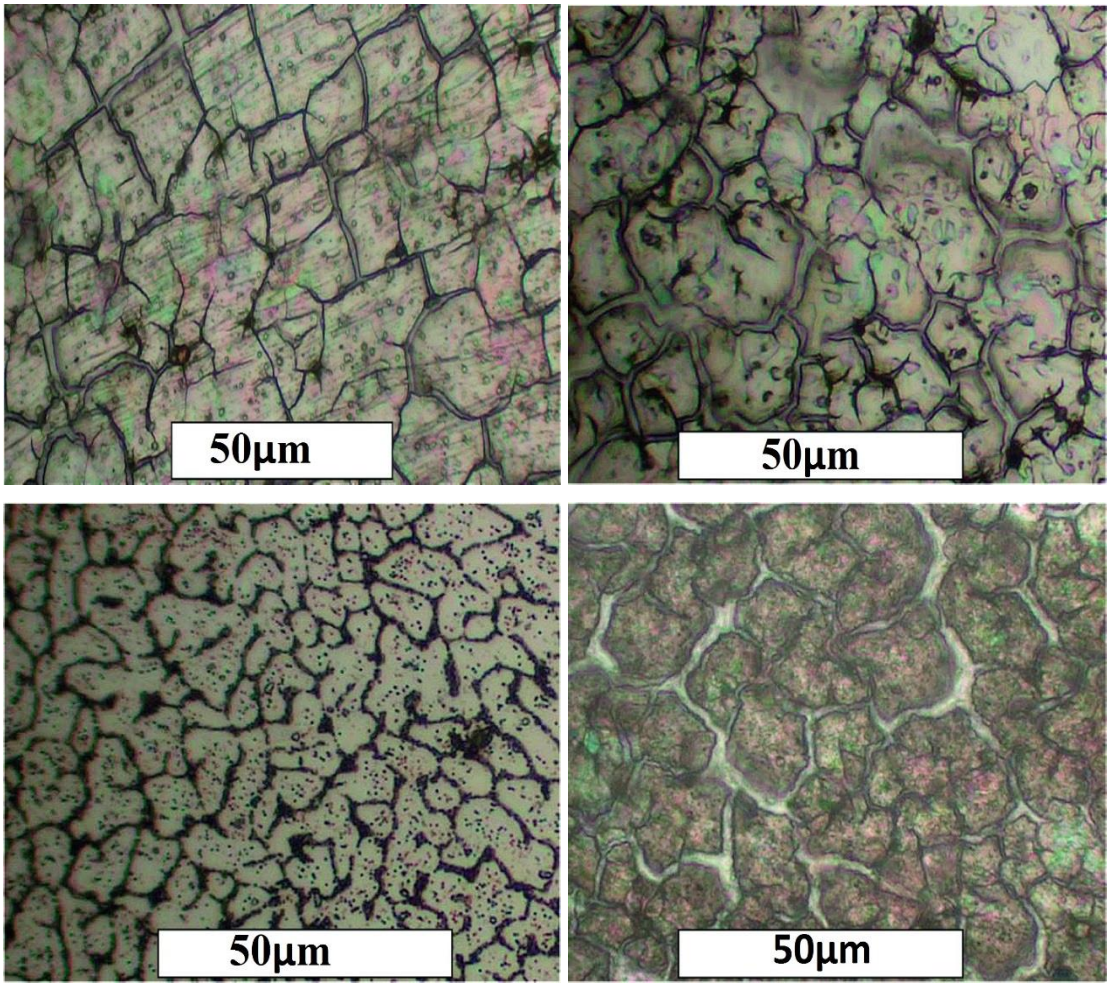

Figure 26: Optical micrographs of the NZ regions (a) base material, (b) unprocessed GTAWed joint, (c) friction stir-processed GTAWed joint, (d) unprocessed FSWed joint [102]

So, the application of FSP on TIG welded joint improved the ductility of the welded joint results revealed best reduced dimple sizes and the micro-hardness of the unprocessed and friction stir processed joints was marginally affected by the friction stir processing technique giving the maximum micro-hardness of 87HV.

The mechanical properties of TIG and TIG+FSP welded joint are evaluated to understand the effect of FSP on TIG welded joint. Fig. 27 (a) shows the micro-hardness distribution of the joint across the welded region and it is showed that the hardness of TIG+FSP welded joint are higher than the TIG welded joints. The highest hardness is substantiation of precipitates induced in the heat affected zone (HAZ) and are significantly affect the weld strength. The TIG+FSP approach greatly enhance the center region of the welds where the stirring effect on the TIG fusion zone, and

beyond that the properties are significantly not changed. The tensile strength of TIG and TIG+FSP joints are investigated as shown in fig. 27(b). The tensile strength of TIG and TIG+FSP welded joints are lower than the base metal. However, the TIG+FSP welded joints showed better performance and its elongation is higher that the TIG welds. Moreover, the ductility of the TIG_FSP welded joints are better than the TIG welds due to absence of porosities and other defects.

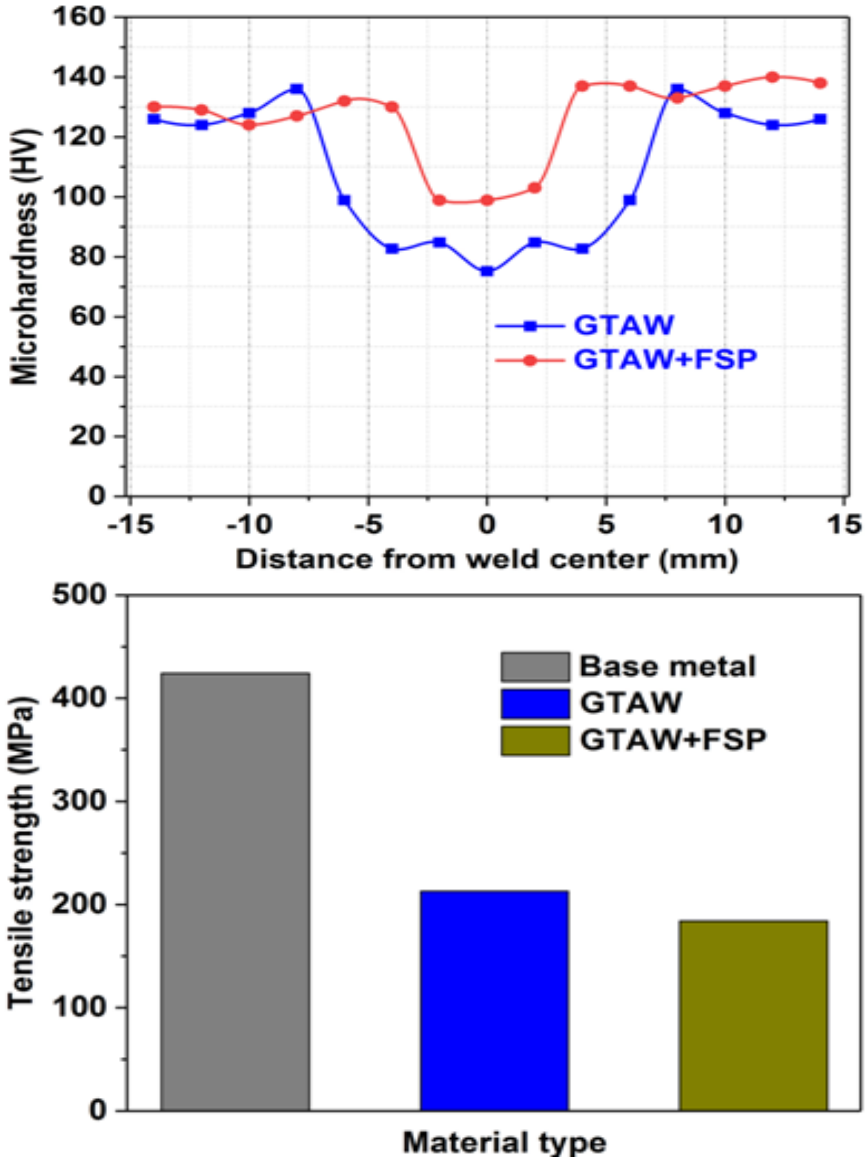

(a) **(b)**

Figure 27:Two different processes across the weld zones, (a) Micro-hardness Distribution, (b) Tensile Strength

3 Objectives

The aim of this work is to evaluate the effect of friction stir processing on TIG welded joints of dissimilar Al-alloy AA6061 and AA7075 with filler wire ER4043 and ER5356. In order to accomplish the main objectives following the sequence of experimental work was planned.

- Fabricate the joint of AA6061 and AA7075 by friction stir welding
- Fabrication of TIG welded joints of AA6061 and AA7075 with filler ER4043 and ER5356.
- Evaluation of chemical composition and mechanical properties of TIG welded joints of AA6061 and AA7075.
- After TIG welding, friction stir processing technique was applied on TIG welded joint with different process parameters namely, tool rotational speed, tool travel speed, and tilt angle.
- RSM techniques have been applied on TIG+FSP welding processing parameters and observed optimized input and output responses.
- Characterization of TIG and TIG+FSP joints using SEM to reveal the joint quality, grain size, and grain orientation.
- Evaluation of fractured surface morphology by SEM machine.
- Evaluation of residual stress of the TIG and TIG+FSP welded joints.
- Thermal analysis of TIG+FSP processes such as temperature distribution.
- Comparison of FSW, TIG and TIG+FSP

CHAPTER-3

Research Methodology

3.1 Flow Chart

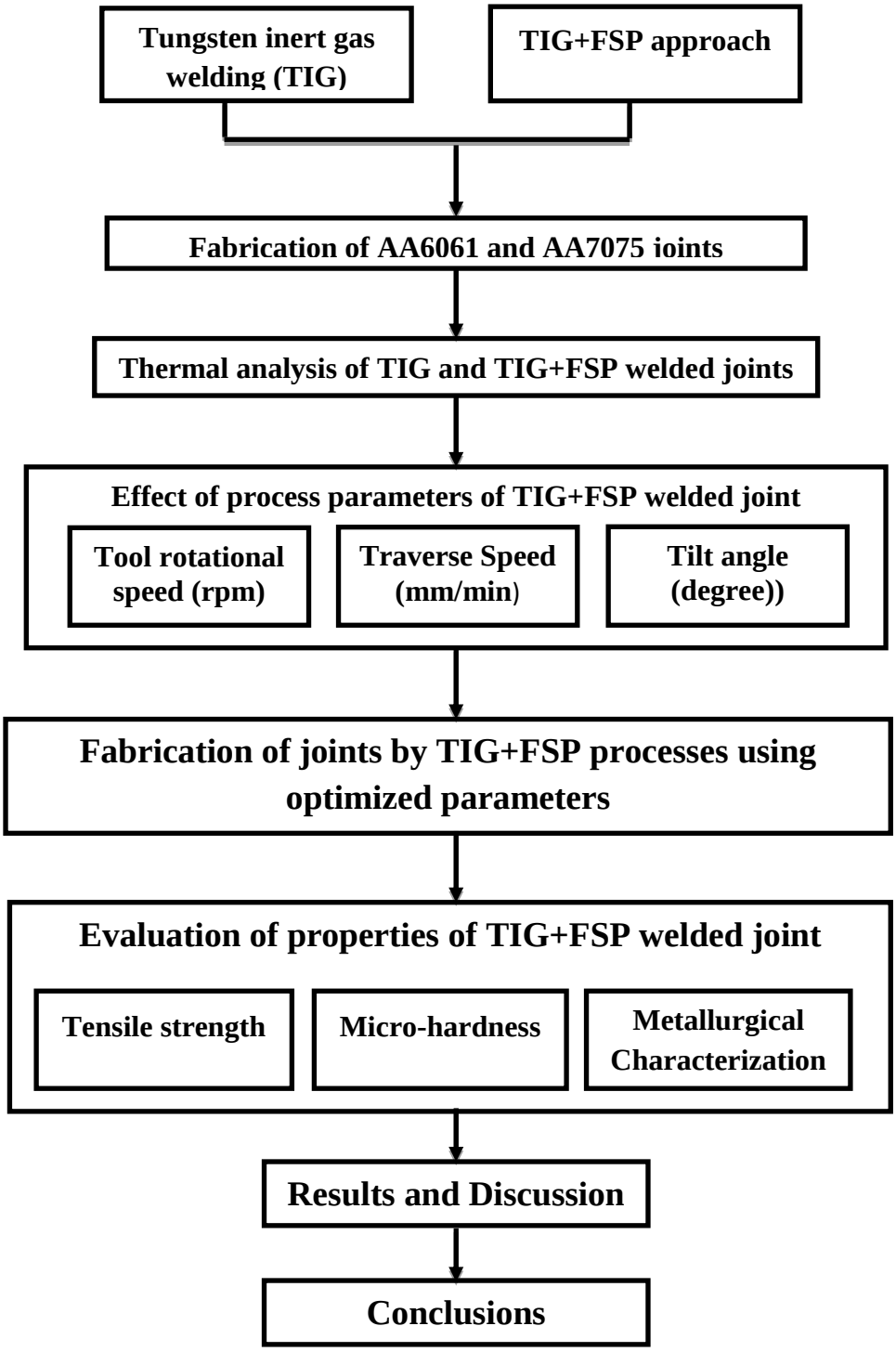

Figure 28: Work Plan

3.2 Chemical composition of base material

The modern development in the automobile sector and defense sector has been transformed from conventional materials to light material such as aluminum alloy. Due to excellent physical and mechanical properties of Al-alloy such as high corrosion resistance, low density, high strength to weight ratio and high thermal conductivity, it is mostly used for making various components such as military aircraft, rocket, and rocket launcher, axle shafts, rims, bumpers, and car bodies [103]. FSW is used in the fabrication of automotive and shipbuilding components, aircraft structural components and reducing structural weight. This solid-state welding is used in defense and aerospace. Many aluminum alloys like AA6061, AA7075 have a large range of applications in defense, it includes fabrication of fuel tank of cryogenic rocket and ammunition hardware [104-108]. Aluminum alloy AA6061 containing silicon (Si) and magnesium (Mg) as its major alloying elements whereas AA7075 containing magnesium (Mg) and zinc (Zn) have major alloying elements. AA6061 has low strength and high ductility and the properties near to the convectional weld zone results in loss strength around 75%. During the welding of aluminum alloy, the oxide layer should be removed for enhancing the properties of the welded joint.

Filler material ER4043 is silicon base aluminum alloy filler wire, in which 4.5 to 6% silicon is used. Thus filler is designed for welding of 6xxx and 7xxx series. It may also be used to weld a 3xxx series. Because silicon base alloy ER4043 has a lower melting point and more fluidity than the other filler wire series and this is mostly preferred by the welders. Weld penetration of ER4043 is re than ER5356 but produces less ductility. ER4043 is not suited for high magnesium content aluminum alloy like 5xxx series except (Mg content less or equal to 2.5 %) i.e. AA5083, AA5086 or AA5456, because Mg_2Si (Magnesium silicide) may be developed in the weld zone to increase crack sensitivity and decrease ductility.

Filler material ER5356 is magnesium base aluminum alloy filler wire, in which up to 6% magnesium is used. This filler wire is most commonly used of other aluminum filler alloy due to its good feed ability and excellent tensile strength, this filler wire mainly designed for 5xxx and 6xxx series alloy. ER5356 is not suitable for a service temperature of more than 65^0. The formation of Al_2Mg at an elevated temperature at

the grain boundaries makes the alloy prone to stress corrosion. The chemical composition of base and filler materials as shown in table 4.

Table 4: Chemical composition of filler wire and parent materials

Material	Si	Cu	Fe	Zn	Mg	Mn	Cr	Ti	Al
ER 4043	5.3	0.025	0.8	0.1	0.05	-	-	0.02	Bal.
ER 5356	0.025	0.015	0.15	0.01	4.9	0.14	0.11	0.09	Bal.
AA7075	0.58	1.2	0.35	5.1	2.1	0.12	0.2	0.05	Bal.
AA6061	0.4-0.8	0.2	0.7	0.25	0.8	0.1	0.2	0.15	Bal.

3.3 Experimental procedure

Experimentation work was done in two-phase. In the first phase, butt welding of AA6061 and AA7075 (6.2 mm thickness) done with the help of TIG welding with filler ER4043 and ER5356. In the second phase, friction stir processing is done on TIG welded joint with different processing parameters. The following steps are as given below.

3.3.1 V groove preparation

Aluminum alloy AA6061 and AA7075 of thickness 6.2 mm was selected as a work-piece material for the present work. Aluminum plates were cut with a dimension of 150 mm x 40 with the help of milling cutter and grinding done at the edge to smooth the surface to be joined. After that, the V groove of 45º angle was made for each plate as shown in fig.29.

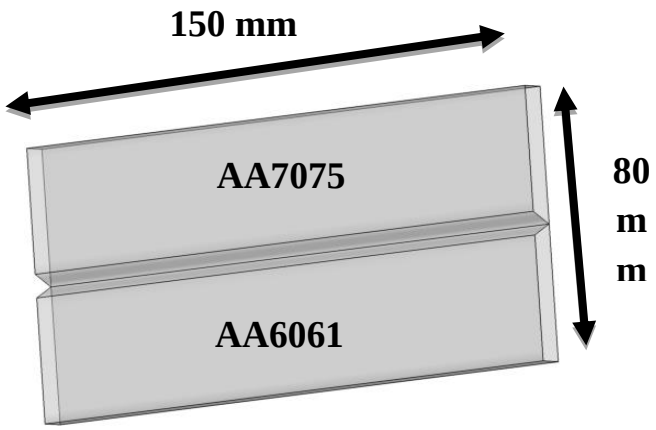

Figure 29: 45º V groove for TIG welded joint

3.3.2 Fabrication of TIG welded joint

3.3.2.1 TIG welding machine

TIG welding is an arc welding that use a non-consumable electrode to produce the weld. This is the main part of the TIG welding setup by which a controlled amount of voltage and current is supplied during welding according to the processing parameters.

3.3.2.2 Rail track

The speed control device is run at the particular speed which is regulated by regulator over this rail track in a straight line.

3.3.2.3 TIG welding torch

The TIG welding torch is fixed with a movable control unit. A tungsten electrode is fixed in the torch and argon gas is flowing through this.

3.3.2.4 Gas cylinder

In TIG welding argon (Ar) is used as an inert gas which is supplied to the welding torch with a particular flow rate so that a stable arc created for welding, the gas flow is control by the valve and regulator.

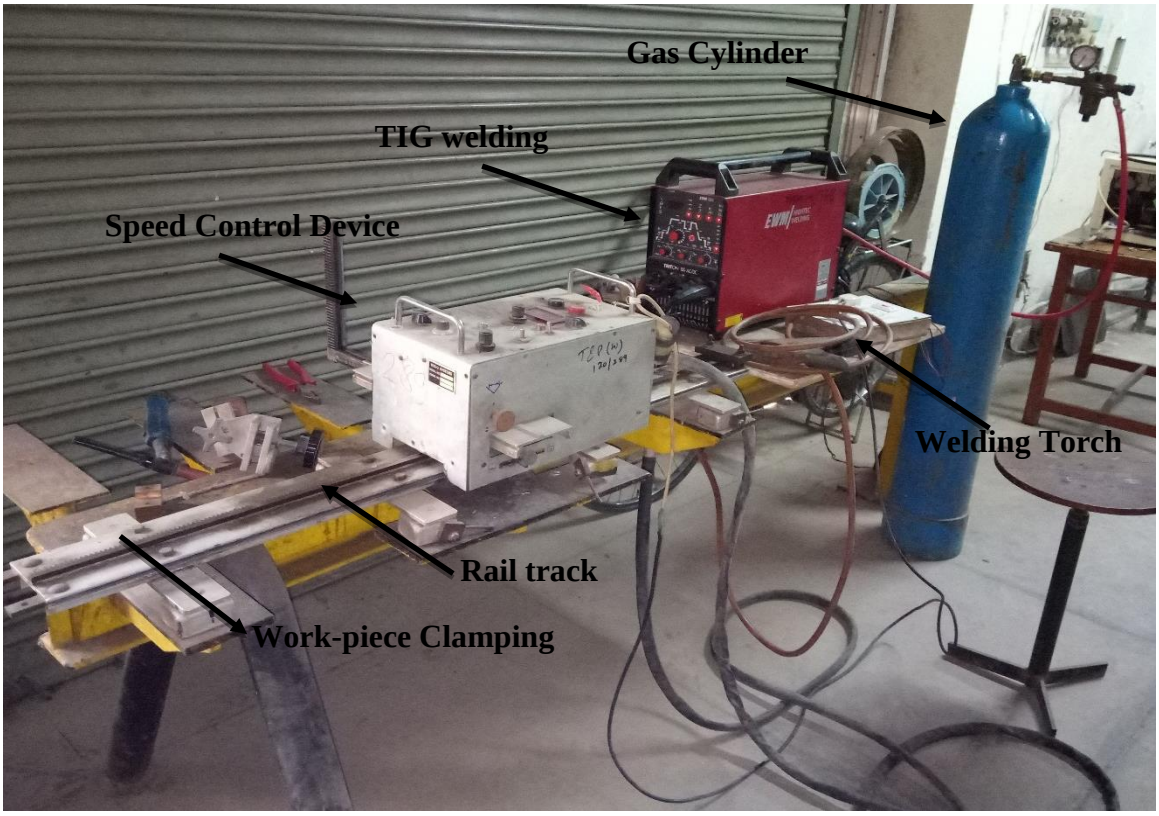

Figure 30: Tungsten inert gas welding machine

3.3.2.5 Speed Control device

The speed control device is a movable device that runs with a predefined speed required for welding. The TIG welding torch is fixed with it using a clamp in a particular angle so that during welding a stable and continuous arc form. The TIG welding can be changed by the regulator. Distance between the work-piece and torch tip can be control by the adjustable knob.

After V groove preparation, aluminum plates are fixed in the working table. The TIG welding creates the arc with the help of a non-consumable electrode to produce a weld with filler ER4043 and ER5356. The weld bead as shown in fig. 31. The welding speed is maintained by the speed control device. This is the main part of the TIG welding setup by which a controlled amount of voltage and current is supplied during welding according to the processing parameters.

Table 5: Processing parameter of TIG welded joint

Working Parameter	Shielding Gas	Current	Voltage	Welding speed
Description	22 *l*/min (Argon)	110 A (ER4043) 125 A (ER5356)	23 V	3.2 mm/sec

(a)

(b)

Figure 31: TIG welded joint of AA6061 and AA7075, (a) with filler 4043, (b) with filler ER5356

The processing parameters and filler wire are strappingly affected by the mechanical properties of the welded joint. In this work, the filler wire of ER4043 and ER5356 of diameter 2.4 mm were used to join a single V groove plate at voltage 23V and current 110 and 125 amp respectively. The weld bead of TIG shown in fig. 31. Argon

(22 *l*/min) is used as a shielding gas and travel speed 3.2 mm/sec to fabricate the joint. TIG welding consists of the following parts.

3.4 Fabrication of TIG+FSP welded joint

3.4.1 Making of FSP tool

In this work, the threaded cylindrical pin profile is used to fabricate the TIG+FSP welded joint because of the threaded pin profile yield defect-free joints and it is preferred over the other pin profile [109] and the material is used for the manufacturing the tool is H13 tool steel due to its high wear and shock resistance among different tool steel grades. The process of manufacturing of tool pin profile as shown in fig. 32.

(a)

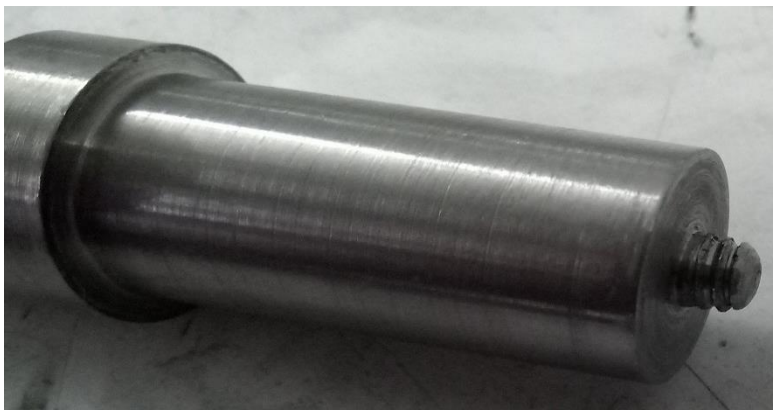

(b)

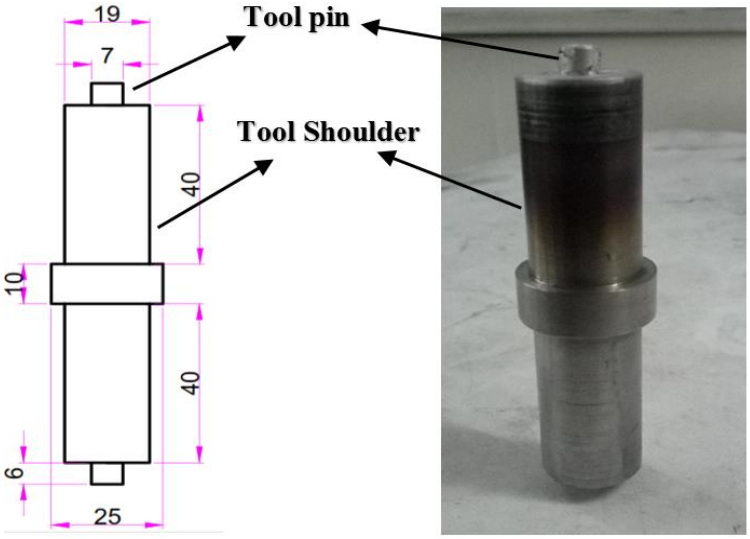

(c)

Figure 32: (a) working on lathe machine, (b) Final FSW tool, (c) FSW tool after experiments

3.4.2 Friction stir processing on TIG welded joint

The TIG welding often results in a defective weld like porosity, micro cracks, coarse grain structure, and high residual stress. To avoid these defects, the top surface of Tungsten inert gas (TIG) welded joints are processed using friction stir processing (FSP). The non-consumable H13 steel tool with pin diameter, shoulder diameter and a pin length of 3 mm, 19.5 mm, and 5.5 mm respectively were used.

In this, the investigation, an indigenously designed computer numerical controlled FSW was used to fabricate the joints. The butting faces of the plates to be joined were milled and polished to make them flat. The surface undergone friction with the shoulder was polished by using emery papers and rubbed with acetone to remove the oxide layer. The TIG-welded plates were rigidly clamped to ensure that the plates should not abut during welding. The rotating tool was slowly plunged into the interface of two materials at a rate of 2 mm/sec until the shoulder surface touched the work-piece surface. A dwell period of 60 sec was maintained for all the joints in order to preheat and soften the preheat zone. The rotating tool was traversed along the weld line at a constant welding speed and finally, the tool was pulled out.

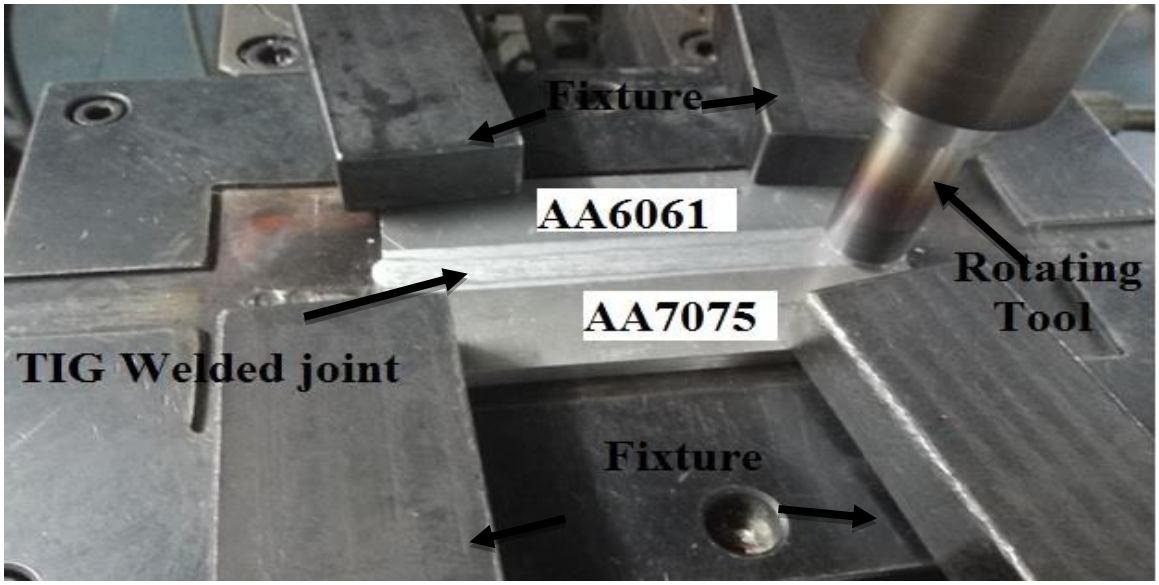

Figure 33: FSP process after TIG welding

The welding was done perpendicular to the rolling direction of the TIG welded joint. Welding process parameters, pin profile, and tool offset exert a significant effect on the material flow pattern and temperature distribution, thereby influencing the microstructural evolution of the material. The process parameters such as tool rotation speed of 1000-1300 rpm, tool traverse speeds of 30-60 mm/min and tool tilt angles of 0-2º were used to fabricate the TIG+FSP welded joints shown in fig. 33. The details of the process parameters used in this investigation are presented in Tables 6 and 7. The threaded cylindrical pin profile was used to fabricate the joints. The tool dimensions and the photograph of the fabricated tools are shown in Fig. 32 (c). There are twenty experiments have been conducted with three independent input variables in which some fabricated joints are shown in fig.34.

Table 6: Processing parameter of friction stir processing and its level

Parameters	Units	Notation	Range	Levels		
				-1	0	1
Tool rotational Speed	rpm	A	1000-1300	1000	1150	1300
Traverse Speed	mm/min	B	30-60	30	45	60
Tilt angle	degree	C	0-2	0	1	2

Figure 34: Various TIG+FSP fabricated joint

Table 7: Design of Experiments

Sample	A:Tools Rotations Speeds (rpm)	B:Traverses Speeds (mm/min)	C:Tilts angles (Degree)
1	1150	45	2
2	1300	30	2
3	1150	45	1
4	1000	60	0
5	1000	45	1
6	1150	45	1
7	1000	30	0
8	1000	60	2
9	1150	45	1
10	1150	60	1
11	1300	60	0
12	1150	45	1
13	1150	45	1
14	1150	45	0
15	1300	60	2
16	1000	30	2
17	1150	30	1
18	1300	45	1
19	1300	30	0
20	1150	45	1

3.4.3 Specimens preparation

The specimens required for tensile testing and characterization were machined from the TIG+FSP welded joints by employing milling cutting and shaper machine process in the form of the strip as shown in fig. 35. The tensile test specimens were prepared according to ASTM E8 standard from these strip as shown in fig.35 (c-d).

(a) (b)

(c)

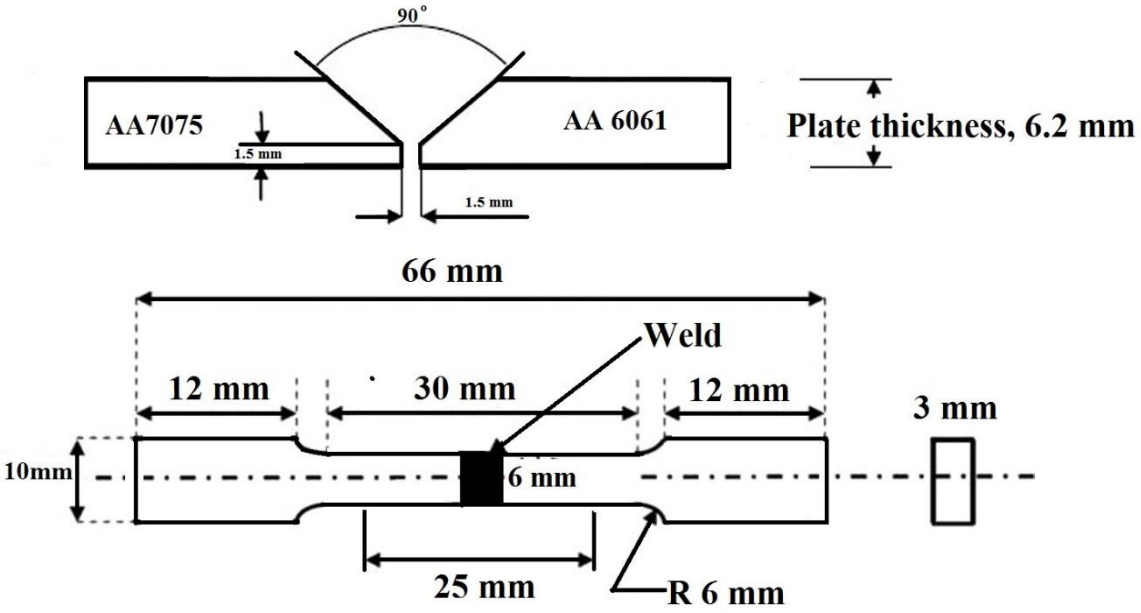

(d)

Figure 35: (a) TIG+FSP welded joint, (b) Strip from welded joint, (c) Tensile test specimens as per ASTM E8, (d) Tensile test specimen dimensions, (e)) finishing of welded plate by shaper

3.4.4 Tensile test

Fig. 35 (c-d) demonstrate the dimension of tensile sub test specimen as per ASTM E8. The tensile test specimens were sliced and machined from the welded joint using a milling cutter and shaper machine. Three specimens were chosen for each welding and the tensile test was performed at room temperature and the average of these three results would be taken. Make sure specimens did not have any crack or notches or other defects that would disparagingly affect the tensile test results.

Figure 36: Universal testing machine (UTM)

3.4.5 Micro-hardness

The micro-hardness distribution of the TIG and TIG+FSP welded joint of AA6061 and AA7075 with different processing parameters were analyzed by the Vickers hardness testing machine. The sample preparations and the testing procedures for the micro-hardness measurements were followed as per the guidelines from ASTM E 384-99 (Standard test method for micro indentation hardness of materials). The micro-hardness was measured at the mid thickness region in the cross-section of the various zones of the joints. Vickers microhardness tester was used to measure the micro-hardness by using the indenting load of 100 gm for a dwell time of 30 sec.

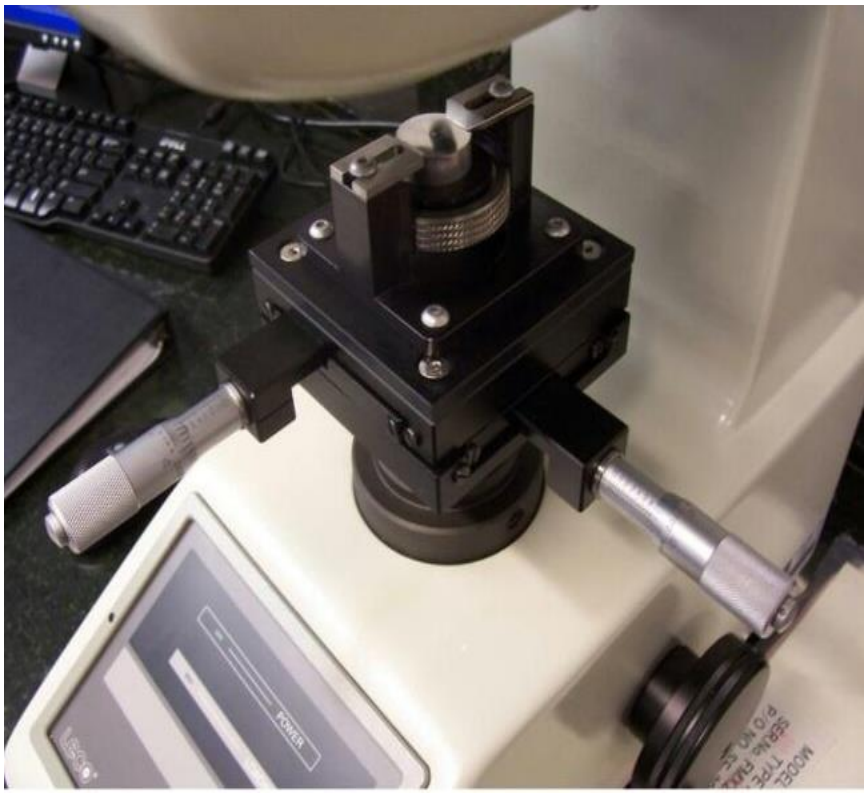

Figure 37: Vickers micro hardness testing process

3.4.6 Residual stress measurement

A mini portable X-ray diffraction apparatus (Pulstec μ-X360) at Delhi technological university, Delhi, India was used to determine the residual stresses in weldment of AA6061 and AA7075 by the cosα method. The X-ray incident angle was set 35º and 5 oscillations were applied. The variation of residual stresses in the transverse direction

of weldment was analyzed. The X-ray incident time was 4-5 min throughout this process for each sample. Under these conditions, the diffracted beam from the workpiece surface has captured the images of the welded plates at 50µm resolution, the size of the beam spot is approximately 2.5 mm for 1.2 mm pinhole collimator.

This method is allowed the stress analysis by capturing the results by a single incident X-ray beam via a 2D detector. It shows the peak center is very stable throughout the welding. The 3D Debye ring and distortion ring of each welded samples.

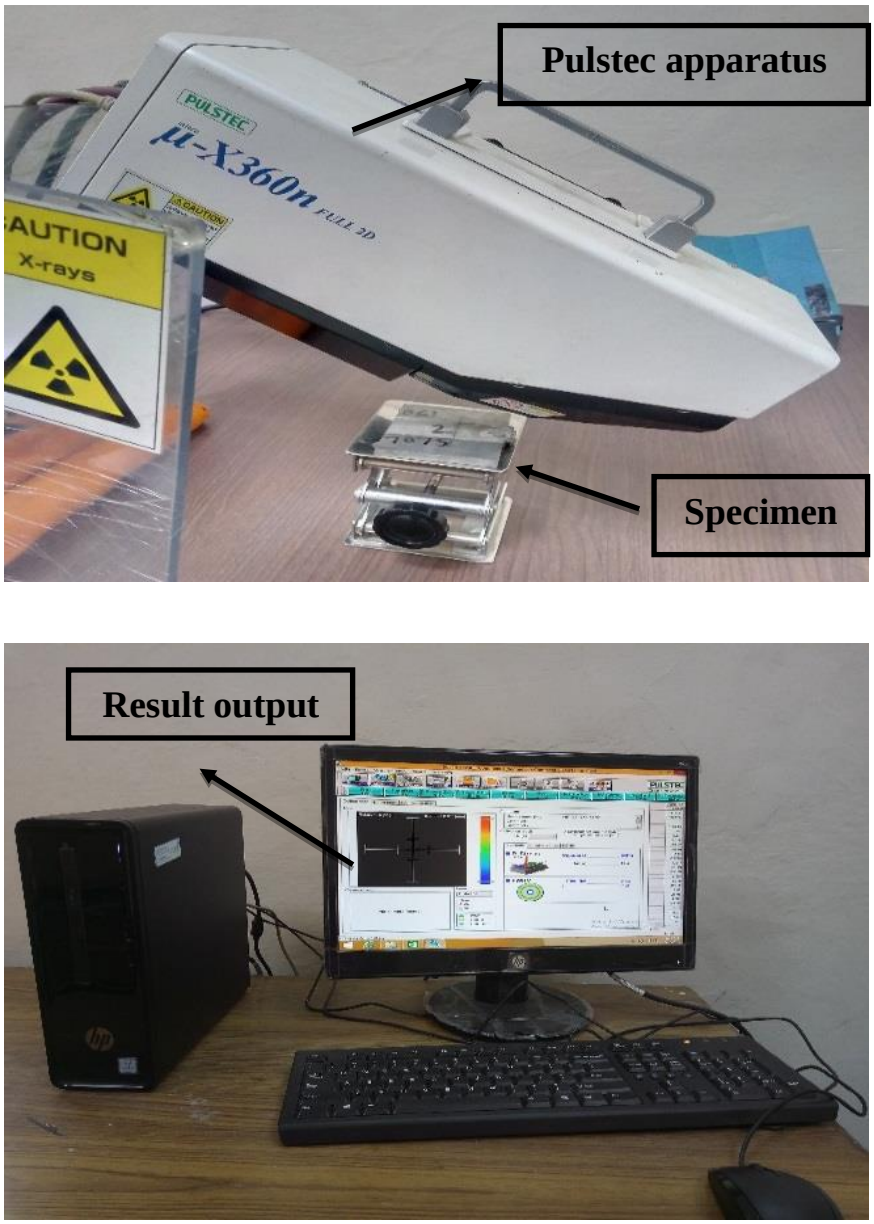

Figure 38: X-Ray diffraction setup

3.4.7 Metallurgical Characteristics Evaluation

In this analysis, some characterization procedures went through to analyze the microstructure of the TIG and TIG+FSP welded joints.

- The specimens having the dimensions (5mm x 5mm x 3 mm) were extracted from the TIG and TIG+FSP welded joints.
- All the sides of the sample were polished by the emery sheets from large grit size to small grit size (i.e. 400 to 2000) to get fine polish.
- Final polishing was done (as shown in fig. 39a-b using alumina powder with the help of the disc polishing machine and the specimens were etched as per ASTM E407 standard with Keller reagent (8 ml HNO_3, 4 ml HF, and 6 ml HCL) and observed by the microscopic machine as shown in fig 39f

(a)

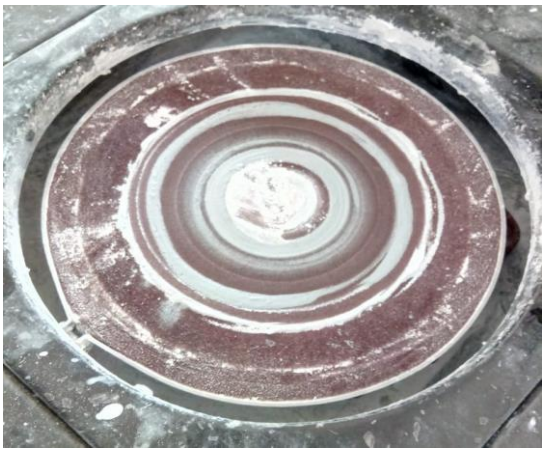

(b)

(c)

(d)

(e) (f)

Figure 39: (a-b) Polishing of welded specimen, (c) making of Keller reagent, (d) specimens after polishing, (e) gold coating machine, (f) SEM machine during testing

- The chemical etchants were mopped and washed in running water after that the specimens were placed in the gold coating machine as shown in fig. 39(e) to coat one layer of gold for the good quality image of the welded joint.
- The gold coated specimens were placed in the microscope machine (as shown in fig. 39 e) to analyze the micrograph of TIG and TIG+FSP welded joints with high magnified SEM images.
- To analyze the fracture specimens extracted from the tensile test. Keller's reagent was applied to reveal the various regions which make ease for the precise identification of the fractured path with high magnified SEM images.
- The chemical composition of the base material and welded joint were analyzed with the help of Energy-dispersive X-ray spectroscopy (EDX/EDS) analysis.

CHAPTER-4

Governing Equations

4 Numerical Modelling [57]

For incompressible flow, the continuity equation in the direction of x, y and z is given by

$$\frac{\partial u_{\mathrm{i}}}{\partial \mathrm{x_i}} = 0 \tag{1}$$

The momentum conservation equation of the heat source is given as

$$\rho \frac{\partial u_{\mathrm{I}}\, u_j}{\partial x_i} = - \frac{\partial \mathrm{P}}{\partial \mathrm{x}_j} + \frac{\partial}{\partial \mathrm{x_I}} \left(\mu \frac{\partial \mathrm{U_j}}{\partial \mathrm{x}_i} + \mu \frac{\partial \mathrm{U}_i}{\partial \mathrm{x_j}} \right) - \rho\, U_1 \left(\frac{\partial \mathrm{U}_j}{\partial \mathrm{x_I}} \right) \tag{2}$$

FSW involves transfer of plasticized material from the front to the back of the FSW tool pin as the tool traverse speed along the welded joint. So, it is suitable to use these equations for friction stir welding. The flow stress can be calculated as

$$\sigma_e = \frac{1}{\alpha} \mathrm{sinh}^{-1} \left[\left(\frac{z}{A} \right)^{1/n} \right] \tag{3}$$

$$\mathrm{A} = 1.80 \times 10^{6} + 1.74 \times 10^{8} (\%\mathrm{C}) - 6.5 \times 10^{7} (\%\mathrm{C})^{2} \tag{4}$$

$$\alpha = 1.07 + 1.70 \times 10^{-4}\, \mathrm{T} - 2.8 \times 10^{-7}\, \mathrm{T}^{2} \tag{5}$$

$$\mathrm{n} = 0.2 + 3.96 \times 10^{-4}\, \mathrm{T} \tag{6}$$

The temperature compensated effective strain is given by

$$\mathrm{Z} = \varepsilon \exp \left(\frac{Q}{RT} \right) \tag{7}$$

The effective strain may be written as

$$\varepsilon = \left(\frac{2}{3} \varepsilon_{ij} \varepsilon_{ij} \right)^{1/2} \tag{8}$$

Where ε_{ij} is given by

$$\varepsilon_{ij} = \frac{1}{2} \left(\frac{\partial u_i}{\partial x_j} + \frac{\partial u_j}{\partial x_i} \right) \tag{9}$$

So, the viscosity can be calculated as

$$\mu = \frac{\sigma_e}{3\varepsilon} \tag{10}$$

The thermal energy conservation equation at steady state is given by

$$\rho C_p \frac{\partial (u_i T)}{\partial x_i} = - \rho C_p U_1 \frac{\partial T}{\partial x_i} + \frac{\partial}{\partial x_i}\left(k \frac{\partial T}{\partial x_i}\right) + S_i + S_b \tag{11}$$

Then S_i may be written as

$$S_i = [(1-\delta)\eta\tau + \delta\mu_f P_N] (\omega r - U_1 \sin\theta) \frac{A_r}{V} \tag{12}$$

During friction stir welding, mixing is not atomic, only grains structure are deformed not mixing of atoms.

$$\varphi = 2\left[\left(\frac{\partial u_1}{\partial x_1}\right)^2 + \left(\frac{\partial u_2}{\partial x_2}\right)^2 + \left(\frac{\partial u_3}{\partial x_3}\right)^2\right] + \left(\frac{\partial u_1}{\partial x_2} + \frac{\partial u_2}{\partial x_1}\right)^2 + \left(\frac{\partial u_1}{\partial x_3} + \frac{\partial u_3}{\partial x_1}\right)^2 + \left(\frac{\partial u_3}{\partial x_2} + \frac{\partial u_2}{\partial x_3}\right)^2 \tag{13}$$

4.1 Boundary conditions

When the work-piece top surface away from the tool shoulder edge, the boundary condition for heat exchange involves both convection and radiation heat transfer. However, at the sides and the bottom surface of the work-piece, the boundary condition for heat exchange involves only convection heat transfer. The heat generation rate at the interface between the tool and the work-piece can be given by

$$f = \frac{J_w}{J_T} = \frac{\sqrt{(k_\rho C_P)_W}}{\sqrt{(k_\rho C_P)_T}} \tag{14}$$

Where T and W denote the tool and work piece respectively. The heat flux continuity on the shoulder interface yields

$$k \left.\frac{\partial T}{\partial z}\right|_{\text{top}} = \frac{J_w}{J_w + J_T} q_1 \text{ in the range of } R_P \leq r \leq R_s \quad (15)$$

Where $J_w$and J_T are the heat conducted to the work-piece and tool respectively

$$J = \sqrt{k\rho\, C_p} \quad (16)$$

Where Cp is heat capacity, ρ and K are density and thermal conductivity respectively

The total heat generation rate may be written as

$$q_1 = [\eta\,(1 - \delta)\,\tau + \delta.\mu_f.P_H]\,(\omega.r - U_1 \sin\theta) \quad (17)$$

The heat transfer coefficient may be calculated as

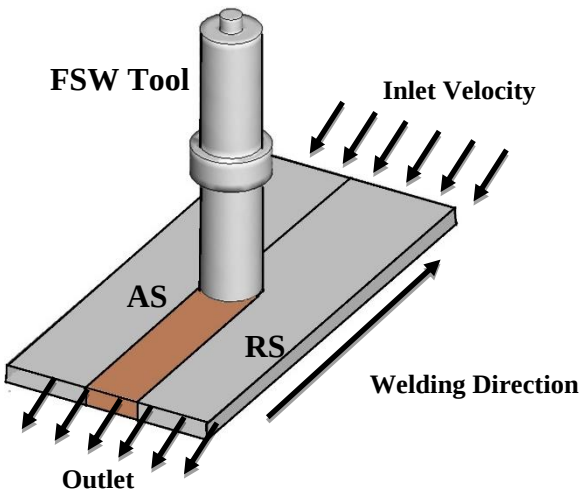

Figure 40: Boundary condition

$$k \left.\frac{\partial T}{\partial z}\right|_{\text{bottom}} = h_b\,(T - T_a) \quad (18)$$

Value of $h_b$can be calculated as

$$h_b = h_{b0}\,(T - T_a)^{0.25} \quad (19)$$

The heat transfer due to radiation and convection is written as

$$k \left.\frac{\partial T}{\partial z}\right|_{\text{top}} = h_t\,(T-T_a) + \sigma\,\varepsilon^1(T^4-T_a^4) \qquad (20)$$

In this model, the computational region is considered as a single-phase visco-plastic non-Newtonian fluid and the FSW tool is considered as rotating in a fixed position as shown in fig.40. The material flows into the computational domain from the inlet velocity and out from outlet velocity at the welding speed (traverse speed). Top, bottom and side surfaces of the work-pieces are considered equivalent to the wall surface, having the same velocity as welding speed but opposite in direction.

Velocity at the tool pin periphery have been defined in terms of tool translation velocity and the tool pin angular velocity

$$\left.\begin{aligned} u &= (1-\delta)(\omega R_P \sin\theta - U1) \\ v &= (1-\delta)\omega R_P \cos\theta \\ \mathrm{w} &= \mathrm{k}\,\frac{\omega}{2\pi} R_P \end{aligned}\right\} \text{in the range } R_P \leq r \leq R_S \qquad (21)$$

Similarly, at the shoulder contact, the velocity boundary condition may be written as

$$\left.\begin{aligned} u &= (1-\delta)(\omega r \sin\theta - U1) \\ v &= (1-\delta)\omega r \cos\theta \end{aligned}\right\} \text{in the range } R_P \leq r \leq R_S \qquad (22)$$

4.2 Material Properties

The density of AA7075 and AA6061 is taken as constant, equals to 2810 kg/m^3 and 2700 kg/m^3 respectively, while the specific heat and thermal conductivity are considered as temperature dependent properties [110] as given below

$$\mathrm{k} = 25.2 + 3.98 \times 10^{-1} \times \mathrm{T} + 7.36 \times 10^{-6} \times \mathrm{T}^2 - 2.25 \times 10^{-7} \times \mathrm{T}^3$$

$$C_P = 929 - 6.27 \times 10^{-1} \times \mathrm{T} + 1.48 \times 10^{-3} \times \mathrm{T}^2 - 4.33 \times 10^{-8} \times \mathrm{T}^3$$

4.3 Residual stress measurement by cosα method

A mini portable X-ray diffraction apparatus (pulstec μ-X360) used for analyzing the residual stresses in the welded joints of AA6061 and AA7075 samples. The X-ray

incident angle was set 35º and ± 5 oscillation was applied. The X-ray incident time was 4-5 min throughout this process for each sample. Under these conditions, a diffracted beam from the workpiece surface has captured the images of the welded plates at 50µm resolution, the size of the beam spot is approximately 2.5 mm for 1.2 mm pinhole collimator.

For residual stress determination, the cosα method was described [35]. The translation from the diffractometer space to the sample inherently more complex due to the 2D planar geometry of the measurement and can be expressed as.

$$q_s = \begin{bmatrix} \cos\eta \sin\psi_0 + \sin\eta \cos\psi_0 \cos\alpha \\ \cos\eta \sin\psi_0 \sin\phi_0 + \sin\eta \cos\psi_0 \sin\phi_0 \cos\alpha + \sin\eta \cos\phi_0 \sin\alpha \\ \cos\eta \cos\psi_0 + \sin\eta \sin\psi_0 \cos\alpha \end{bmatrix} \tag{23}$$

The strain projection along (η, α) coordinates can be written as in terms of scattering vector and strain component as

$$\varepsilon_\alpha = q_i q_j \varepsilon_{ij}$$

$$\varepsilon_{ij} = \frac{1+\nu}{E}\sigma_{ij} - \delta_{ij}\frac{\nu}{E}\sigma_{kk} \tag{24}$$

So, the strain projection may be written as

$$\varepsilon_\alpha = \frac{1+\nu}{E} q_i q_j \sigma_{ij} - \frac{\nu}{E}\sigma_{kk} \tag{25}$$

Now, defining two parameters a_1 and a_2 for linear determination of σ_{11} and σ_{22}

$$a_1 = \frac{1}{2}[(\varepsilon_\alpha - \varepsilon_{\pi+\alpha}) + (\varepsilon_{-\alpha} - \varepsilon_{\pi-\alpha})] \tag{26}$$

$$a_2 = \frac{1}{2}[(\varepsilon_\alpha - \varepsilon_{\pi+\alpha}) - (\varepsilon_{-\alpha} - \varepsilon_{\pi-\alpha})] \tag{27}$$

After re-expressing of equations (26) and (27) to lead the final relationship for this method.

$$a_1 = \frac{1+\nu}{E} \sin 2\psi_0 \sin 2\eta \cos\alpha \left[\sigma_{11}(1+\cos 2\phi_0) + \sigma_{22}(1-\cos 2\phi_0) + 2\sigma_{12}(\sin 2\phi_0)\right] \quad (28)$$

$$a_2 = \frac{1+\nu}{E} \sin\psi_0 \sin 2\eta \sin\alpha \left[\sigma_{22} \sin 2\phi_0 - \sigma_{11} \sin 2\phi_0 + 2\sigma_{12} \cos 2\phi_0\right] \quad (29)$$

at $\phi_0 = 0$, the above equations will be

$$a_1 = \sigma_{11}\frac{1+\nu}{E} \sin 2\psi_0 \sin 2\eta \cos\alpha \quad (30)$$

$$a_2 = 2\sigma_{12}\frac{1+\nu}{E} \sin\psi_0 \sin 2\eta \sin\alpha \quad (31)$$

Thus the term cosα in the equation (30) is the origin of the name for this method

The value of stresses after re-expression maybe written as

$$\sigma_{11} = -\frac{E}{1+\nu} \frac{1}{\sin 2\psi_0 \sin 2\eta} \quad (32)$$

$$\sigma_{12} = -\frac{E}{2(1+\nu)} \frac{1}{\sin 2\psi_0 \sin^2 \eta} \quad (33)$$

CHAPTER-5

Results and Discussion

5 Results and Discussion

5.1 Effect of filler rod on mechanical properties of TIG welded joint

The filler material used during the TIG welding process plays a significant role in aluminum alloy welded joints. In this work, the filler material ER4043 and ER5356 are used to join AA6061 and AA7075 Al-alloy. Butt joints are made on 6 mm thick plates using 23 V for both filler wire, 110 amp and 125 amp are used for ER4043 and ER5356 respectively. The rate of argon gas 22 *l*/min is used with a welding speed of 3.2 mm/sec.

The filler material ER4043 is silicon base aluminum alloy filler wire, in which 4.5 to 6% silicon is used. Thus filler is designed for welding of 6xxx and 7xxx series. Because silicon base, alloy ER4043 has a lower melting point and more fluidity than the other filler wire series and this is mostly preferred by the welders. The weld penetration of ER4043 is re than ER5356 but produces less ductility. ER4043 is not suited for high magnesium content aluminum alloy like 5xxx series except (Mg content less or equal to 2.5 %) i.e. AA5083, AA5086 or AA5456, because of Mg_2Si (Magnesium silicide) may be developed in the weld zone to increase the crack sensitivity and decrease ductility.

The filler material ER5356 is magnesium base aluminum alloy filler wire, in which up to 6% magnesium is used. This filler wire is most commonly used of other aluminum filler alloy due to its good feed ability and excellent tensile strength, this filler wires mainly designed for 5xxx, 6xxx and 7xxx series alloy. ER5356 is not suitable for a service temperature of more than 65^0. The formation of Al_2Mg at an elevated temperature at the grain boundaries makes the alloy prone to stress corrosion.

Table 8: Mechanical properties of TIG welded joint

Processing Parameters	Average Tensile Strength (MPa)	Average Strain (%)	Average Hardness (HV)	Average Residual stress (MPa)
TIG with filler ER4043	158.6	20.1	66	72
TIG with filler ER 5356	176.2	21.9	74	63

5.1.1 Tensile strength

In order to analyze the effect of filler rod ER 4043 and ER 5356 on TIG welded joint of AA6061 and AA 7075, the tensile load is applied on the welded joint by universal testing machine (UTM) at Delhi technological university, Delhi as shown in fig. 36. It was observed that both welded specimens with filler ER 4043 and ER 5356 were fractured in the welded region. The specimens before and after the tensile test are shown in fig. 41. The tensile stress, micro-hardness at fusion zone and residual stress at fusion zone were analyzed based on the average of three test values as presented in table 8. The engineering stress-strain diagram for both test specimens as shown in fig. 42. The filler ER 5356 present in the welded joint makes more compact pressure leading to increase bond strength instead of filler ER4043. The grain size in the fusion zone for ER5356 is smaller than the ER4043. The tensile strength with filler ER5356 was obtained higher than ER4043 [111]. The tensile properties of the welded joint of aluminum alloys depend on the size and shapes of the alloying elements in the eutectic mixture [112].

(a)

(b)

Figure 41: Tensile test specimens of filler ER4043 and ER 5356, (a) before tensile test, (b) after tensile test

The average tensile strength of the TIG-welded joint of AA6061 and AA7075 with filler ER 4043 and ER 5356 was 158.6 MPa and 176.2 MPa respectively. The tensile test results demonstrate that the stress and strain for all three specimens were approximately the same and the results confirm that the fracture cannot take place in the fusion zone.

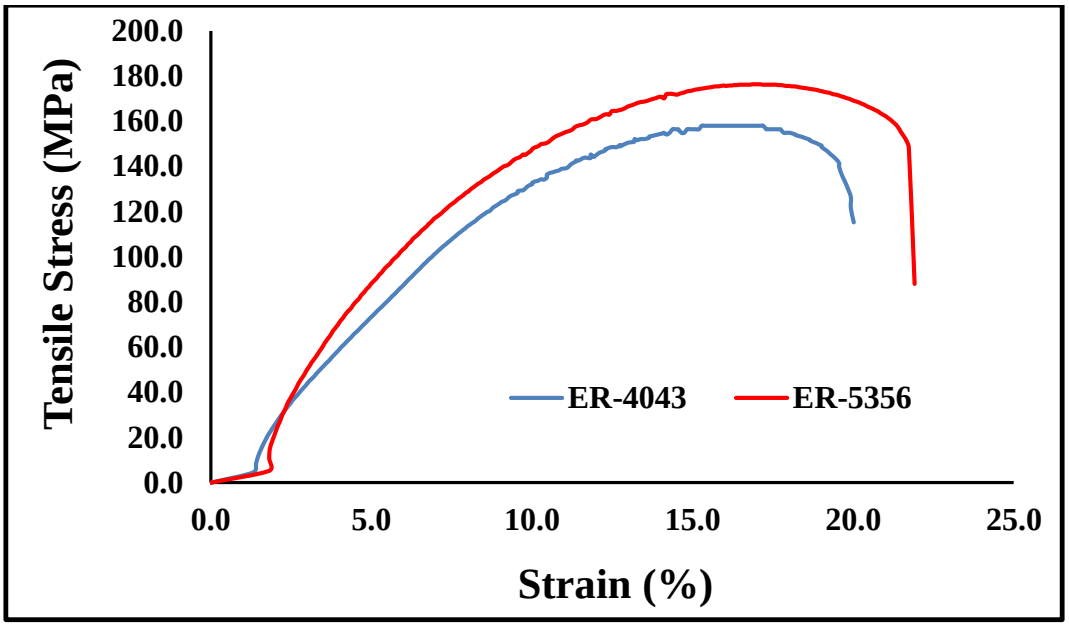

Figure 42: Stress strain diagram of TIG welded joint with filler ER 4043 and ER 5356

5.1.2 Micro-hardness

The micro-hardness value across the weldment in the transverse direction was measured with the help of Vickers hardness testing machine and these micro-hardness variations of the different zone (Fusion zone, heat-affected zone, and base material) for both fillers (ER 4043 and ER 5356) as shown in fig.43. The average micro-hardness value of different zone was presented in table 9. It was found that the micro-hardness value for HAZ was higher than the fusion zone (FZ). The average hardness value of FZ for filler ER 4043 and ER 5356 was approximately 66 HV and 74 HV respectively. The higher hardness value is dependent on the existence of alloying elements such as magnesium (Mg) and silicon (Si) and these two elements amalgamate and go through precipitation reaction and form precipitates of Mg_2Si [113].

Table 9: Average micro-hardness value of various zone

Position	Average hardness (HV)	
	ER 4043	ER 5356
Fusion zone	66	74
HAZ from AA 7075	110	123
HAZ from AA 6061	71	82
AA7075	132	137
AA6061	88	98

The hardness variation for both sides by using filler ER 5356 is higher as compared to the welded joint by using filler ER 4043 due to the low segregation of strengthening phases and refined microstructure. The welded joint made by ER 4043 shows columnar grains whereas fine equiaxed grains were found in the joints made by ER 5356. The average hardness value at HAZ is higher than the FZ for both welded samples, and these values were 110 HV and 123 HV respectively.

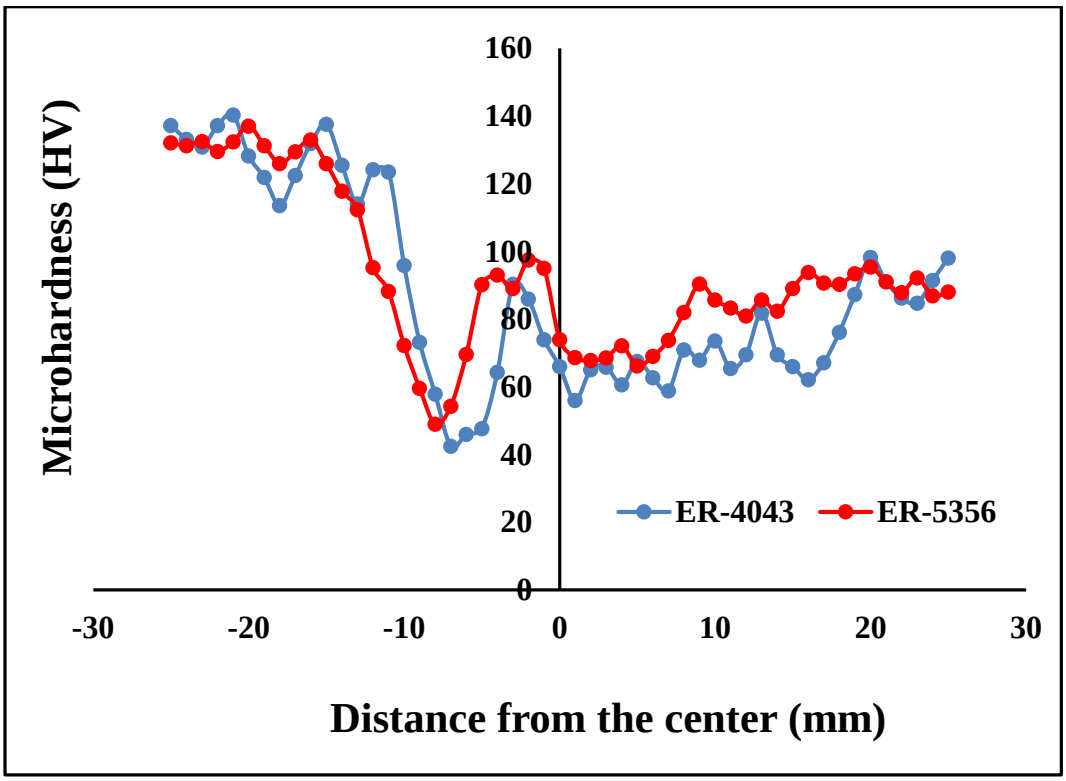

Figure 43: Micro-hardness of TIG welded joint with filler ER 4043 and ER 5356

5.1.3 Residual stress

The residual stresses in the weldment of AA 6061 and AA7075 with filler ER 4043 and ER 5356 were determined by the cosα method. The cosα method was introduced in japan for residual stress analysis in 1978 [114]. This method is allowed the stress analysis by capturing the results by a single incident X-ray beam via a 2D detector. It shows the peak center is very stable throughout the welding. Debye ring and distortion ring is obtained by using cosα method. An investigation has been done to analyze the residual stress. The 3D Debye ring and distortion ring of welded samples are shown in fig. 44.

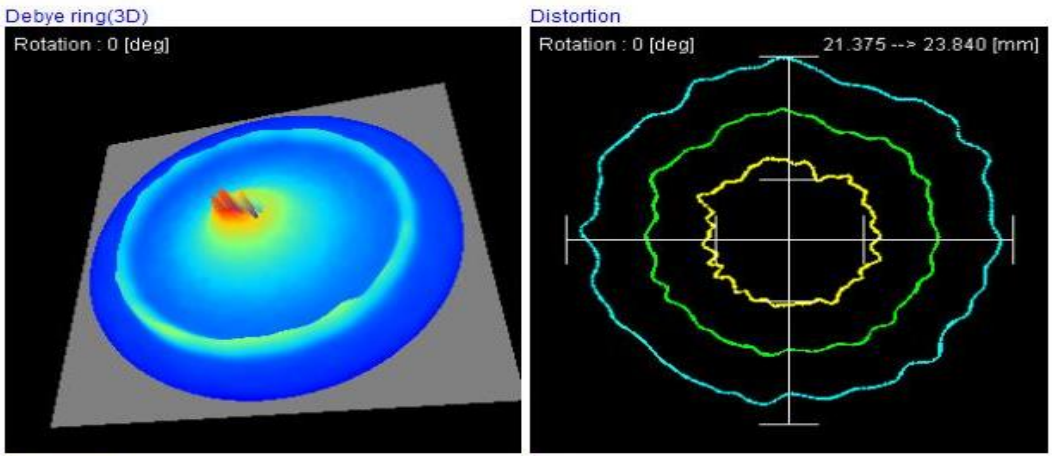

(a)

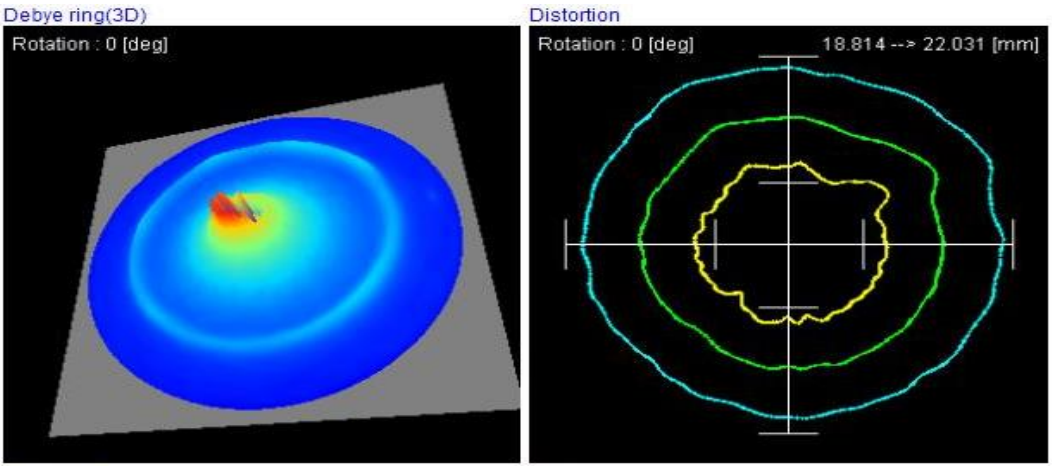

(b)

Figure 44: 3D Debye ring and 2D Distortion ring at the center of the welded joint, (a) filler ER 4043, (b) Filler ER 5356

The X-ray incident angle was set 35º and ±5 oscillation was applied. The variation of residual stresses in the transverse direction of weldment with filler ER4043 and ER5356 are shown in fig. 45. Residual stresses (compressive or tensile) will influence the mechanical behavior of the welded joint. It can reduce brittle fracture strength, buckling strength and cracking in the weldment. Residual stress is also influenced by the prediction of brittle failure and affect the lifetime prediction of the component [115-118]. Residual stress contributes both negative and positive effects on the weldment, generally, the tensile residual stress leads to a negative effect on the weldment [119].

The base material AA7075 on LHS of the weldment shows a minimum compressive residual stress, however, the residual stress gradually increases from the base material to towards the weldment and then decreases till second base material AA6061. The maximum residual stress occurs in the location where the equivalent of the plastic strain is decreased suddenly. The maximum compressive residual stress 77MPa was located at the fusion zone (FZ) of the TIG weldment with filler ER4043, whereas 63 MPa compressive residual stress was obtained at FZ with filler ER 5356.

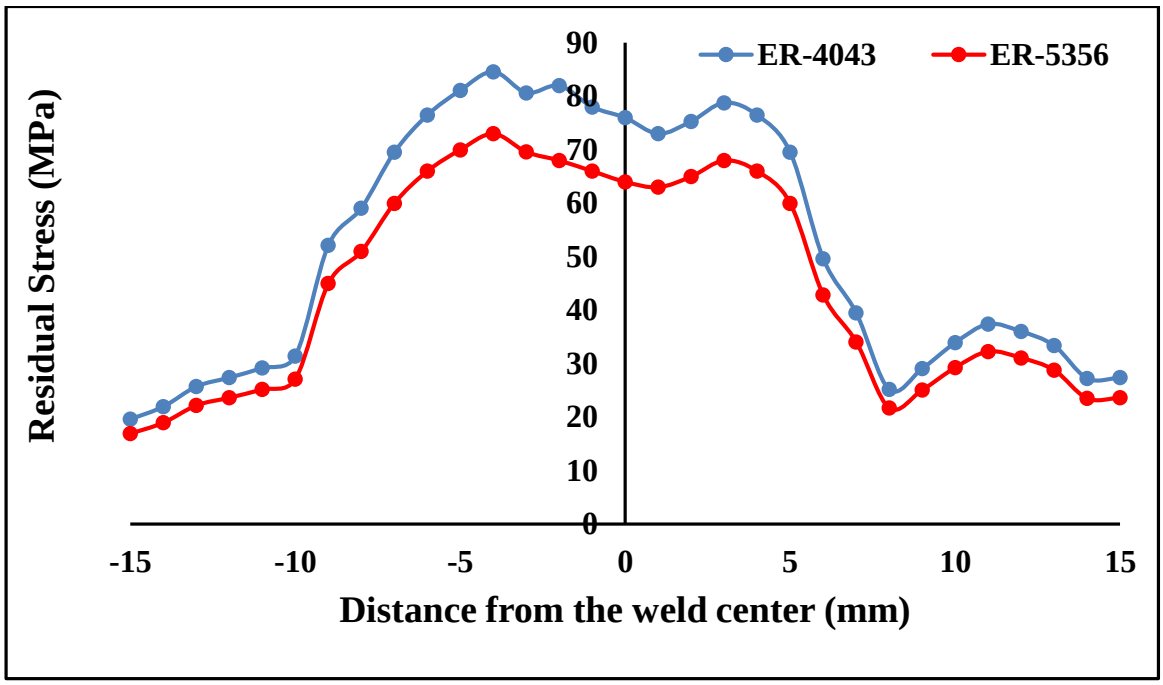

Figure 45: Residual stress of TIG welded joint with filler ER 4043 and ER 5356

5.1.4 Microstructure analysis of TIG welded joint

5.1.4.1 EDX analysis

The energy-dispersive X-ray spectroscopy (EDX/EDS) of tungsten, inert gas welded joint with filler ER4043 and TIG+FSP welded joint has been analyzed. It was found that the atomic percentage of Al and Si in the welded joint is higher than the other elements. Fig. 46 illustrates the EDX image while table 10-11, shows the percentage of element concentration at fusion zone (FZ) in the TIG welded joint with filler ER4043 and ER 5356. The percentage of aluminum being highest (84.30%), Si is 4.66% (2nd highest) and Zn is 2.54% (3rd highest) in TIG welded joint with filler ER 4043, whereas the percentage of aluminum being highest (90.98%), Mg is 4.25 % (2nd highest) and Si is 2.67% (3rd highest) found in TIG welded joint with filler ER 5356 as shown in table 10 and 11. The alloying elements like Zinc (Zn), Magnesium (Mg) and Silicon (Si) elements were found in the weldment besides the aluminum (Al) and it was found that Mg, Zn, and Si created the phase after the precipitation reaction in the weldment. The very high intensity was found from aluminum, because of the fragmentation of precipitates the intensity of Mg_2Si and $MgZn_2$ was decreasing in tungsten inert gas welded joint.

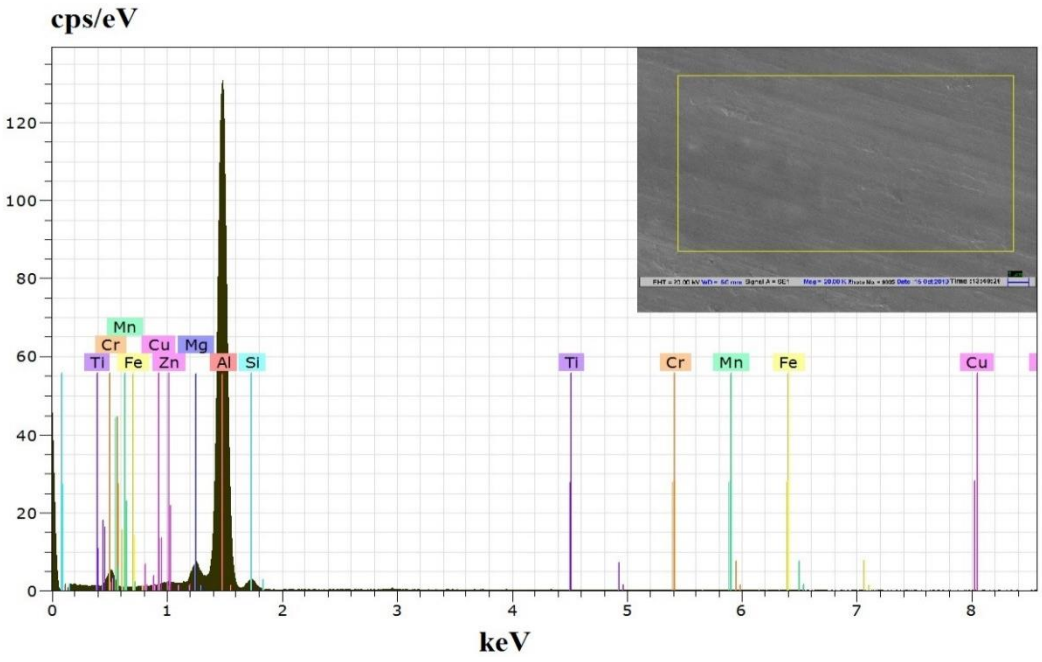

(a)

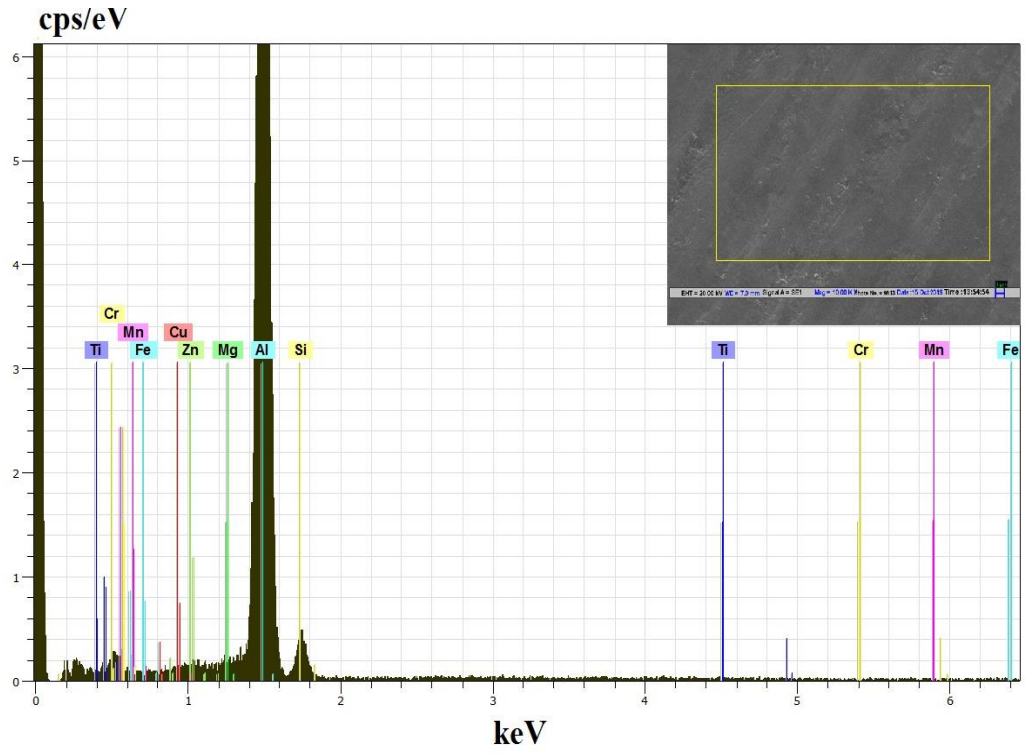

(b)

Figure 46: EDX analysis of TIG welded joint in fusion zone with filler ER4043 and filler ER 5356

Table 10: Concentration of elements in TIG welded joint of AA6061 and AA7075 with filler ER 4043

Elements (%)	Point-1	Point-2	Point-3	Average
Al	83.1	81.5	88.3	84.30
Si	3.47	5.94	4.58	4.66
Zn	2.81	2.61	2.2	2.54
Cu	2.62	2.2	1.84	2.22
Fe	2.5	2.04	1.72	2.09
Mg	1.77	1.88	1.13	1.59
Mn	1.25	1.22	0.86	1.11
Cr	0.9	0.96	0.47	0.78

Table 11: Concentration of elements in TIG welded joint of AA6061 and AA7075 with filler ER 5356

Elements	Point-1	Point-2	Point-3	Average
Al	90.98	89.93	90.21	90.37
Mg	4.36	4.12	4.27	4.25
Si	2.45	2.84	2.71	2.67
Zn	1.81	2.64	2.41	2.29
Cu	0.14	0.15	0.14	0.14
Cr	0.09	0.1	0.09	0.09
Mn	0.08	0.09	0.08	0.08
Fe	0.06	0.05	0.06	0.06
Ti	0.03	0.08	0.03	0.05

5.1.4.2 XRD analysis

X- Ray diffraction is used for examine the phase detection of dissimilar welded joint AA6061 and AA7075 with filler ER4043 and ER 5356 were found four major phases Al, Al_2CuMg, $MgZn_2$and Mg_2Si as shown in fig. 47.

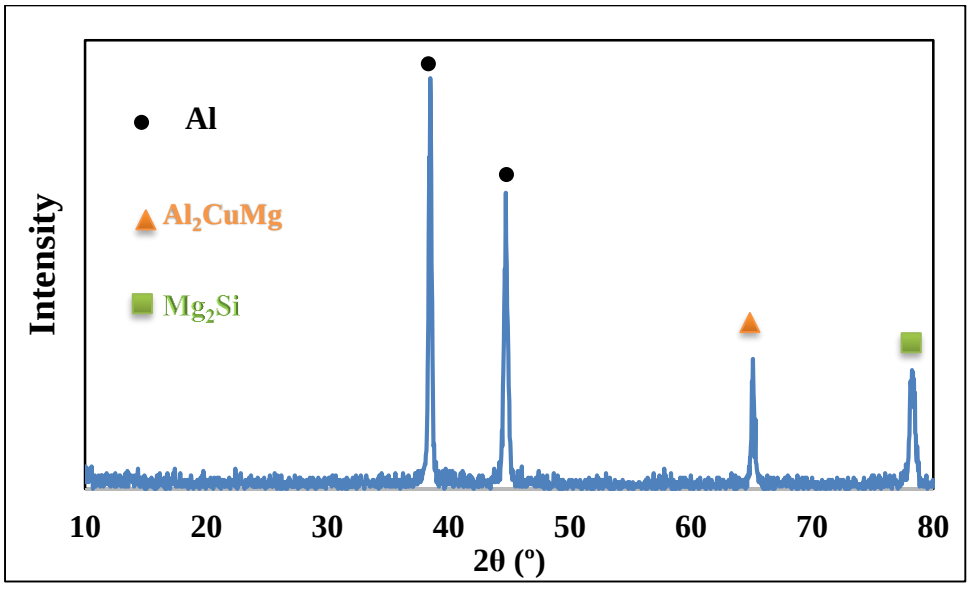

(a)

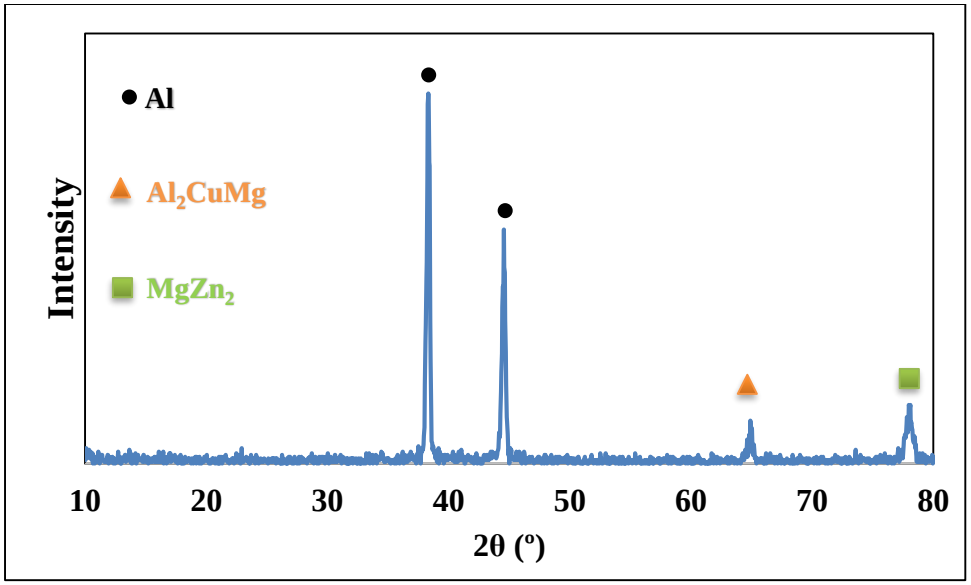

(b)

Figure 47: XRD peaks, (a) with filler ER 4043, (b) with filler ER 5356

Magnesium (Mg) and Silicon (Si) elements were found in the weldment besides the aluminum (Al), it is found that Mg and Si created the phase after the precipitation reaction in the weldment. The very high intensity was found from aluminum, because of the fragmentation of precipitates the intensity of Mg_2Si was increases after the TIG welded joint with filler ER 4043 and ER 5356. The alloying elements such as Si and Mg existing in the weld center make precipitation reaction and form a strong precipitate of Mg_2Si to give a higher strength. The same phase of Al_2CuMg was detected in both welded specimens.

5.1.4.3 Microstructure analysis

The weld bead of welded specimens AA6061 and AA7075 with filler ER 4043 and ER 5356 as shown in fig. 48. It was found that high depth and good penetration were achieved with filler ER 5356 weldments as compared to ER 4043, but full penetration could not be achieved in both specimens due to lack of parameter optimization on voltage, current and welding speed.

The microstructure of TIG-welded joints with filler, ER 4043 and ER 5356 was observed at fusion zone (FZ) using high magnification as shown in fig. 49. The fusion

zone shows an equiaxed dendritic structure and this zone was made due to melting and re-solidification during the welding process [113].

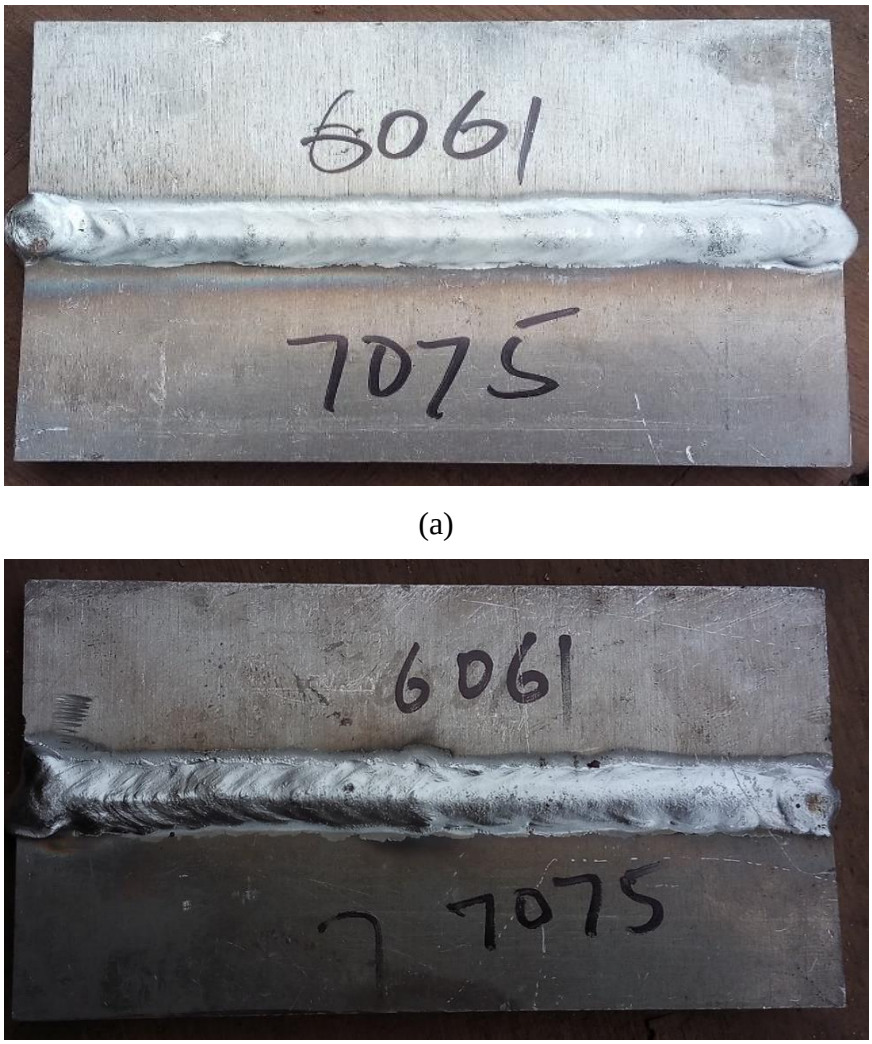

(a)

(b)

Figure 48: TIG welded joint of AA6061 and AA7075, (a) with filler 4043, (b) with filler ER5356

Fig. 49 shows the precipitate of Mg_2Si the compound in Al-matrix. A weld disseminated precipitate of the Mg_2Si the intermetallic compound was responsible for improved the mechanical properties of welded joints with filler ER 5356. Fine equiaxed grains were observed in filler ER 5356 which are capable to accommodate contraction strains more easily, it means more ductile columnar grains were observed which may result in enhanced tensile strength.

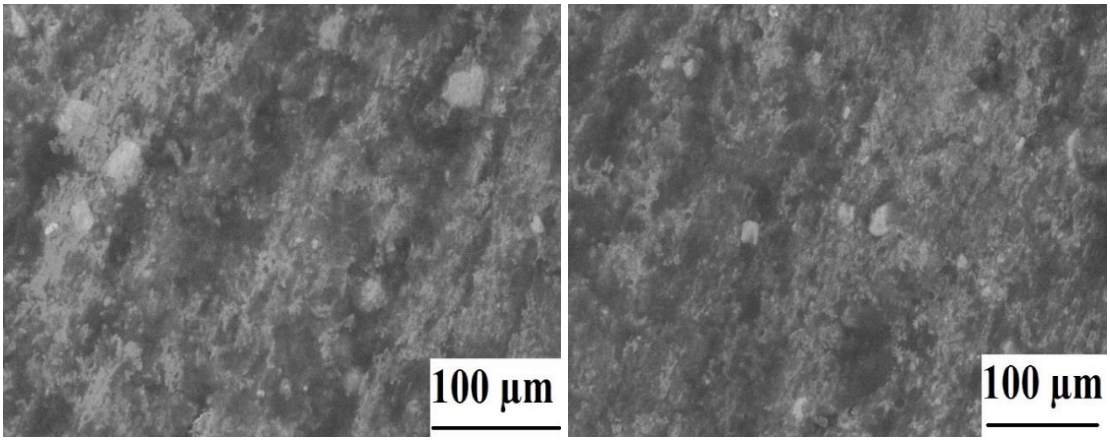

(a) (b)

Figure 49: Optical images of TIG welded joint at fusion zone (a) filler ER 4043, (b) filler ER 5356

Table 12: Grain sizes of TIG welded joint at various zone

Grain size (µm)			
Filler material	HAZ AA6061	Fusion zone	HAZ AA7075
ER 4043	22.1	20.4	28.4
ER 5356	24.8	18.2	26.2

The grain size of TIG weldment was analyzed by the Image J software and observed grain size in fusion zone with filler ER4043 and ER5356 are 20.4µm, and 18.2 µm as shown in table 12. The grain sizes at HAZ of AA7075 and AA6061 for both welded specimens were found differed slightly. The average grains size in the heat-affected zone from AA 6061 was 22.1 µm and 24.8 µm with filler ER 4043 and ER 5356 respectively, whereas average grains size in the heat-affected zone from AA 7075 were 28.4 µm and 26.2 µm with filler ER 4043 and ER 5356 respectively. The improvement of grains size of welded joint with filler ER 5356 at the fusion zone in 10.78% higher than filler 4043.

5.1.4.4 Fractured Analysis

Fig. 50 shows the fractured surface after the tensile test. In this analysis, two modes of failures were observed. The large dimples and quasi cleavage with a sharp edge and various depth were found on the fractured tensile specimen's surface of the TIG-

welded joint with filler ER4043, whereas fine dimple and large void were found in TIG welded joint with filler ER5356 as shown in fig. 50 (a-b).

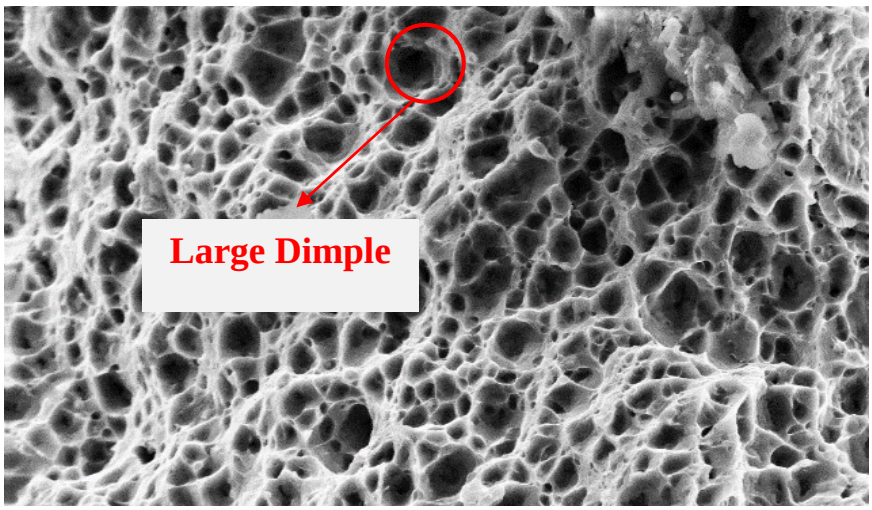

(a)

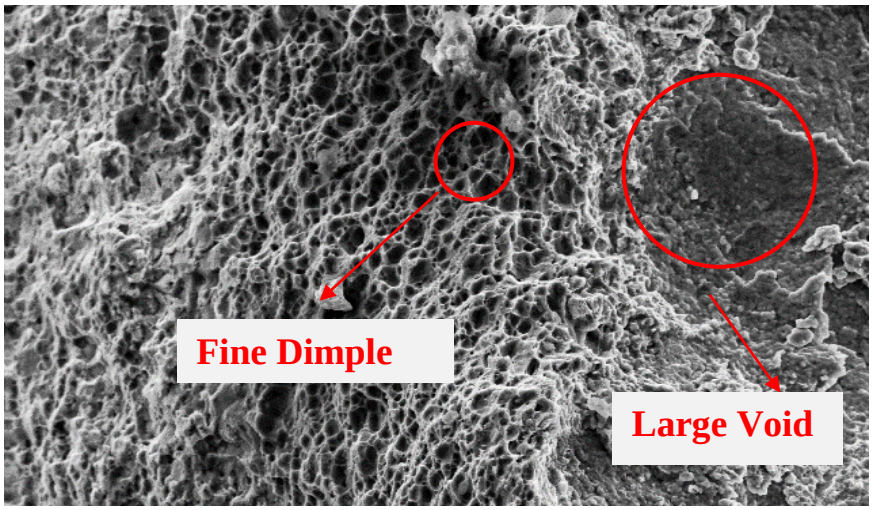

(b)

Figure 50: Fractured images of TIG welded joint (a) filler ER 4043, (b) filler ER 5356

Many large and equiaxed dimples were observed in TIG welded joint with filler ER4043 whereas the main fractured mode was quasi cleavage with a lot of tiny dimples gathered around the large and quasi cleavage dimples found in filler ER5356 which shows the ductile fracture and this is the evidence of crack nucleation and growth 4mm away from the weld line. The ductile fracture of the welded joint occurs, an improvement in ductility may be achieved when the cavity nucleation could be suppressed [120]. The maximum inter-facial normal stress depends upon the grain

particle size and the volume fraction of the grain particles [121]. The fractured surface at room temperature was shown in fig. 50.

5.2 Optimization of process parameters of TIG+FSP welded joints of filler ER4043

After TIG welding, FSP technique was used on TIG weldment to improve the welding quality and mechanical properties as shown in fig.51. The non-consumable H13 steel tool with pin diameter, shoulder diameter and pin length of 7 mm, 19.5 mm, and 5.5 mm respectively was used is shown in fig. 32. The input parameters range which are in TIG+FSP welded joint have been taken as rotational speed (1000 rpm to 1300 rpm), feed rate (30-60 mm/min) and tilt angles (0^0-2^0).

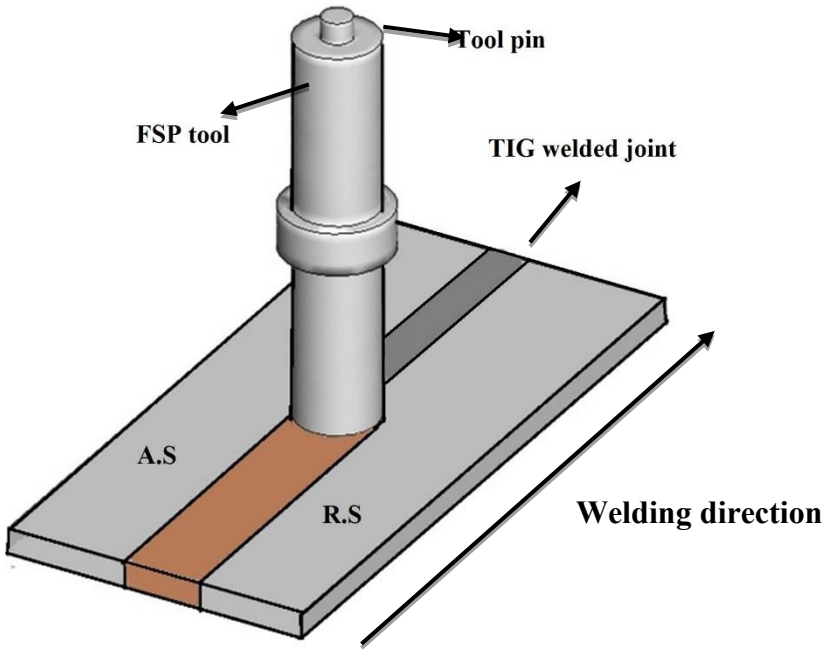

Figure 51:TIG+FSP welding approach

Fig. 52 demonstrate the dimension of tensile sub test specimen (ASTM E8) and the sampling schematic for joint characterization. The tensile test specimens were sliced and machined from the TIG+FSP welded joint using milling cutter and shaper machine. Single pass FSP is used to fabricate TIG+FSP welded joint is shown in fig. 51. The tensile test were performed on computer controlled UTM machine of weldment at room temperature using different processing parameters. Three sub

tensle specimen were tested and average of these three results are taken. As recommended by the design expert software, twenty joints were fabricated which are as shown in fig.34.

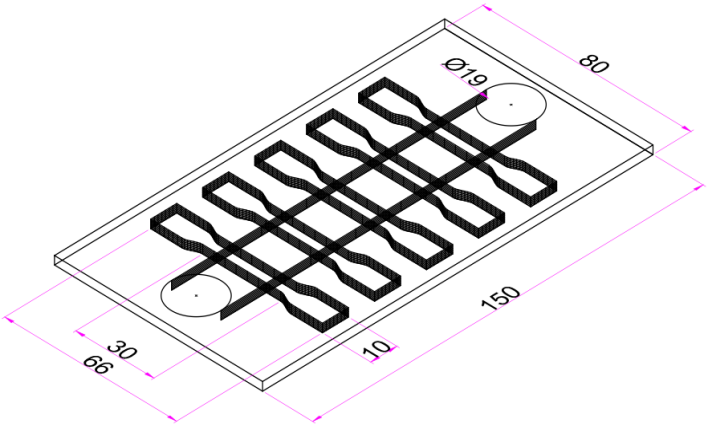

Figure 52: Dimension of TIG+FSP welded tensile test specimen

RSM techniques which is used to optimize the independent variable influences the dependent variables. Based on central composite design (CCD), all the experiments have been conducted according to the design experiments, where the lower and upper was coded as -1 and +1. The face centered CCD contains twenty experimental observations with three independent input variable. The Processing parameter of TIG welding and friction stir processing and its level are shown in tables 13.

Table 13: Processing parameter of friction stir processing and its level

Parameters	Units	Notation	Range	Levels		
				-1	0	1
Tool rotational Speed	rpm	A	1000-1300	1000	1150	1300
Traverse Speed	mm/min	B	30-60	30	45	60
Tilt angle	degree	C	0-2	0	1	2

5.2.1 Tensile strength

In order to analyze the effect of friction stir processing on the TIG-welded joint, the tensile load applied on TIG and TIG+FSP welded joint by universal testing machine (UTM) at room temperature and fractured surfaces obtained from the tensile test were compared with one another. Three test specimens were tested at each condition and

the average of these three results are presented in Table 14. The tensile strength of the weldment made by TIG and TIG+FSP techniques are compared. Due to the absence of porosity, small grain size and presence of extra material in the welded region with filler wire, the tensile strength of TIG+FSP obtained higher value than the conventional TIG joining process. Filler ER5356 present in the welded joint makes more compact pressure leading to increase bond strength instead of filler ER4043. The grain size in the fusion zone for ER5356 is smaller than the ER4043. The tensile strength with filler ER5356 was obtained higher than ER4043 [111]. According to Hall Petch equation $\sigma_1 = \sigma_i + kd^{(-1/2)}$, the tensile strength is inversely proportional to the grain size [122]. The tensile strength of the TIG-welded joint using filler 4043 and 5356 was calculated 158.6 MPa and 176.2 MPa respectively which is less than the TIG+FSP as shown in the table 14.

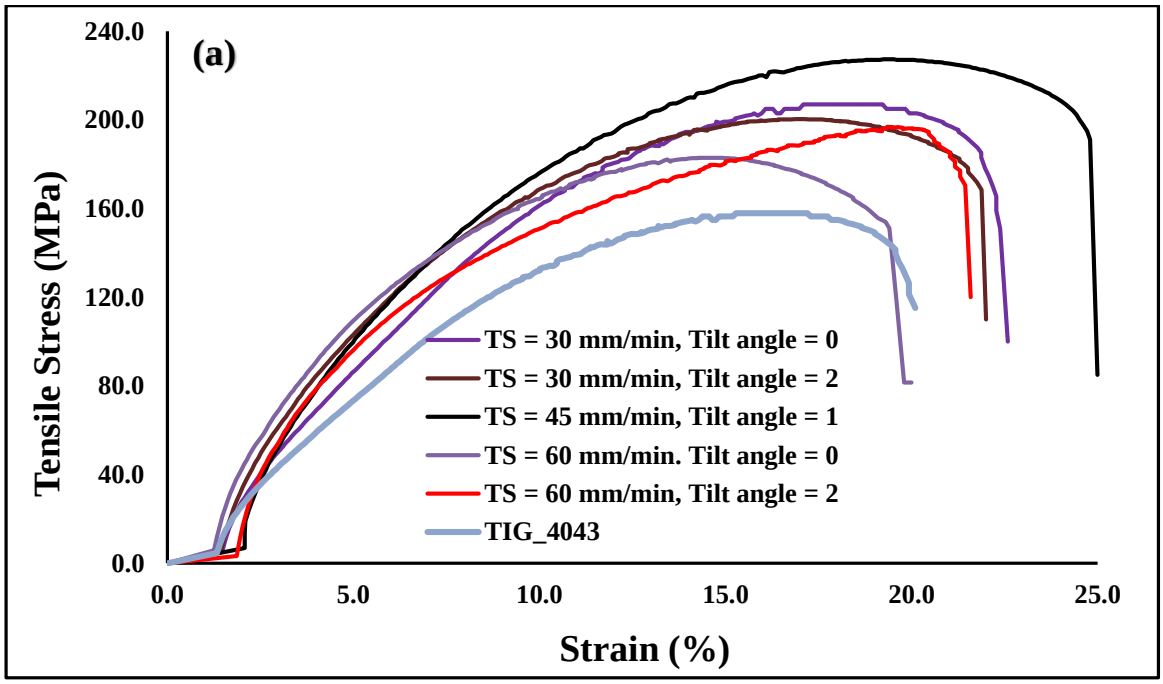

The tensile strength of the TIG+FSP welded joint increased with increasing tool rotational speed. The highest tensile strength (255 MPa) was observed in TIG+FSP with filler ER 4043 at tool rotational 1300 rpm with feed rate 45 mm/min and tilt angle 1º, whereas minimum tensile strength (183 MPa) was observed at tool rotational 1000 rpm with feed rate 60 mm/min and tilt angle 0º.

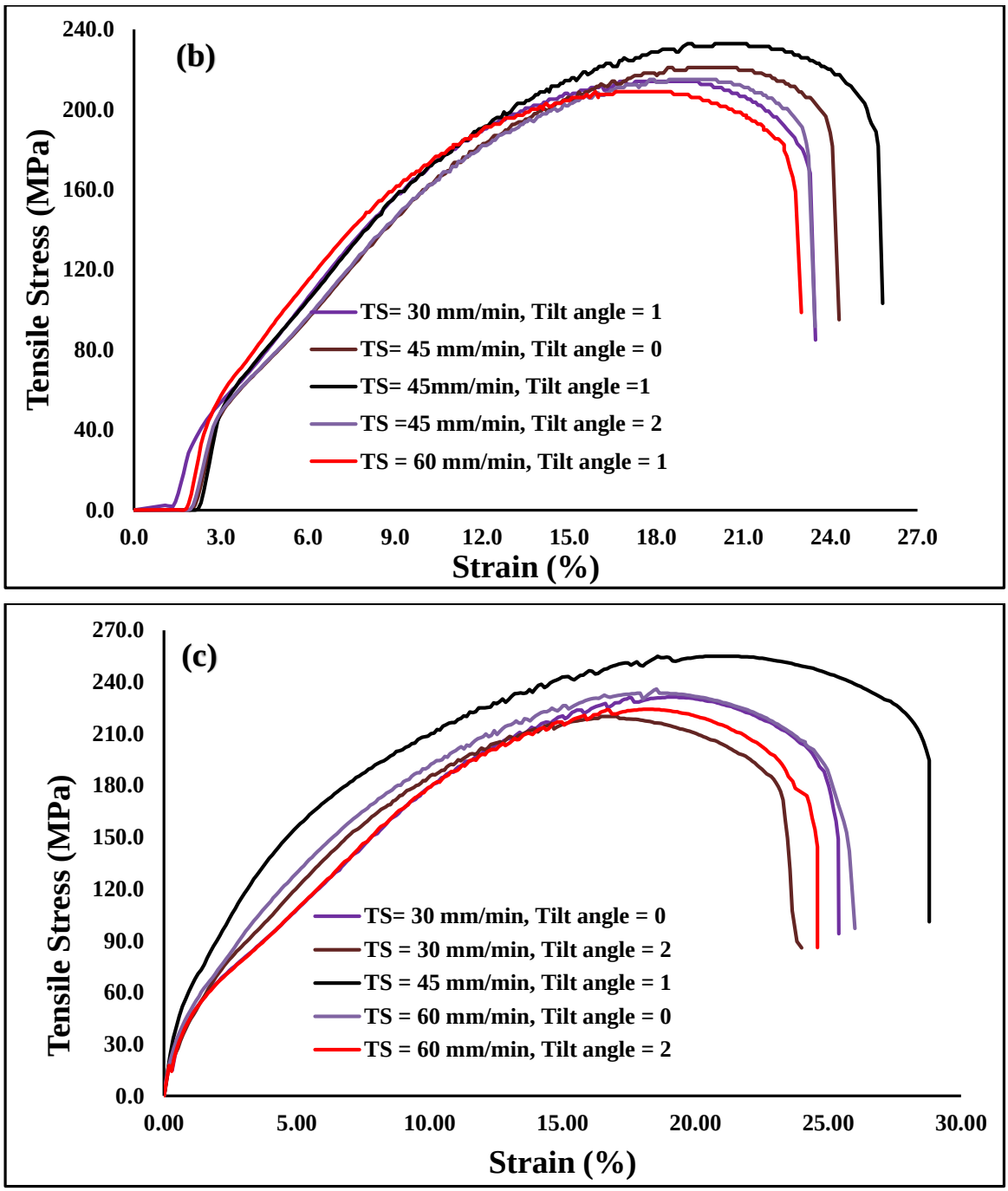

Figure 53: Stress strain diagram of TIG+FSP welded joint, (a) Tool rotation 1000 rpm, (b) Tool rotation 1150 rpm, (c) Tool rotation 1300 rpm

Three statistical parameters are investigated i.e., standard deviation (SD), standard error (SE) and 95% confidence interval for TIG+FSP welded joint with filler ER4043 as shown in table 14-17. The standard deviation (SD) provides the deviance of the experimental values from the mean it may be calculated as SD= $[\Sigma(X_i - M)^2/(N-1)]^{1/2}$ and the standard error is a quantity used to measure how to close the prediction

values to the experimental values. SE is calculated as $SE=SD/N^{1/2}$, where N= No of observation and M= mean.

The confidence interval has shown that tensile strength and hardness increased with increasing tool rotation, whereas residual stress decreased with increasing tool rotation.

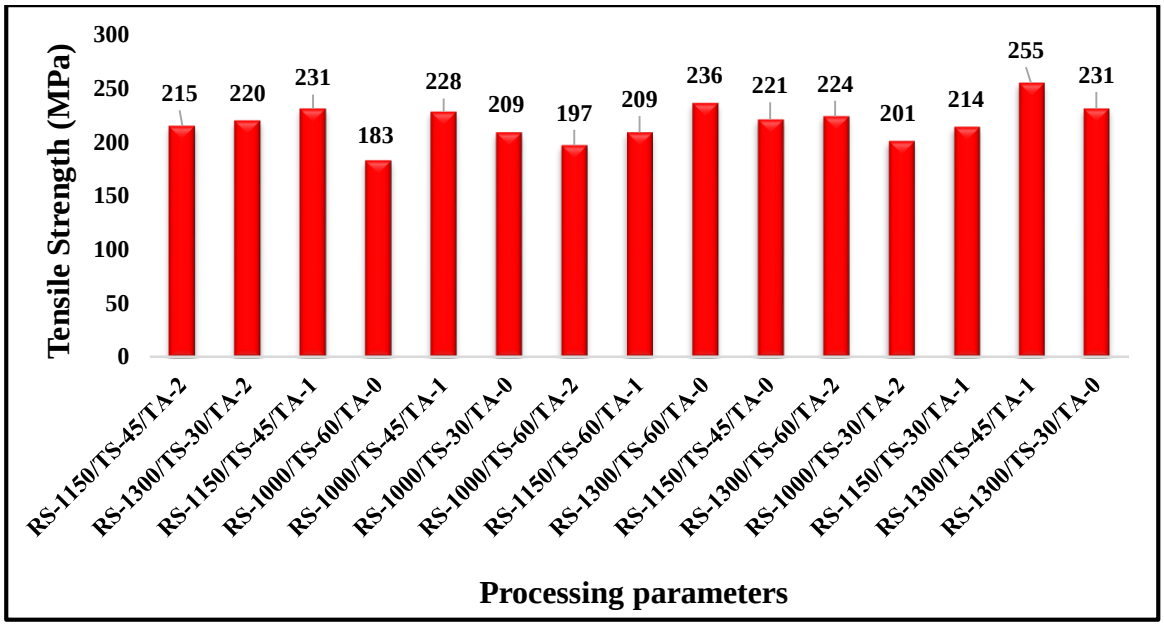

Figure 54: Variation of tensile strength to the processing parameters

5.2.2 Micro-hardness

The micro-hardness distribution of the TIG-welded joint of AA6061 and AA7075 with different filler wire and TIG+FSP weldments with different processing parameters were analyzed by Vickers hardness testing results are shown in fig.55-56. Vickers micro-hardness machine was used for measuring the hardness across the welded joints with a load of 100 grams and dwell time 30 sec. The hardness distributions are asymmetrical in the weld center due to the microstructure of the advancing side and retreating side introduced by unsteady plastic flow from the base metal to the weld center [123]. The hardness slopes downward from the base metal to the welded region. The hardness fluctuates largely on the advancing side while the hardness holds steady in the retreating side [124]. The alloying elements such as Si and Mg existing in the weld center make precipitation reaction and form a strong precipitate of Mg_2Si to give a higher strength. It showed a significant difference,

where the welded joint using filler ER4043 showed a lower average hardness value compared to filler ER5356. The maximum hardness value at the center of weldment for filler ER4043 is 105 HV at tool rotational 1300 rpm with feed rate 45 mm/min and tilt angle 1º as shown in fig. 56. The filler wire ER4043 shows the columnar grains while fine equiaxed grains are found in ER5356. It may be analyzed that the fine equiaxed grains improve mechanical properties than the columnar grains [125].

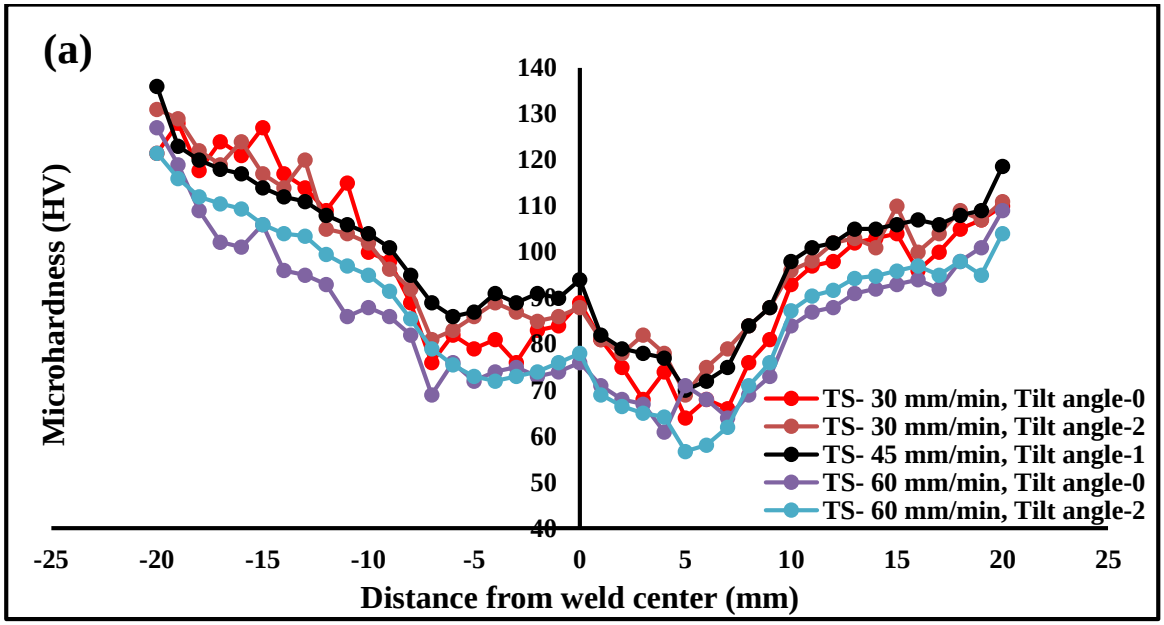

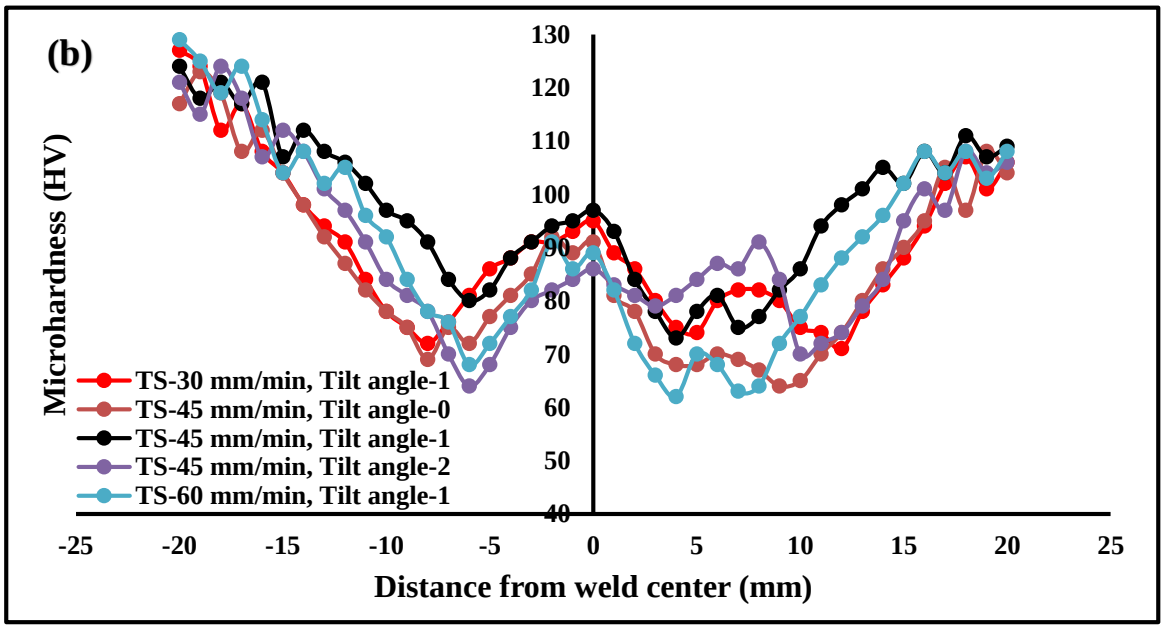

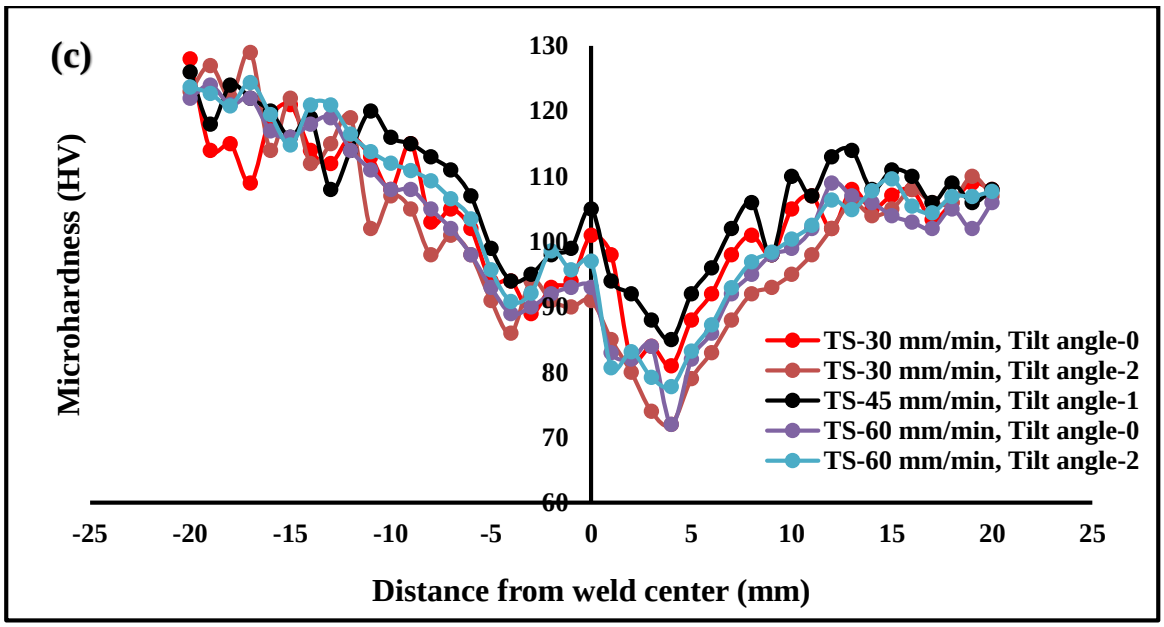

Figure 55: Distribution of micro-hardness of welded joint, (a) TIG welding, (b-d) TIG+FSP welded joint, (b) tool rotation 1000 rpm, (c) Tool rotation 1150 rpm, (d) Tool rotation 1300 rpm

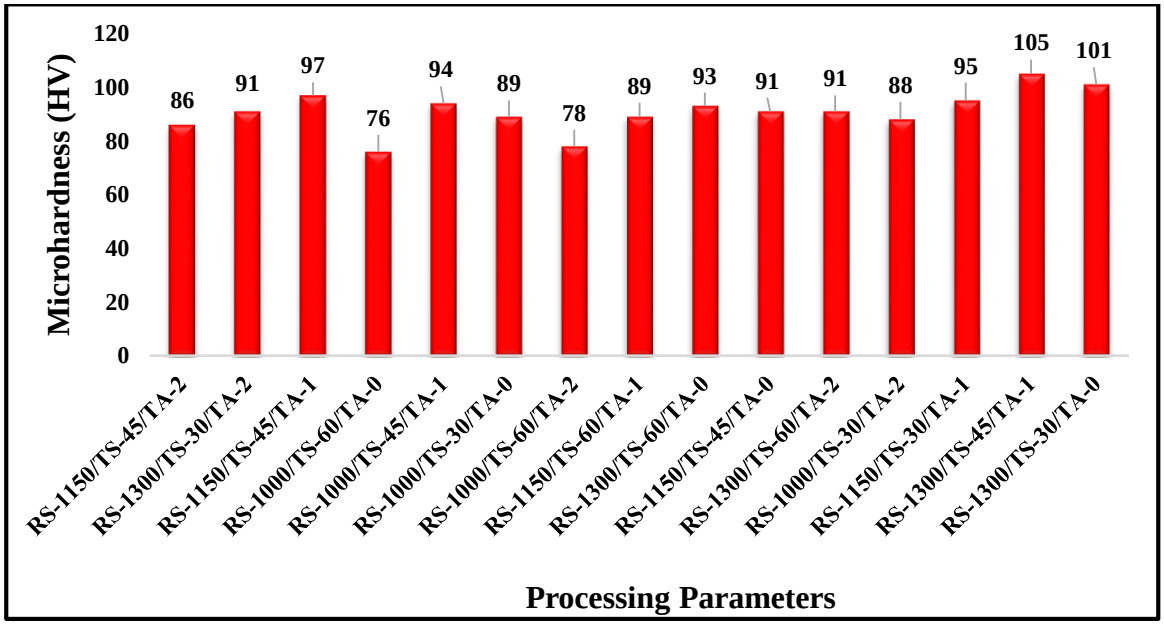

Figure 56: Variation of Micro-hardness to the processing parameters

Table 14: Tensile strength of TIG+FSP welded joint with filler ER4043

Processing Parameter			Tensile Strength (MPa)			Mean Tensile Strength MPa	Standard Deviation	Standard error	95% confidence Interval	
A:Tool Rotation Speed (rpm)	B:Traverse Speed (mm/min)	C:Tilt angle (degree)	Specimen 1	Specimen 2	Specimen 3				Minimum	Maximum
1150	45	2	215.6	215.0	214.5	215.0	0.55	0.32	214.4	215.7
1300	30	2	220.0	221.0	219.0	220.0	1.00	0.58	218.9	221.1
1150	45	1	231.0	231.5	230.5	231.0	0.50	0.29	230.4	231.6
1000	60	0	183.6	183.5	182.0	183.0	0.90	0.52	182.0	184.0
1000	45	1	228.0	227.5	228.5	228.0	0.50	0.29	227.4	228.6
1150	45	1	232.8	232.4	231.1	232.1	0.89	0.51	231.1	233.1
1000	30	0	208.4	210.4	208.2	209.0	1.22	0.70	207.6	210.4
1000	60	2	197.4	196.5	197.2	197.0	0.47	0.27	196.5	197.6
1150	45	1	234.1	232.4	232.6	233.0	0.93	0.54	232.0	234.1
1150	60	1	208.6	208.6	209.8	209.0	0.69	0.40	208.2	209.8
1300	60	0	236.0	236.5	235.5	236.0	0.50	0.29	235.4	236.6
1150	45	1	229.0	227.8	227.2	228.0	0.92	0.53	227.0	229.0
1150	45	1	232.5	232.5	231.0	232.0	0.87	0.50	231.0	233.0
1150	45	0	221.0	221.0	221.4	221.1	0.23	0.13	220.9	221.4
1300	60	2	224.6	224.0	223.8	224.1	0.42	0.24	223.7	224.6
1000	30	2	201.3	200.8	201.1	201.1	0.25	0.15	200.8	201.4
1150	30	1	214.8	213.2	214.0	214.0	0.80	0.46	213.1	214.9
1300	45	1	256.0	254.8	254.2	255.0	0.92	0.53	254.0	256.0
1300	30	0	231.5	230.8	230.4	230.9	0.56	0.32	230.3	231.5
1150	45	1	228.4	228.0	227.6	228.0	0.40	0.23	227.5	228.5

Table 15: % elongation of TIG+FSP welded joint with filler ER4043

Processing Parameter			Elongation (%)			Mean Elongation (%)	Standard Deviation	Standard error	95% confidence Interval	
A:Tool Rotation Speed (rpm)	B:Traverse Speed (mm/min)	C:Tilt angle (degree)	Specimen 1	Specimen 2	Specimen 3				Minimum	Maximum
1150	45	2	24.5	23.2	22.8	23.5	0.89	0.51	22.5	24.5
1300	30	2	25.0	26.0	24.0	25.0	1.00	0.58	23.9	26.1
1150	45	1	24.4	25.3	26.2	25.3	0.90	0.52	24.3	26.3
1000	60	0	19.4	21.2	19.4	20.0	1.04	0.60	18.8	21.2
1000	45	1	25.8	24.8	24.4	25.0	0.72	0.42	24.2	25.8
1150	45	1	25.9	26.2	24.2	25.4	1.08	0.62	24.2	26.7
1000	30	0	21.8	23.1	22.8	22.6	0.68	0.39	21.8	23.3
1000	60	2	21.9	22.4	20.6	21.6	0.93	0.54	20.6	22.7
1150	45	1	26.5	24.8	25.3	25.5	0.87	0.50	24.5	26.5
1150	60	1	23.5	22.1	23.3	23.0	0.76	0.44	22.1	23.8
1300	60	0	26.2	25.4	26.4	26.0	0.53	0.31	25.4	26.6
1150	45	1	25.8	24.0	25.3	25.0	0.93	0.54	24.0	26.1
1150	45	1	25.8	25.0	25.6	25.5	0.42	0.24	25.0	25.9
1150	45	0	25.2	24.0	23.6	24.3	0.83	0.48	23.3	25.2
1300	60	2	24.8	24.0	25.0	24.6	0.53	0.31	24.0	25.2
1000	30	2	23.2	22.0	20.8	22.0	1.20	0.69	20.6	23.4
1150	30	1	23.4	22.8	24.3	23.5	0.75	0.44	22.6	24.4
1300	45	1	28.5	28.6	29.4	28.8	0.49	0.28	28.3	29.4
1300	30	0	25.4	25.0	25.8	25.4	0.40	0.23	24.9	25.9
1150	45	1	25.2	24.4	25.4	25.0	0.53	0.31	24.4	25.6

Table 16: Micro-hardness of TIG+FSP welded joint with filler ER4043

Processing Parameter			Micro-hardness (HV)			Mean Micro-hardness (HV)	Standard Deviation	Standard error	95% confidence Interval	
A:Tool Rotation Speed (rpm)	B:Traverse Speed (mm/min)	C:Tilt angle (degree)	Specimen 1	Specimen 2	Specimen 3				Minimum	Maximum
1150	45	2	86.5	86.0	85.6	86.0	0.45	0.26	85.5	86.5
1300	30	2	91.0	90.4	91.5	91.0	0.55	0.32	90.3	91.6
1150	45	1	97.6	96.4	97.0	97.0	0.60	0.35	96.3	97.7
1000	60	0	76.5	76.0	75.4	76.0	0.55	0.32	75.3	76.6
1000	45	1	94.2	94.8	93.0	94.0	0.92	0.53	93.0	95.0
1150	45	1	98.0	98.5	97.4	98.0	0.55	0.32	97.3	98.6
1000	30	0	89.0	89.4	88.5	89.0	0.45	0.26	88.5	89.5
1000	60	2	78.2	77.8	78.0	78.0	0.20	0.12	77.8	78.2
1150	45	1	100.2	101.5	101.2	101.0	0.68	0.39	100.2	101.7
1150	60	1	89.6	89.0	88.4	89.0	0.60	0.35	88.3	89.7
1300	60	0	92.6	93.0	93.4	93.0	0.40	0.23	92.5	93.5
1150	45	1	98.1	98.0	98.0	98.0	0.06	0.03	98.0	98.1
1150	45	1	99.4	98.4	99.2	99.0	0.53	0.31	98.4	99.6
1150	45	0	91.2	90.8	91.0	91.0	0.20	0.12	90.8	91.2
1300	60	2	91.0	90.2	91.8	91.0	0.80	0.46	90.1	91.9
1000	30	2	88.6	86.2	89.2	88.0	1.59	0.92	86.2	89.8
1150	30	1	95.4	95.6	94.0	95.0	0.87	0.50	94.0	96.0
1300	45	1	104.8	105.0	105.3	105.0	0.25	0.15	104.7	105.3
1300	30	0	101.0	100.4	101.5	101.0	0.55	0.32	100.3	101.6
1150	45	1	99.0	99.6	98.5	99.0	0.55	0.32	98.4	99.7

Table 17: Residual Stress of TIG+FSP welded joint with filler ER4043

Processing Parameter			Residual Stress (Mpa)			Mean Residual Stress (MPa)	Standard Deviation	Standard error	95% confidence Interval	
A:Tool Rotation Speed (rpm)	B:Traverse Speed (mm/min)	C:Tilt angle (degree)	Specimen 1	Specimen 2	Specimen 3				Minimum	Maximum
1150	45	2	48.0	48.5	47.4	48.0	0.55	0.32	47.3	48.6
1300	30	2	27.0	26.0	28.0	27.0	1.00	0.58	25.9	28.1
1150	45	1	40.0	38.4	38.6	39.0	0.87	0.50	38.0	40.0
1000	60	0	54.6	56.4	54.0	55.0	1.25	0.72	53.6	56.4
1000	45	1	42.0	43.0	41.0	42.0	1.00	0.58	40.9	43.1
1150	45	1	34.6	33.4	34.0	34.0	0.60	0.35	33.3	34.7
1000	30	0	63.0	65.0	61.0	63.0	2.00	1.15	60.7	65.3
1000	60	2	72.0	73.0	74.0	73.0	1.00	0.58	71.9	74.1
1150	45	1	40.0	39.4	37.6	39.0	1.25	0.72	37.6	40.4
1150	60	1	56.2	53.0	52.8	54.0	1.91	1.10	51.8	56.2
1300	60	0	41.0	39.0	43.0	41.0	2.00	1.15	38.7	43.3
1150	45	1	39.0	38.5	39.6	39.0	0.55	0.32	38.4	39.7
1150	45	1	40.0	39.0	41.0	40.0	1.00	0.58	38.9	41.1
1150	45	0	42.4	43.0	43.6	43.0	0.60	0.35	42.3	43.7
1300	60	2	48.2	49.6	49.2	49.0	0.72	0.42	48.2	49.8
1000	30	2	66.2	64.5	64.2	65.0	1.08	0.62	63.7	66.2
1150	30	1	50.0	46.5	50.6	49.0	2.21	1.28	46.5	51.5
1300	45	1	29.0	26.7	28.3	28.0	1.18	0.68	26.7	29.3
1300	30	0	35.0	30.0	31.0	32.0	2.65	1.53	29.0	35.0
1150	45	1	38.0	39.6	39.4	39.0	0.87	0.50	38.0	40.0

5.2.3 Residual Stress

Residual stresses (compressive or tensile) will influence the mechanical behavior of the welded joint. It can reduce brittle fracture strength, buckling strength and cracking in the weldment. Residual stress is also influenced the prediction of brittle failure and affect the life time prediction of the component [55-58]. Residual stress contributes both negative and positive effect to the weldment. Generally, the tensile residual stress lead to negative effect to the weldment [50, 57].

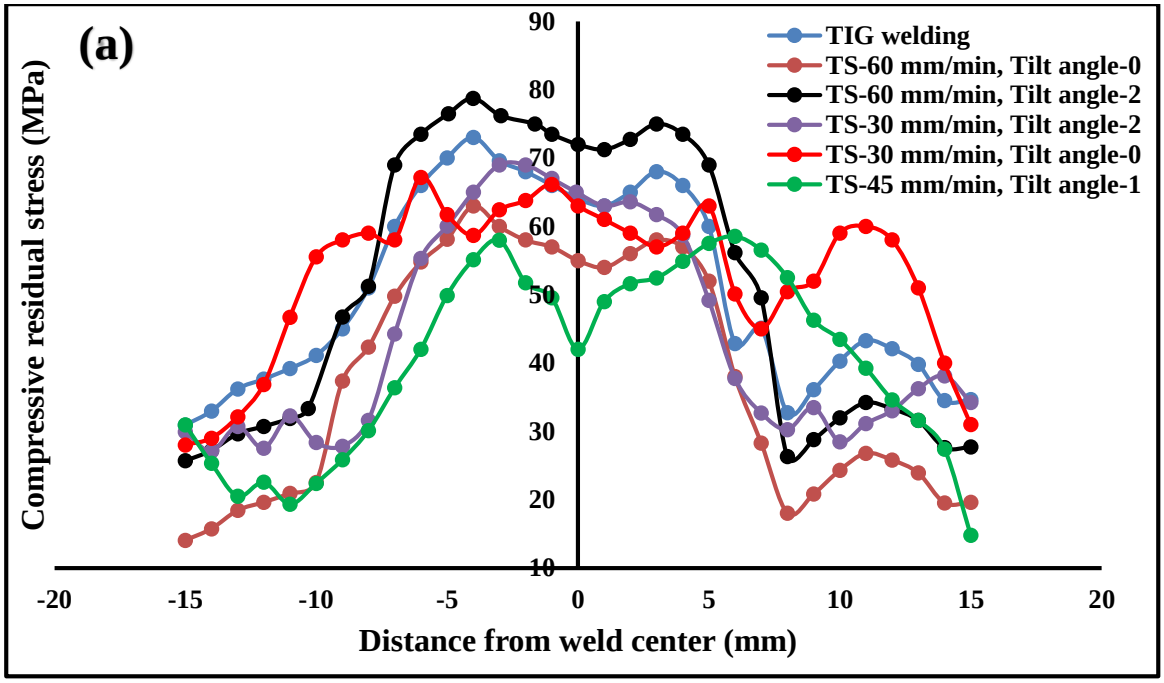

A mini portable X-ray diffraction apparatus (Pulstec μ-X360) at Delhi technological university, Delhi, India was used to determine the residual stresses in weldment of AA6061 and AA7075 by the cosα method. The X ray incident angle was set 35^0 and ±5 oscillations were applied. The variation of residual stresses in transverse direction of TIG and TIG+FSP welded joint are shown in fig. 57. The base material AA7075 on LHS of the weldment shows a minimum compressive residual stress, however the residual stress gradually increases from base material to towards the weldment and then decrease till second base material AA6061. The maximum compressive residual stress 77 MPa were located at the fusion zone (FZ) of the TIG weldment with filler ER4043, whereas minimum compressive residual stress 28 MPa was obtained at stir

zone (SZ) of the TIG+FSP at tool rotation 1300 rpm, traverse speed 45 mm/min and tilt angle 1º.

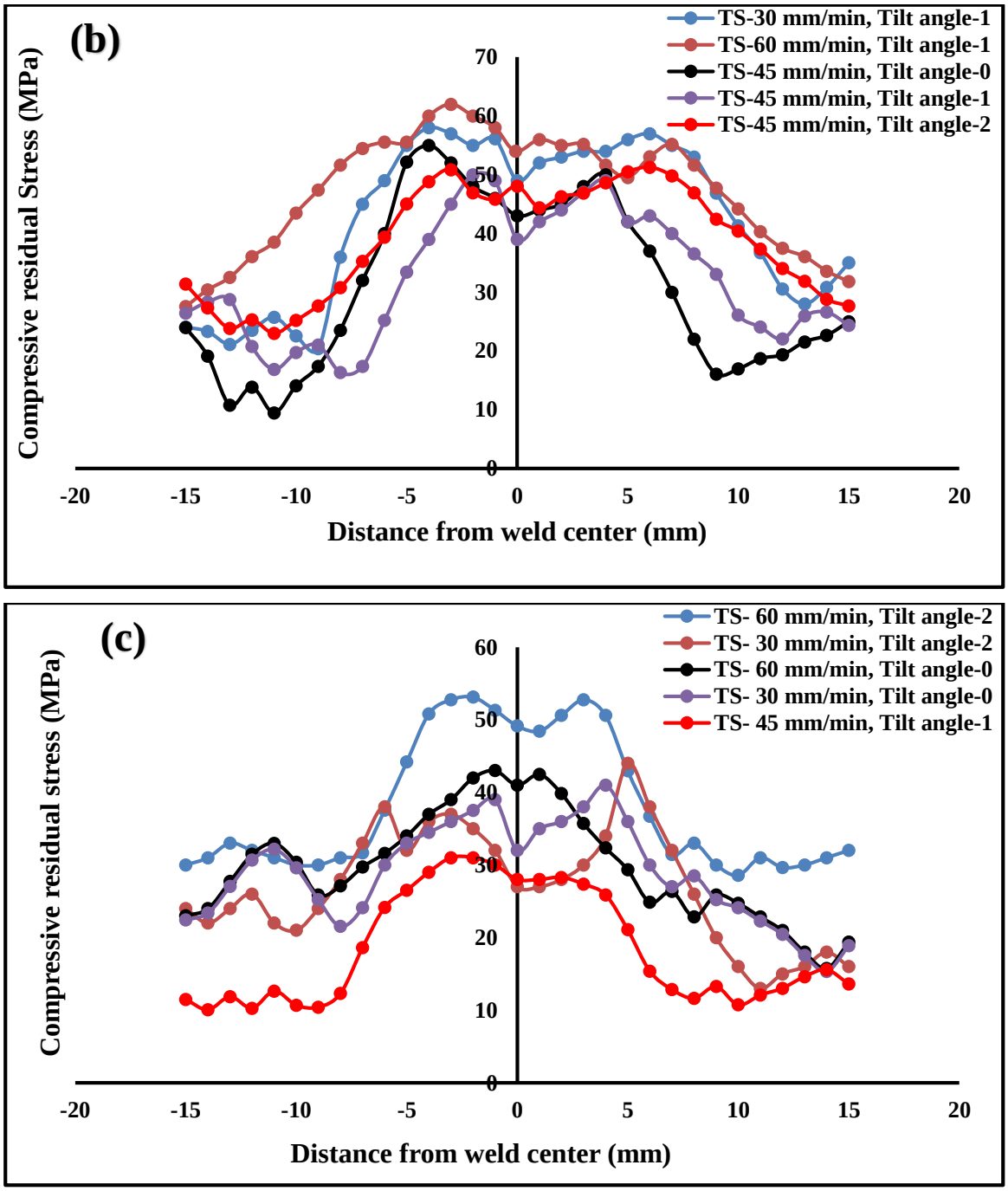

Figure 57: Variation of residual stress to the processing parameters of TIG+FSP, (a) tool rotation 1000 rpm, (b) Tool rotation 1150 rpm, (c) Tool rotation 1300 rpm

The residual stresses profile of TIG+FSP were not symmetrical about the center line of the weldment for both the cases. The left side peak value of the weldment was greater than the right side, because the forming processes is different for retreating side (RS) and advancing side (AS).

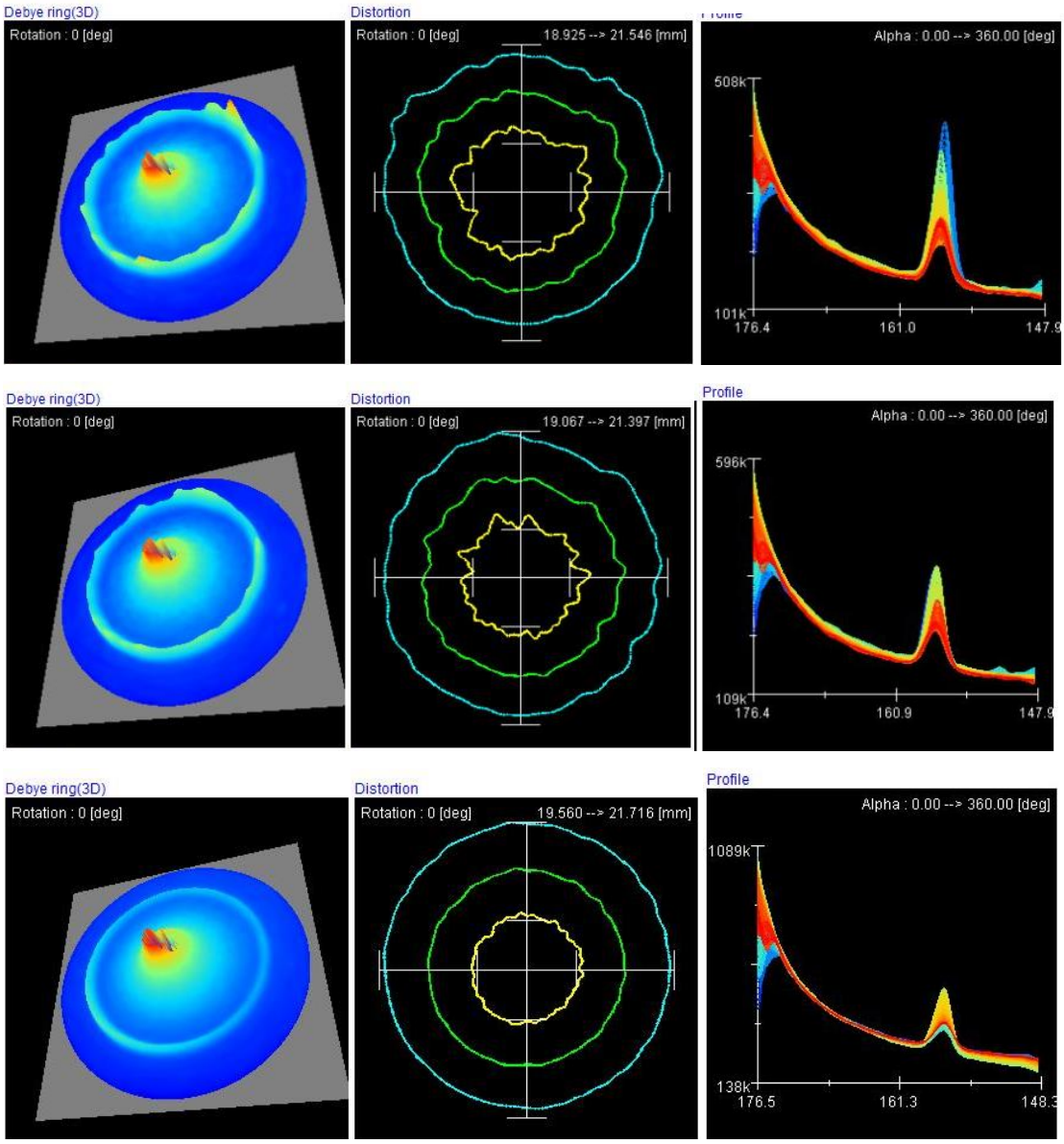

(c)

Figure 58: 3D Debye ring, distortion ring and residual stress profile at the center of the welded joint, (a) TIG joint with filler ER 4043, (b) TIG+FSP sample No. 12 (c) Sample No. 17

The value of residual stress obtained by the experimental methods. Fig.57 shows a comparison between tool rotation and the compressive residual stress, grouped by traverse speed and tilt angle. It can be seen that the compressive residual stresses decrease for a given value of pitch as the traverse speed and tilt angle increases. Although measured peak residual stress increases with as traverse speed decreases, tensile stress appears to be limited to the softened weld zone instead, resulting in a narrowing of the tensile region [126].

Fig. 58 shows the 3D Debye ring, distortion ring and residual stress profile (with respect to alpha angle) of TIG and TIG+FSP welded joint. The residual stress peaks for all the specimens were between 150º to 160º. The red contour indicates higher concentration of residual stress at fusion and stir zone of the welded joint, while blue contour indicates minimum amount of residual stress. The full width at half maximum (FWHM) was measured at different position of the welded joint by Pulstec μ-X360 machine. If the residual stress peak is thicker than the FWHM value will be higher, results in fine grain structures.

5.2.4 Developing the mathematical model

The empirical relationship for response variable was developed by ANOVA techniques which are presented in eqs. (34-37). the actual experimental TIG+FSP process parameters and their level as shown in table 4. The developed models were evaluated by Fisher's F test at 95% confidence level. As per model adequacy, the standard Fisher's F value must be more than the calculated value of F. When the lack of fit is not significant then the models are significant. The ANOVA's for the responses for tensile stress, % elongation, micro-hardness at nugget and residual stress at nugget for TIG+FSP welded joint are reported in tables 18-21. The developed final mathematical empirical equations in the coded form have been given below.

The tool rotational speed coefficient (A) has negative, it implies that the tensile stress increases when the tool rotation speed decreases, because high rotational speed produced high heat which expand the HAZ and weaken the microstructure bonds. Whereas high traverse speed minimizes the detrimental effect of tool rotation speed. The tilt angle is also affecting the tensile stress when the tilt angle is increases. The symmetric microstructure and uniform plastic flow under the shoulder are found in

the nugget zone (NZ) [127]. The relationship between input process parameters and heat index at stir zone (SZ) was analyzed [128]. The rotational speed is directly proportional to the heats index. Due to high frictional heats generated between the work-piece and rotating tool, the high temperature is generated [129]. When welding time increases, the temperature of shoulder is also increases which give the adverse consequence on mechanical properties of weldment. On the other hand, if welding time is low then the heat of tool shoulder does not produce much heat such that low mechanical properties were found in the welded joint.

Table 18: ANOVA for tensile strength (surface quadratic model)

Tensile Strength						
Sources	Sums of squares	df	Mean of square	F-value	P-value	
Model	4815.80	9	535.09	54.18	< 0.0001	significant
A-Tool Rotation Speed	2190.40	1	2190.40	221.81	< 0.0001	significant
B-Traverse speed	67.60	1	67.60	6.85	0.02576	significant
C-Tilt Angle	52.90	1	52.90	5.36	0.04318	significant
AB	190.13	1	190.13	19.25	0.00136	significant
AC	105.13	1	105.13	10.65	0.00853	significant
BC	55.13	1	55.13	5.58	0.03977	significant
A^2	390.02	1	390.02	39.50	0.00010	significant
B^2	900.02	1	900.02	91.14	0.00010	significant
C^2	369.46	1	369.46	37.41	0.00011	significant
Residual	98.75	10	9.88			
Lack of Fit	75.42	5	15.08	3.23	0.11188	not significant
Pure Error	23.33	5	4.67			
Cor Total	4914.55	19				
Std. Dev.	3.14	R^2	0.98			
Mean	221.35	Adjusted R^2	0.96			
C.V. %	1.42	Predicted R^2	0.67			
		Adeq Precision	31.82			

$$\text{Tensile strength} = 744.65 - 1.19A + 4.39B + 40.79C + 0.002AB - 0.024AC + 0.175BC + 0.0005\,A^2 - 0.08\,B^2 - 11.59C^2 \quad (34)$$

$$\text{Elongation} = 92.15 - 0.153A + 0.541B + 5.47C + 0.00023AB - 0.0031AC + 0.018BC + 0.00007A^2 - 0.0093B^2 - 1.46C^2 \quad (35)$$

$$\text{Micro-hardness} = 223.97 - 0.286A + 0.539B + 22.91C + 0.00083AB - 0.01AC + 0.0916BC + 0.00013A^2 - 0.02B^2 - 8.09C^2 \quad (36)$$

$$\text{Residual stress} = 13.86 + 0.373A - 6.6B - 3.28C + 0.0017AB - 0.0133AC + 0.233BC - 0.000226A^2 + 0.051B^2 + 5.4C^2 \quad (37)$$

Table 19: ANOVA for elongation (%) (Surface quadratic model)

% elongation						
Sources	Sums of squares	df	Mean of square	F-value	P-value	
Model	67.03	9	7.45	75.13	< 0.0001	significant
A-Tool Rotation Speed	30.98	1	30.98	312.49	< 0.0001	significant
B-Traverse speed	0.53	1	0.53	5.34	0.0435	significant
C-Tilt Angle	0.68	1	0.68	6.82	0.0260	significant
AB	2.21	1	2.21	22.24	0.0008	significant
AC	1.81	1	1.81	18.21	0.0016	significant
BC	0.60	1	0.60	6.10	0.0331	significant
A^2	6.53	1	6.53	65.87	< 0.0001	significant
B^2	12.23	1	12.23	123.40	< 0.0001	significant
C^2	5.85	1	5.85	59.06	< 0.0001	significant
Residual	0.99	10	0.10			
Lack of Fit	0.72	5	0.14	2.69	0.150332	not significant
Pure Error	0.27	5	0.05			
Cor Total	68.02	19				
Std. Dev.	0.31	R^2	0.99			
Mean	24.30	Adjusted R^2	0.97			
C.V. %	1.30	Predicted R^2	0.77			
		Adeq Precision	37.430814			

Table 20: ANOVA for micro-hardness at nugget (surface quadratic model)

Microhardness						
Sources	Sums of squares	df	Mean of square	F-value	P-value	
Model	1017.00	9	113.00	37.73	< 0.0001	significant
A-Tool Rotation Speed	313.60	1	313.60	104.70	< 0.0001	significant
B-Traverse speed	136.90	1	136.90	45.71	< 0.0001	significant
C-Tilt Angle	25.60	1	25.60	8.55	0.0152	significant
AB	28.13	1	28.13	9.39	0.0120	significant
AC	21.13	1	21.13	7.05	0.0241	significant
BC	15.13	1	15.13	5.05	0.0484	significant
A^2	23.27	1	23.27	7.77	0.0192	significant
B^2	57.96	1	57.96	19.35	0.0013	significant
C^2	180.02	1	180.02	60.10	< 0.0001	significant
Residual	29.95	10	3.00			
Lack of Fit	20.62	5	4.12	2.21	0.2023	not significant
Pure Error	9.33	5	1.87			
Cor Total	1046.95	19				
Std. Dev.	1.73	R^2	0.97			
Mean	92.95	Adjusted R^2	0.95			
C.V. %	1.86	Predicted R^2	0.84			
		Adeq Precision	25.21			

When the rotational speed of tool is less than the 1000 rpm then the worm hole at R.S was observed due to insufficient of metal transportation and insufficient heat generation in TIG+FSP welded joint, whereas when the TRS is higher than the 1300 rpm then the high heat was observed in the NZ, results widen the HAZ and weaken the microstructure bonds. Pin holes' defect was observed at traverse speed less than 30 mm/min due excessive heat input per unit length in the weldment. When feed rate is greater than 60 mm/min, the bottom tunnel in the advancing side was perceived due to inadequate flow of material and insufficient heat input in the weldment. ANOVA table for tensile strength with respect to selective variables of TIG+FSP welded joint of AA6061 and AA7075 reveals that the Fisher's F value is 54.18 which shows that

the model is significant. Chance of fisher's F value due to error is only 0.01% is shown in table 18.

Table 21: ANOVA for residual stress at nugget (surface quadratic model)

Residual stress						
Sources	Sums of squares	df	Mean of square	F-value	P-value	
Model	2676.67	9	297.41	30.00	< 0.0001	significant
A-Tool Rotation Speed	1440.00	1	1440.00	145.27	< 0.0001	significant
B-Traverse speed	122.50	1	122.50	12.36	0.00558	significant
C-Tilt Angle	72.90	1	72.90	7.35	0.02186	significant
AB	128.00	1	128.00	12.91	0.00490	significant
AC	32.00	1	32.00	3.23	0.10260	significant
BC	98.00	1	98.00	9.89	0.01043	significant
A^2	71.27	1	71.27	7.19	0.02304	significant
B^2	357.96	1	357.96	36.11	0.00013	significant
C^2	80.46	1	80.46	8.12	0.01728	significant
Residual	99.13	10	9.91			
Lack of Fit	75.79	5	15.16	3.25	0.1109	not significant
Pure Error	23.33	5	4.67			
Cor Total	2775.80	19				
Std. Dev.	3.15	RÂ²	0.96			
Mean	44.90	Adjusted R^2	0.93			
C.V. %	7.01	Predicted R^2	0.79			
		Adeq Precision	21.79			

In mathematical model, the product p value of TRS (A) and TS (B) for TIG+FSP welded joint is less than 0.05 which shows these terms to be significant. The ANOAVA table 19 shows the elongation of TIG+FSP welded joint, the fisher's F value is 75.13, which shows the model is significant. The coefficient of R^2 shows the goodness of fits of the models. Value of R^2 (0.9799) for tensile strength shows that 97.99% of the complete variability is analyzed by the model after considering the significant factor. The difference between R^2 (97.99%) and adjusted R^2 (96.18%) is 1.81%, which shows that the 1.81% of the total variation is not elucidated by the

model and it also indicate that the model is not over fitted. The fisher's F value of ANOVA surface quadratic model for percentage elongation, micro-hardness at nugget and residual stress at nugget are 75.13, 37.72, and 30.00 respectively as shown in table 19-21. These values shown that the model is significant. The chance of fisher's F values for percentage elongation, micro-hardness at nugget and residual stress at nugget due to error are only 0.01% for each.

5.2.5 Influence of process parameter on response parameters

The predicted vs experimental values for tensile stress, % elongation, micro-hardness and residual stress of TIG+FSP welded joint is shown in fig. 59.

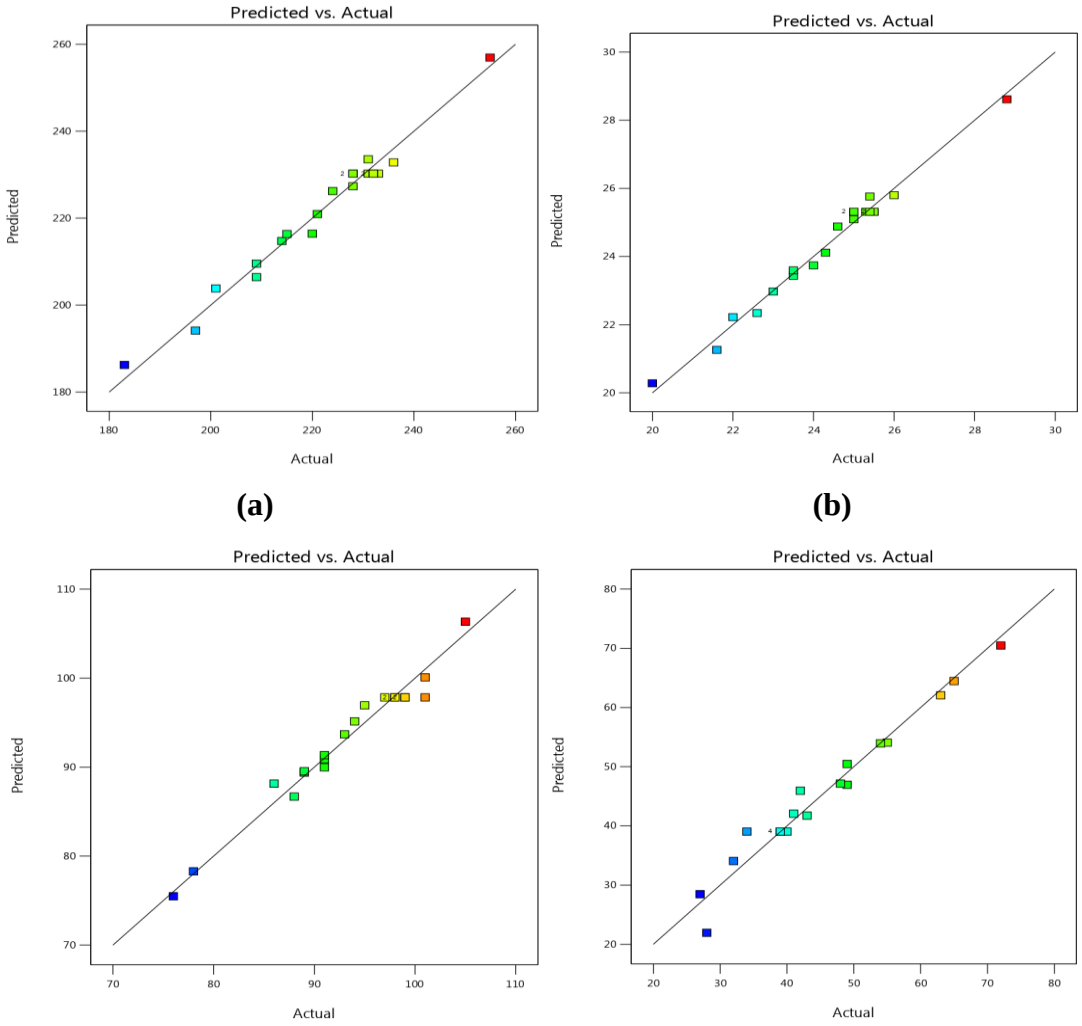

Figure 59: Predicted vs experimental, (a) Tensile strength, (b) Percentage Elongation, (c) Micro-hardness, (d) Residual Stress

It shows the response variables are lying on the straights lines which indicates that the errors are uniformly scattered throughout the model. These plots show excellent correlation of predicted and experimental values of the response values. All the above correlation divulges a good adequacy of the regression models

The significance of high frictional heat can be revealed as coarsening and dissolutions of resilient precipitate in weld nugget zones. Due to more heating cycle and friction among the work-piece and rotating tool, the high temperature is generated [75, 129]. 3D responses surfaces plot and contour of tensile strength, % elongation, residual stress and micro-hardness are shown in fig. 60-63. When the tool rotation speed increases, tensile stress also increases due to strain hardening effect convinced by tool stirring, whereas excess heat input play the predominant role at high tool rotation speed such lower tensile strength was observed when the tool rotation decreases.

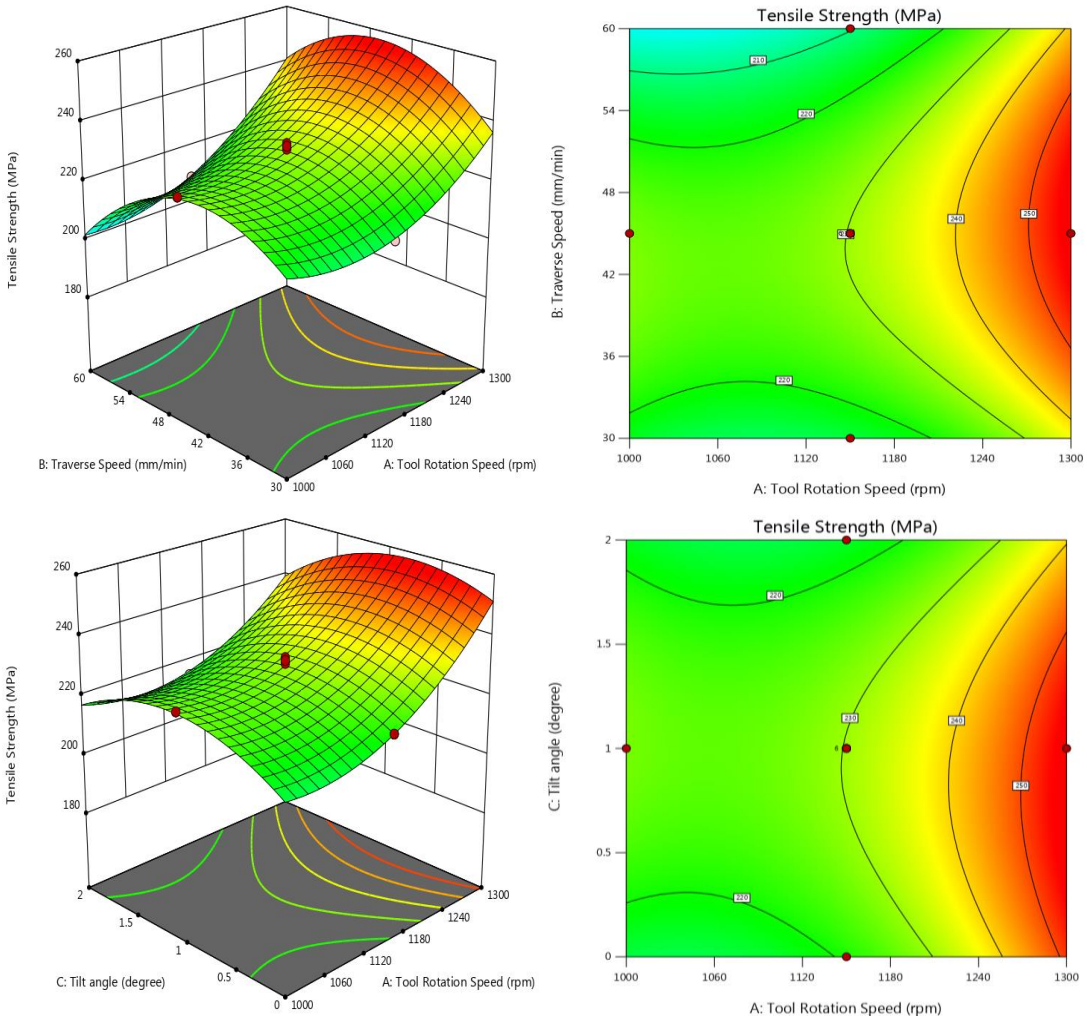

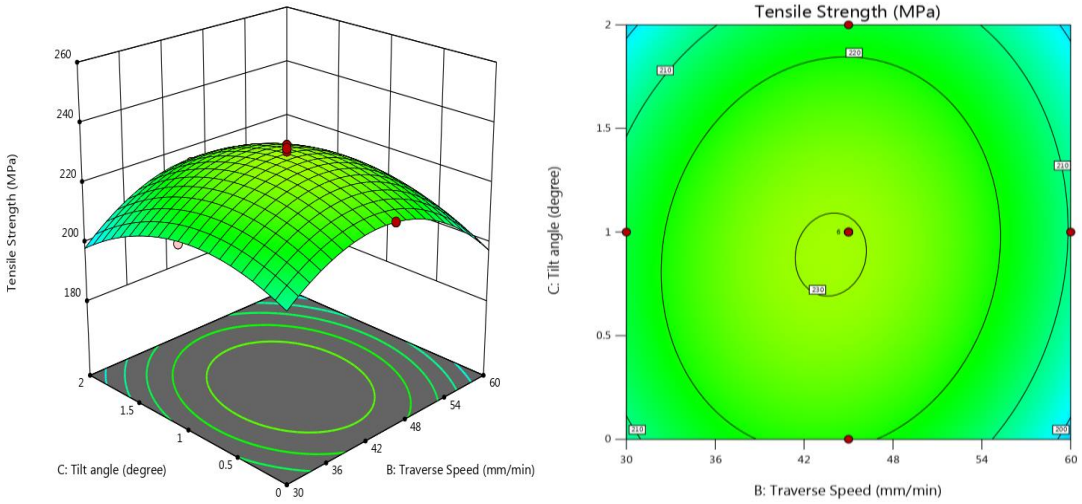

Figure 60: 3D response surface plot and contour plot for Tensile strength of TIG+FSP welded joint with filler ER 4043

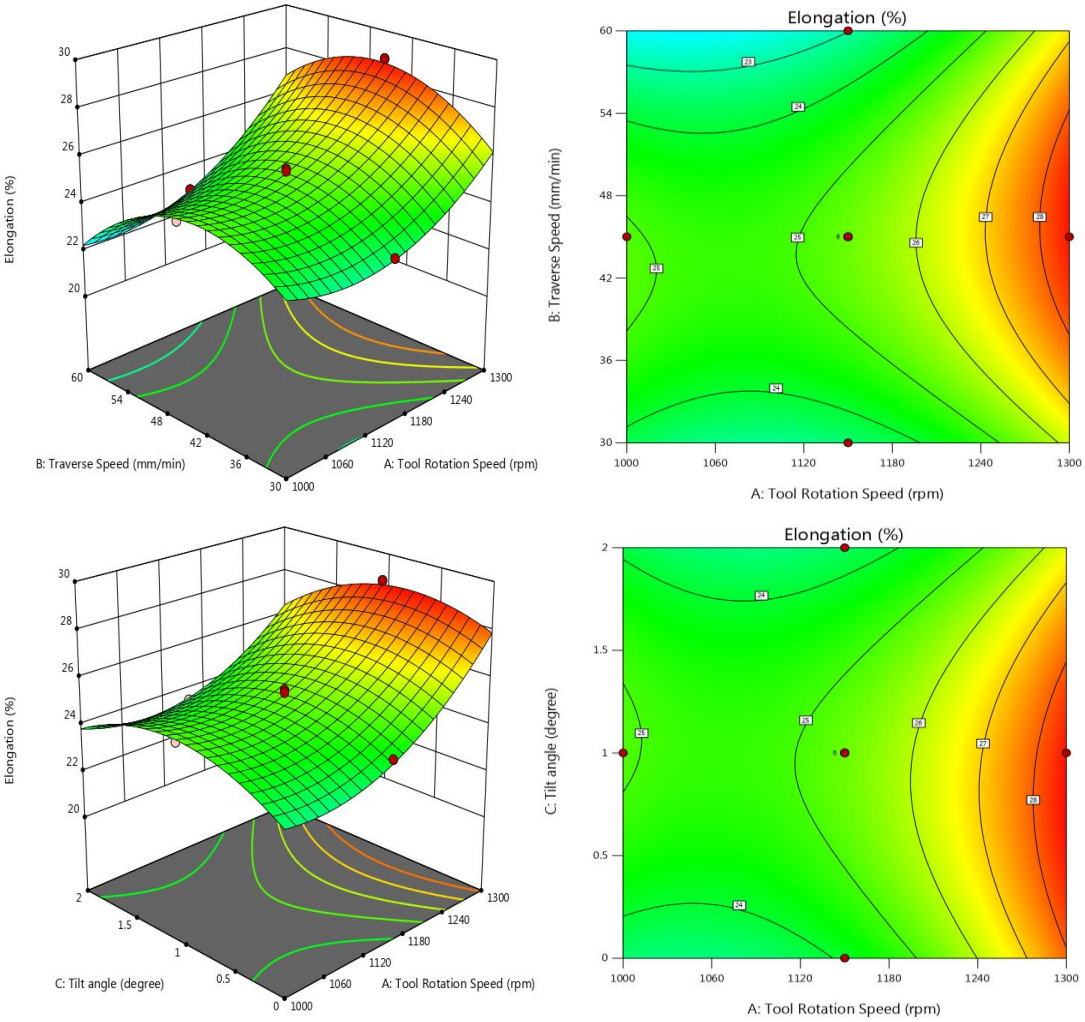

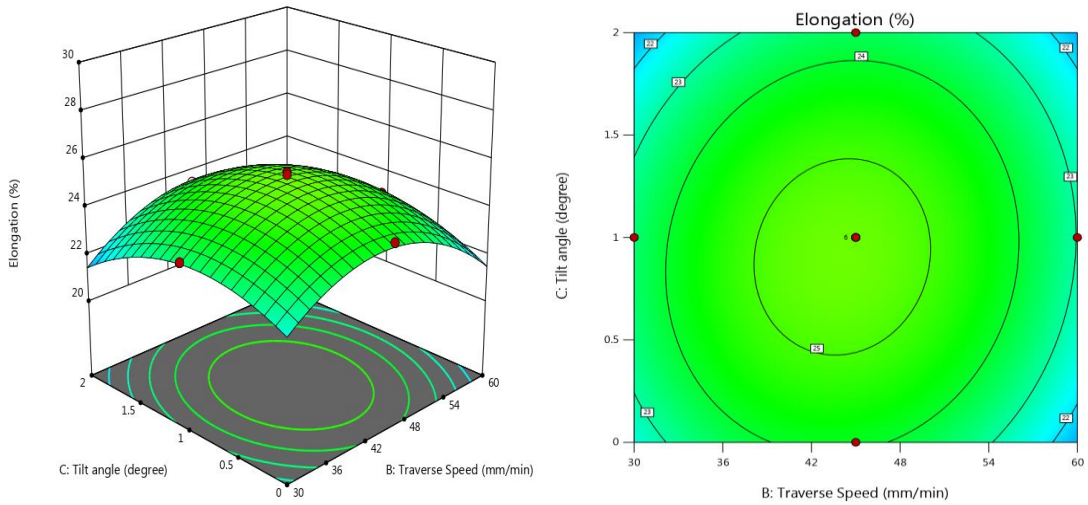

Figure 61: 3D response surface plot and contour plot for percentage elongation of TIG+FSP welded joint with filler ER 4043

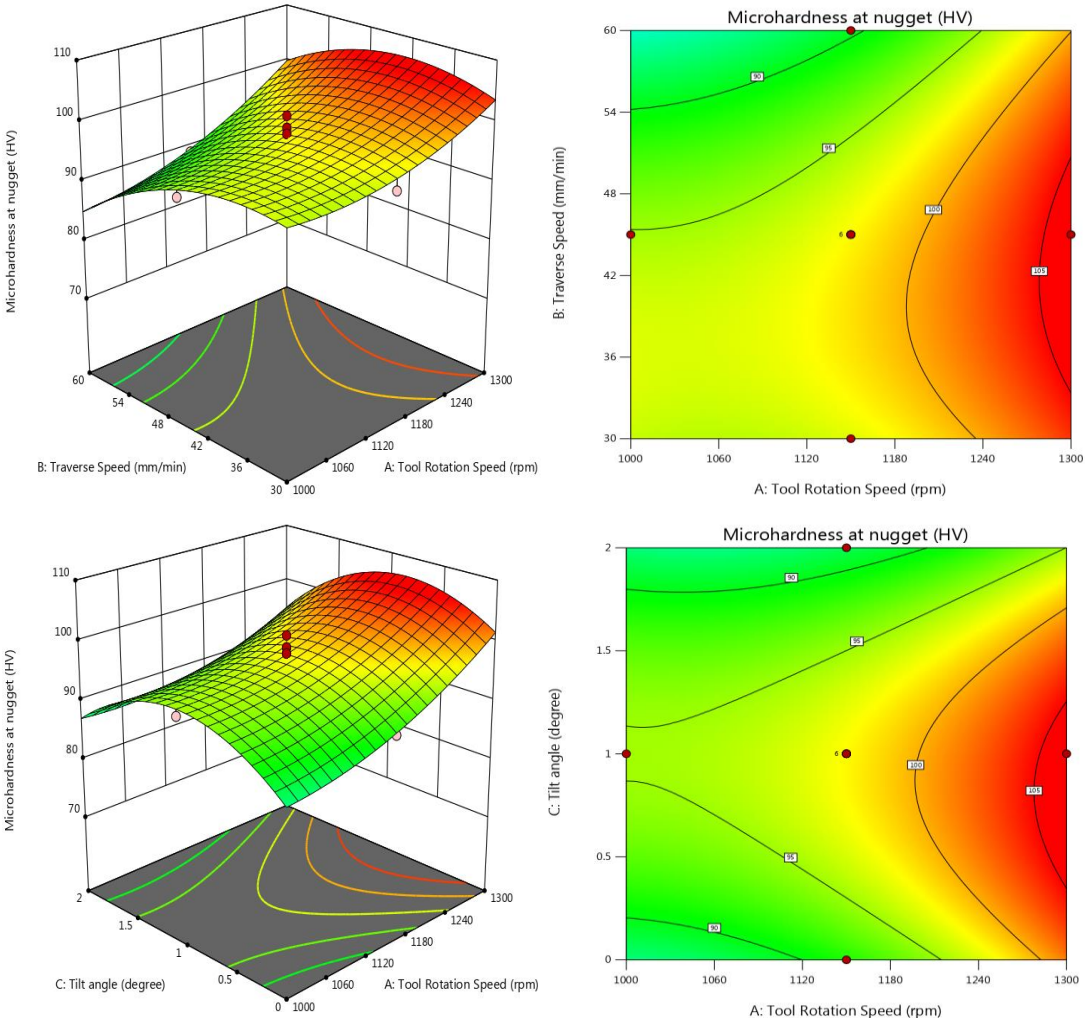

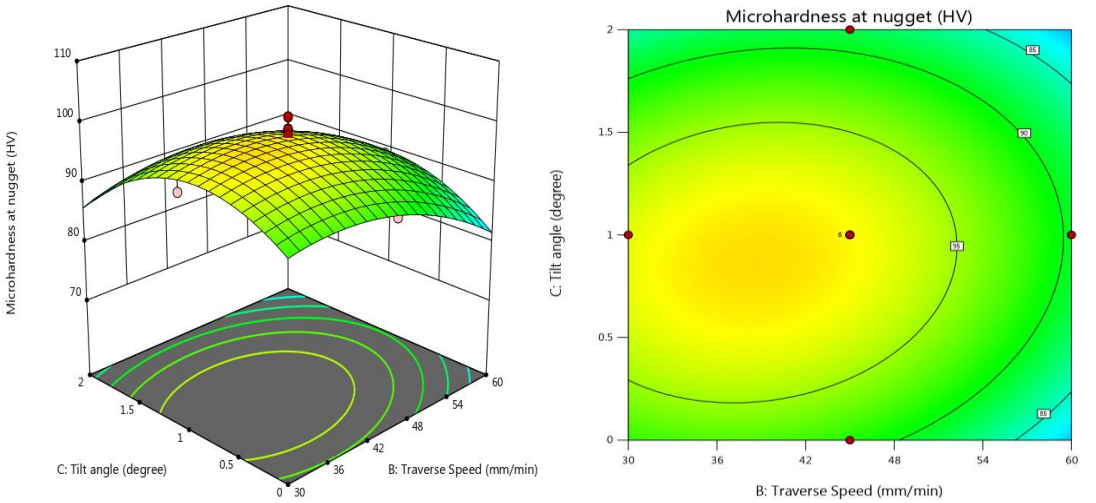

Figure 62: 3D response surface plot and contour plot for micro-hardness at nugget zone of TIG+FSP welded joint with filler ER 4043

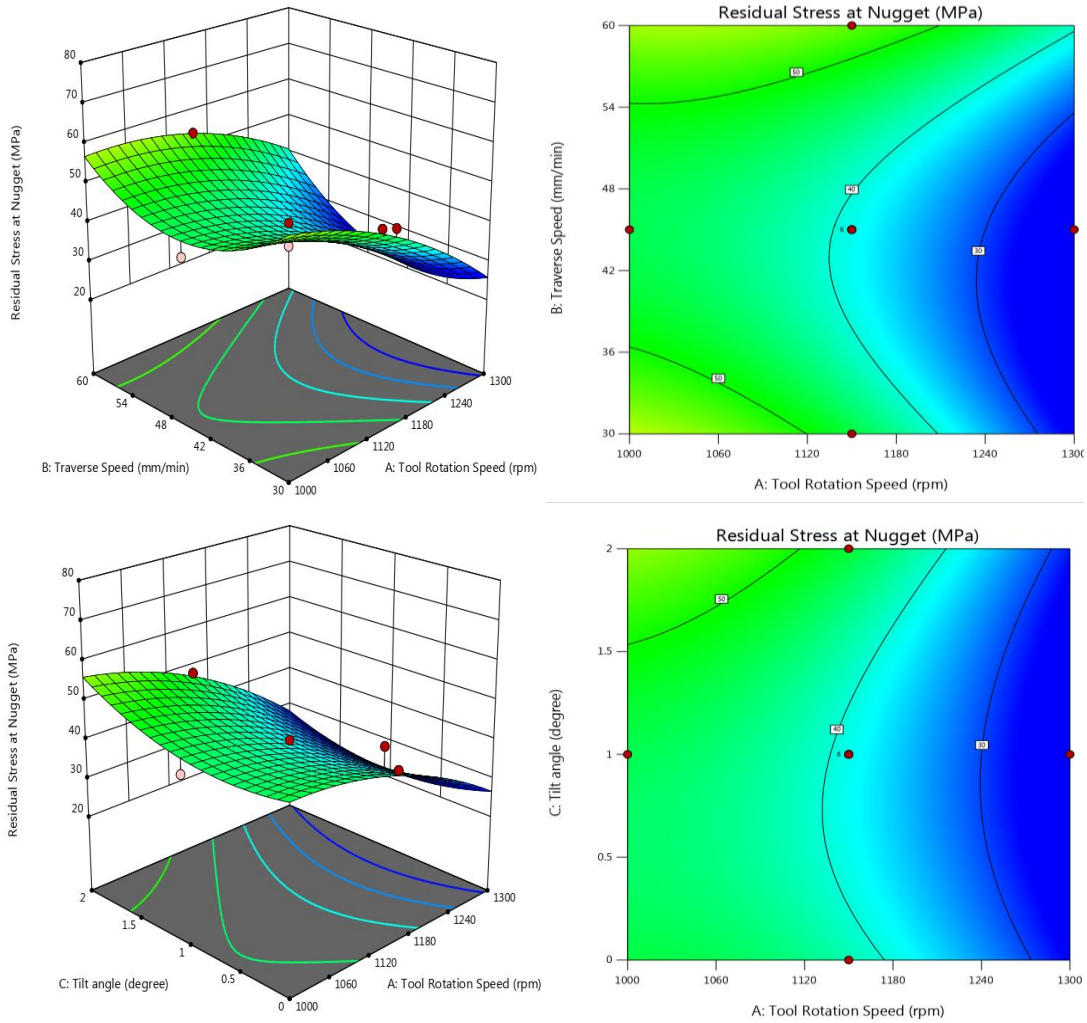

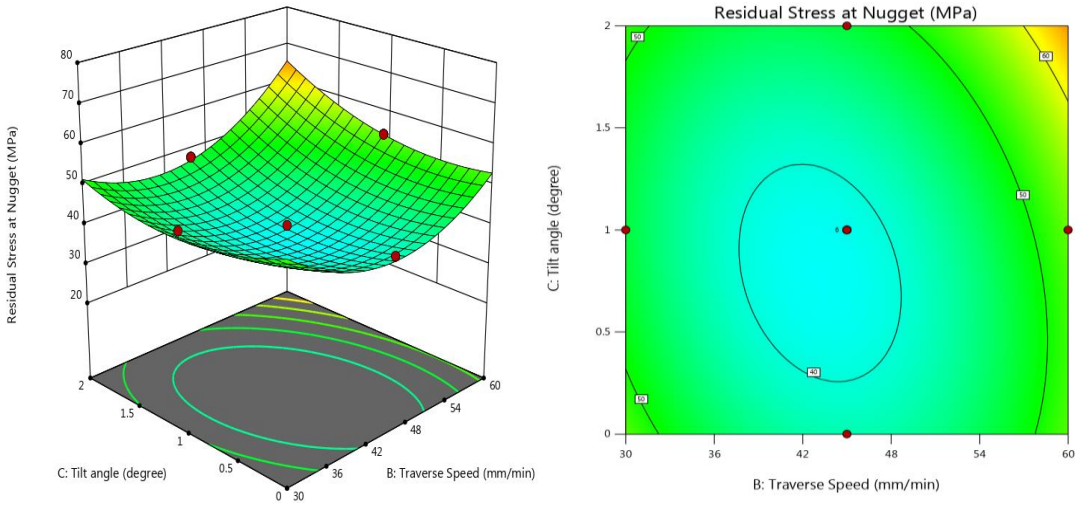

Figure 63: 3D response surface plot and contour plot for residual stress at the nugget zone of TIG+FSP welded joint with filler ER 4043

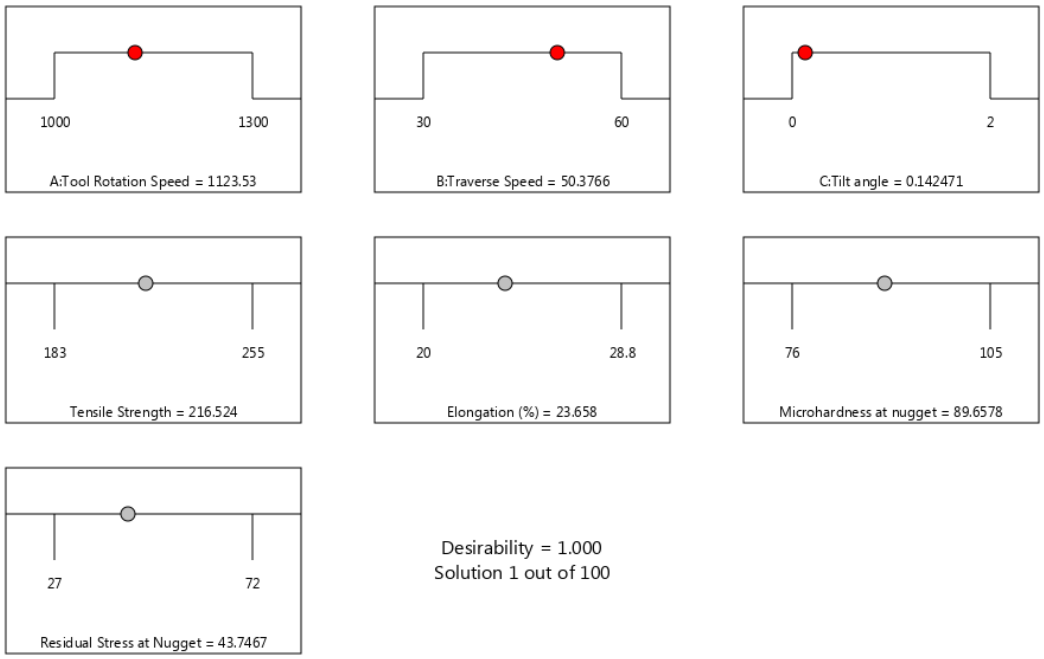

Figure 64: Ramp function graph for input parameter and Multi response optimization

As the feed rate increases then tensile strength first increases then decreases. The minimum tensile strength i.e.183 MPa was found at lower tool rotation speed (1000 rpm) due to inadequate tool stirring action. The maximum tensile strength (255 MPa) was observed at 1300 rpm, 45 mm/min and 1^0, when the feed rate or traverses speed increases, the tensile strength and hardness also increases up to a certain value. Large heat was found in the welded region at lower feed rate. As the feed rate increases, the

influences of thermal cycle on the welded joint weakened leading to enhancement in tensile stress and micro-hardness of the welded joints as shown in fig. (60-63). The cube function graph of multi response optimization as shown in fig. 64. This methodology is used to optimize for more than one objective function. The desirable value is 1 for optimized value of the input processing parameters and responses. The optimized value of tensile strength, percentage elongation, micro-hardness at nugget zone and residual stress at nugget zone are 216.52 MPa, 23.65, 89.65 HV and 43.74 MPa respectively, whereas the optimized value of tool rotational speed, feed rate and tilt angle are 1123.53 rpm, 50.37 mm/min and 0.1424 respectively as shown in fig.64.

5.2.6 XRD analysis of TIG and TIG+FSP welded joint

X- Ray diffraction is used for examine the phase detection of dissimilar TIG+FSP welded joint of AA6061 and AA7075 with filler ER4043 and found three major phases Al, Al_2CuMg, and Mg_2Si as shown in fig. 65. Magnesium (Mg) and Silicon (Si) elements were found in the weldment besides the aluminum (Al), it is found that Mg and Si created the phase after the precipitation reaction in the weldment. A very high intensity was found from aluminum, because of fragmentation of precipitates the intensity of Mg_2Si was increases after friction stir processing on TIG welded joint with filler ER4043 [129, 132]. The alloying elements such as Si and Mg existing in weld center make precipitation reaction and form a strong precipitate of Mg_2Si to give a higher strength. Same phase of Al_2CuMg was detected in both the nugget zone. Micro-hardness of the TIG+FSP joints are based on boundary energy, brittle intermetallic formation, strain hardening and precipitates formation in the joint.

Fine recrystallized grains and increase of grain boundaries in the (SZ) of AA6061 and AA7075 joints predict higher micro-hardness. Because of fine precipitates and fine grains structure, the stir zone is associated with plastic deformation and high temperature, due to precipitates formation at high temperature along the grain boundaries. When the rotational speed of tool is less than the 1000 rpm then the worm hole at R.S was observed due to insufficient of metal transportation and insufficient heat generation in TIG+FSP welded joint, whereas when the TRS is higher than the 1300 rpm then the high heat was observed in the NZ, results widen the HAZ and weaken the microstructure bonds. Pin holes' defect was observed at traverse speed

less than 30 mm/min due excessive heat input per unit length in the weldment. When feed rate is greater than 60 mm/min, the bottom tunnel in the advancing side was perceived due to inadequate flow of material and insufficient heat input in the weldment.

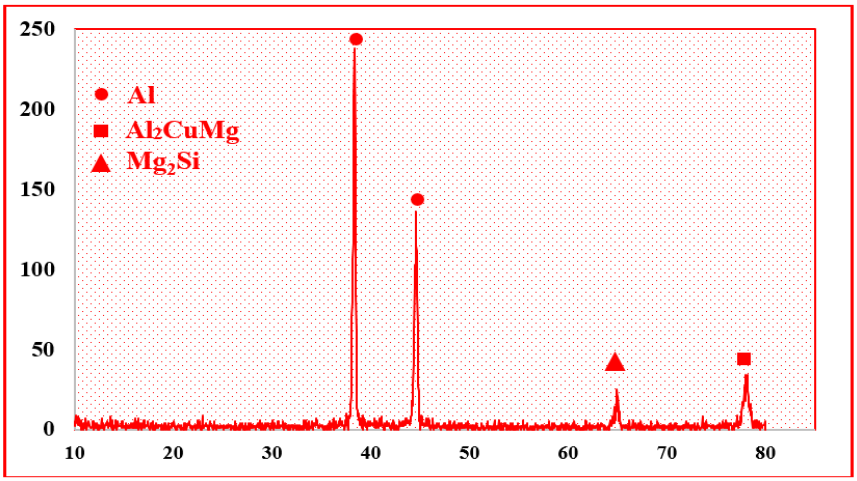

Figure 65: XRD peaks of TIG+FSP welding of filler ER 4043

5.2.7 Microstructure Analysis

The microstructure of TIG welded joint of Al-6061 and 7075 with filler ER4043 were observed at different location using various magnifications. Fig.66 shows the different zones of TIG welded joint such as welded zone, fusion zone and HAZ. Fusion zone was formed due to re-solidification and melting during the welding. The dispersed precipitates of Mg_2Si intermetallic compound were observed in welded region and coarse equiaxed grains were also observed in fusion zone. The equiaxed grains is absent due to the material close to the fusion line provides plenty of sources for the crystal nucleation of the liquid metal during the TIG welding [130]. Fine grains with small precipitates was reported in heat affected zone (HAZ) as compare to other zone. The relationship between heat input and the grain size measured by electron backscatter diffraction (EBSD) in the stir zone [131]. The mean grain size generally decreased with the heat input under the studies conditions. The revealed relationship was characterized by a significant experimental scattering. This deteriorates their predictive ability and therefore require a deeper understanding for the heat input and grain growth. The heat input is directly related to the variation of the welding

temperature. The final grain size in the stir zone is depended on the peak welding temperature and weakly on the cooling rate [78].

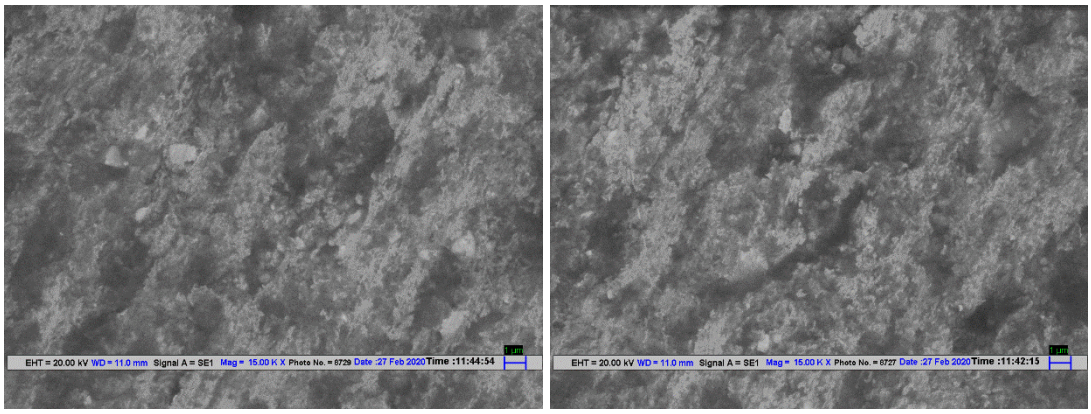

Figure 66: SEM images of TIG welded joint with filler ER 4043 (a) Fusion Zone, (b) HAZ

Three different zones have been recognized in TIG+FSP weldment at low magnification due to mechanical and thermal stresses caused by the processing parameters. These zones are nugget zone (NZ), thermo-mechanically affected zone (TMAZ), and heat affected zone (HAZ) are shown in fig. 67. The formation of nugget zone shape in TIG+FSP welded joint is recognized to the maximum deformation and plasticization in the material which shows the fine recrystallized equiaxed grains. The formation of nugget shapes depends on thermal gradient, processing parameters and tools geometry in the work-piece. Therefore, coarse grain structure of TIG welded joint is transformed into the uniform and fine grains structures in the weld nugget zone due to adequate softening of material revealed the maximum tensile strength and micro-hardness of the TIG+FSP welded joint as shown in fig.68.

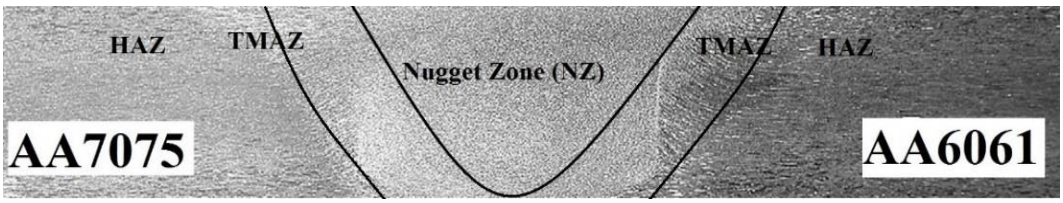

Figure 67: Optical micrograph of various zone for TIG+FSP welded joint of AA7075 and AA6061

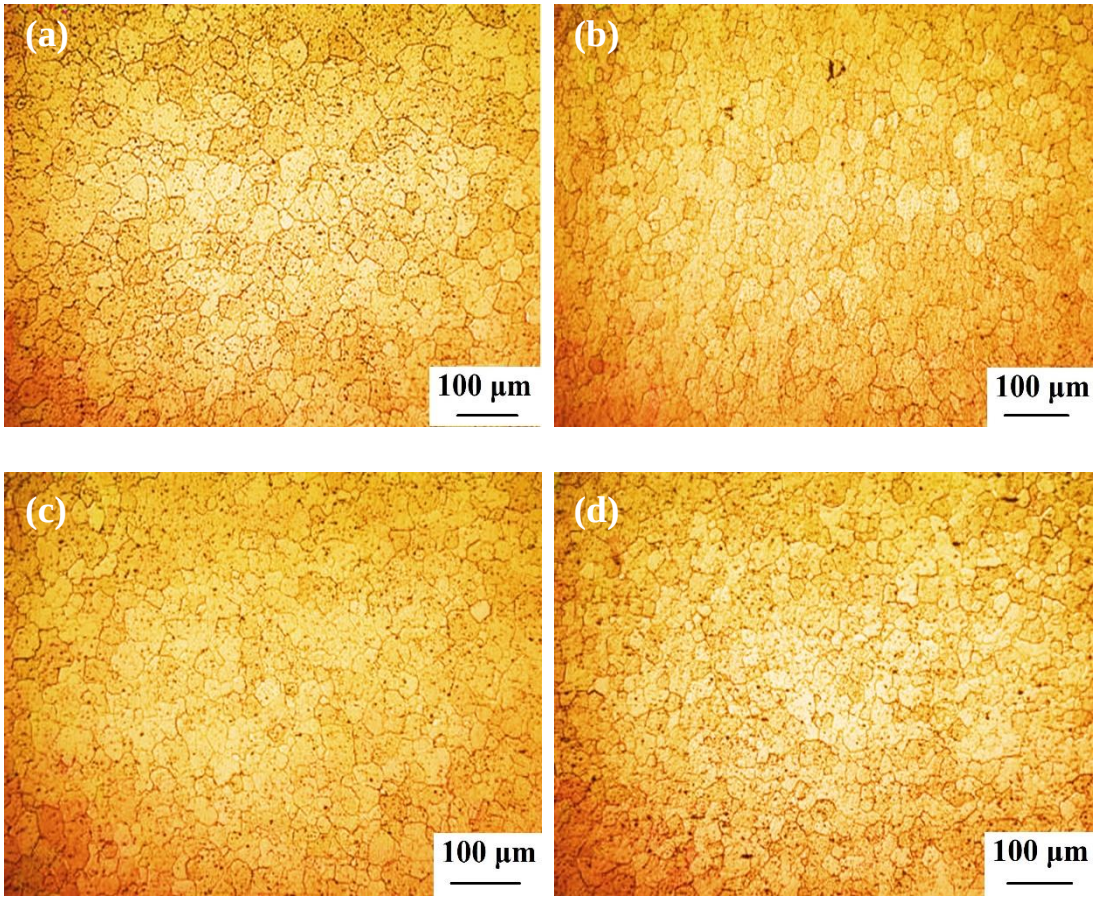

Figure 68: Optical images of TIG+FSP welded joint at nugget zone (a) Sample 1, (b) Sample 5, (c) Sample 12, (d) Sample 18

At high welding speed, the weld nugget zone is more homogenous than those produce low welding speed because high heat input gives the effective recrystallization and more homogenous temperature distribution in weld nugget zone. The grains size in stir zone change crucially which is depend on the heat input and processing parameters [133-134]. The grain sizes of TIG weldment were analyzed by the image J software and observed grain size in fusion zone at three different positions are 19.2µm, 19.8 µm and 18.5 µm whereas 6.4 µm, 5.9 µm and 6.3 µm were observed in TIG+FSP welded joint at 1300 rpm, 45 mm/min with 1º tilt angle as shown in fig.69.

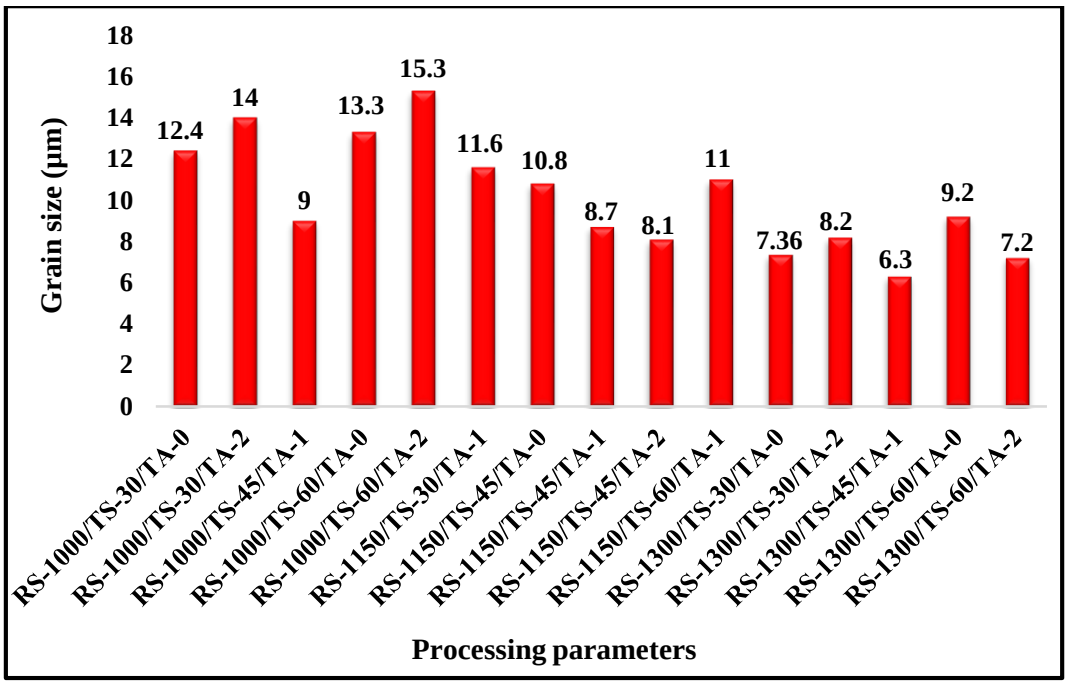

Figure 69: Variation of grain size at the nugget zone to the processing parameters

5.2.8 Fracture Surface analysis

Fractured surfaces of the fragmented tensile specimens were analyzed by SEM machine to understand the effect of microstructure on the failure pattern of TIG and TIG+FSP welded joints. There is some important observation can be made. All TIG welded specimens are failed at the welded joint whereas most of the TIG+FSP welded joint failed on the advancing side while some specimens were failed at retreating side because fracture was initiated from the interface of TMAZ and stir zone in retreating side. The reasons for such localized fracture behavior explained by the analyzing the texture, grain size and strain localization characteristics in retreating side [134]. The Scanning electron microscope (SEM) fractograph has been taken from the fractured tensile test specimen of TIG and TIG+FSP welded joint of AA6061 and AA7075 at room temperature as shown in fig.70. The fracture morphology between the TIG and TIG+FSP shows the clear difference that TIG welded portion shows the deep dimples whereas TIG+FSP welded portion shows shallow dimples with fractured lines this is the evdence of crack nuleation and growth 4mm away from the weld line. The small grain particles was found in the TIG+FSP welded zone while big grains was found in TIG welded region.

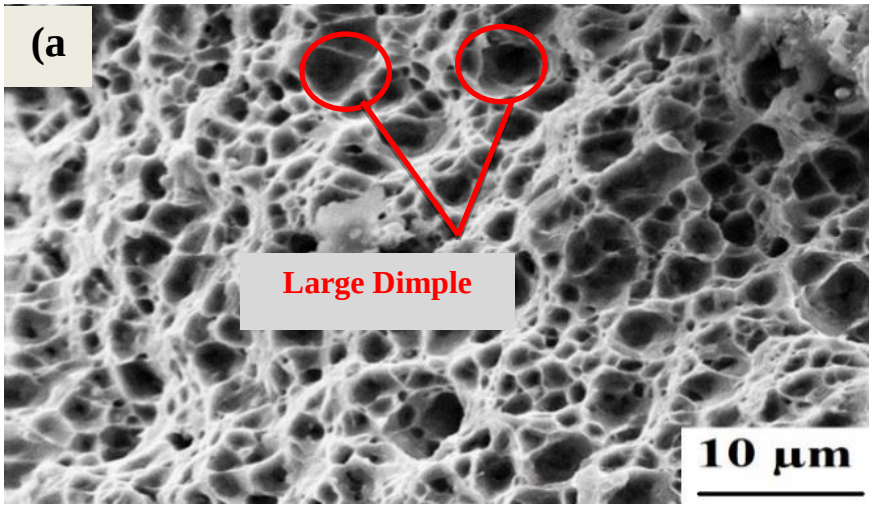
(a
Large Dimple
10 µm

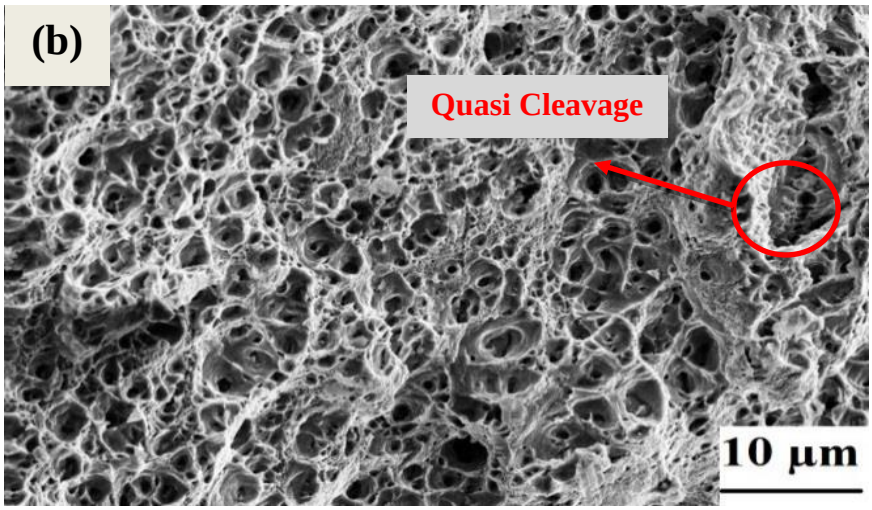
(b)
Quasi Cleavage
10 µm

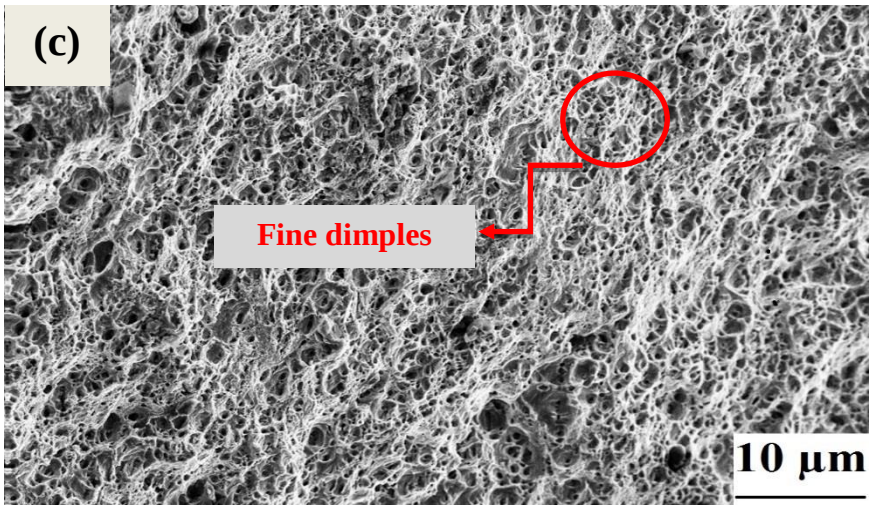
(c)
Fine dimples
10 µm

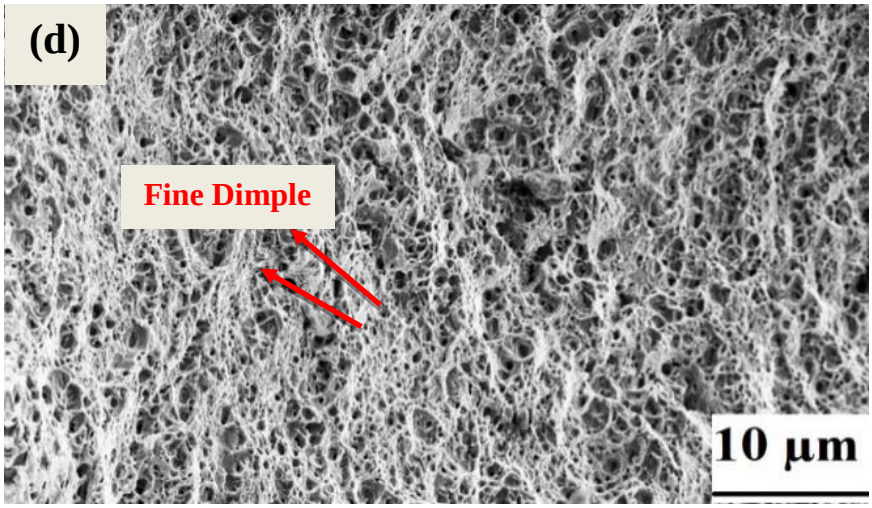

Figure 70: SEM images of tensile fractured specimen, (a) TIG welded joint with filler ER 4043, (b) TIG+FSP welded joint (sample 4), (c) TIG+FSP welded joint (sample 9), (d) TIG+FSP welded joint (sample 18)

There are numbers of small and big silicon particles are observed in both fractured specimens. Because of formation and consequent growth and coalescence of cavity or voids, the ductile fracture of welded joint occurs, an improvement in ductility may be achieved when the cavity nucleation could be suppressed [120]. The maximum interfacial normal stress is depending upon the grain particle size and the volume fraction of the grain particles [121]. The coalescence of micro-voids result in equiaxed dimples on tensile fracture surface normal to the loading axis. Hence, the equiaxed and spherical dimples on a flat crater bottom loaded in tension and elongated ellipsoidal dimples on the shear lips oriented at 45^0. SEM fractograph of the fractured tensile test specimen shows the size and distribution of large void and cavity of different TIG+FSP welded joint. The fractured surface is characterized by ductile dimple and some area of large void as shown in fig. 70. The fine dimple percentage increases by the variation of process parameters of TIG+FSP welded joint. The cavity formation occurred due to precipitate coarsening that layer coalesce led to the shear rupture.

5.3 Optimization of process parameters of TIG+FSP welded joints of filler ER 5356

The aluminum alloy plates of AA6061 and AA7075 with dimension 80 x 40x 6.2 mm was welded by TIG welding with filler ER 5356. The FSP approach was used on TIG welded joint to enhance the mechanical properties of TIG welded joints. The plates were cleaned with acetone to eradicate the dirt and oil to remove the oxide layer before the TIG+FSP welding approach. The non-consumable H13tool steel with pin diameter, shoulder diameter and pin length of 7 mm, 19.5 mm, and 5.5 mm respectively was used is shown in fig. 32. The input parameters range which are in TIG+FSP welded joint have been taken as rotational speed (1000 rpm to 1300 rpm), feed rate (30-60 mm/min) and tilt angles (0^0-2^0).

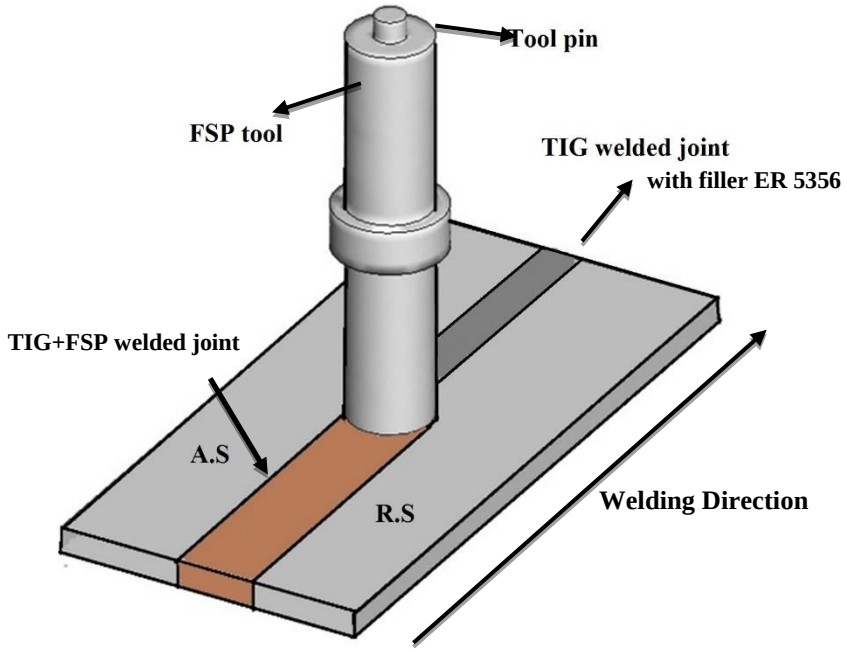

Figure 71: TIG+FSP welding with filler ER 5356

Fig. 72 demonstrate the dimension of tensile sub test specimen (ASTM E8) and the sampling schematic for joint characterization. The tensile test specimens were sliced and machined from the TIG+FSP welded joint using milling cutter and shaper machine. Single pass FSP is used to fabricate TIG+FSP welded joint is shown in fig. 71. The tensile test were performed on computer controlled UTM machine of weldment at room temperature using different processing parameters. Three sub

tensle specimen were tested and average of these three results are taken. As recommended by the design expert software, twenty joints were fabricated with different processing parameters.

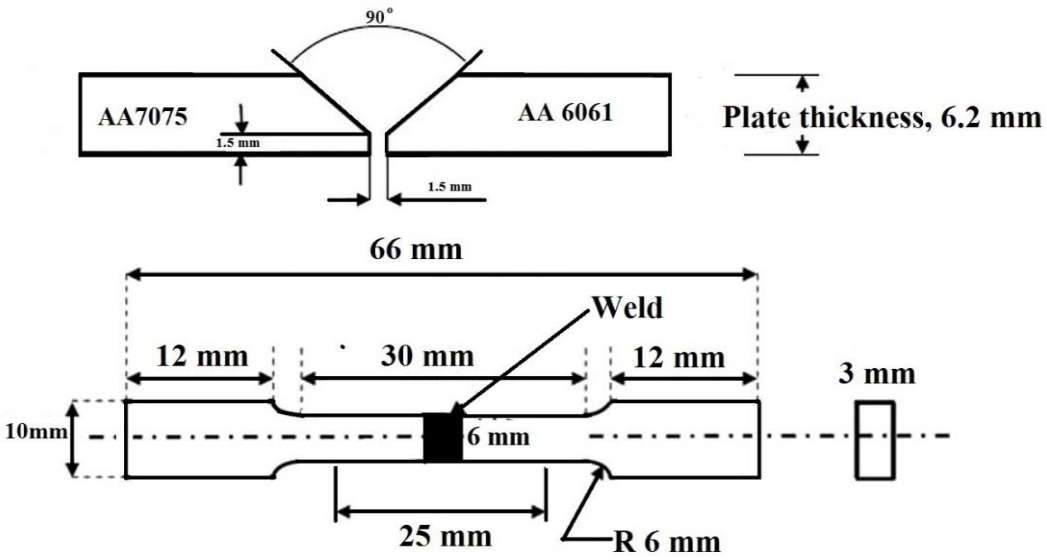

(a)

(b)

Figure 72: (a) Dimension of TIG+FSP welded tensile specimen, (b) Tensile specimen along the welding direction

Various investigators have used several experimental design techniques for developing regression equations but CCD is one of the best and precise design

technique [34, 135-138]. Based on central composite design (CCD), all the experiments have been conducted according to the design experiments, where the lower and upper was coded as -1 and +1. The face centered CCD contains twenty experimental observations with three independent input variable namely tool rotational speed, traverse speed and tilt angle. The Processing parameter of TIG+FSP welding and its level are shown in table 22.

Table 22: Processing parameter of TIG+FSP welding with filler ER 5356 and its level

Parameters	Units	Notation	Range	Levels		
				-1	0	1
Tool rotational Speed	rpm	A	1000-1300	1000	1150	1300
Traverse Speed	mm/min	B	30-60	30	45	60
Tilt angle	degree	C	0-2	0	1	2

5.3.1 Tensile strength

Fig. 73 shows the stress strain diagram for TIG+FSP welded joint with filler ER 5356 of dissimilar aluminum alloy AA6061 and AA 7075, the tensile strength of all welded joints are lower than the base materials AA7075 and some specimens were fractured from the welded region whereas some fractured were observed on base material AA6061 side at position in heat affacted zone (HAZ) region where the hardness and strength minima were located, to find out the tensile strength of these types of welded joint the tensile test specimens were sliced along the length of the welding as shown in fig. 72 (b). Past researchers investigated previously that dissimilar friction stir welded joints of aluminum alloys, the welded joints generally fractured at locations in HAZ on the weaker parent material side [139-140]. The highest tensile strength (281 MPa) was obtained at tool rotation 1300 rpm, traverse speed 30 mm/min and tilt angle 2º which is 59.48% higher than the TIG welded joint. The ultimate tensile strength increases with increase of tool rotational speed. The increases of ultimate tensile strength are occurring because TIG+FSP at higher welding speed or with AA 6061 on the A.S induced less heat input and less severe precipitate coarsening in the heat affected zone.

Due to the absence of porosity, small grain size and presence of extra material in the welded region with filler wire, the tensile strength of TIG+FSP obtained higher value than the conventional TIG joining process. Filler ER5356 present in the welded joint makes more compact pressure leading to increase bond strength.

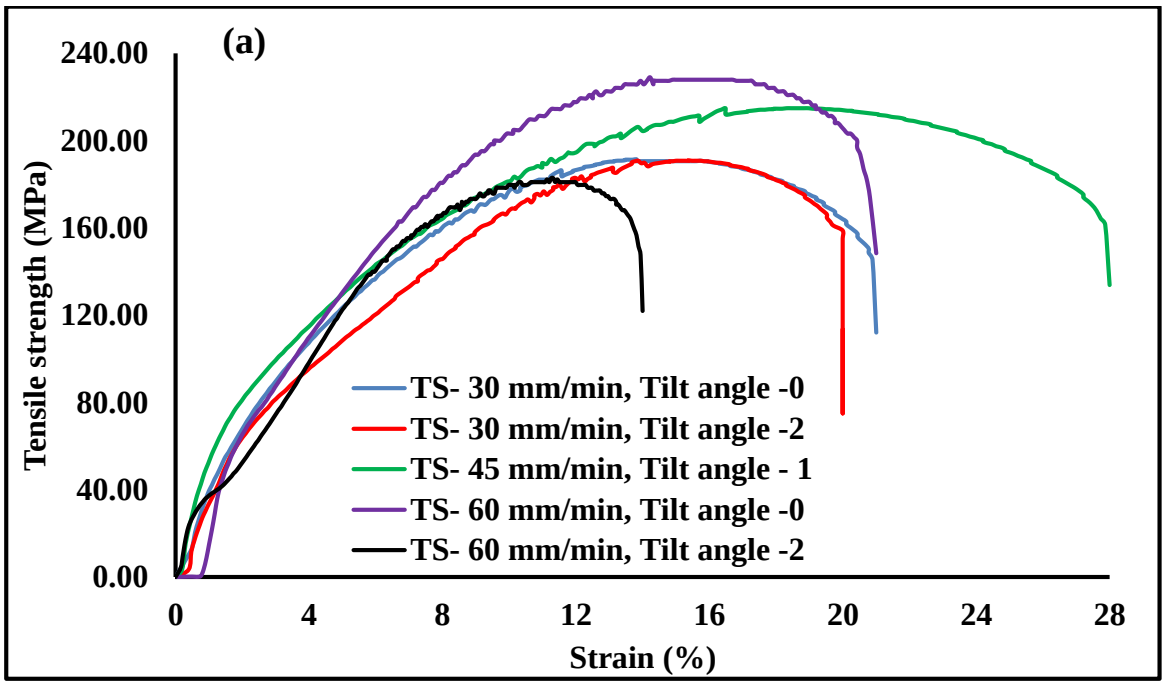

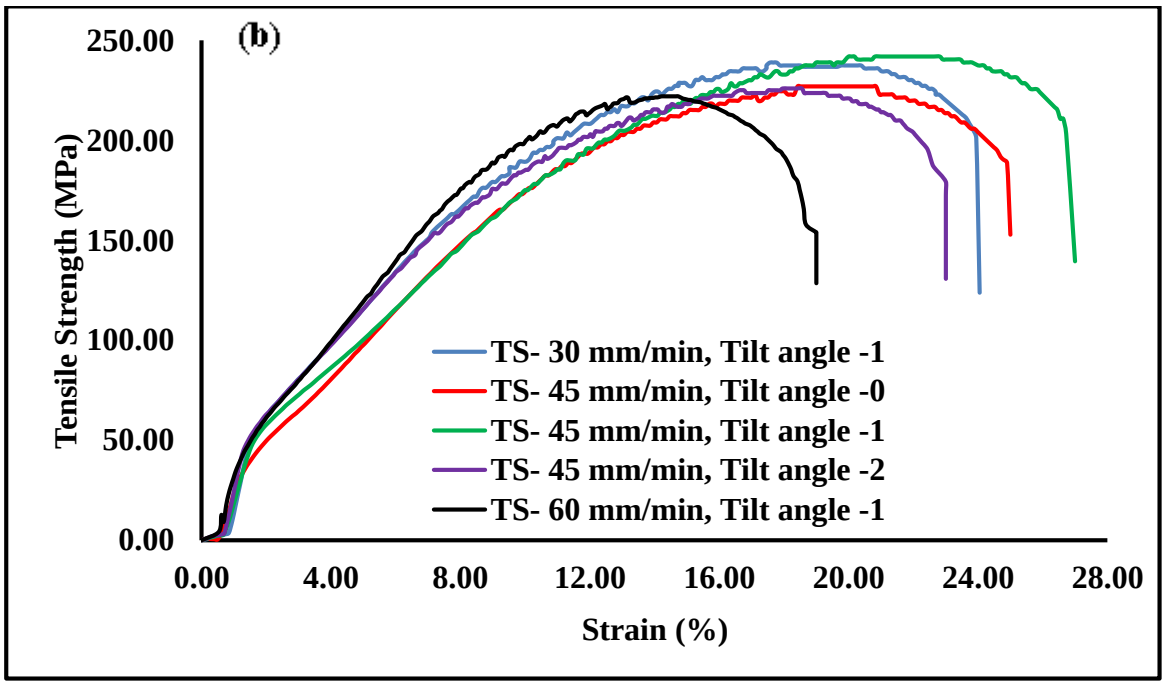

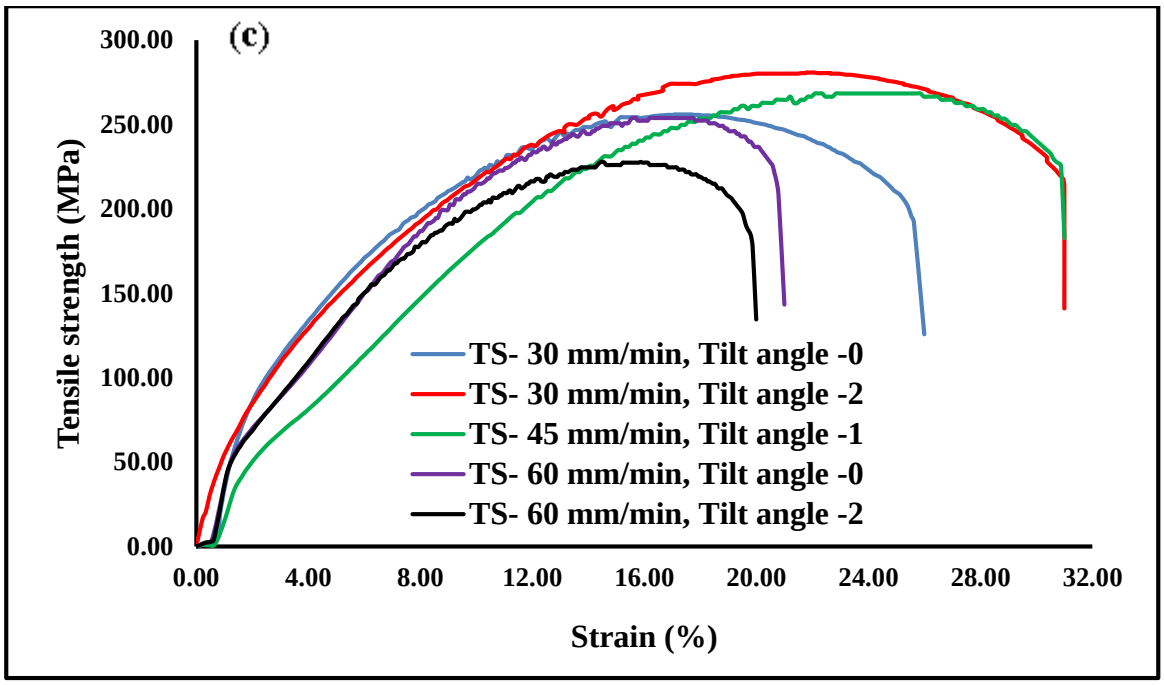

Figure 73: Stress strain diagram of TIG+FSP welded joint, (a) Tool rotation 1000 rpm, (b) Tool rotation 1150 rpm, (c) Tool rotation 1300 rpm

The grain size of TIG+FSP welded joint with filler ER5356 is smaller than the TIG welded joint. According to Hall Petch equation $\sigma_1 = \sigma_i + kd^{(-1/2)}$, the tensile strength is inversely proportional to the grain size [122]. The tensile strength of the TIG-welded joint using filler ER 5356 was calculated as 176.2 MPa, which is much less than the TIG+FSP as shown in the table 23.

The tensile strength of the TIG+FSP welded joint increased with increasing tool rotational speed. The highest tensile strength (281MPa) was observed in TIG+FSP with filler ER 4043 at tool rotational 1300 rpm with feed rate 30 mm/min and tilt angle 2º. Three statistical parameters are investigated i.e., standard deviation (SD), standard error (SE) and 95% confidence interval for TIG+FSP welded joint with filler ER4043 and ER5356 as shown in table 23-26. The standard deviation (SD) provides the deviance of the experimental values from the mean it may be calculated as SD= $[\Sigma(X_i - M)^2/(N-1)]^{1/2}$ and the standard error is a quantity used to measure how to close the prediction values to the experimental values. SE is calculated as $SE=SD/N^{1/2}$, where N= No of observation and M= mean.

The confidence interval has shown that tensile strength and hardness increased with increasing tool rotation, whereas residual stress decreased with increasing tool rotation.

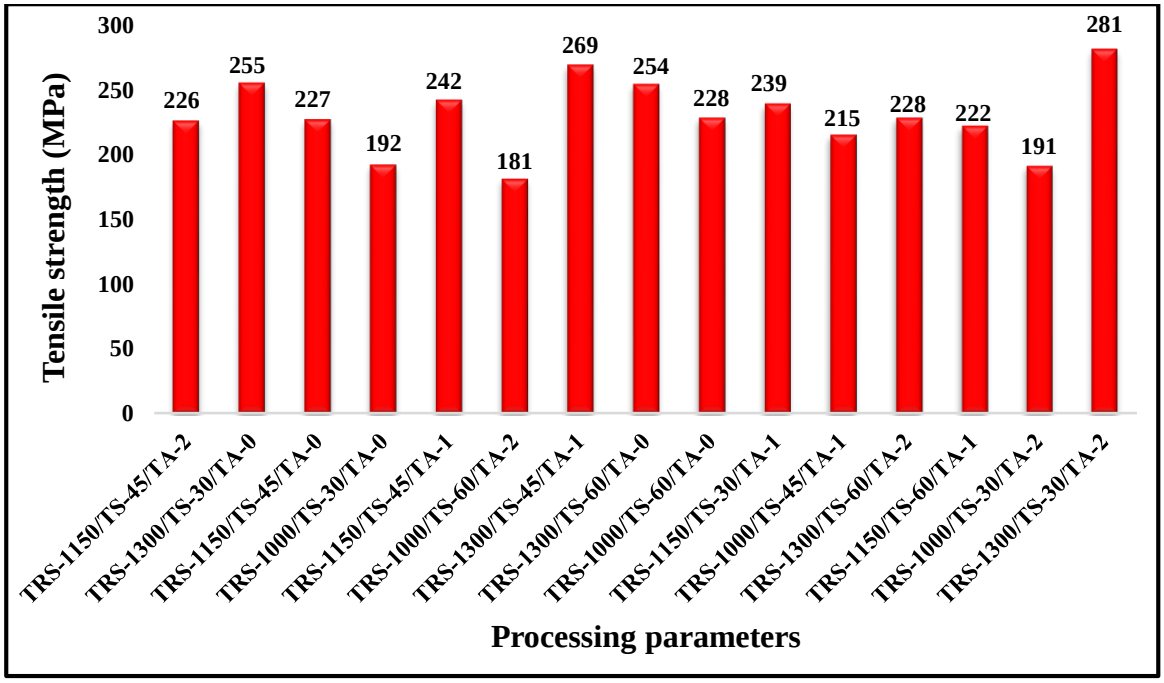

Figure 74: Variation of tensile strength to the processing parameters at nugget zone

5.3.2 Micro-hardness

The tensile strength and fracture point locations of the TIG+FSP welded joints depends on the hardness distributions and welding defects of the welded joints. When the joints are defects free then the tensile strength of the welded joints are dependent on the micro-hardness distribution of the joints. As we know that the friction stir welded joint is a heterogeneous composite which including their interfaces, possess different mechanical properties [141-143]. The micro-hardness distribution of the TIG+FSP welded joint of AA6061 and AA7075 with ER 5356 filler wire with different processing parameters were analyzed by Vickers hardness testing results are shown in fig.75-76. Vickers micro-hardness machine was used for measuring the hardness across the welded joints with a load of 100 grams and dwell time 30 sec.

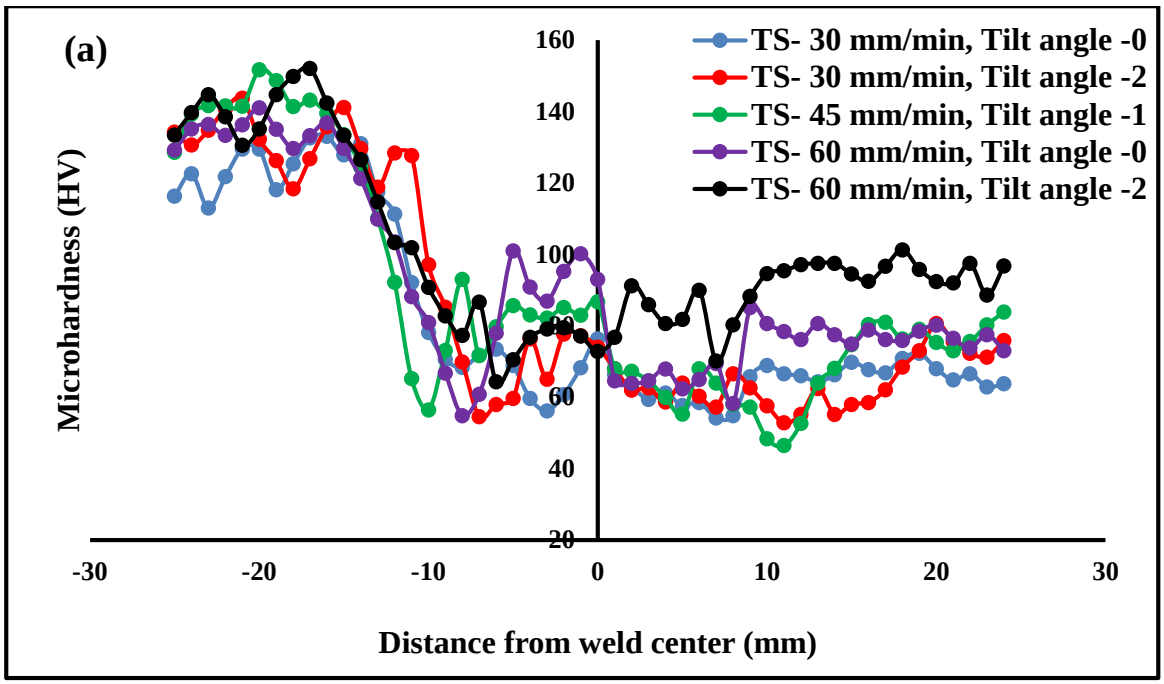
(a)
Microhardness (HV)
160
140
120
100
80
60
40
20
-30
-20
-10
0
10
20
30
Distance from weld center (mm)
TS- 30 mm/min, Tilt angle -0
TS- 30 mm/min, Tilt angle -2
TS- 45 mm/min, Tilt angle -1
TS- 60 mm/min, Tilt angle -0
TS- 60 mm/min, Tilt angle -2

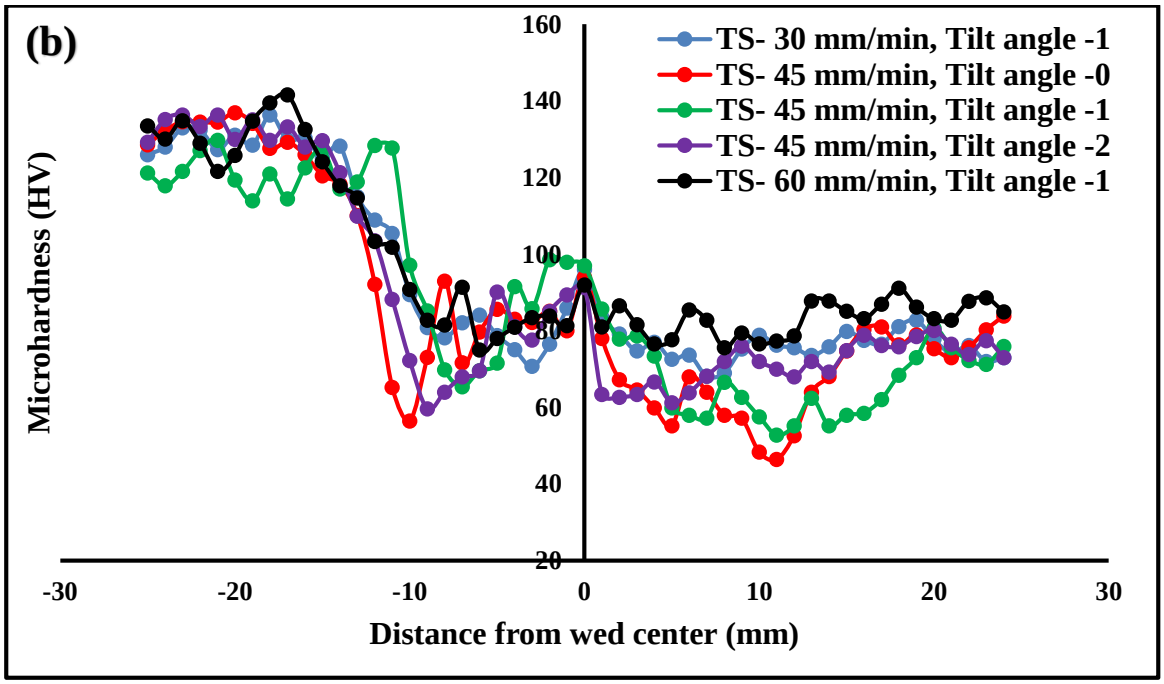
(b)
Microhardness (HV)
160
140
120
100
80
60
40
20
-30
-20
-10
0
10
20
30
Distance from wed center (mm)
TS- 30 mm/min, Tilt angle -1
TS- 45 mm/min, Tilt angle -0
TS- 45 mm/min, Tilt angle -1
TS- 45 mm/min, Tilt angle -2
TS- 60 mm/min, Tilt angle -1

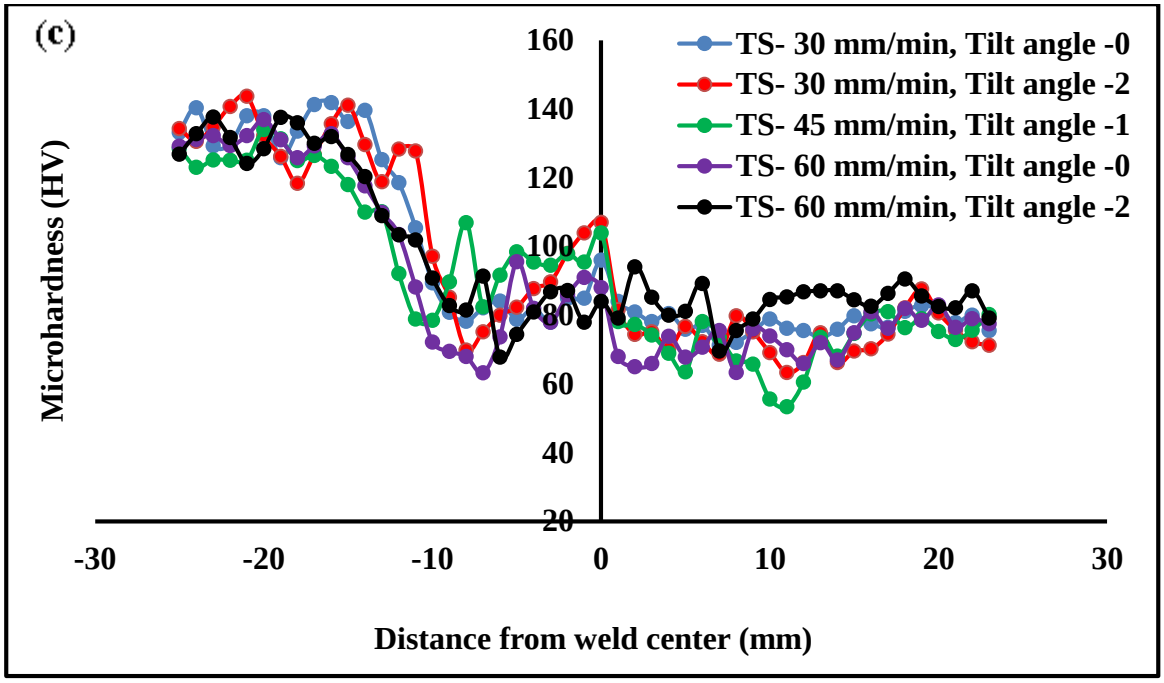

Figure 75: Distribution of micro-hardness of welded joint, (a-c) TIG+FSP welded joint, (a) Tool rotation 1000 rpm, (b) Tool rotation 1150 rpm, (c) Tool rotation 1300 rpm

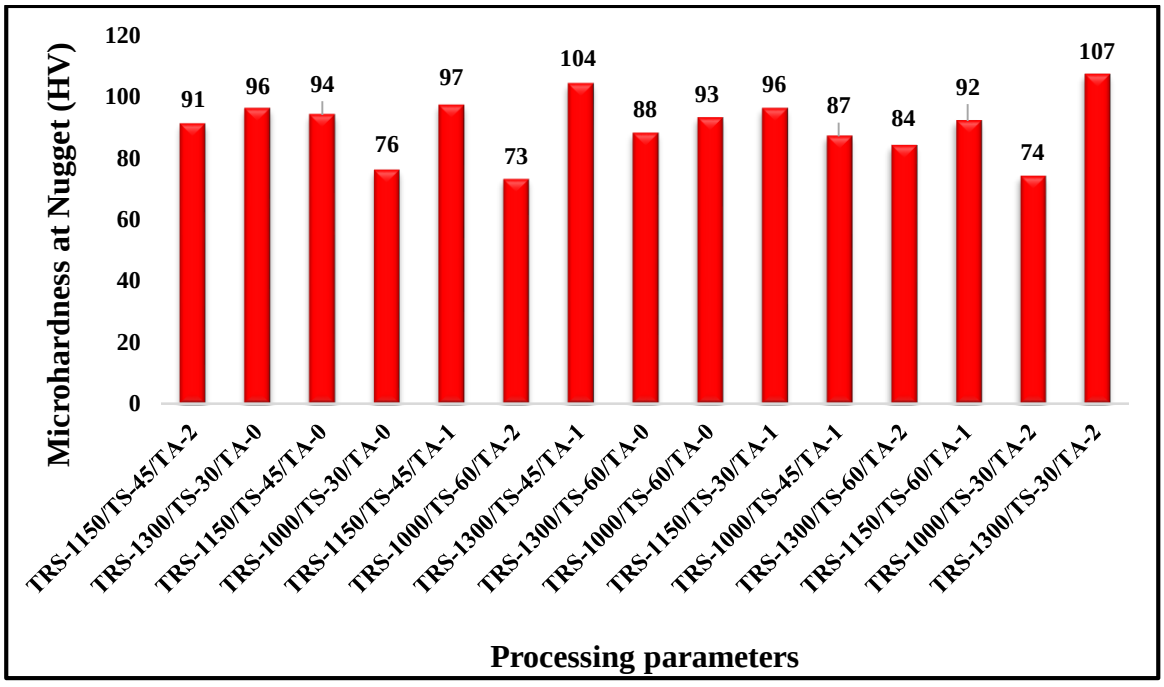

Figure 76: Variation of Micro-hardness to the processing parameters

The hardness distributions are asymmetrical in the weld center due to the microstructure of the advancing side and retreating side introduced by unsteady

plastic flow from the base metal to the weld center [123]. It can be seen that the micro-hardness distribution region including one nugget zone two thermo-mechanically affected zone two heat affected zone has occurred in the TIG+FSP welded joints, therefore the tensile strength of the welded joints is lower than the parent material [144]. The hardness slopes downward from the base metal to the welded region. The hardness fluctuates largely on the advancing side while the hardness holds steady in the retreating side [124]. The alloying elements such as Si and Mg existing in the weld center make precipitation reaction and form a strong precipitate of Mg_2Si to give a higher strength.

Fig. 76, the stir zone has the highest micro-hardness as compare to other adjacent regions, this is due to fine and equiaxed grains and related grain boundary strengthening, whereas thermo-mechanically affected zone and heat affected zone shows the low hardness due to dissolution of strengthening precipitates, grain coarsening, over aging and elevated temperatures experienced during the FSW process. The highest hardness value (107 HV) at nugget zone was observed at tool rotation 1300 rpm, traverse speed 30 mm/min and 2º tilt angle, while the boundary between the TMAZ and HAZ on the A.S (failure location in the tensile test) exhibited the lowest hardness value as compare to stir zone as shown in fig. 76.

Table 23: Tensile strength of TIG+FSP welded joint with filler ER 5356

Processing Parameter			Tensile Strength (MPa)			Mean Tensile Strength MPa	Standard Deviation	Standard error	95% confidence Interval	
A:Tool Rotation Speed (rpm)	B:Traverse Speed (mm/min)	C:Tilt angle (degree)	Specimen 1	Specimen 2	Specimen 3				Minimum	Maximum
1150	45	2	227.2	226.9	224.0	226.0	1.77	1.02	224.0	228.0
1300	30	0	255.0	256.8	253.2	255.0	1.80	1.04	253.0	257.0
1150	45	0	227.0	226.0	228.0	227.0	1.00	0.58	225.9	228.1
1000	30	0	193.0	190.4	192.6	192.0	1.40	0.81	190.4	193.6
1150	45	1	243.6	240.2	242.2	242.0	1.71	0.99	240.1	243.9
1000	60	2	182.4	179.4	181.2	181.0	1.51	0.87	179.3	182.7
1300	45	1	269.8	268.0	269.2	269.0	0.92	0.53	268.0	270.0
1150	45	1	235.2	234.3	235.6	235.0	0.67	0.38	234.3	235.8
1150	45	1	239.2	236.8	238.0	238.0	1.20	0.69	236.6	239.4
1300	60	0	255.2	252.8	254.0	254.0	1.20	0.69	252.6	255.4
1150	45	1	236.2	236.4	235.4	236.0	0.53	0.31	235.4	236.6
1000	60	0	226.4	229.2	228.4	228.0	1.44	0.83	226.4	229.6
1150	30	1	240.2	238.6	238.2	239.0	1.06	0.61	237.8	240.2
1150	45	1	236.2	236.6	235.2	236.0	0.72	0.42	235.2	236.8
1000	45	1	215.0	214.3	215.6	215.0	0.65	0.38	214.2	215.7
1300	60	2	229.3	228.2	226.4	228.0	1.46	0.85	226.3	229.6
1150	60	1	223.5	222.2	220.4	222.0	1.56	0.90	220.3	223.8
1000	30	2	190.4	191.6	191.0	191.0	0.60	0.35	190.3	191.7
1150	45	1	236.2	236.0	235.7	236.0	0.25	0.15	235.7	236.3
1300	30	2	281.6	281.0	280.8	281.1	0.42	0.24	280.7	281.6

Table 24: % elongation of TIG+FSP welded joint with filler ER 5356

Processing Parameter			Elongation (%)			Elongation (%)	Standard Deviation	Standard error	95% confidence Interval	
A:Tool Rotation Speed (rpm)	B:Travers e Speed (mm/min)	C:Tilt angle (degree)	Specimen 1	Specimen 2	Specimen 3				Minimum	Maximum
1150	45	2	23.5	22.2	23.2	23.0	0.68	0.39	22.2	23.7
1300	30	0	26.2	26.6	25.2	26.0	0.72	0.42	25.2	26.8
1150	45	0	24.5	25.6	24.8	25.0	0.57	0.33	24.3	25.6
1000	30	0	20.4	21.5	21.0	21.0	0.55	0.32	20.3	21.6
1150	45	1	27.2	26.7	27.0	27.0	0.25	0.15	26.7	27.3
1000	60	2	14.2	13.4	14.4	14.0	0.53	0.31	13.4	14.6
1300	45	1	30.6	31.2	31.2	31.0	0.35	0.20	30.6	31.4
1150	45	1	26.2	24.8	27.1	26.0	1.16	0.67	24.7	27.3
1150	45	1	28.0	27.6	28.4	28.0	0.40	0.23	27.5	28.5
1300	60	0	20.8	21.4	20.7	21.0	0.38	0.22	20.5	21.4
1150	45	1	25.3	26.4	26.2	26.0	0.59	0.34	25.3	26.6
1000	60	0	20.4	21.6	21.0	21.0	0.60	0.35	20.3	21.7
1150	30	1	24.8	23.5	23.6	24.0	0.72	0.42	23.1	24.8
1150	45	1	26.3	25.8	26.0	26.0	0.25	0.15	25.7	26.3
1000	45	1	28.7	27.6	27.7	28.0	0.61	0.35	27.3	28.7
1300	60	2	20.4	19.9	19.6	20.0	0.40	0.23	19.5	20.4
1150	60	1	19.5	18.4	19.2	19.0	0.57	0.33	18.4	19.7
1000	30	2	19.6	20.2	20.3	20.0	0.38	0.22	19.6	20.5
1150	45	1	25.3	26.4	26.2	26.0	0.59	0.34	25.3	26.6
1300	30	2	30.5	31.6	30.8	31.0	0.57	0.33	30.3	31.6

Table 25: Micro-hardness of TIG+FSP welded joint with filler ER 5356

Processing Parameter			Micro-hardness (HV)			Mean Micro-hardness (HV)	Standard Deviation	Standard error	95% confidence Interval	
A:Tool Rotation Speed (rpm)	B:Traverse Speed (mm/min)	C:Tilt angle (degree)	Specimen 1	Specimen 2	Specimen 3				Minimum	Maximum
1150	45	2	91.5	90.4	91.0	91.0	0.55	0.32	90.3	91.6
1300	30	0	96.6	96.2	95.2	96.0	0.72	0.42	95.2	96.8
1150	45	0	94.6	93.4	94.0	94.0	0.60	0.35	93.3	94.7
1000	30	0	76.4	76.0	75.6	76.0	0.40	0.23	75.5	76.5
1150	45	1	97.8	96.5	96.8	97.0	0.68	0.39	96.3	97.8
1000	60	2	74.0	73.5	71.6	73.0	1.27	0.73	71.6	74.5
1300	45	1	104.0	104.8	103.2	104.0	0.80	0.46	103.1	104.9
1150	45	1	97.0	97.3	96.6	97.0	0.35	0.20	96.6	97.4
1150	45	1	100.5	100.2	100.0	100.2	0.25	0.15	99.9	100.5
1300	60	0	88.0	87.6	88.4	88.0	0.40	0.23	87.5	88.5
1150	45	1	100.0	99.0	98.0	99.0	1.00	0.58	97.9	100.1
1000	60	0	94.0	92.0	93.0	93.0	1.00	0.58	91.9	94.1
1150	30	1	96.6	96.0	95.4	96.0	0.60	0.35	95.3	96.7
1150	45	1	98.2	98.0	98.2	98.1	0.12	0.07	98.0	98.3
1000	45	1	87.6	87.0	87.0	87.2	0.35	0.20	86.8	87.6
1300	60	2	83.4	84.4	84.2	84.0	0.53	0.31	83.4	84.6
1150	60	1	92.0	91.2	92.8	92.0	0.80	0.46	91.1	92.9
1000	30	2	74.0	75.0	73.2	74.1	0.90	0.52	73.0	75.1
1150	45	1	94.0	93.5	94.5	94.0	0.50	0.29	93.4	94.6
1300	30	2	107.0	107.4	107.0	107.1	0.23	0.13	106.9	107.4

Table 26: Residual Stress of TIG+FSP welded joint with filler ER 5356

Processing Parameter			Residual Stress (Mpa)			Mean Residual Stress (MPa)	Standard Deviation	Standard error	95% confidence Interval	
A:Tool Rotation Speed (rpm)	B:Traverse Speed (mm/min)	C:Tilt angle (degree)	Specimen 1	Specimen 2	Specimen 3				Minimum	Maximum
1150	45	2	60.0	59.0	59.0	59.3	0.58	0.33	58.7	60.0
1300	30	0	26.0	24.0	23.0	24.3	1.53	0.88	22.6	26.1
1150	45	0	39.0	38.0	41.0	39.3	1.53	0.88	37.6	41.1
1000	30	0	52.0	52.0	53.0	52.3	0.58	0.33	51.7	53.0
1150	45	1	24.0	23.0	23.0	23.3	0.58	0.33	22.7	24.0
1000	60	2	68.0	67.0	69.0	68.0	1.00	0.58	66.9	69.1
1300	45	1	18.0	20.0	19.0	19.0	1.00	0.58	17.9	20.1
1150	45	1	26.0	22.0	24.0	24.0	2.00	1.15	21.7	26.3
1150	45	1	27.0	29.0	28.0	28.0	1.00	0.58	26.9	29.1
1300	60	0	44.0	44.0	47.0	45.0	1.73	1.00	43.0	47.0
1150	45	1	32.0	33.0	29.0	31.3	2.08	1.20	29.0	33.7
1000	60	0	35.0	35.8	34.2	35.0	0.80	0.46	34.1	35.9
1150	30	1	41.0	42.0	41.0	41.3	0.58	0.33	40.7	42.0
1150	45	1	32.0	34.0	31.0	32.3	1.53	0.88	30.6	34.1
1000	45	1	34.0	36.0	35.0	35.0	1.00	0.58	33.9	36.1
1300	60	2	55.0	52.0	56.0	54.3	2.08	1.20	52.0	56.7
1150	60	1	52.8	51.2	52.0	52.0	0.80	0.46	51.1	52.9
1000	30	2	64.0	60.0	64.0	62.7	2.31	1.33	60.1	65.3
1150	45	1	28.0	28.0	29.0	28.3	0.58	0.33	27.7	29.0
1300	30	2	19.0	19.0	17.0	18.3	1.15	0.67	17.0	19.6

5.3.3 Residual Stress for TIG+FSP welded joint with filler ER 5356

The friction stir welding creates negligible residual stresses in the welded specimen. The residual stresses are also affect the mechanical properties of welded joint, so the accurate prediction of residual stresses in the welded joint based on different processing parameters are difficult [145-146]. The residual stresses were calculated at the distance from -15 to 15 mm with the help of X-ray diffraction (XRD) Pulstec μ-X360 machine by cosα method, welded region were covered within the range and residual stress was measured at every 1 mm distance. It can be seen that the residual stress of TIG, TIG+FSP weld and vicinity is characterized by compressive residual stresses. During this process it was observed that the residual stress on AA7075 is lower than the AA6061. Generally, the tensile residual stress lead to negative effect to the weldment, whereas compressive residual stress shows the positive effect to the welded joint [50, 57]. In this measurement all the residual stresses were found to be compressive. The variation of residual stresses in transverse direction of TIG+FSP welded joint with filler ER 5356 are shown in fig. 77 (a-c).

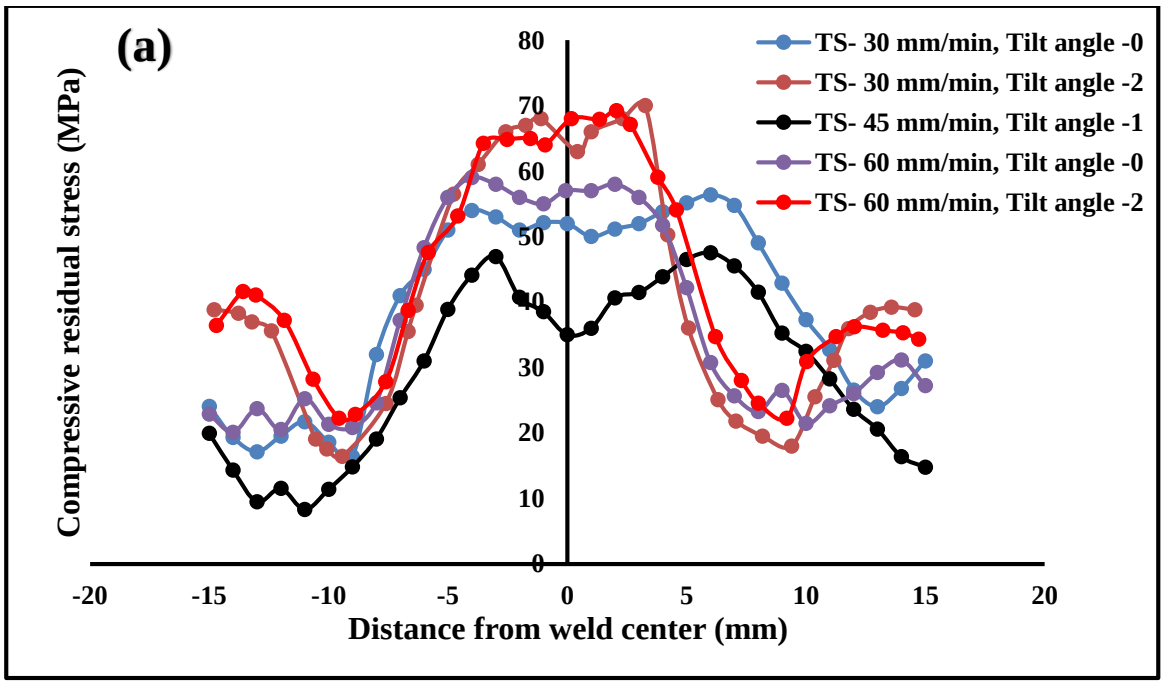

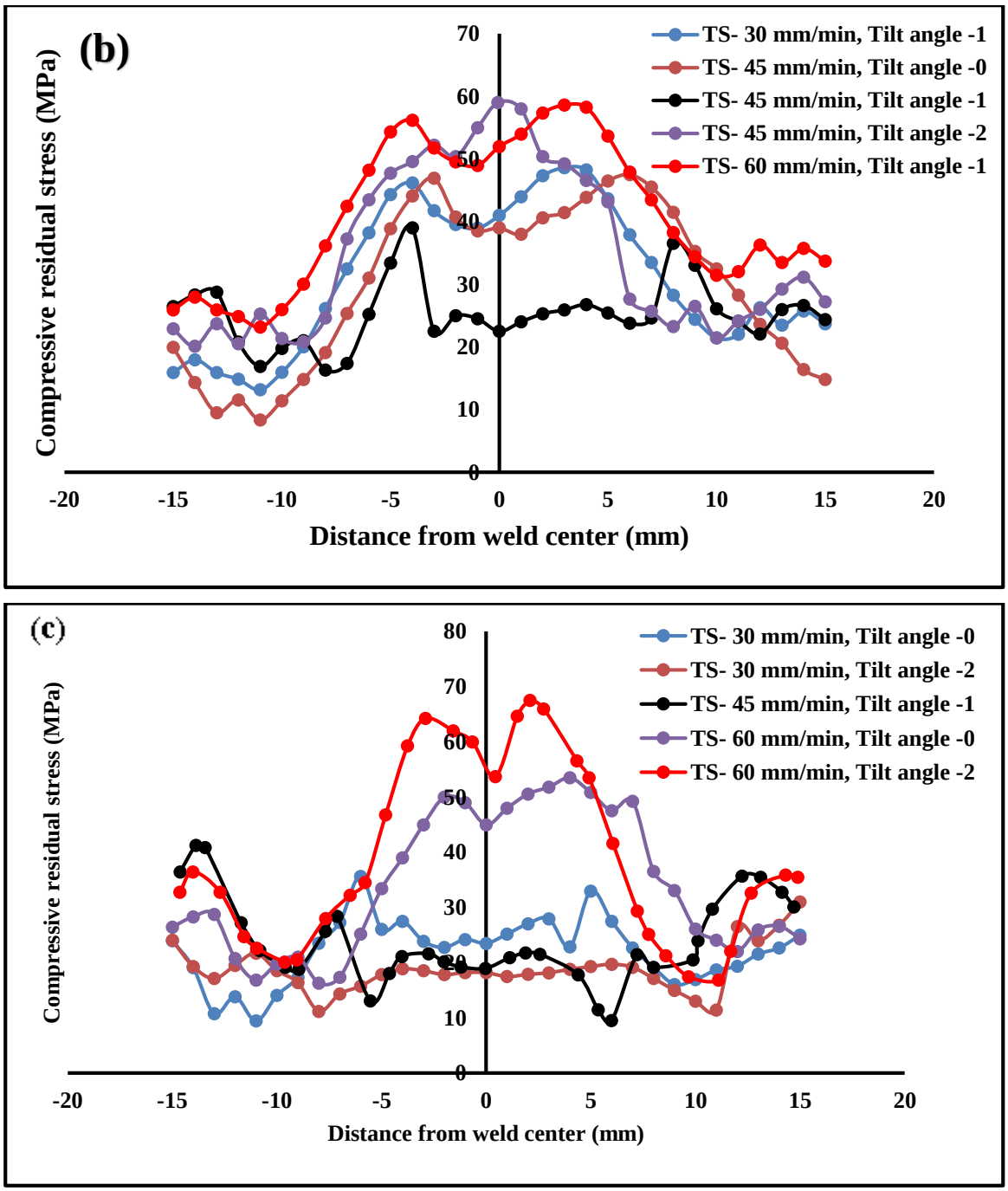

Figure 77: Variation of residual stress to the processing parameters of TIG+FSP, (a) tool rotation 1000 rpm, (b) Tool rotation 1150 rpm, (c) Tool rotation 1300 rpm

The base material AA7075 on LHS of the weldment shows a minimum compressive residual stress, however the residual stress gradually increases from base material to towards the weldment and then decrease till second base material AA6061. The maximum compressive residual stress 63MPa were located at the fusion zone (FZ) of the TIG weldment with filler ER 5356, whereas minimum compressive residual stress

18 MPa was obtained at stir zone (SZ) of the TIG+FSP at tool rotation 1300 rpm, traverse speed 30 mm/min and tilt angle 2º.

The residual stresses profile of TIG+FSP were not symmetrical about the center line of the weldment for both the cases. The left side peak value of the weldment was greater than the right side, because the forming processes is different for retreating side (RS) and advancing side (AS).

Fig. 78 shows the 3D Debye ring, distortion ring and residual stress profile (with respect to alpha angle) of TIG and TIG+FSP welded joint. The residual stress peaks for all the specimens were between 150º to 160º. The red contour indicates higher concentration of residual stress at fusion and stir zone of the welded joint, while blue contour indicates minimum amount of residual stress. The full width at half maximum (FWHM) was measured at different position of the welded joint by Pulstec μ-X360 machine. If the residual stress peak is thicker than the FWHM value will be higher, results in fine grain structures.

The value of residual stress obtained by the experimental methods. Fig.77 shows a comparison between tool rotation and the compressive residual stress, grouped by traverse speed and tilt angle. It can be seen that the compressive residual stresses decrease for a given value of pitch as the traverse speed and tilt angle increases. Although measured peak residual stress increases with as traverse speed decreases, tensile stress appears to be limited to the softened weld zone instead, resulting in a narrowing of the tensile region [126]. The minimum value of compressive residual stress (18 MPa) is obtained at tool rotational speed of 1300 rpm, traverse speed 30 mm/min and tilt angle 2^0. A 71.43 % variation is observed in TIG welding and TIG+FSP welding.

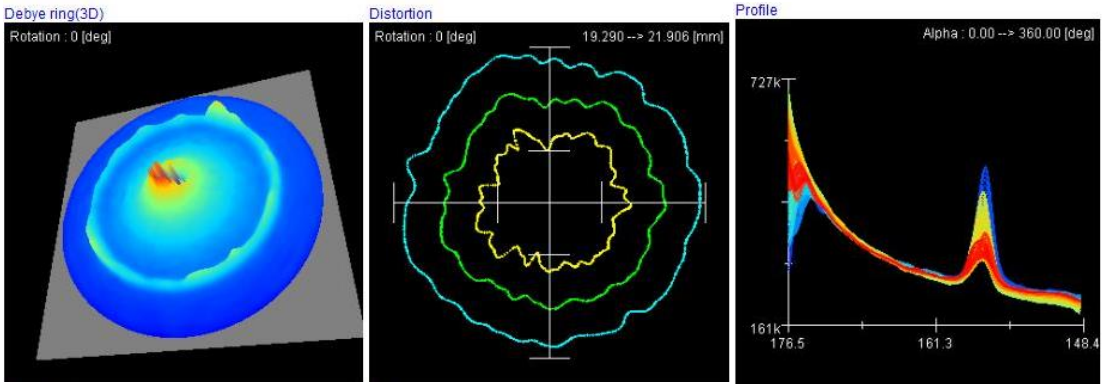

(a)

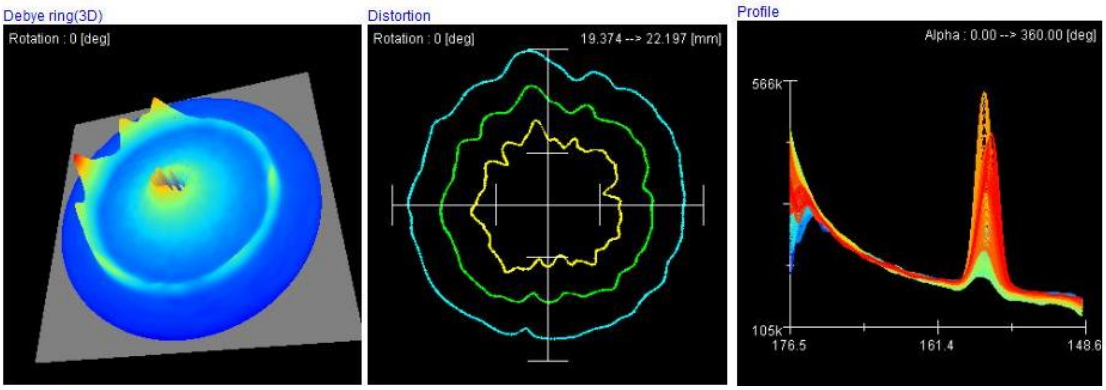

(b)

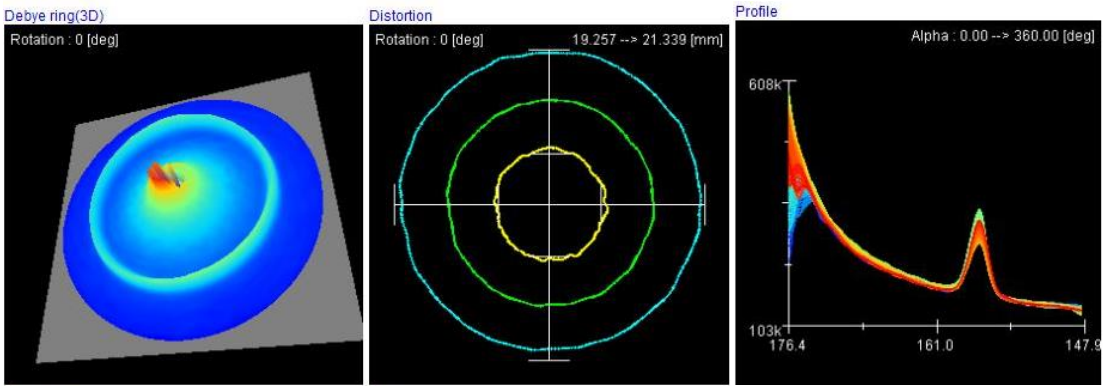

(c)

Figure 78: 3D Debye ring, distortion ring and residual stress profile at the center of the welded joint, (a) TIG joint with filler ER 5356, (b) TIG+FSP sample No. 9 (c) Sample No. 20

5.3.4 Developing the mathematical model

Twenty experiments are used as input data to generate mathematical equation using response surface methodology with the help of design expert software. The response functions are ultimate tensile strength, strain, micro-hardness at nugget zone and residual stress at nugget zone whereas input parameters are tool rotational speed (A), traverse speed (B) and tilt angle (c). It may be expressed as

Tensile strength = $f(A, B, C)$

% Elongation = $f(A, B, C)$

Micro-hardness = $f(A, B, C)$

Residual stress = $f(A, B, C)$

The second order polynomial regression equation which is represent the response surface is given by

$$Y=a_0+\sum a_i x_i+\sum a_{ii} x_i^2+\sum a_{ij} x_i x_j$$

The selected polynomial can be expressed as

$$Y=a_0+a_1A+a_2B+a_3C+a_{11}A^2+a_{22}B^2+a_{33}C^2+a_{12}A\times B+a_{13}A\times C+a_{23}B\times C$$

Where a0 is the average response, coefficient a_1, a_2, a_3 are linear terms, the coefficients a_{11}, a_{22}, a_{33} are quadratic terms and the coefficient a_{12}, a_{13}, and a_{23} are interaction terms. All the coefficients were evaluated and tested for their significance at 95% confidence level. The final mathematical model for TIG+FSP welded joint with filler ER 5356 was developed by ANOVA technique using second order regression equations are given as below. As per model adequacy, the standard Fisher's F value must be more than the calculated value of F, then the model will have considered to be adequate with 95% confidence level. When the lack of fit is not significant, then the models are significant. The ANOVA's for the responses for tensile stress, % elongation, micro-hardness at nugget and residual stress at nugget for TIG+FSP welded joint are reported in tables 27-30. The developed final mathematical empirical equation in the coded form have been given below.

$$\text{Tensile strength} = 72.94 - 0.206A + 8.06B + 6.03C - 0.0044AB + 0.04AC - 0.816BC + 0.00024\,A^2 - 0.027\,B^2 - 10.09C^2$$

$$\text{Elongation} = 116.9 - 0.2657A + 2.595B - 2.42C - 0.00055AB + 0.01AC - 0.1BC + 0.000129A^2 - 0.0226B^2 - 2.59C^2$$

$$\text{Micro-hardness} = -242.57 + 0.371A + 4.64B - 6.76C - 0.0026AB + 0.024AC - 0.275BC - 0.00009A^2 - 0.0165B^2 - 5.22C^2$$

$$\text{Residual stress} = -154.20 + 0.696A - 8.63B + 5.66C + 0.0038AB - 0.0341AC + 0.308BC - 0.00039A^2 + 0.0476B^2 + 13.22C^2$$

The tool rotational speed coefficient (A) has positive, it implies that the tensile stress increases when the tool rotation speed increases, because high rotational speed can significantly improve the mechanical properties of the friction stir welded joint of

aluminum alloy. Whereas high traverse speed minimizes the detrimental effect of tool rotation speed. The tilt angle is also affect the tensile stress, because when the tilt angle is increases. The symmetric microstructure and uniform plastic flow under the shoulder are found in the nugget zone (NZ) [127]. The relationship between input process parameters and heat index at stir zone (SZ) was analyzed [128]. The rotational speed is directly. proportional to the heats index. Due to high frictional heats generated between the work-piece and rotating tool, the high temperature is generated [129]. When welding time increases, the temperature of shoulder is also increases which give the adverse consequence on mechanical properties of weldment. On the other hand, if welding time is low then the heat of tool shoulder does not produce much heat such that low mechanical properties was found in the welded joint.

Table 27: ANOVA for tensile strength (surface quadratic model)

Tensile Strength						
Sources	Sums of squares	df	Mean of square	F-value	P-value	
Model	11255.6	9	1250.62	96.70	< 0.0001	significant
A-Tool Rotation Speed	7840.0	1	7840.00	606.21	< 0.0001	significant
B-Traverse speed	202.5	1	202.50	15.66	0.0026	significant
C-Tilt Angle	240.1	1	240.10	18.57	0.00154	significant
AB	800.0	1	800.00	61.86	< 0.0001	significant
AC	288.0	1	288.00	22.27	0.0008	significant
BC	1200.5	1	1200.50	92.83	< 0.0001	significant
A^2	80.5	1	80.46	6.22	0.031756	significant
B^2	102.0	1	102.02	7.89	0.018517	significant
C^2	280.0	1	280.02	21.65	0.000904	significant
Residual	129.3	10	12.93			
Lack of Fit	96.5	5	19.30	2.94	0.130894	not significant
Pure Error	32.8	5	6.57			
Cor Total	11385.0	19				
Std. Dev.	3.6	R^2	0.99			
Mean	231.6	Adjusted R^2	0.98			
C.V. %	1.6	Predicted R^2	0.92			
		Adeq Precision	39.91			

Table 28: ANOVA for elongation (%) (Surface quadratic model)

% elongation						
Sources	Sums of squares	df	Mean of square	F-value	P-value	
Model	338.02	9	37.56	57.54	< 0.0001	significant
A-Tool Rotation Speed	62.50	1	62.50	95.75	< 0.0001	significant
B-Traverse speed	72.90	1	72.90	111.69	< 0.0001	significant
C-Tilt Angle	3.60	1	3.60	5.52	0.04074	significant
AB	12.50	1	12.50	19.15	0.001385	significant
AC	18.00	1	18.00	27.58	0.00037	significant
BC	18.00	1	18.00	27.58	0.000372	significant
A^2	23.27	1	23.27	35.65	0.000137	significant
B^2	71.27	1	71.27	109.19	< 0.0001	significant
C^2	18.46	1	18.46	28.28	0.000338	significant
Residual	6.53	10	0.65			
Lack of Fit	3.03	5	0.61	0.86	0.56131	not significant
Pure Error	3.50	5	0.70			
Cor Total	344.55	19				
Std. Dev.	0.81	R^2	0.98			
Mean	24.15	Adjusted R^2	0.96			
C.V. %	3.35	Predicted R^2	0.92			
		Adeq Precision	31.038			

The statistical results of developed empirical correlation as shown in table 27-30. The predicted empirical relationship value perfectly matches with the experimental value when R^2 value is 1. The lower value to standard error and higher value of R^2 towards 1 indicate that the empirical relationships are adequate and can be used to predict the responses without considerable error. The higher value of adjusted R^2 increases variation and indicates more useful variables in the existing model. In this developed model, results give a higher R^2 value of 0.9526, 0.9056, 0.9207 and 0.913 and adjusted R^2 value of 0.91, 0.8206, 0.8493 and 0.8347 for ultimate tensile strength, % elongation, micro-hardness at NZ and residual stress at NZ respectively.

Table 29: ANOVA for micro-hardness at nugget (surface quadratic model)

Microhardness						
Sources	Sums of squares	df	Mean of square	F-value	P-value	
Model	1630.93	9	181.21	72.28	< 0.0001	significant
A-Tool Rotation Speed	577.60	1	577.60	230.39	< 0.0001	significant
B-Traverse speed	36.10	1	36.10	14.40	0.00351	significant
C-Tilt Angle	32.40	1	32.40	12.92	0.00488	significant
AB	276.13	1	276.13	110.14	< 0.0001	significant
AC	105.13	1	105.13	41.93	< 0.0001	significant
BC	136.13	1	136.13	54.30	< 0.0001	significant
A^2	13.64	1	13.64	5.44	0.04185	significant
B^2	38.20	1	38.20	15.24	0.00294	significant
C^2	75.14	1	75.14	29.97	0.000271	significant
Residual	25.07	10	2.51			
Lack of Fit	3.57	5	7.1	2.83	0.9645	not significant
Pure Error	21.50	5	4.30			
Cor Total	1656.00	19				
Std. Dev.	1.58	R^2	0.98			
Mean	92.00	Adjusted R^2	0.97			
C.V. %	1.72	Predicted R^2	0.96			
		Adeq Precision	30.81			

Table 30: ANOVA for residual stress at nugget (surface quadratic model)

Residual stress						
Sources	Sums of squares	df	Mean of square	F-value	P-value	
Model	4029.23	9	447.69	14.00	< 0.0001	significant
A-Tool Rotation Speed	864.90	1	864.90	27.05	0.00040	significant
B-Traverse speed	313.60	1	313.60	9.81	0.01066	significant
C-Tilt Angle	448.90	1	448.90	14.04	0.00380	significant
AB	595.13	1	595.13	18.61	0.00152	significant
AC	210.13	1	210.13	6.57	0.02820	significant
BC	171.13	1	171.13	5.35	0.04326	significant
A^2	211.64	1	211.64	6.62	0.02776	significant

B^2	316.45	1	316.45	9.90	0.01040	significant
C^2	481.14	1	481.14	15.05	0.00306	significant
Residual	319.77	10	31.98			
Lack of Fit	254.44	5	50.89	3.89	0.08098	not significant
Pure Error	65.33	5	13.07			
Cor Total	4349.00	19				
Std. Dev.	5.65	R^2	0.93			
Mean	38.50	Adjusted R^2	0.86			
C.V. %	14.69	Predicted R^2	0.68			
		Adeq Precision	14.00			

5.3.5 Adequacy of developed model

When the rotational speed of tool is less than the 1000 rpm then the worm hole at R.S was observed due to insufficient of metal transportation and insufficient heat generation in TIG+FSP welded joint, whereas when the TRS is higher than the 1300 rpm then the high heat was observed in the NZ, results widen the HAZ and weaken the microstructure bonds. Pin holes' defect was observed at traverse speed less than 30 mm/min due excessive heat input per unit length in the weldment. When feed rate is greater than 60 mm/min, the bottom tunnel in the advancing side was perceived due to inadequate flow of material and insufficient heat input in the weldment. ANOVA table for tensile strength with respect to selective variables of TIG+FSP welded joint with filler ER 5356 of AA6061 and AA7075 reveals that the Fisher's F value for tensile strength is 22.35 which shows that the model is significant. Chance of fisher's F value due to error is only 0.01% is shown in table 27. The ANOAVA table 28 shows the elongation of TIG+FSP welded joint, the fisher's F value is 10.66, which shows the model is significant. The coefficient of R^2 shows the goodness of fits of the models. Value of R^2 (0.9526) for tensile strength shows that 95.26% of the complete variability is analyzed by the model after considering the significant factor. The difference between R^2 (95.26%) and adjusted R^2 (91%) is 4.26%, which shows that the 4.26% of the total variation is not elucidated by the model and it also indicate that the model is not over fitted. The fisher's F value of ANOVA surface quadratic model for percentage elongation, micro-hardness at nugget and residual stress at nugget are

10.66, 12.9, and 11.66 respectively as shown in table 27-30. These values shown that the model is significant.

5.3.6 Influence of process parameter on response parameters

The predicted vs. experimental values for ultimate tensile stress, % elongation, micro-hardness and residual stress of TIG+FSP welded joint with filler ER 5356as shown in fig. 79. The scattered plots are very closed to 45º line; it shows the response variables are lying on the straights lines which indicates that the error are uniformly scattered throughout the model. These plot shows excellent correlation of predicted and experimental values of the response values. All the above correlation divulges a good adequacy of the regression models.

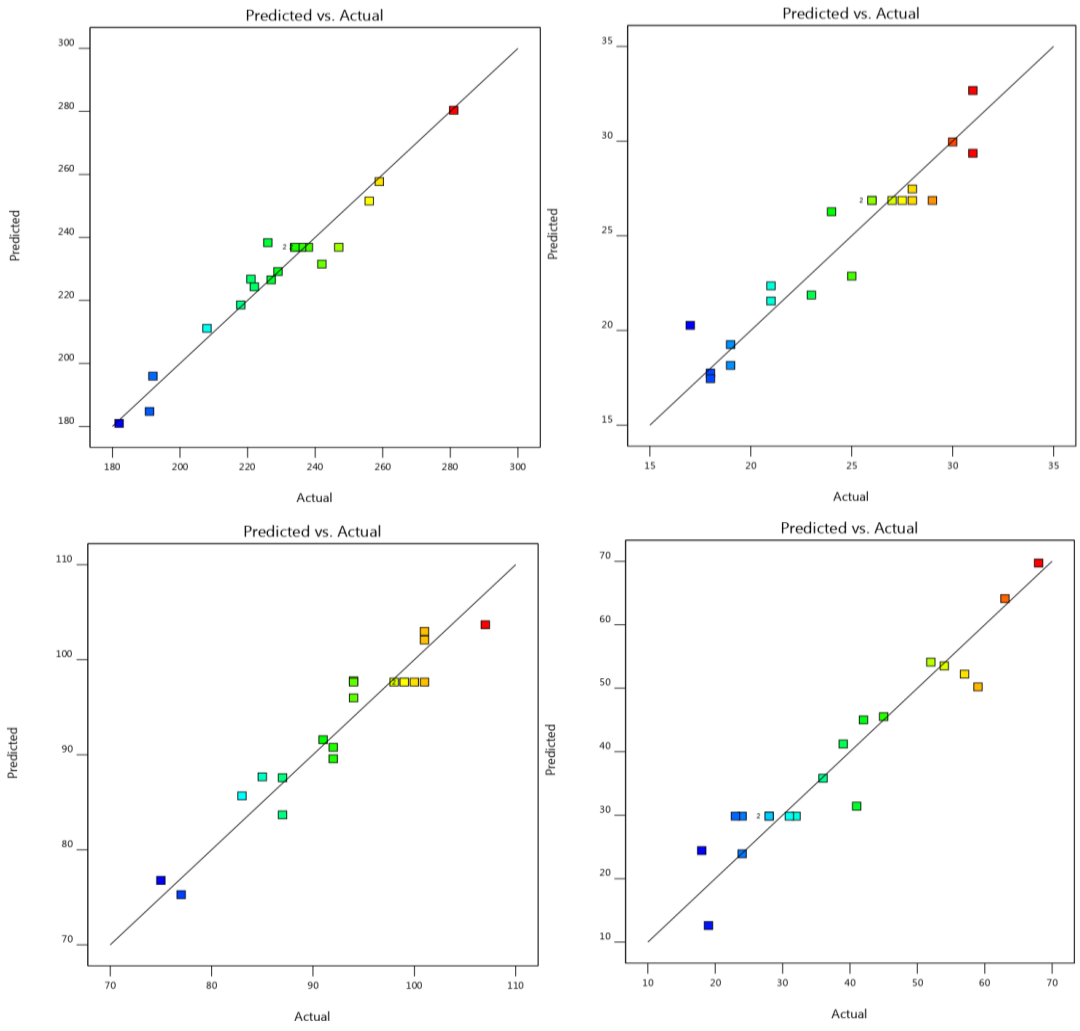

Figure 79: Predicted vs experimental, (a) Tensile strength, (b) Percentage Elongation, (c) Micro-hardness, (d) Residual Stress

Fig. 80-83, shows the 3D responses surfaces plot and contour of tensile strength, % elongation, residual stress and micro-hardness at nugget zone from the regression model. The optimum output responses are exhibited by the apex of the response surfaces. It is easier to understand the interaction of factor on the response by examining the 3D responses and contour plots.

The significance of high frictional heat can be revealed as coarsening and dissolutions of resilient precipitate in weld nugget zones. Due to more heating cycle and friction among the work-piece and rotating tool, the high temperature is generated [75, 129]. When the tool rotation speed increases, tensile stress also increases due to strain hardening effect convinced by tool stirring, whereas excess heat input play the predominant role at high tool rotation speed such lower tensile strength was observed when the tool rotation decreases.

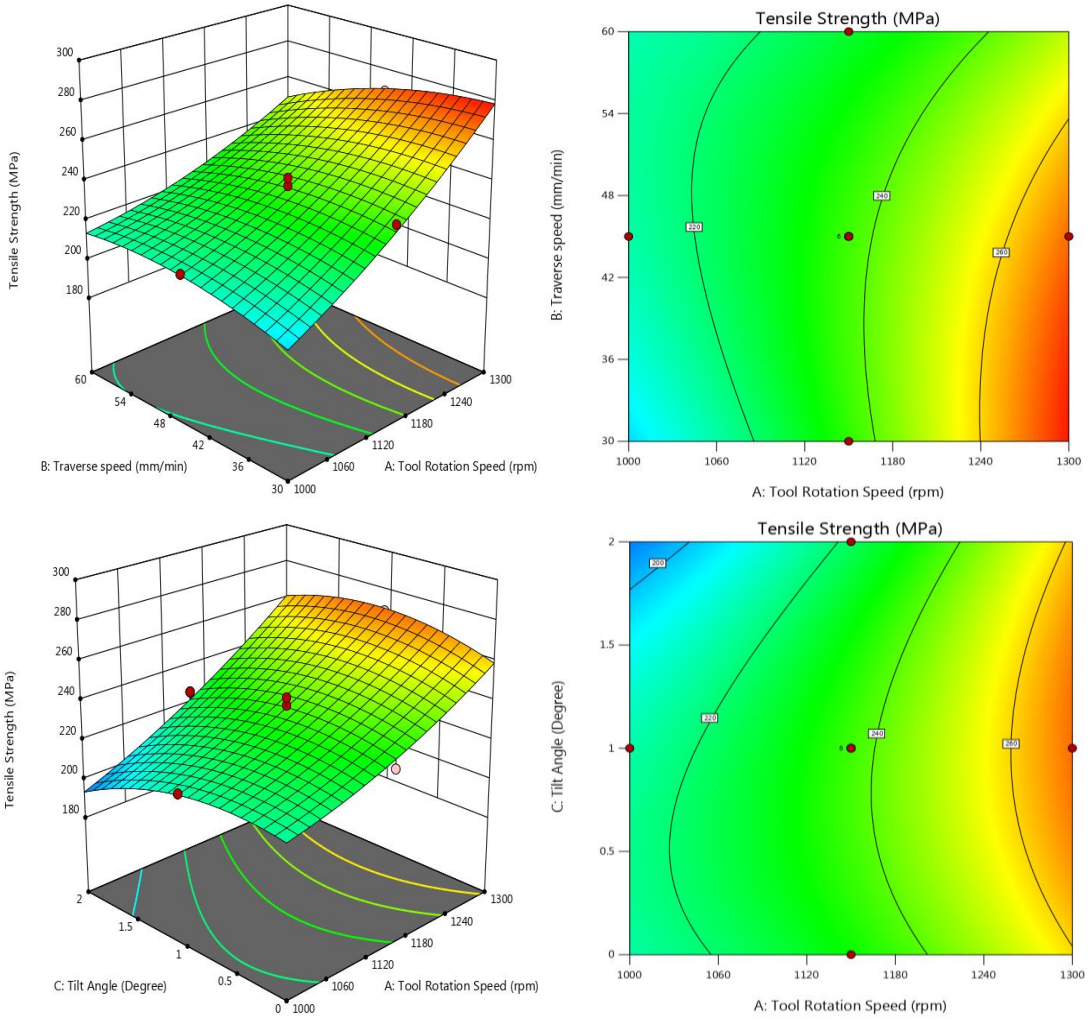

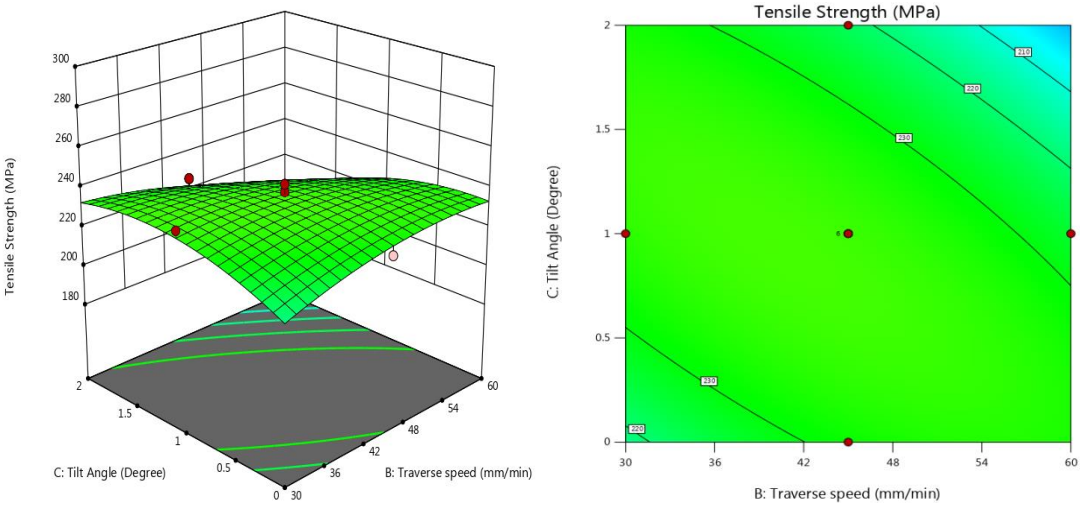

Figure 80: 3D response surface plot and contour plot for tensile strength of TIG+FSP welded joint with filler ER 5356

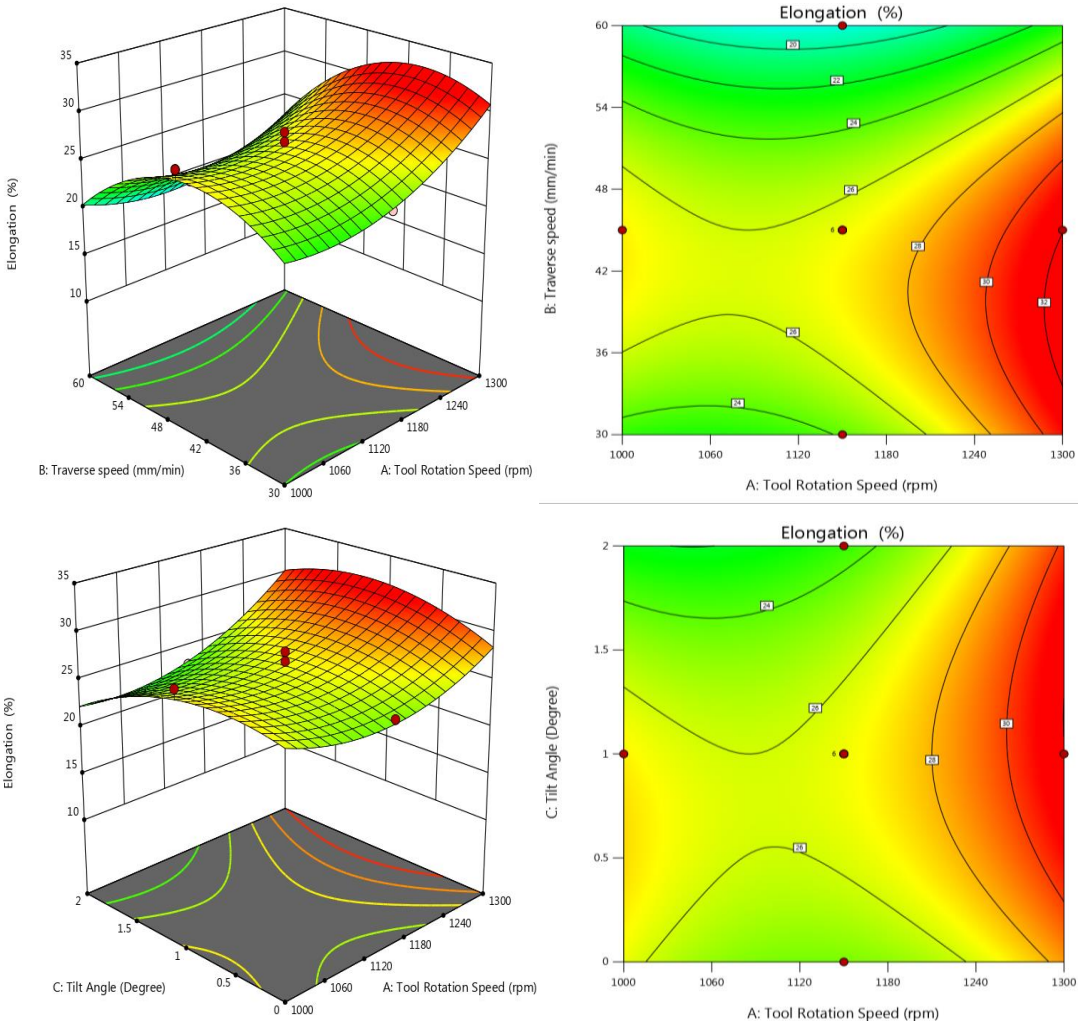

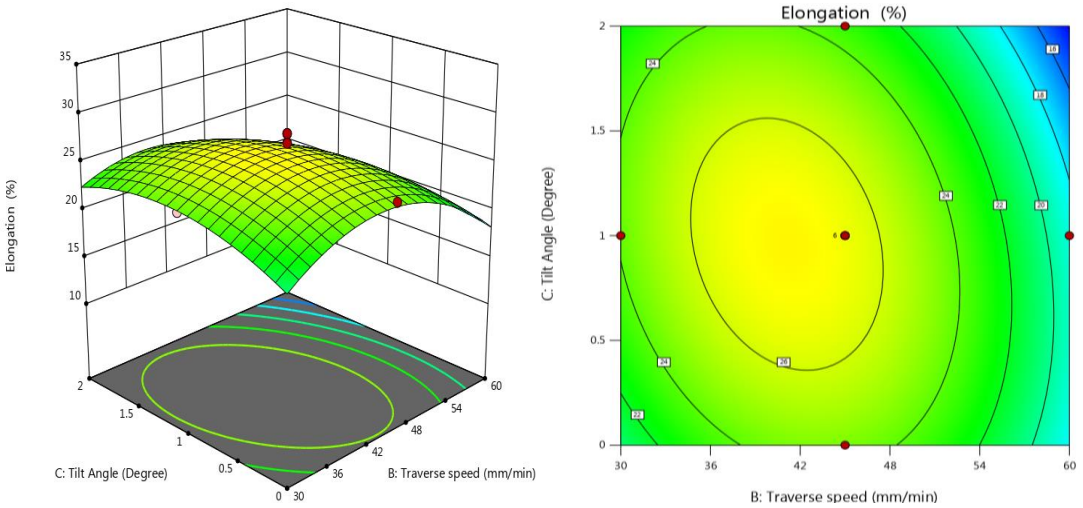

Figure 81: 3D response surface plot and contour plot for % elongation of TIG+FSP welded joint with filler ER 5356

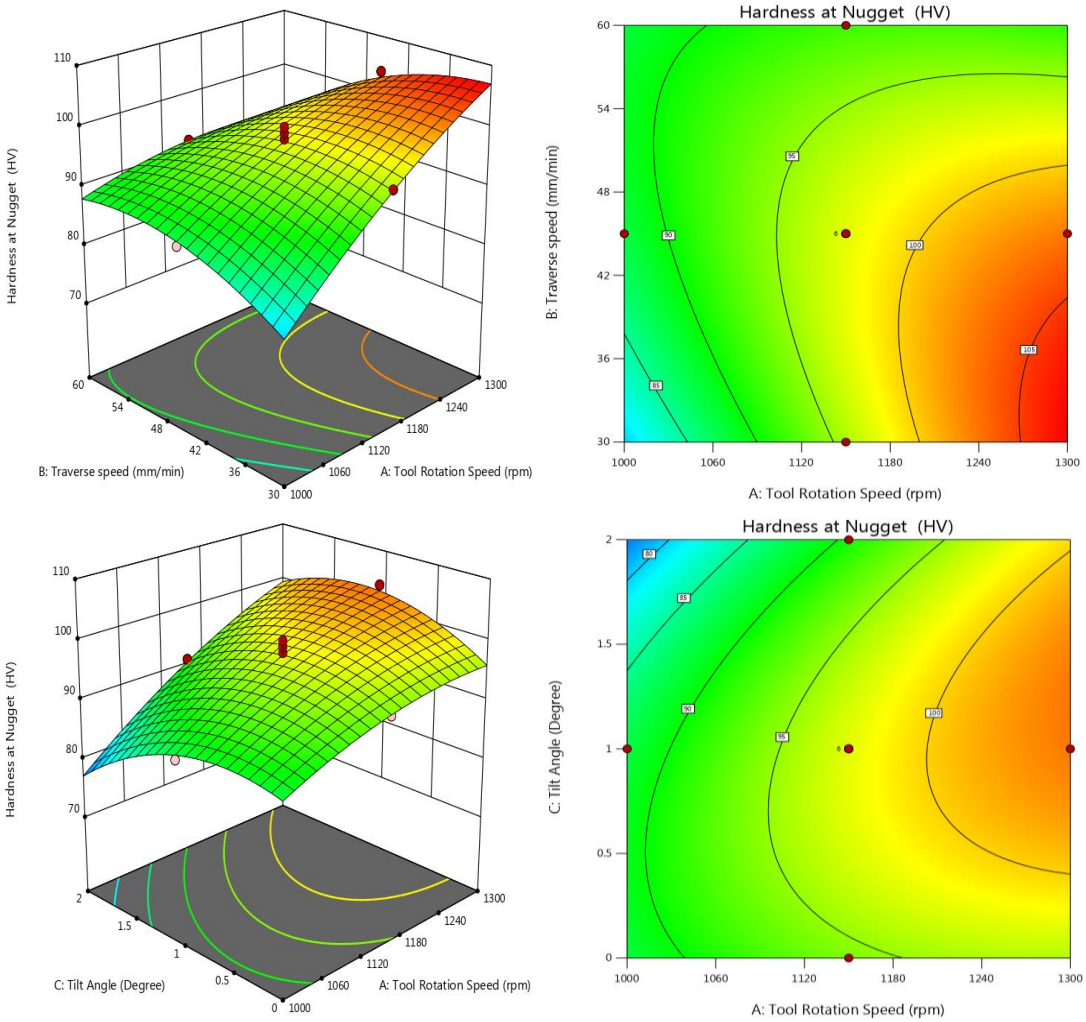

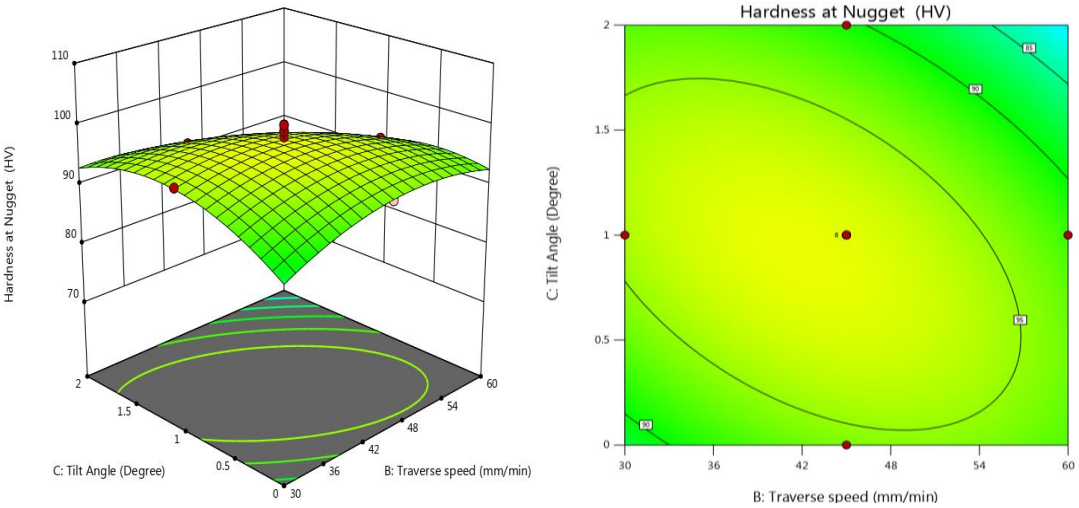

Figure 82: 3D response surface plot and contour plot for micro-hardness at nugget zone of TIG+FSP welded joint with filler ER 5356

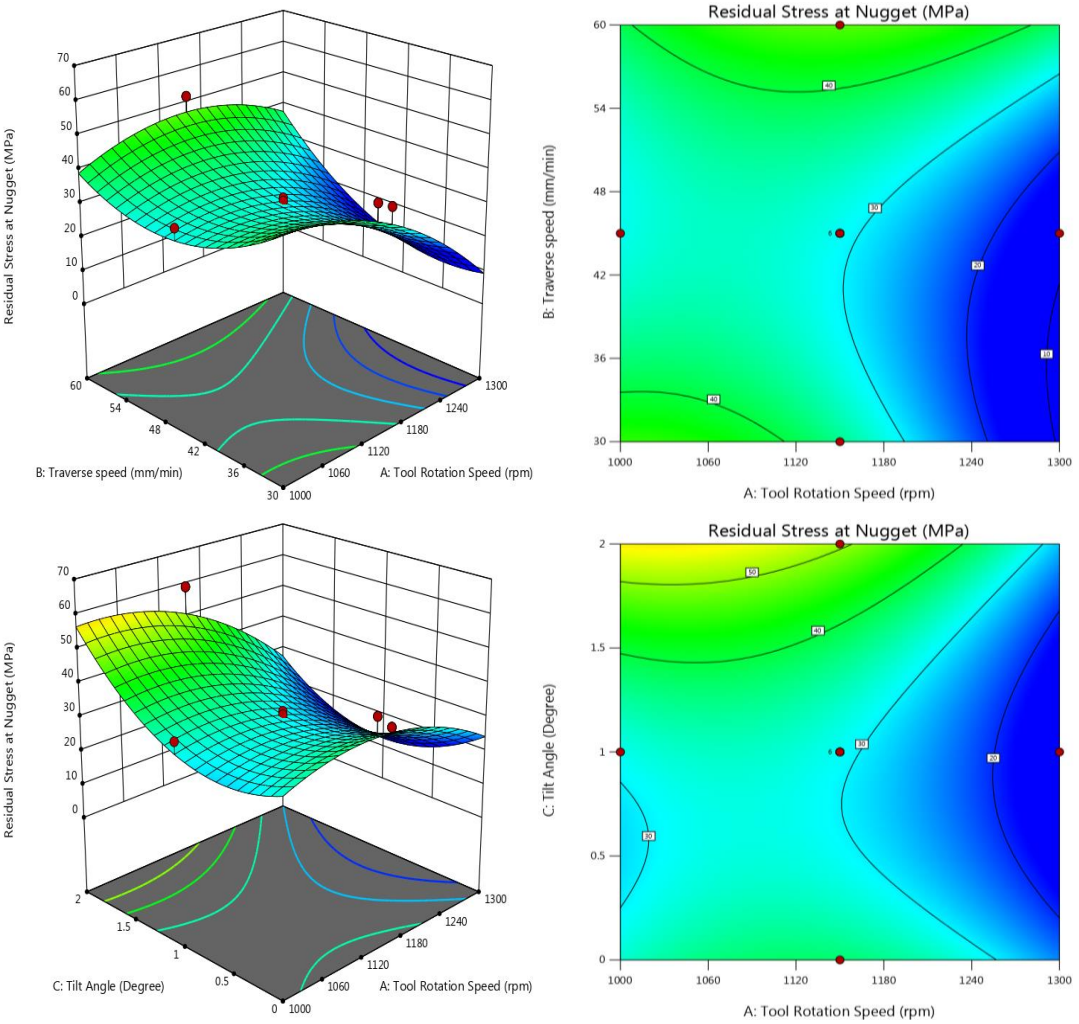

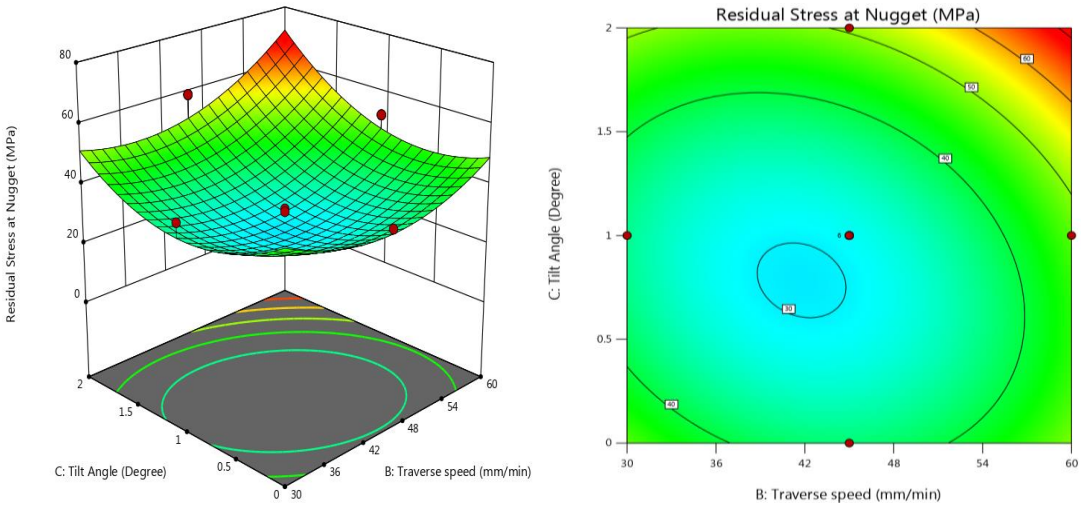

Figure 83: 3D response surface plot and contour plot for residual stress at nugget zone of TIG+FSP welded joint with filler ER 5356

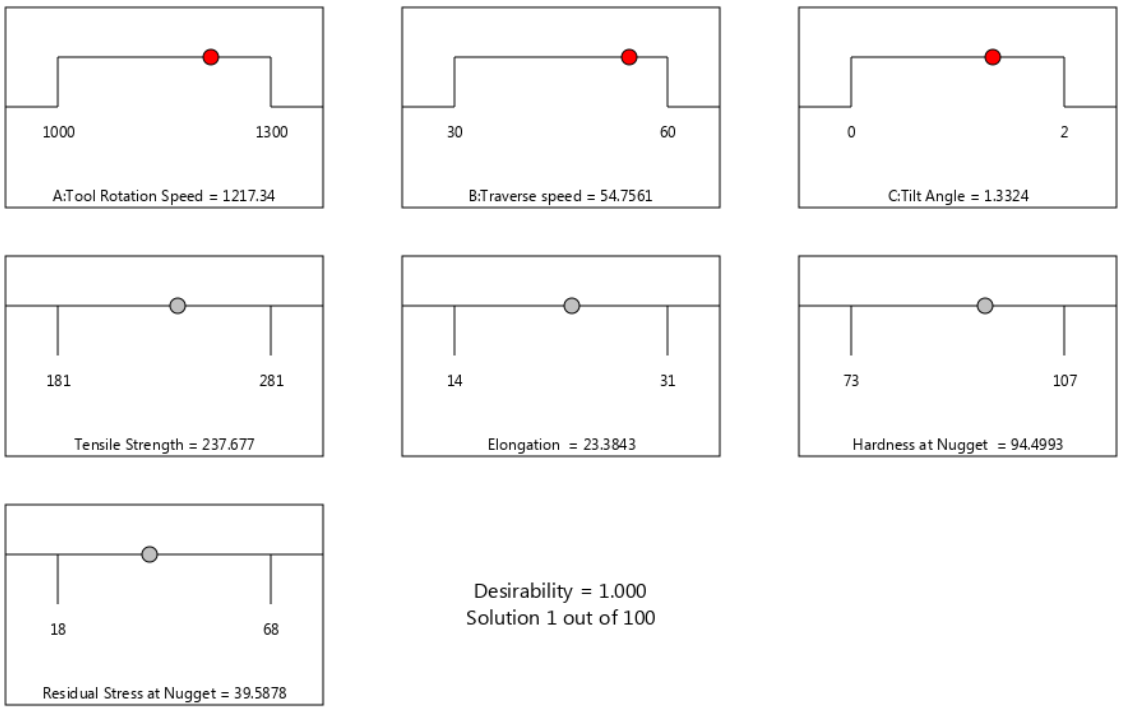

Figure 84: Ramp function graph for input parameter and multi response optimization for TIG+FSP welded joint with filler ER 5356

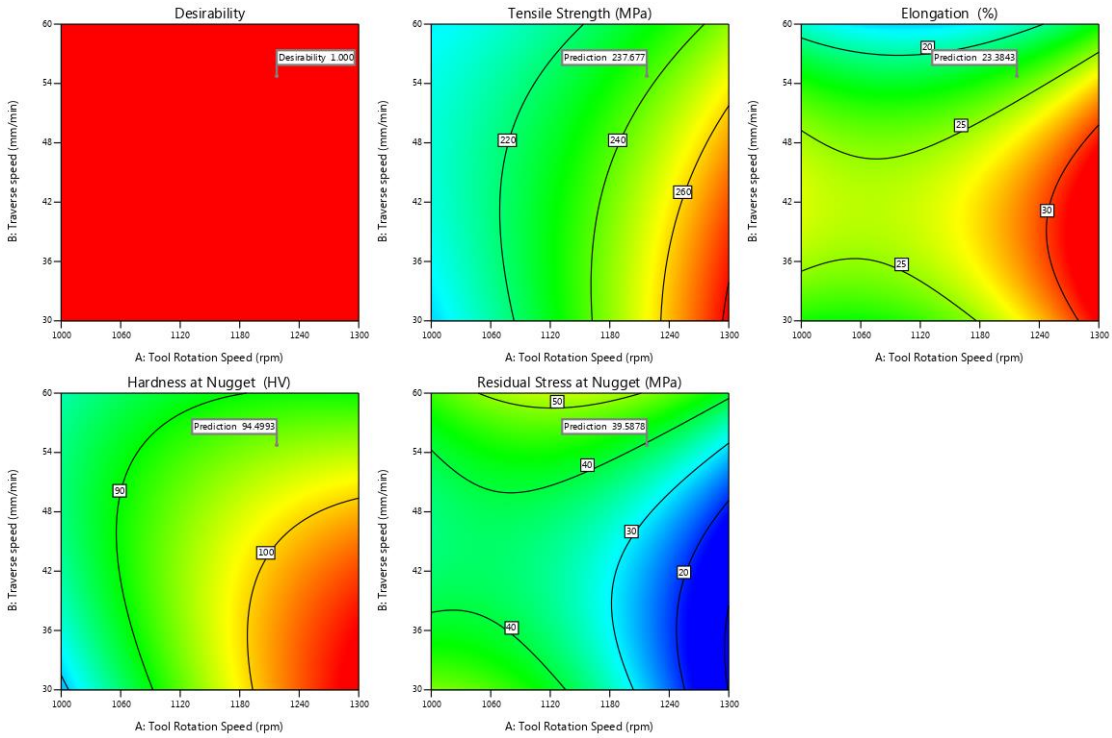

Figure 85: Optimized out responses of TIG+FSP welded joint with filler ER 5356

As the feed rate increases then tensile strength increases. The minimum tensile strength i.e.182 MPa was found at tool rotation speed 1000 rpm, traverse speed 30 mm/min and tilt angle 0º due to inadequate tool stirring action. The maximum tensile strength (281 MPa) was observed at 1300 rpm, 30 mm/min and 2^0, when the feed rate or traverses speed increases, the tensile strength and hardness also increases up to a certain value. Large heat was found in the welded region at lower feed rate. As the feed rate increases, the influences of thermal cycle on the welded joint weakened leading to enhancement in tensile stress and micro-hardness of the welded joints as shown in fig. (80-83). The ramp function graph of multi response optimization as shown in fig. 84. This methodology is used to optimize for more than one objective function. The desirable value is 1 for optimized value of the input processing parameters and responses. The optimized value of tensile strength, percentage elongation, micro-hardness at nugget zone and residual stress at nugget zone are 237.67 MPa, 23.38%, 94.49 HV, and 39.58 MPa, respectively, whereas the optimized value of tool rotational speed, feed rate and tilt angle are 1217.34 rpm, 54.75 mm/min, and 1.33º respectively as shown in fig.84-85.

5.3.7 XRD analysis of TIG and TIG+FSP welded joint with filler ER 5356

The recrystallization and plastic deformation of TIG+FSP welded joints by friction heat and stir action occurred during friction stir welding. These may be lead to change of phase constituents in SZ. Furthermore, three major phases Al_2CuMg, $MgZn_2$, and Mg_2Zn are found in weld nugget zone. These zones give a high strength to welded joint. So, an XRD analysis in the stir zone of the welded joint is quit important. In this work, the XRD analysis of TIG+FSP welded joint of filler ER 4043 and ER 5356 carried out. The XRD results of fusion zone of TIG welded joint and weld nugget zone of TIG+FSP welded joints are shown in fig.86. Magnesium (Mg) and Silicon (Si) elements were found in the weldment besides the aluminum (Al), it is found that Mg and Si created the phase after the precipitation reaction in the weldment. A very high intensity was found from aluminum, because of fragmentation of precipitates the intensity of Mg_2Si was increases after friction stir processing on TIG welded joint with filler ER4043 [129, 132]. The alloying elements such as Si and Mg existing in weld center make precipitation reaction and form a strong precipitate of Mg_2Si to give a higher strength. Same phase of Al_2CuMg was detected in both the nugget zone. Micro-hardness of the TIG+FSP joints are based on boundary energy, brittle intermetallic formation, strain hardening and precipitates formation in the joint.

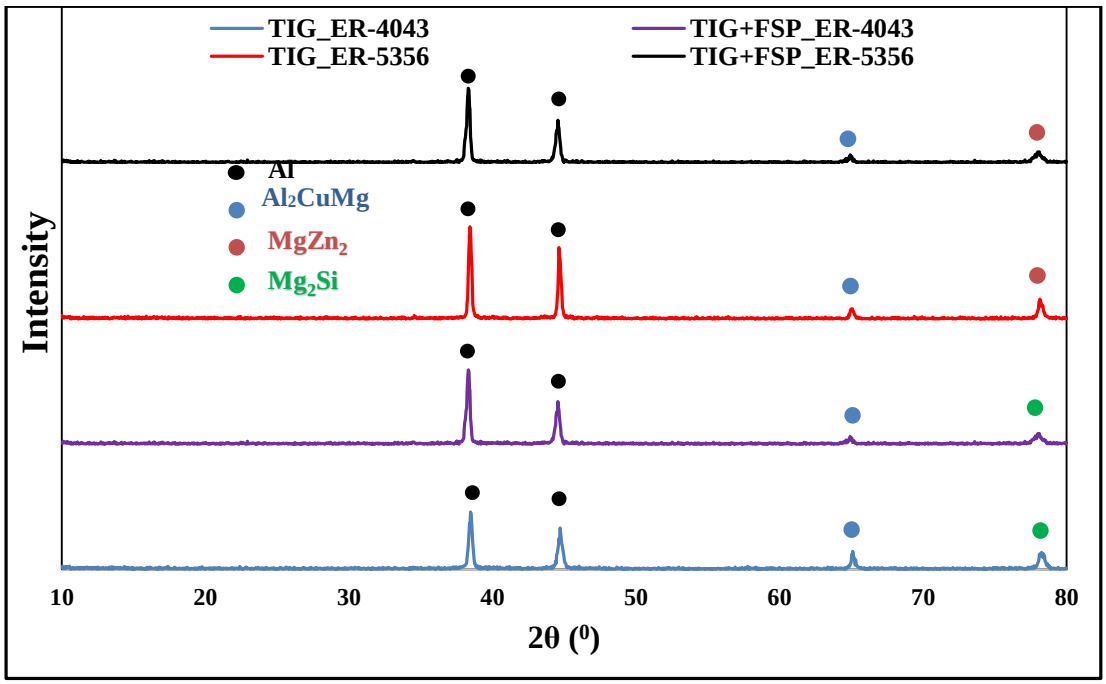

Figure 86: XRD peaks of TIG+FSP welding of filler ER 4043 and ER 5356

Fine recrystallized grains and increase of grain boundaries in the (SZ) of AA6061 and AA7075 joints predict higher micro-hardness. Because of fine precipitates and fine grains structure, the stir zone is associated with plastic deformation and high temperature, due to precipitates formation at high temperature along the grain boundaries. When the rotational speed of tool is less than the 1000 rpm then the worm hole at R.S was observed due to insufficient of metal transportation and insufficient heat generation in TIG+FSP welded joint, whereas when the TRS is higher than the 1300 rpm then the high heat was observed in the NZ, results widen the HAZ and weaken the microstructure bonds. Pin holes defect was observed at traverse speed less than 30 mm/min due excessive heat input per unit length in the weldment. When feed rate is greater than 60 mm/min, the bottom tunnel in the advancing side was perceived due to inadequate flow of material and insufficient heat input in the weldment.

5.3.8 Microstructure Analysis of TIG and TIG+FSP welded joint with filler ER 5356

The microstructure images of TIG and TIG+FSP welded joint of AA 6061 and AA7075 with filler ER 5356 were taken from fusion zone and stir zone respectively with different processing parameters. These were compared to each other on the basic of grain size. Higher magnification was carried out on the samples in order to present each zone clearly. The measurements were taken of the width of the sample cross-section and the center of the height on the weld metal.

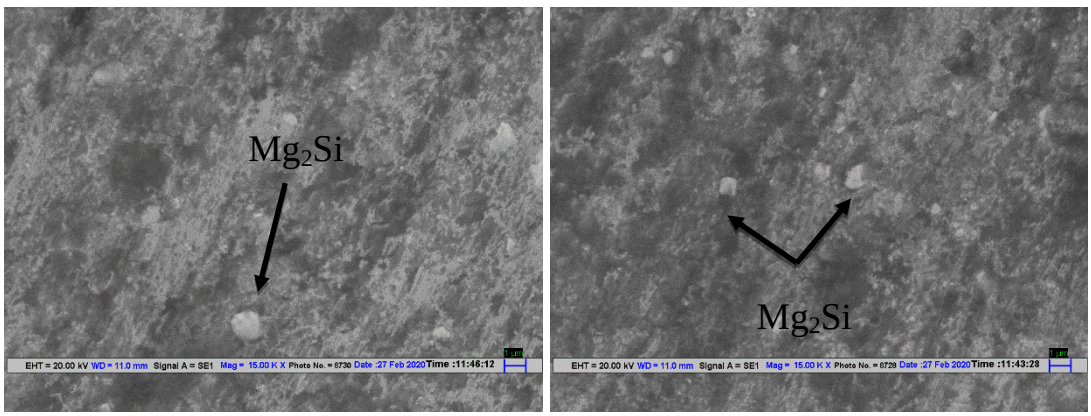

Figure 87: SEM images of TIG welded joint (a) Fusion Zone, (b) HAZ

Fig. 87, shows the precipitate of Mg_2Si compound in Al-matrix. A weld disseminated precipitate of the Mg_2Si intermetallic compound were responsible for improved the mechanical properties of welded joint with filler ER 5356. Fine equiaxed grains were observed in filler ER 5356 which are capable to accommodate contraction strains more easily, it means more ductile columnar grains were observed which may results to enhanced tensile strength. The dispersed precipitates of Mg_2Si intermetallic compound were observed in welded region and coarse equiaxed grains were also observed in fusion zone. The equiaxed grains is absent due to the material close to the fusion line provides plenty of sources for the crystal nucleation of the liquid metal during the TIG welding [130]. Fine grains with small precipitates was reported in heat affected zone (HAZ) as compare to other zone.

The micrograph of TIG+FSP welded joints with filler ER 5356 with different processing parameters as shown in fig. 88 (a-d). The TIG+FSP joint fabricated with 7 mm tool pin diameter, and 6 mm pin length exhibited the presence of fine and equiaxed grains in weld nugget zone. The uniform distribution of fine grains in the weld nugget zone due to adequate softening of material revealed the maximum tensile strength and micro-hardness [133], whereas the coarse grains structure were found the weld nugget zone is due to excess heat and severe plastic deformation, results declined micro-hardness and tensile strength [147].The formation of nugget zone shape in TIG+FSP welded joint is recognized to the maximum deformation and plasticization in the material which shows the fine recrystallized equiaxed grains. The formation of nugget shapes depends on thermal gradient, processing parameters and tools geometry in the work-piece. Therefore, coarse grain structure of TIG welded joint is transformed into the uniform and fine grains structures in the weld nugget zone due to adequate softening of material revealed the maximum tensile strength and micro-hardness of the TIG+FSP welded joint as shown in fig.88. The relationship between heat input and the grain size measured by electron backscatter diffraction (EBSD) in the stir zone [131]. The mean grain size generally decreased with the heat input under the studies conditions. The revealed relationship was characterized by a significant experimental scattering. This deteriorates their predictive ability and therefore require a deeper understanding for the heat input and grain growth. The heat input is directly related to the variation of the welding temperature. The final grain size in the stir zone is depended on the peak welding temperature and weakly on the cooling rate [78].

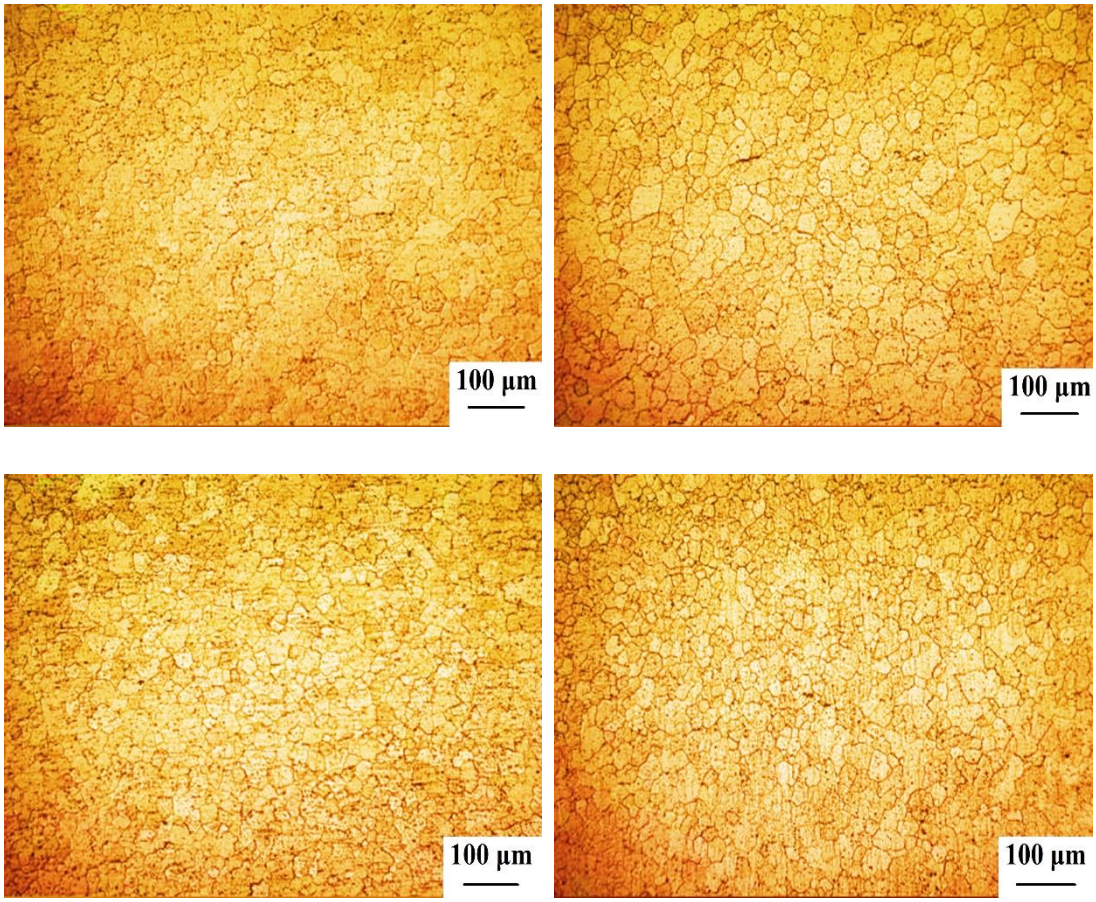

Figure 88: Optical images of TIG+FSP welded joint with filler ER 5356 (a) Sample 1, (b) Sample 4, (c) Sample 14, (d) Sample 20

The grain size of TIG and TIG+FSP weldment were analyzed by the image J software and observed grain size in fusion zone and nugget zone respectively. Fig. 89, shows the effect of FSP processing parameters on TIG welded joint. The average grains size of the TIG+FSP welded joints are finer than the TIG welded joints. It can be concluding that the rotational speed has a significant effect of grain size of the welded joint. When the rotational speed increases, grain size decreases, this observation give the satisfactory amount of assurance with Yupeng Li [148].

The grain size in the heat affected zone varied greatly in shape and size, Due to temperature cycles and plastic deformation, most of the grains were irregularly elongated, while some equiaxed grains smaller than the base metal, which shows the occurrence of partial recrystallization. The grain size in the stir zone was refined equiaxed grains throughout the nugget zone, which was distinctly different to the HAZ and TMAZ. The average minimum grain size i.e. 4.3 µm was observed in

TIG+FSP with filler ER5356 in nugget zone at tool rotational speed 1300 rpm, traverse speed 30 mm/min with tilt angle 2º as shown in fig. 89.

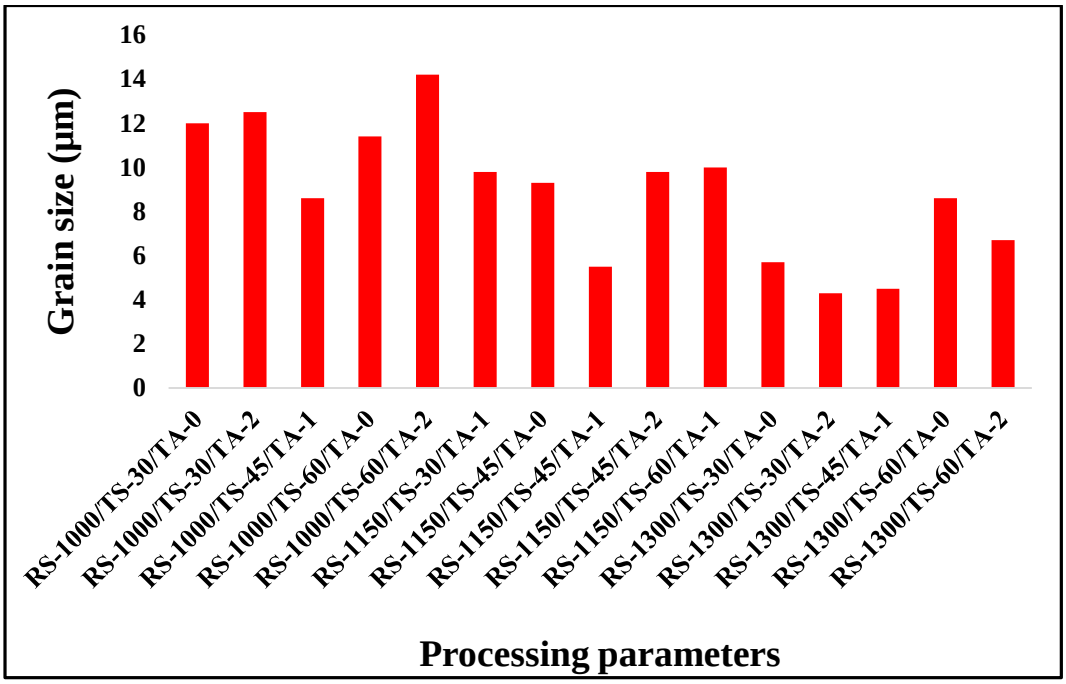

Figure 89: Variation of grain size at the nugget zone to the processing parameters

5.3.9 Fracture Surface analysis

The tensile fractured surfaces were characterized by SEM machine to understand the effect of microstructure on the failure pattern of TIG and TIG+FSP welded joints. The fractured tensile images show the maximum and minimum tensile strength. The minimum tensile strength specimen shows the large and shear dimples, whereas the maximum tensile strength specimen shows the fine and equiaxed dimples. The TIG+FSP welded joint with maximum tensile strength exhibited precipitates of $MgZn_2$ in the weld nugget zone. There is some important observation can be made. All TIG welded specimens are failed at the welded joint whereas most of the TIG+FSP welded joint failed on the advancing side while some specimens were failed at retreating side because fracture was initiated from the interface of TMAZ and stir zone in retreating side. The reasons for such localized fracture behavior explained by the analyzing the texture, grain size and strain localization characteristics in retreating side [135]. The Scanning electron microscope (SEM) fractograph has been taken from

the fractured tensile test specimen of TIG and TIG+FSP welded joint of AA6061 and AA7075 at room temperature as shown in fig.90. The fracture morphology between the TIG and TIG+FSP shows the clear difference that TIG welded portion shows the large and deep dimples whereas TIG+FSP welded portion shows fine and shallow dimples. this is the evdence of crack nuleation and growth 4mm away from the weld line. The small grain particles was found in the TIG+FSP welded zone while big grains was found in TIG welded region.

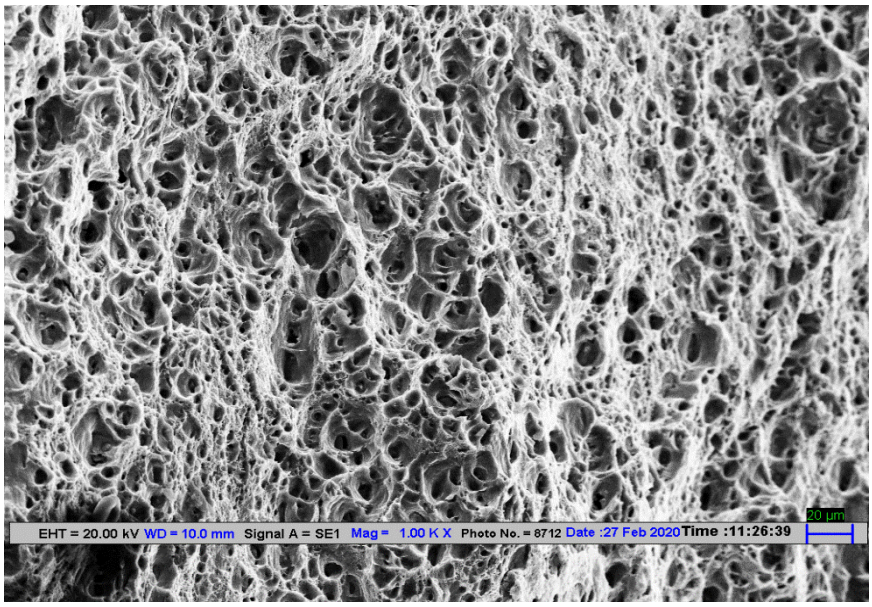

(a)

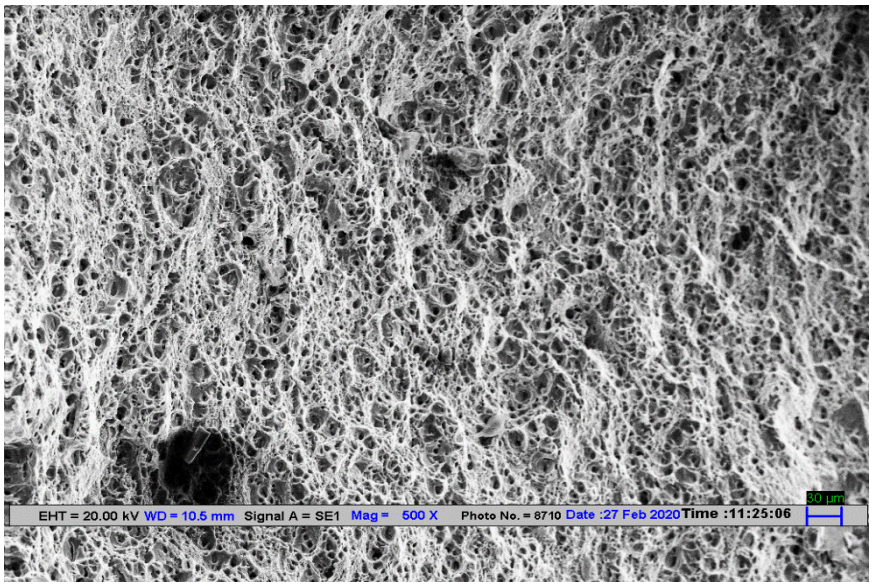

(b)

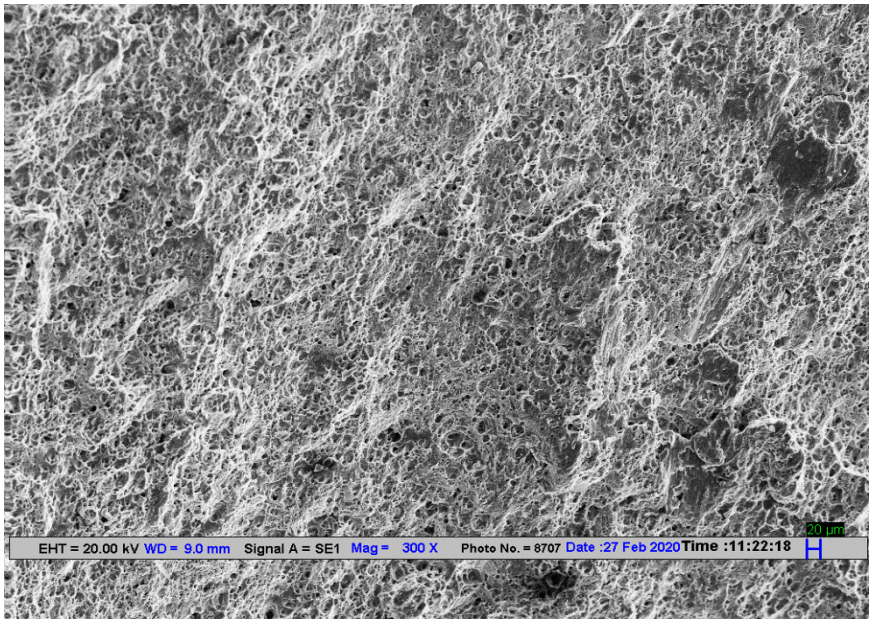

(c)

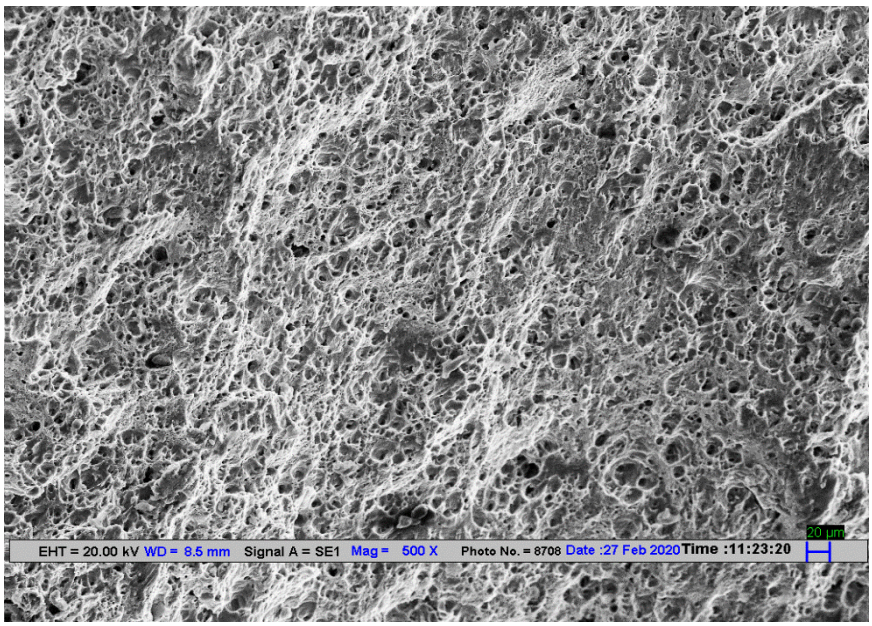

(d)

Figure 90: SEM images of tensile fractured specimen, (a) TIG welded joint with filler ER 4043, (b) TIG+FSP welded joint (sample 4), (c) TIG+FSP welded joint (sample 9), (d) TIG+FSP welded joint (sample 18)

There are some charactertics in the fractured surface of TIG+FSP welded specimens with filler ER 5356, which illustrated both the cleavage and ductile fracture mechanicms. The quasi cleavage is explained this type of fracture mechanism, and is regularly separated characteristic on fracture surface that reveals features of both plastic deformation and cleavage [149].

There are numbers of small and big silicon particles are observed in both fractured specimens. Because of formation and consequent growth and coalescence of cavity or voids, the ductile fracture of welded joint occurs, an improvement in ductility may be achieved when the cavity nucleation could be suppressed [120]. The maximum interfacial normal stress is depending upon the grain particle size and the volume fraction of the grain particles [121]. The coalescence of micro-voids result in equiaxed dimples on tensile fracture surface normal to the loading axis. Hence, the equiaxed and spherical dimples on a flat crater bottom loaded in tension and elongated ellipsoidal dimples on the shear lips oriented at 45^0. The fractured images of welded joint confirmed the higher elongation of the welded joints at higher input, which shows more fine dimples and fewer facets as compare to that joints welded at lower heat input conditions [150]. SEM fractograph of the fractured tensile test specimen shows the size and distribution of large void and cavity of different TIG+FSP welded joint. The fractured surfaces are characterized by ductile dimple and some area of large void as shown in fig. 90. The fine dimple percentage increases by the variation of process parameters of TIG+FSP welded joint. The cavity formation occurred due to precipitate coarsening that layer coalesce led to the shear rupture.

5.3.10 Model Validation

To confidently use CFD results for investigating the TIG+FSP process, the CFD model has to be correctly defined and a thorough validation has to be achieved. The model was first applied to simulate the experimental work on friction stir welded joint of Al-alloy 6061 carried out by Hwang el al [151]. The experimental temperatures were measured by thermocouple units placed equally at a distance of 5 mm, along the traverse direction of the rotating tool. The tool rotational speed and traverse speed, was 920 rpm and 20 mm/min respectively. The present simulation result was validated by this experimental results which gives the satisfactory amount of assurance in the fidelity of the simulation of welded joints as shown in table 31.

Table 31: Validation of temperature variation of FSWed joint of AA6061 [151]

Author	Rotation speed (rpm)	Traverse speed (mm/min)	Maximum temperature (ºC)
Present result	920	20	398
Hwang et al [154]	920	20	386

5.3.11 Temperature variation in TIG+FSP process

The experimental temperature results of TIG+FSP measured by thermocouples. The advancing side temperatures in the transverse direction are A_1, A_2, A_3, and A_4 and the retreating side has R_1, R_2, R_3, and R_4. The peak temperature of advancing side is marginally higher than the retreating side [152-153]. The temperature of FSP tool is symmetric about the tool axis. The high temperature in the vicinity of the welding tool is attributed to the localized heat generation. During the TIG+FSP process, the temperature of the base plate around the welding tool is around the 765K. It is still lower than the melting point of AA6061 and AA7075. When the position weld bead is far away from the FSP tool, the temperature drops quickly as shown in fig. 92(a-b). Fig.91 shows the temperature distribution plot for TIG+FSP welding at 160 s. During this simulation, eight points were observed to obtain the temperature-time curves which can be compared with the experimental results. The area around the FSP tool reached the maximum temperature. The maximum temperature was observed 760K at the advancing side whereas minimum temperature was observed 307K at the retreating side. Higher heat is generated in the SZ at high tool rotation, the prevailing thermal conditions are controlled by the distribution and availability of precipitates in the matrix. Fig. 93 shows the temperature variation profile on the mid-section of the top surface of (TIG+FSP) welded joint with different processing parameters. The region where its peak temperature is higher almost 450º C in (TIG+FSP) of AA6061 and AA7075 aluminum alloy at tool rotational speed of 1600 rpm. The heat is transmitted to the aluminum alloy which is preheated during tool rotation. The initial heating was predicted as the monitoring thermal contour of the rotating tool. When the rotating tool moves on the monitoring location, the temperature contour leads to slow cooling. Due to the relation between tool pin rotation and material flow, the higher shearing rate was observed at (A.S). Thus the temperature of (RS) is slightly lower than the (AS), while almost the symmetric temperature was observed at the bottom of the welded joint.

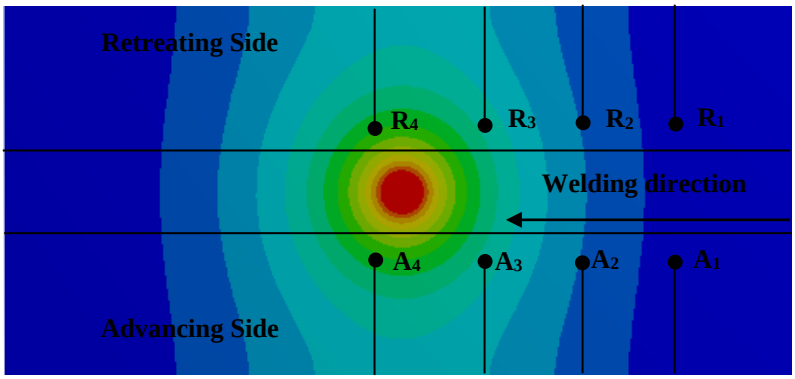

Figure 91: Temperature contour of TIG+FSP at 160 s

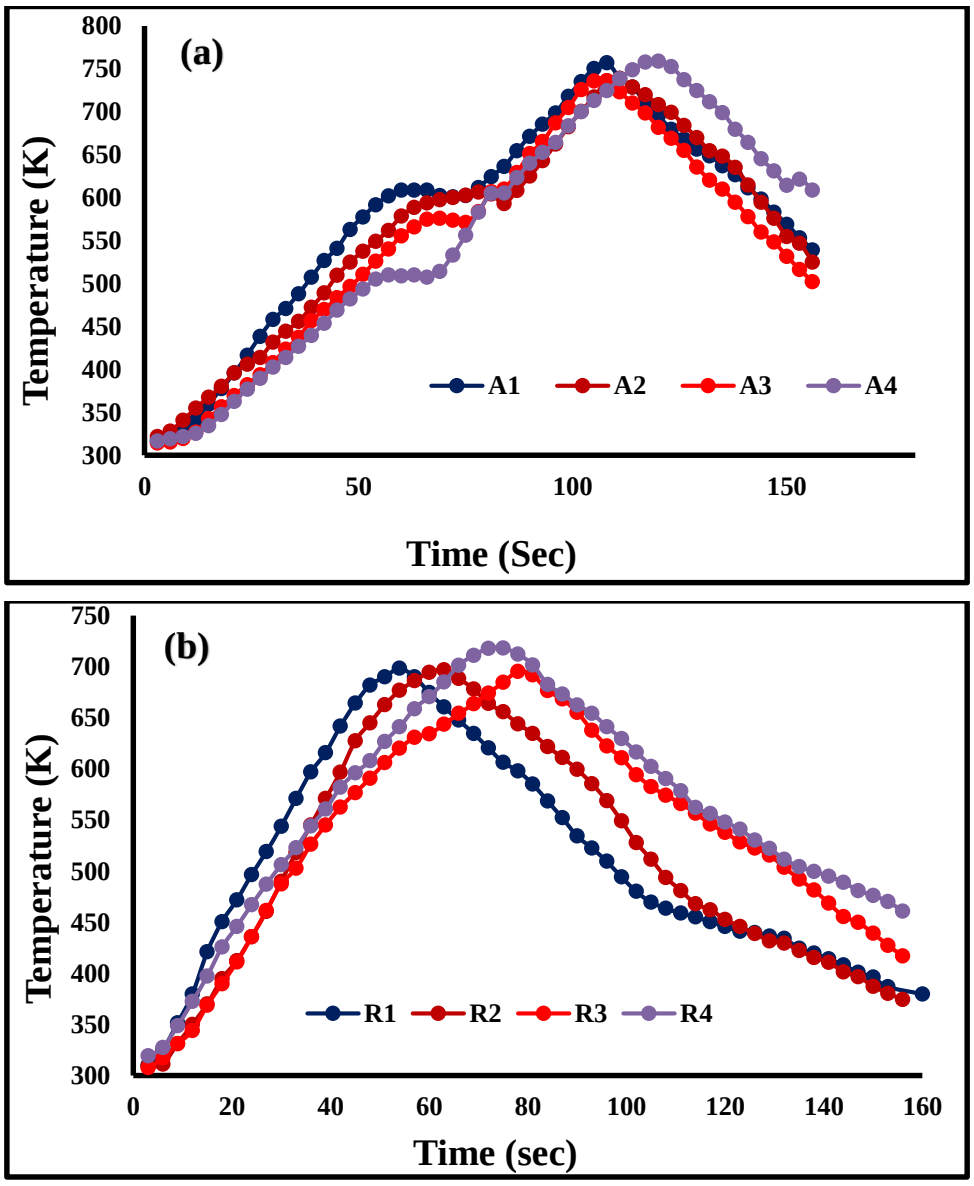

Figure 92: Variation of temperature during TIG+FSP welding: (a) Advancing side, (b) Retreating side

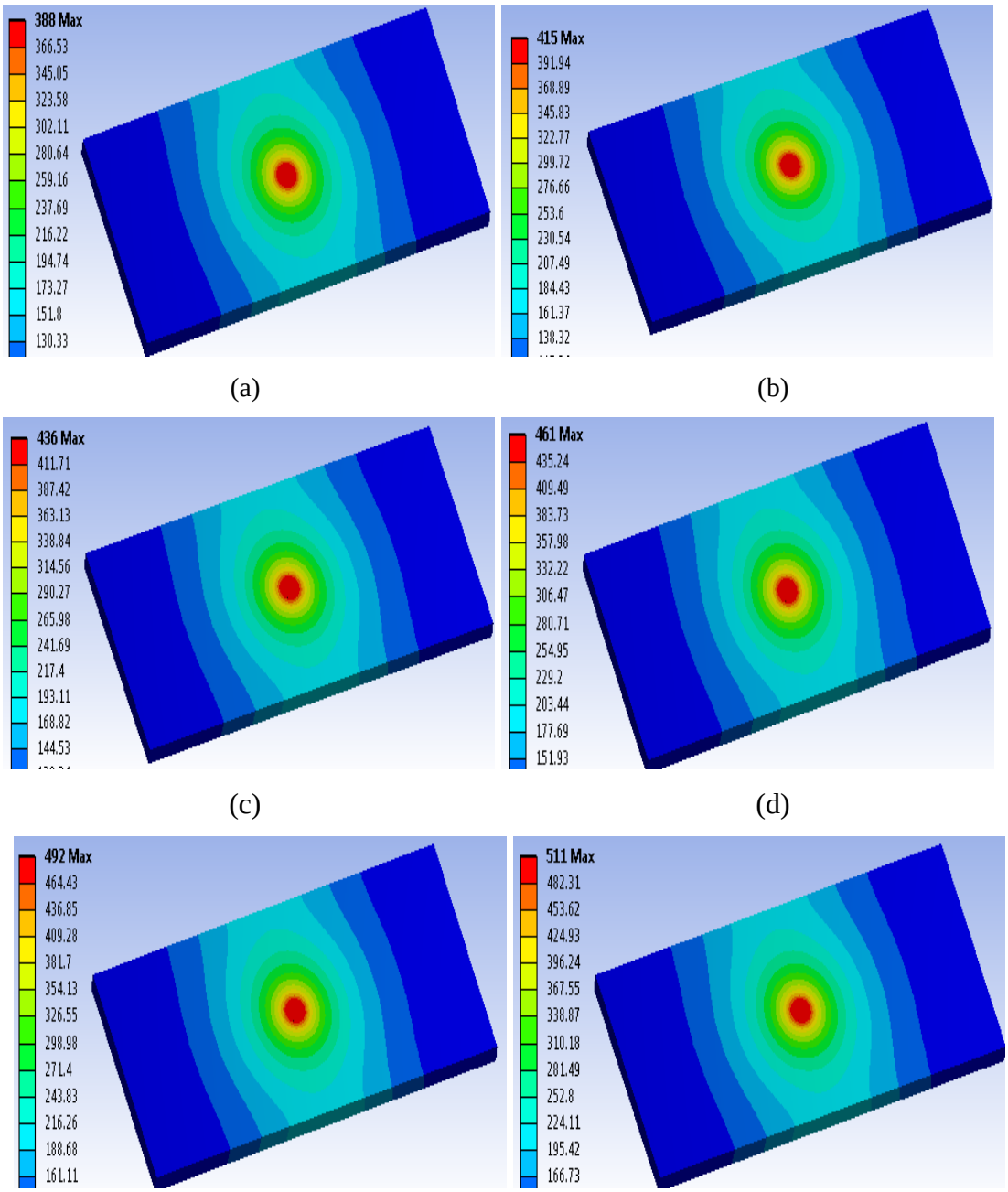

Figure 93: Temperature distribution at the center of the TIG+FSP welded joint, (a) 800 rpm, (b) 1000 rpm, (c) 1100 rpm (d) 1150 rpm, (e) 1200 rpm, (f) 1300 rpm

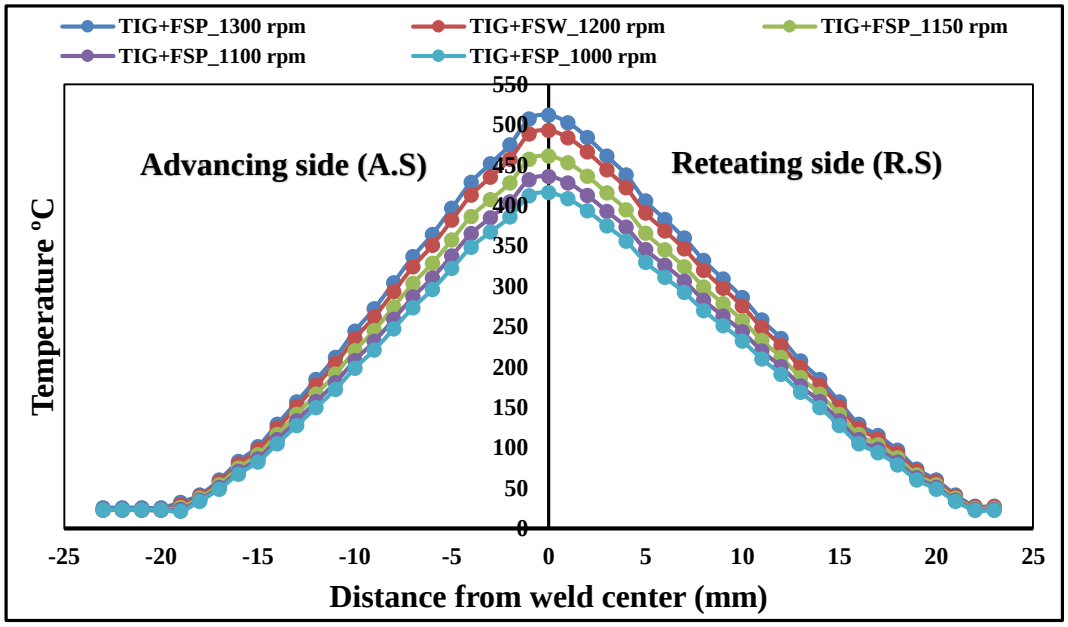

Figure 94: Variation of temperature distribution at different processing parameters of TIG+FSP welded joint

Table 32: Heat generation at various processing parameters of TIG+FSP welded joint

Rotation speed (rpm)	Traverse speed (mm/min)	Maximum temperature (°C)	Maximum Heat Flux W/m^2 (10^6)
1000	44	415	4.11
1100		436	4.421
1150		461	4.72
1200		492	5.02
1300		511	5.33

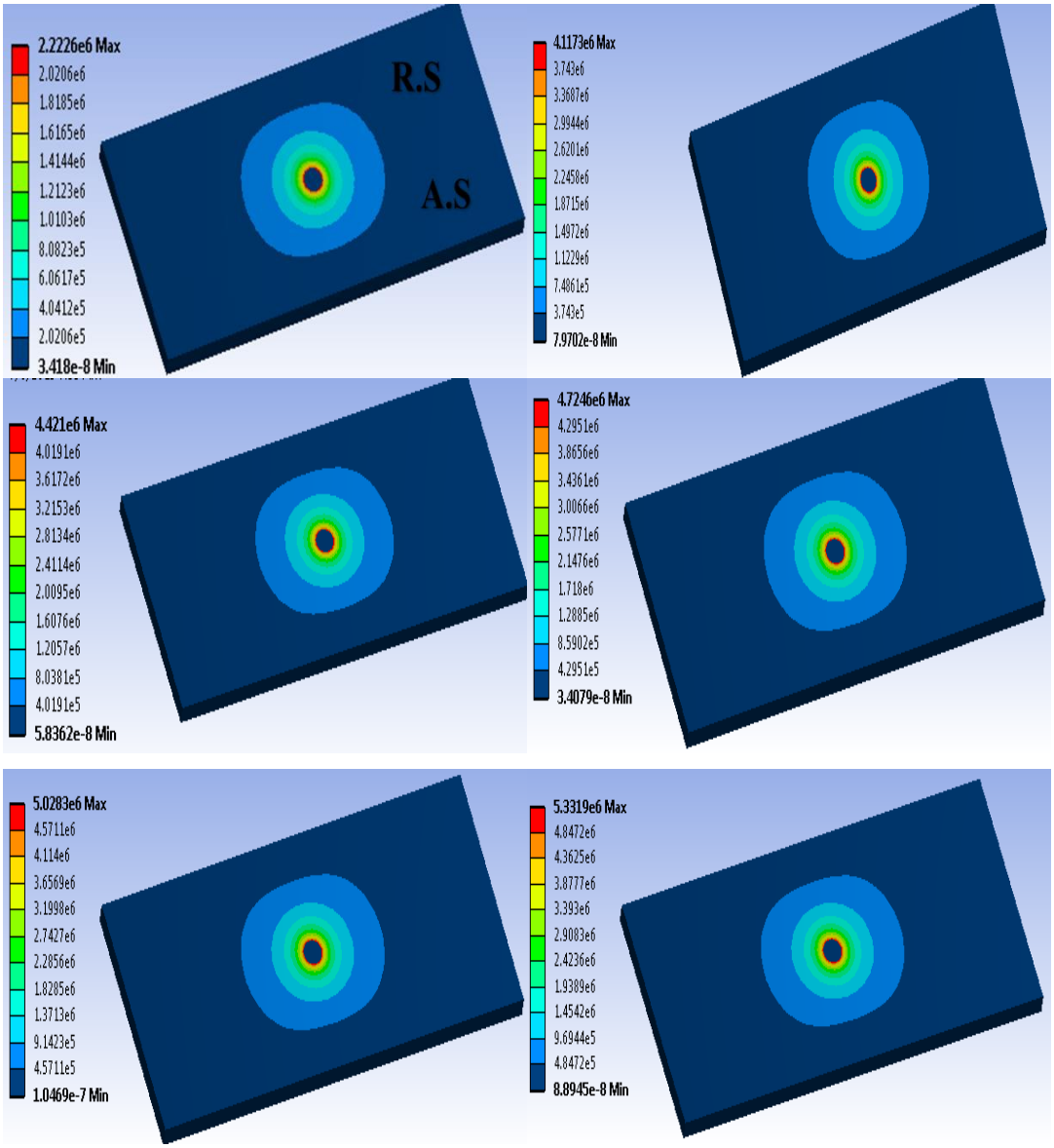

Figure 95: The heat flux at the center of TIG+FSP welded joint, (a) 800 rpm, (b) 1000 rpm, (c) 1100 rpm, (d) 1150 rpm, (e) 1200 rpm, (f) 1300 rpm

The estimated maximum temperature about 515º C was calculated in the stir zone of the TIG+FSP welded joint at tool rotation of 1600 rpm whereas 408º C was calculated in the stir zone at 800 rpm. The temperature and heat flux distribution with different processing parameters are shown in fig.95. In general, the temperature values at the (A.S) about 10-25º C greater than the (R.S), When the tool approaches the target location then there is a rapid change in the temperature, while the slower cooling rate was observed when the tool moves away from the target location [154]. The variation of heat flux at the tool workpiece interface is shown in fig. 95. It was observed that the heat flux is directly proportional to the tool rotational speed. The maximum heat

flux about 5.33 x 10^6 w/m^2 was obtained in the SZ at 1600 rpm, whereas minimum heat flux was obtained at 1000 rpm. The non-uniformity was observed in the heat flux pattern at different processing parameters of the tool, because the rapid recirculation of plasticized material, the heat flux rate does not lead to the variation of local temperature.

5.4 Mechanical properties of friction stir welded joint of AA6061 and AA7075

5.4.1 Tensile strength of FSWed joint

The tensile strength of friction stir welded joint of dissimilar Al-alloys of AA7075 and AA6061 was observed at tool rotational speed of 1300 pm, traverse speed of 30 mm/min with tilt angle 2°. The tensile specimens were fractured in thermo-mechanically affected zone (TMAZ) where the hardness was located as a minimum. In other dissimilar aluminum alloys, the FSW joints were failed at the location of the HAZ [138]. The tensile stress of FSWed joints was lower than the parent material. The tensile stress of the FSWed joints has a tendency to increase with the precipitation hardening of the parent metal. The strength and ductility of defect-free welded joints are dependent on the thermal properties of base metal [155-156]. The coarse grains precipitates within the grains boundary was observed due to dissolution of the fine precipitates during FSW process which influence the tensile properties of the weldments. The percentage elongation and ductility of the weldment were lower than those of the parent material [143]. If the welded joints are free from defects, then the tensile strength of the weldments is only dependent on the hardness of the FSW joints [157]. The stress-strain curve of the FSWed joint as shown in fig. 96. The average tensile strength of FSWed of AA6061 and AA7075 was observed as 221.3 MPa. It was observed that the tensile properties of the FSWed joints are highly affected by tool rotational speed [158]. As the tool rotational speed increased, the tensile strength also increased. At lower tool rotational speed, the heat was generated at the SZ which inadequate to strain the plasticized metal that occurred in inferior consolidation of the metal which deteriorated the mechanical properties of the FSWed joints. Therefore, the optimized tool rotational speed was necessary to generate frictional heat as it fabricated defect free joints by adequate straining of plasticized metal with recrystallized grains [159]. The higher tool rotational speed influence the

straining rate of the plasticized metal caused the change in the precipitation and grain size in the SZ [160].

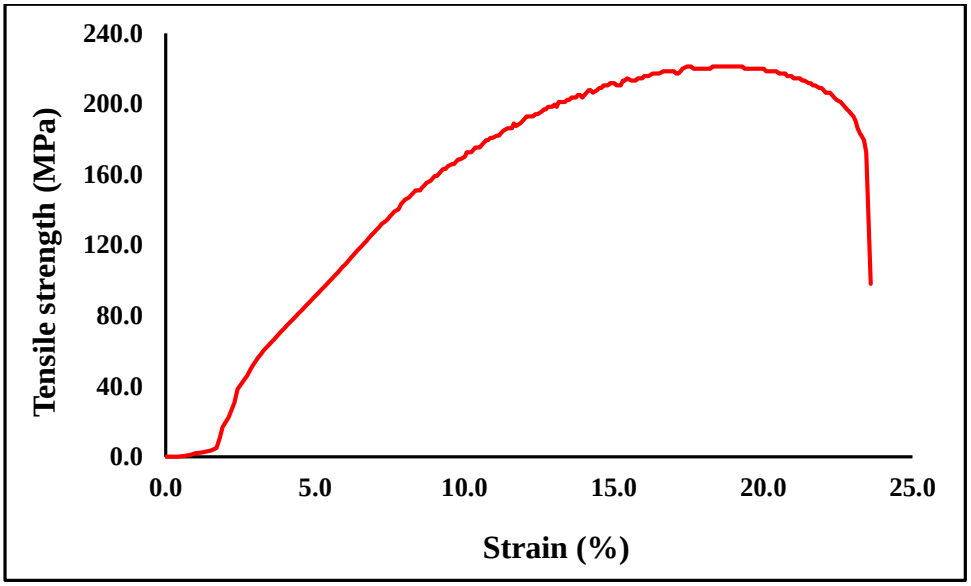

Figure 96: Stress strain diagram of friction stir welded joint of AA6061 and AA7075

5.4.2 Microhardness of FSWed joint

Fig. 97 shows the microhardness distribution of FSWed joint of AA6061 and AA7075. The average hardness value from the HAZ and fusion zone were slightly different at base metal of AA7075 and AA6061. The microhardness of SZ was slightly higher as compare to TMAZ and HAZ which was attributed to small grain size. The decreasing trend of micro-hardness in TMAZ is due to the dissolution of precipitates and lower hardness was pronounced in the HAZ due to the coarsening of precipitates [161]. The slightly low hardness was observed in HAZ due to the coarsening of strengthening precipitates and desertion of the Guinier-Preston (G.P) zones. More probably comprehensive severe coarsening and dissolution of precipitates occurred in TMAZ due to the analogous effect of solution treatment. The material experienced higher temperatures in the nugget zone due to re-precipitation after complete dissolution takes place. When the AA6061 was positioned on the A.S and low tool rotational speed was used then the transition of micro-hardness in the SZ from aluminum alloy 6061 to 7075 was more gradual and observed more effective material mixing The minimum hardness was observed in the HAZ from the AA6061

side. The microhardness directly affects the phase dispersion microstructure and dislocation density. In the conventional friction stir welding process, inducing high heat input and thermal cycle cause grain growth and roughen the microstructure of the SZ. The microhardness variation plays a significant role to detect the metallurgical phase in the welded region. Due to the cooling rate and solidification sequence, the micro-hardness and grain size were detecting the major effect at the bottom and middle of the welded joint.

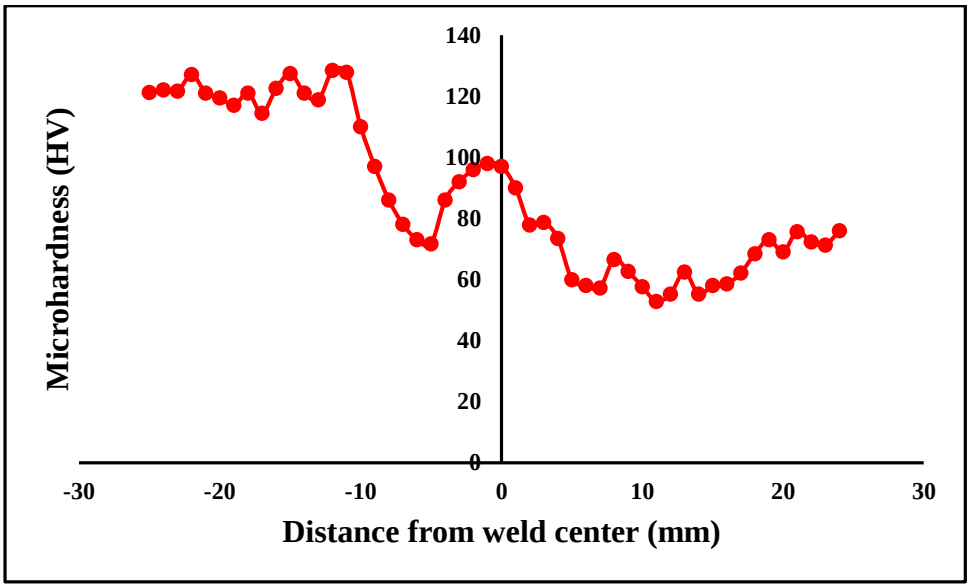

Figure 97: Microhardness distribution of FSWed joint AA6061 and AA7075

5.4.3 Optical microstructure of FSWed joint

The macroscopic advents of the cross-section of 12 mm weld as shown in fig. 98, the TIG-welded joints are known to have defects such as porosity, large grain structure, micro crack, and insufficient consolidation of material in the fusion zone. However, FSW has reduced almost all these defects, based on the microstructural characterization of grains boundary, three different zones have identified in the FSWed joint, i.e. SZ, TMAZ, and HAZ. The banding pattern was appearing in SZ from the retreating side (RS), and this band geometry was observed at high tool rotational speed. The grains structure very small in the band pattern. The same result was also reported by past investigation [162]. The SZ was characterized by equiaxed and fine grains structure because of dynamic recrystallization (DRX) on in divergence to the base metal microstructure. The DRX occurs in the SZ due to high thermal

exposure and strain during the FSP. The degree of heat input and material deformation are both decreased when welding speed increased at constant tool rotational speed.

Figure 98: Macrostructure of the TIG+FSP welded joint of AA6061 and AA7075

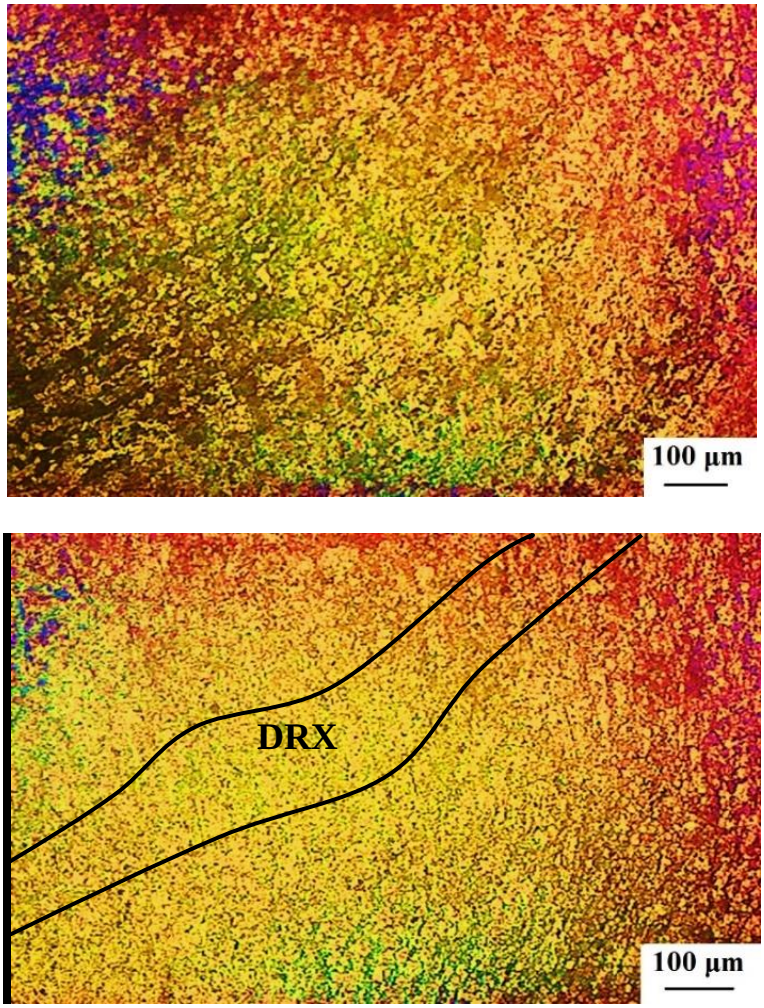

Figure 99: Optical microstructure of FSWed joint, (a) TMAZ (b) Stir zone

The superior weld quality was observed when the FSW tool rotates on base plates AA6061 and AA7075, the AA7075 was placed on the RS and AA6061 was placed on AS. In the friction stir welding the frictional heat under the tool shoulder gives the

higher temperature because the material flow around the rotating tool was moved from the AS to the RS so, the temperature of the materials on the AS was higher than the RS [26]. Due to the precipitation of Mg_2Si, the rate of dissolution on the AS was greater than that on RS during welding. When the stirring probe was moved away from the welding plate, the driving force for re-precipitation increases, and the temperature decreases which leads to a lower equilibrium volume fraction, and the atomic mobility of Mg_2Si particles was not reached in the SZ. The tool rotational speed promotes the dissolution of grains during stirring and observed that the precipitates may be fragmented dissolved completely at higher tool rotational speed [163]. The grains size in the stir zone in FSW welded were much finer than grains size in the fusion of TIG welded joint. The grain size in the stir zone at high tool rotational speed (1300 rpm) was observed from 14-18 µm observed by image J software. This could be explained since the materials in the dynamic recrystallization (DRX) were exposure to a lower temperature than materials in the stir zone far away from the TMAZ. The grain growth rate and the migration velocity of grain boundaries can be decreases at lower temperatures and this lower temperature of the DRX region refine the particles of the Mg_2Si precipitate. The temperature distribution during FSW is asymmetric throughout the weldment, where AS side temperature was higher than the RS side [54]. Due to dynamic recrystallization (DRX), the stir zone was characterized by fine and equiaxed grains structure as shown in fig. 99.

5.4.4 Fracture surface morphology

The fractured surface morphology of tensile test specimens for FSWed has been investigated is shown in fig. 100. The fractured surface was distinguished by the SEM machine to comprehend the influence of the microstructure of the failure pattern of the welded joint. The FSW fractured surface shows the tiny and equiaxed dimples with micro voids, which shows the ductile fracture. The FSWed joints were failed at TMAZ because the fracture was commenced from the interface of HAZ and TMAZ in the R.S, this type of fracture behavior was also explained by the analyzing the strain localization, grain size characteristics, and texture in the R.S [164]. The FSWed fractures illustrate agglomerative and microporous ductile fractures. The microstructure of base metal (AA6061 and AA7075) is uniform and finer than TIG and TIG+FSP welded joints., and it was also observed from the fracture morphology

that the size of the dimples of both the welded joints are larger than the base metal, because of this reason, the tensile strength of the base metal is much higher than the both welded joints. The quasi cleavage with ductile fracture was observed in FSWed joint and it was regularly separated characteristic on the fracture surface that reveals features of both cleavage and plastic deformation [150].

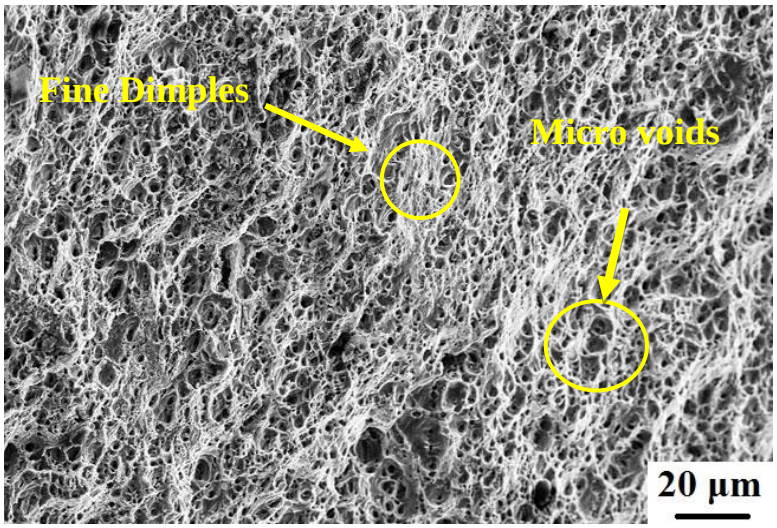

Figure 100: Fractured surface morphology of FSWed joint

5.5 % improvement of FSW and TIG+FSP welded joint as compare to TIG welded joint

The percentage improvement of tensile strength of FSWed joint and TIG+FSP welded joint with filler ER 4043 and ER5356 as shown in table 33-34. The friction stir processed of TIG welded joint with filler ER4043 having tool rotational speed 1300 rpm, traverse speed 45 mm/min and tilt angle 1° showed maximum % improvement of 60.78%, whereas 59.48% improvement was observed in TIG+FSP welded joint with filler ER5356 at tool rotational speed of 1300 rpm, traverse speed of 30 mm/min with tilt angle 2°.

The percentage improvement in tensile strength of friction stir welded joint was observed as 25.59% which was very less as compare to TIG+FSP welded joint.

Table 33: % Improvement of FSW and TIG+FSP welded joint with filler ER 4043 as compare to TIG welded joint

% Improvement							
Process	A: Tool Rotation Speed (rpm)	B:Traverse Speed (mm/min)	C:Tilt angle (degree)	Tensile strength	Strain	Hardness	Residual stress
FSW joint	1300	30	2	25.59	7.76	31.08	55.38
TIG+FSP	1150	45	2	35.56	16.92	30.3	37.66
	1300	30	2	38.71	19.4	37.88	64.94
	1150	45	1	45.65	25.87	46.97	49.35
	1000	60	0	15.38	-0.5	15.15	28.57
	1000	45	1	43.76	24.38	42.42	45.45
	1150	45	1	46.28	26.37	48.48	55.84
	1000	30	0	31.78	12.44	34.85	18.18
	1000	60	2	24.21	7.46	18.18	6.49
	1150	45	1	46.91	26.87	53.03	49.35
	1150	60	1	31.78	14.43	34.85	29.87
	1300	60	0	48.8	29.35	40.91	46.75
	1150	45	1	43.76	24.38	48.48	49.35
	1150	45	1	46.28	26.87	50	48.05
	1150	45	0	39.34	20.9	37.88	44.16
	1300	60	2	41.24	22.39	37.88	36.36
	1000	30	2	26.73	9.45	33.33	15.58
	1150	30	1	34.93	16.92	43.94	36.36
	1300	45	1	60.78	43.28	59.09	63.64
	1300	30	0	45.65	26.37	53.03	58.44
	1150	45	1	43.76	24.38	50	49.35

Table 34: % Improvement of FSW and TIG+FSP welded joint with filler ER 5356 as compare to TIG welded joint

% Improvement							
Process	A: Tool Rotation Speed (rpm)	B:Traverse Speed (mm/min)	C:Tilt angle (degree)	Tensile strength	Strain	Hardness	Residual stress
FSW joint	1300	30	2	25.59	7.76	31.08	55.38
TIG+FSP	1150	45	2	28.26	5.02	22.97	6.35
	1300	30	0	44.72	18.72	29.73	61.9
	1150	45	0	28.83	14.16	27.03	38.1
	1000	30	0	8.97	-4.11	2.7	17.46
	1150	45	1	37.34	23.29	31.08	63.49
	1000	60	2	2.72	-36.07	-1.35	-7.94
	1300	45	1	52.67	41.55	40.54	69.84
	1150	45	1	33.37	18.72	31.08	61.9
	1150	45	1	35.07	27.85	35.14	55.56
	1300	60	0	44.15	-4.11	18.92	28.57
	1150	45	1	33.94	18.72	33.78	50.79
	1000	60	0	29.4	-4.11	25.68	44.44
	1150	30	1	35.64	9.59	29.73	34.92
	1150	45	1	33.94	18.72	32.43	49.21
	1000	45	1	22.02	27.85	17.57	44.44
	1300	60	2	29.4	-8.68	13.51	14.29
	1150	60	1	25.99	-13.24	24.32	17.46
	1000	30	2	8.4	-8.68	2.7	3.08
	1150	45	1	33.94	18.72	27.03	55.56
	1300	30	2	59.48	41.55	44.59	71.43

CHAPTER-6

Conclusions

6 Conclusions and future work

6.1 Conclusions

The present investigation has been carried out to assess the influences of friction stir processing on TIG welded joints to observed the optimum combination of parameters to attain better mechanical and metallurgical properties of pulse TIG and TIG+FSP welded joints of dissimilar aluminium alloys AA6061 and AA7075. From this study following conclusions can be obtained.

- The tensile strength, micro-hardness and residual stress of friction stir welded joint was observed 221.3 MPa, 97 HV and 29 MPa respectively at tool rotational speed of 1300 rpm, traverse speed of 30 mm/min with tilt angle 2^0.
- To increases the tool rotational speed and decrease the feed rate, leads to increases in heat input in TIG+FSP welded joint.
- The tensile strength of TIG welded joints with filler ER4043 and ER5356 was observed 158.6 MPa and 176.2 MPa respectively.
- The residual stress of TIG welded joints with filler ER4043 and ER5356 was observed 77 MPa and 63 MPa respectively
- The maximum tensile strength (255 MPa), microhardness (105 HV) and minimum residual stress (28.3 MPa) for TIG+FSP welded joints were observed at tool rotational speed of 1300 rpm, traverse speed of 45 mm/min with tilt angle 1 with filler ER4043.
- The maximum tensile strength (281.1 MPa), microhardness (107.1 HV) and minimum residual stress (18.3 MPa) for TIG+FSP welded joints were observed at tool rotational speed of 1300 rpm, traverse speed of 30 mm/min with tilt angle 2 with filler ER5356.
- The empirical relationships were developed to analyze the tensile strength, % strain, residual stress and microhardness of TIG+FSP welded joint of AA6061 and AA7075 at 95% confidence level.
- Optimized value of tensile stress, percentage strain, microhardness at nugget zone and residual stress at nugget zone are 218.82 MPa, 24.15, 90.21 HV and 45.19 MPa respectively, whereas the optimized processing parameters i.e. tool rotational speed, feed rate and tilt angle are 1076.24 rpm, 37.76 mm/min and 1.73^0 respectively for filler ER 4043.

- Optimized value of tensile stress, percentage strain, microhardness at nugget zone and residual stress at nugget zone are 266.66 MPa, 29.74, 103.19 HV and 21.66 MPa respectively, whereas the optimized processing parameters i.e. tool rotational speed, feed rate and tilt angle are 1278.12 rpm, 35.95 mm/min and 1.75^0 respectively for filler ER 5356.
- The predicted peak values of temperature at the weld region were calculated by the ANSYS software and found the maximum temperature about 515ºC at tool rotation of 1300 rpm.
- The grains in the nugget zone in TIG+FSP welded joint was observed much finer than the TIG welded joint at fusion zone.
- The large dimples and quasi cleavage with a sharp edge and various depths were found on the fractured tensile specimen surface of low tool rotational speed whereas fine dimples were found at high tool rotational speed of TIG+FSP welded joints.
- The friction stir processing of TIG welded joint with filler ER4043 having tool rotational speed 1300 rpm, traverse speed 45 mm/min and tilt angle 1° showed maximum % improvement of 60.78%, whereas 59.48% improvement in tensile strength was observed in TIG+FSP welded joint with filler ER5356 at tool rotational speed of 1300 rpm, traverse speed of 30 mm/min with tilt angle 2°.
- The percentage improvement in tensile strength of friction stir welded joint was observed as 25.59% which was very less as compare to TIG+FSP welded joint.

6.2 Scope of future work

The present experimental work has been carried out to assess the influences of friction stir processing on TIG welded joints to improve the microstructure and mechanical properties of TIG welded joints and observed the optimum combination of input and output responses of TIG+FSP welded joints of dissimilar aluminium alloys AA6061 and AA7075. It is recommended that the following future work should be done.

- Influence of friction stir processing on Metal Inert Gas (MIG) welded joints to improve the microstructure and mechanical properties of MIG welded joint.
- In this work, only threaded cylindrical pin profile is used to improve the mechanical properties of TIG welded joints, different pins profile can be used to improve the welded joint strength.
- Friction stir processing can be done after achieving the high depth and good penetration of TIG welded joints to optimize the processing parameters of TIG welding i.e. current, voltage, welding speed and gas flow rate.
- The friction stir welding can be done with friction surface cladding using consumable FSW tool.

List of publications

1. Husain Mehdi, R.S Mishra (2016), Mechanical Properties and Microstructure Studies in Friction Stir Welding (FSW)Joints of Dissimilar Alloy-A Review, Journal of Achievements of Materials and Manufacturing Engineering **(Scopus)**, ISSN: 1734-8412, vol-77, issue1, pp 31-40.
2. Husain Mehdi, R.S. Mishra (2019), Analysis of Material Flow and Heat Transfer in Reverse Dual Rotation Friction Stir Welding: A Review, International Journal of Steel Structure **(Springer)** (SCI), ISSN: 2093-6311, vol-19, issue-2, pp 422-434.
3. Husain Mehdi, R.S. Mishra (2019), Study of the influence of friction stir processing on tungsten inert gas welding of different aluminum alloy, SN Applied Sciences **(Springer)**, ISSN: 2523-3971, vol-1, issue-7, 712.
4. Husain Mehdi, R.S. Mishra (2020), Investigation of mechanical properties and heat transfer of welded joint of AA6061 and AA7075 using TIG+FSP welding approach, Journal of Advanced Joining Processes **(Elsevier)**, ISSN: 2666-3309, vol-1, issue-1, 100003.
5. Husain Mehdi, R.S. Mishra (2020), Effect of Friction Stir Processing on Microstructure and Mechanical Properties of TIG Welded Joint of AA6061 and AA7075, Metallography, Microstructure, and Analysis **(Springer)**, vol-9, pp 403-418. DOI: https://doi.org/10.1007/s13632-020-00640-7.
6. Husain Mehdi, R.S. Mishra (2020), Effect of friction stir processing on mechanical properties and heat transfer of TIG-welded joint of AA6061 and AA7075, Defence Technology **(Elsevier) (I.F- 1.26)**, ISSN: 2214-9147, DOI: https://doi.org/10.1016/j.dt.2020.04.014.
7. Husain Mehdi, R.S. Mishra (2020), Influence of friction stir processing on weld temperature distribution and mechanical properties of TIG welded joint of AA6061 and AA7075 Transactions of the Indian Institute of Metals **(Springer), (I.F- 1.17)** vol-73, 1773-1788
   DOI: https://doi.org/10.1007/s12666-020-01994-w.
8. Husain Mehdi, R.S Mishra, an experimental analysis and optimization of process parameters of AA6061 and AA7075 welded joint by TIG+FSP welding using RSM, Advances in Materials and Processing Technologies (Taylor and Francis) **(Scopus).** https://doi.org/10.1080/2374068X.2020.1829952**.**

Conference paper details

1. Husain Mehdi, R.S. Mishra (2017), Optimization of process parameters of TIG+FSP welded joint of different Al-alloy by response surface methodology, International conference of advanced research and innovation in Engineering (ICARIE-2017), at MIT Meerut, 26-27 August 2017. Paper ID: ICARIE- 2017-159.
2. Husain Mehdi, R.S. Mishra (2017), Influence of friction stir processing om microstructure and mechanical properties of TIG welded joint of dissimilar Al-alloy, International conference of advanced research and innovation in Engineering (ICARIE-2017), at MIT Meerut, 26-27 August 2017. Paper ID: ICARIE- 2017- 165.

References

[1] Rai. R, De A. Bhadeshia HKDH, Debroy T, Friction stir welding tools, science and technology of welding and joining, 16, 325-342, 2011.

[2] C.J. Dawes, P.L. Threadgill, E.J.R. Spurgin, and D.G. Staines, "Development of the New Friction Stir Technique for Welding Aluminum—Phase II," TWI member report 5651/35/95, Nov 1995.

[3] Christian B. Fuller, Friction Stir Tooling: Tool Materials and Designs , Friction Stir Welding and Processing, pp7-35, 2007. DOI:10.1361/fswp2007p007.

[4] L. Christodoulou, W. Palko, and C. Fuller, Equipment and Processing Variables Affecting Friction Stir Processing of NiAl Bronze, Friction Stir Welding and Processing III, K.V. Jata, M.W. Mahoney, R.S. Mishra, and T.J. Lienert, Ed., TMS, 2005, p 57–66 48.

[5] M.W. Mahoney, C.B. Fuller, W.H. Bingel, and M. Calabrese, "Friction Stir Processing of Cast NiAl Bronze," THERMEC 2006, July 4–8, 2006 (Vancover, Canada), TMS.

[6] M.W. Mahoney, W.H. Bingel, S.R. Sharma, and R.S. Mishra, Microstructural Modification and Resultant Properties of Friction Stir Processed Cast NiAl Bronze, Mater. Sci. Forum, Vol 426–432, 2003, p 2843–2848.

[7] Fu Zhi-Hong, HE Di-qiu, Wang Hong, friction str welding of aluminum alloys, Journal of Wuhan university of Technology, Material Science edition 19: 61-64.

[8] R.S. Mishra and Zy Ma (2005), Friction stir welding and processing, Materil science and Engineering R 50: 1-78.

[9] Greitmann MJ and Peter Deimel (2005), friciton stir welding- Innovative technology for joining aluminum components, Otto-graf journal 16: 185-192.

[10] Ghosh M, Kumar K, Kailas SV, Ray AK 920100, Optimization of friction stir welding parameters for dissimilar aluminum alloys, Materials and Design 31: 3033-3037.

[11] K. S. Anil Kumar, S. M. Murigendrappa, Hemantha Kumar, and Himanshu Shekhar, Effect of tool rotation speed on microstructure and tensile properties of FSW joints of 2024-T351 and 7075-T651 reinforced with SiC nano particle: The role of FSW single pass, AIP Conference Proceedings 1943, 020056 (2018).

[12] Barenji, R. V. (2016). Effect of tool traverse speed on microstructure and mechanical performance of friction stir welded 7020 aluminum alloy. Proceedings of the Institution of Mechanical Engineers, Part L: Journal of Materials: Design and Applications, 230(2), 663–673.

[13] Narges Dialami , Miguel Cervera and Michele Chiumenti, Effect of the Tool Tilt Angle on the Heat Generation and the Material Flow in Friction Stir Welding, Metals 2019, 9, 28.

[14] Y.Wang, X.L Shi, R.S mishra, T.J Watson, "Friction stir welding of devitrified AL-4.0Y-4.0Ni-0.9Co alloy produced by amorphose powder", Scripta Materialia 56 (2007) 971-974.

[15] Indrajeet Charit, Rajiv S. Mishra, Murray W. Mahoney, "Multi sheet structure in 7475 aluminum by FSW in concert with post weld superplastic forming", Scripta Materialia 47 (2002) 631-636.

[16] J.Q. Su, T.W Nelson, R.S Mishra, M.Mahoney, "Microstructure investigation of friction stir welding 7050-T651 aluminum, acta materialia, 2002.

[17] Z.Y.Ma, S.R Mishra, R.S Mishra, "Effect of Friction Stir Processing on the microstructure of CastA356 Al", Material Science and Engineering A 433 (2006), 269-278.

[18] Patric B. Berdon, Willam H. Bingel, R.S Mishra, "Friction Stir Processing: A Tool to homogenize nano composite Al Alloy, Scripta mater, 44 (2001), 61-66.

[19] Z.Y.Ma, R.S Mishra, M.W. Mahoney," Super plastic deformation behavior of friction stir processed 7075Al alloy", Acta Materialia 50 (2002), 4419-4430.

[20] S. Jana, R.S. Mishra, J.A Baumann, G. Grant, " Effect of process parameters on abnormal grain growth during FSP of a cast Al-Alloy", Material Science and Engineering A, 528 (2010) 189-199.

[21] Jian Qing Su, T.W Nelson, T.R. McNelley, "Development of Nano crystalline structure in Cu during Friction Stir Processing", Material Science and Engineering A, 525 (2011) 5458-5464.

[22] Nilesh Kumar, R.S Mishra, " Ultrafined Grained Al-Mg-Sc Alloy via friction Stir Processing", Metallurgical and Materials Transaction, 44A (2013) 934-945.

[23] Z.Y Ma, S.R Sharma, R.S Mishra, " Effect of Multipass Friction Stir Processing on Microstructure and tensile propeties of a Cast Al-Si Alloy", Scripta Materialia, 54 (2006) 1623-1626.

[24] Z.y.Ma, R.S Mishra, F.C Liu, “Super plastic behaviour of Micro-region in two pass friction stir processing 7075Al alloy”, Materialia Science and Engineering A 505 (2009) 70-78.

[25] Jianqing Su, Jiye Wang, R.S Mishra, Ray Xu, “ Microstructure and Mechanical Properties of Friction Stir Processing Ti-6Al-4V Alloy”, Material Science and Engineering A 573 (2013) 67-74

[26] Omar S. Salih, Hangan Ou, W.Sun, D.G McCartney, “A review of friction stir welding of aluminum matrix composite”, Material and Design 86 (2015) 61-71

[27] S.R. Ren, Z.Y. Ma and L.Q. Chen , Effect of welding parameters on tensile properties and fracture behavior of friction stir welded Al–Mg–Si alloy, Scripta Materialia 56 (2007) 69–72.

[28] Y.S. Sato, Y. Kurihara, S.H.C. Park, H. Kokawa, N. Tsuji , Friction stir welding of ultrafine grained Al alloy 1100 produced by accumulative roll-bonding, Scripta Materialia 50 (2004) 57–60.

[29] A. Barcellona, G. Buffa, L. Fratini, D. Palmeri, On microstructural phenomena occurring in friction stir welding of aluminum alloys, Journal of Materials Processing Technology 177 (2006) 340–343

[30] T. Minton, D.J. Mynors , Utilization of engineering workshop equipment for friction stir welding, Journal of Materials Processing Technology 177 (2006) 336–339.

[31] H.W. Zhang, Z. Zhang, J.T. Chen, 3D modeling of material flow in friction stir welding under different process parameters, Journal of Materials Processing Technology 183 (2007) 62–70.

[32] Olivier Lorrain, Véronique Favier, Hamid Zahrouni, Didier Lawrjaniec, Understanding the material flow path of friction stir welding process using unthreaded tools, Journal of Materials Processing Technology 210 (2010) 603–609.

[33] Cemal Meran, The joint properties of brass plates by friction stir welding, Materials and Design 27 (2006) 719–726.

[34] Hasan Okuyucu, Adem Kurt, Erol Arcaklioglu, Artificial neural network application to the friction stir welding of aluminum plates, Materials and Design 28 (2007) 78–84.

[35] Z. Zhang, H.W. Zhang , Numerical studies on the effect of transverse speed in friction stir welding, Materials and Design 30 (2009) 900–907.

[36] Moataz M. Attallah, Hanadi G. Salem, Friction stir welding parameters: a tool for controlling abnormal grain growth during subsequent heat treatment, Materials Science and Engineering A 391 (2005) 51–59.

[37] Wang Kuai-she, WU Jia-lei, Wang Wen, ZHOU Long-hai, LIN Zhao-xia, KONG Liang, Underwater friction stir welding of ultrafine grained 2017 aluminum alloy, J. Cent. South Univ. (2012) 19: 2081-2085.

[38] A. Pirondi, L. Collini, D. Fersini, Fracture and fatigue crack growth behaviour of PMMC friction stir welded butt joints, Engineering Fracture Mechanics 75 (2008) 4333–4342.

[39] Y.G. Kim, H. Fujii, T. Tsumura, T. Komazaki, K. Nakata, Three defect types in friction stir welding of aluminum die casting alloy, Materials Science and Engineering A 415 (2006) 250–254.

[40] Yingchun Chen, Huijie Liu, Jicai Feng, Friction stir welding characteristics of different heat-treated-state 2219 aluminum alloy plates, Materials Science and Engineering A 420 (2006) 21–25.

[41] Yutaka S. Sato, Mitsunori Urata, and Hiroyuki Kokawa, Parameters Controlling Microstructure and Hardness during Friction-Stir Welding of Precipitation-Hardenable Aluminum Alloy 6063, Metallurgical And Materials Transactions A, Volume 33a, March 2002—625-635.

[42] Jerry Wong, Patricia Zambrano, Indira Escamilla, Bernardo Gonzalez, Victor Mucino, Rafael Colás, Friction stir linear welding of an aluminum alloy, Advanced Materials Research Vol. 68 (2009) pp 116-121.

[43] Su, T. Nelson and C. Sterling. “Friction stir processing of large-area bulk UFG aluminum alloys”. Scripta Materialia 52 (2005) pp.135-140.

[44] M. Peel, A. Steuwer, M. Preuss and P. Withers. “Microstructure, mechanical roperties and residual stresses as a function of welding speed in aluminum A5083 friction stir welds”, Acta Materialia, Volume 51, Issue 16, (2003), pp.4791-4801.

[45] K.Jata and S. Semiatin. “Continuous dynamic recrystallization during friction stirs welding of high strength aluminum alloys”. Scripta Materialia, Volume 43, Issue: 8, pp.743-74.

[46] Benavides, Y. Li, L. E. Murr, D. Brown and J. McClure. “Low-temperature friction-stir welding of 2024 aluminum” **,** Scripta Materialia, Vol. 41, Issue 8, pp. 809-815.

[47] Y. Kwon, I. Shigematsu and N. Saito. “Mechanical properties of fine-grained aluminum alloy produced by friction stir process”. Scripta Materialia 49 (2003) pp. 785-789.

[48] Vijay Soundararajan, Srdja Zekovic, Radovan Kovacevic,Thermo-mechanical model with adaptive boundary conditions for friction stir welding of Al 6061, International Journal of Machine Tools & Manufacture 45 (2005) 1577–1587, Received 5 January 2005; accepted 15 February 2005,Available online 21 April 2005.

[49] P. Heurtier a, M.J. Jones b, C. Desrayaud a, J.H. Driver a,*, F. Montheillet a, D. Allehaux c, Mechanical and thermal modelling of Friction Stir Welding, Journal of Materials Processing Technology 171 (2006) 348–357, Received 16 April 2004; received in revised form 1 January 2005; accepted 6 July 2005.

[50] Zhang & H. W. Zhang, Material behaviors and mechanical features in friction stir welding process International Journal of Advanced Manufacturing and Technology (2007) 35:86–100.

[51] G. Buffa, J.Hua, R. Shivpuri, L. Fratini, A continuum based fem model for friction stir welding—model development, Materials Science and Engineering A 419 (2006) 389–396.

[52] L. Commin, M. Dumont, J.-E. Masse, L. Barrallier, Friction stir welding of AZ31 magnesium alloy rolled sheets: Influence of processing parameters, Acta Materialia 57 (2009) 326–334.

[53] G. Buffa, A. Ducato, L. Fratini, Numerical procedure for residual stresses prediction in friction stir welding, Finite Elements in Analysis and Design 47 (2011) 470–476.

[54] C. Hamilton, S. Dymek, A. Sommers , A thermal model of friction stir welding in aluminum alloys, International Journal of Machine Tools & Manufacture 48 (2008) 1120–1130.

[55] C. Hamilton, A. Sommers, S. Dymek, A thermal model of friction stir welding applied to Sc-modified Al–Zn–Mg–Cu alloy extrusions, International Journal of Machine Tools & Manufacture 49 (2009) 230–238.

[56] Mohamed Assidi, Lionel Fourment, Simon Guerdoux, Tracy Nelson, Friction model for friction stir welding process simulation: Calibrations from welding experiments, International Journal of Machine Tools & Manufacture 50 (2010) 143–155.

[57] R. Nandan, G.G. Roy, T.J. Lienert, T. Debroy Three-dimensional heat and material flow during friction stir welding of mild steel, Acta Materialia 55 (2007) 883–895

[58] M. Maalekian, E. Kozeschnik, H.P. Brantner, H. Cerjak , Comparative analysis of heat generation in friction welding of steel bars, Acta Materialia 56 (2008) 2843–2855.

[59] L. Commin, M. Dumont, J.-E. Masse, L. Barrallier, Friction stir welding of AZ31 magnesium alloy rolled sheets: Influence of processing parameters, Acta Materialia 57 (2009) 326–334

[60] Z. Zhang, H.W. Zhang, Numerical studies on controlling of process parameters in friction stir welding, journal of materials processing technology 209 (2009) 241–270

[61] D. Jacquin, B. de Meester, A. Simar, D. Deloison, F. Montheillet, C. Desrayaud, A simple Eulerian thermomechanical modeling of friction stir welding, Journal of Materials Processing Technology 211 (2011) 57–65.

[62] Mustafa, B. The influence of stirrer geometry on bonding and mechanical properties in friction stir welding process. Materials and Design 2004, 35, 343–347.

[63] Thomas, W.M.; Nicholas, E.D. Friction stir welding for the transportation industries. Materials and Design 1997, 18 (4/6), 269–273.

[64] M Krishna, Dr K C Udaiyakumar, D K Mohan Kumar and H Mohammed Ali, Analysis on effect of using different tool pin profile and mechanical properties by friction stir welding on dissimilar aluminum alloys Al6061 and Al7075, IOP Conf. Series: Materials Science and Engineering 402 (2018) 012099.

[65] K. Elangovan, V. Balasubramanian, and M. Valliappan, Effect of Tool Pin Profile and Tool Rotational Speed on Mechanical Properties of Friction Stir Welded AA6061 Aluminum Alloy, Materials and Manufacturing Processes, 23: 251–260, 2008.

[66] Vijay, S.J., and Murugan, N., (2010), Influence of tool pin profile on the metallurgical and mechanical properties of friction stir welded Al-10wt.% TiB2 metal matrix composite, Materials and Design, Vol.31(7), pp.3585–3589.

[67] Pothur Hema, Experimental Investigations on AA 6061 Alloy Welded Joints by Friction Stir Welding, Aluminum Alloys and Composites,2020, Chapter (8), https://doi.org/10.5772/intechopen.89797.

[68] Olivier Lorrain, Véronique Favier, Hamid Zahrouni, Didier Lawrjaniec, Understanding the material flow path of friction stir welding process using unthreaded tools, Journal of Materials Processing Technology 210 (2010) 603–609.

[69] S. Dharani Kumar, S. Sendhil Kumar, Investigation of mechanical behavior of friction stir welded joints of AA6063 with AA5083 aluminum alloys, Mechanics and Mechanical Engineering 2019; 23:59–63.

[70] Kwon, Y.J., Shigematsu, I., and Saito, N., (2004), Mechanical Property Improvements in Aluminum Alloy through Grain Refinement using Friction Stir Process, Materials Transactions, Vol.45(7), pp.2304–2311.

[71] Sato, Y.S., Urata, M., Kokawa, H., and Ikeda, K., (2002), Reproduction of Ultra-Fine Grains in Equal Channel Angular Pressed Al Alloy 5083 by Friction Stir Process, In ASM Proceedings of the International Conference: Trends in Welding Research , 262–266.

[72] Liu, H.J., Zhang, H.J., and Yu, L., (2011), Effect of welding speed on microstructures and mechanical properties of underwater friction stir welded 2219 aluminum alloy, Materials and Design, Vol.32(3), pp.1548–1553.

[73] Hassan., (2002), The Effect of welding condition on the nugget zone in friction stir welds AA 7010 alloy, In 6th International trends in Welding Research Conference Proceedings, 287–292.

[74] Hassan, K.A.A., Norman, A.F., Price, D.A., and Prangnell, P.B., (2003), Stability of nugget zone grain structures in high strength Al-alloy friction stir welds during solution treatment, Acta Materialia, Vol.51(7), pp.1923–1936.

[75] Zhang, H.J., Liu, H.J., and Yu, L., (2011), Microstructure and mechanical properties as a function of rotation speed in underwater friction stir welded aluminum alloy joints, Materials and Design, Vol.32(8-9), pp.4402–4407.

[76] Dehghani, M., Amadeh, A., and Akbari Mousavi, S.A.A., (2013), Investigations on the effects of friction stir welding parameters on intermetallic and defect formation in joining aluminum alloy to mild steel, Materials and Design, Vol.49(4) , pp.33–441.

[77] Rajakumar, S., Muralidharan, C., and Balasubramanian, V., (2011), Statistical analysis to predict grain size and hardness of the weld nugget of friction-stir-welded AA6061-T6 aluminum alloy joints, The International Journal of Advanced Manufacturing Technology, Vol.57(1-4), pp.151–165.

[78] Sato, Y.S., Onuma, T., Ikeda, K., and Kokawa, H., (2016), Experimental verification of heat input during friction stir welding of Al alloy 5083, Science and Technology of Welding and Joining, Vol.21(4), pp.325–330.

[79] Moataz M. Attallaha, Hanadi G. Salemb, Friction stir welding parameters: a tool for controlling abnormal grain growth during subsequent heat treatment, Materials Science and Engineering A 391 (2005) 51–59.

[80] Lakshminarayanan, A.K., and Balasubramanian, V., (2008), Process parameters optimization for friction stir welding of RDE-40 aluminum alloy using Taguchi technique, Transactions of Nonferrous Metals Society of China, Vol.18(3), pp.548–554.

[81] Shen, J.J., Liu, H., and Cui, W., (2010), Effect of welding speed on microstructure and mechanical properties of friction stir welded copper, Materials and Design, Vol.31(8), pp.3937–3942.

[82] El-Nasr, and Abo, A.B.A., (2010), Mechanical Properties and Fracture Behavior of Friction Stir Welded 7075-T6 Al Alloy, Journal of Engineering and Computer Sciences, Vol.3(2), pp.147–161.

[83] Zhang, Z., Xiao, B.L., and Ma, Z.Y., (2014), Influence of water cooling on microstructure and mechanical properties of friction stir welded 2014Al-T6 joints, Materials Science and Engineering: A, Vol.614, pp.6–15.

[84] Crawford, R., Cook, G.E., Strauss, A.M., Hartman, D.A., and Stremler, M.A. (2006), Experimental defect analysis and force prediction simulation of high weld pitch friction stir welding, Science and Technology of Welding and Joining, Vol.11(6), pp.657-665.

[85] Sato, Y.S., Park, S.H.C., Michiuchi, M., and Kokawa, H., (2004), Constitutional liquation during dissimilar friction stir welding of Al and Mg alloys, Scripta Materialia, Vol.50(9), pp.1233–1236.

[86] Muhayat N., Zubaydi A., Sulistijono, Yuliadi M.Z., Effect of tool tilt angle and tool plunge depth on mechanical properties of friction stir welded AA 5083 joints, Appl. Mech. Mater., 2014, 493, 709-714.

[87] Kumar, K., and Kailas, S.V., (2008a), The role of friction stir welding tool on material flow and weld formation, Materials Science and Engineering A, Vol.485(1-2), pp.367–374.

[88] Elyasi, M., Aghajani Derazkola, H., & Hosseinzadeh, M. (2016). Investigations of tool tilt angle on properties friction stir welding of A441 AISI to AA1100

aluminum. Proceedings of the Institution of Mechanical Engineers, Part B: Journal of Engineering Manufacture, 230(7), 1234–1241.

[89] C. Rajendran, K. Srinivasan, V. Balasubramanian, H. Balaji, P. Selvaraj, Effect of tool tilt angle on strength and microstructural characteristics of friction stir welded lap joints of AA2014-T6 aluminum alloy, Trans. Nonferrous Met. Soc. China 29(2019) 1824-1835.

[90] Krishna, G.G., Reddy, P.R., and Hussain, M.M., (2014), Effect of Tool Tilt Angle on Aluminum 2014 Friction Stir Welds, Global Journal of Researches in Engineering, Vol.14(7), pp.1-14.

[91] Adeosun, S.O., Balogun, S.A., Sekunowo, O.I., and Usman, M. A., (2010), Effects of Heat Treatment on Strength and Ductility of Rolled and Forged Aluminum 6063 Alloy, Materials Characterization, Vol.9(8), pp.763–773.

[92] Hu, Z., Yuan, S., Wang, X., Liu, G., and Huang, Y., (2011), Effect of post-weld heat treatment on the microstructure and plastic deformation behavior of friction stir welded 2024, Materials and Design, Vol.32(10), pp.5055–5060.

[93] Bayazid, S., Farhangi, H., Asgharzadeh, H., Radan, L., Ghahramani, A., and Mirhaji, A., (2016), Effect of cyclic solution treatment on microstructure and mechanical properties of friction stir welded 7075 Al alloy, Materials Science and Engineering: A, Vol.649(1), pp.293–300.

[94] Chaitanya Sharma, Dheerendra Kumar Dwivedi, Pradeep Kumar, Effect of post weld heat treatments on microstructure and mechanical properties of friction stir welded joints of Al–Zn–Mg alloy AA7039, Materials and Design 43:134–143.

[95] Guven Ipekoglu, Gurel Cam, Treatment on the Properties of Dissimilar Friction-Stir-Welded Joints between AA7075 and AA6061 Aluminum Alloys, Metallurgical and Materials Transactions A 45A (7):3074-3087, 2014.

[96] Hakan Aydın, Ali Bayram, Ismail Durgun, The effect of post-weld heat treatment on the mechanical properties of 2024-T4 friction stir-welded joints, Materials and Design 31(5):2568-2577.

[97] Rui-dong, F., Zeng-qiang, S., Rui-cheng, S., Ying,L., Hui-jie, L., and Lei, L., (2011), Improvement of weld temperature distribution and mechanical properties of 7050 aluminum alloy butt joints by submerged friction stir welding, Materials and Design, Vol.32(10), pp.4825–4831.

[98] Wanchuck Woo, Hahn Choo, Donald W. Brown, Zhili Feng, Influence of the Tool Pin and Shoulder on Microstructure and Natural Aging Kinetics in a Friction-Stir-Processed 6061–T6 Aluminum Alloy, Metallurgical and Materials Transactions A, 38a, 2007—69-76.

[99] Chen, Y.C., Feng, J.C., and Liu, H.J., (2009), Precipitate evolution in friction stir welding of 2219-T6 aluminum alloys, Materials Characterization, 60(6) 476–481.

[100] Sivaraj, P.,Kanagarajan, D., and Balasubramanian, V., (2014a), Effect of post weld heat treatment on fracture toughness properties of friction stir welded AA7075-T651 aluminum alloy joints, Journal of Manufacturing Engineering, Vol.9(2), pp.110–115.

[101] Krishnaja Devireddy, Venkateswarlu Devuri, Murali Mohan Cheepu, Balina Kranthi Kumar, Analysis of the Influence of Friction Stir Processing on Gas Tungsten Arc Welding of 2024 Auminum Alloy Weld Zone, International Journal of Mechanical and Production Engineering Research and Development 8 (1) 2018 243-252

[102] Mabuwa S, Msomi V, Effect of Friction Stir Processing on Gas Tungsten Arc-Welded and Friction Stir-Welded 5083-H111 Aluminum Alloy Joints, Advances in Materials Science and Engineering, 2019 1-14.

[103] Mosneaga, V. A., Mizutani, T., Kobayashi, T. and Toda, H. 2002. Impact Toughness of Weldments in Al-Mg-Si Alloys. Mater. Trans. 43: 1381-1389.

[104] Masubuchi, K., 1980. Analysis of Welded Structures - Residual Stresses, Distortion, and their Consequences. New York, Pergamon Press.

[105] Huang, C. & Kou, S. Partially melted zone in Aluminum welds-liquation mechanism and directional soldification. Welding Journal, 2000, 79(5), 113s-120s.

[106] Biddle, A.P. & Wilson, W.A. Variable polarity plasma arc welding on the space shuttle external tank. Welding Journal, 1984, 63, 27–35.

[107] Albertini, G.; Bruno, G.; Dunn, B.D.; Fiori, F.; Reimers, W. & Wright, J.S. Comparative neutron and X-ray residual stress measurements on Al-2219 welded plate. Mater. Sci. Eng.: A, 1997, 224(1-2), 157-165. doi:10.1016/S0921-5093(96)10546-3.

[108] Xu, W.; Liu, J.; Luan, G. & Dong, C. Microstructure and mechanical properties of friction stir welded joints in 2219-T6 aluminum alloy. Materials Design, 2009, 30(9), 3460-3467

[109] M. Ilangovan, S. Rajendra Boopathy, V. Balasubramanian, Effect of tool pin profile on microstructure and tensile properties of friction stir welded dissimilar AA 6061eAA 5086 aluminium alloy joints, Defence Technology 11 (2015) 174-184.

[110] Arora A, De A, DebRoy T. Toward optimum friction stir welding tool shoulder diameter. Scripta Mater 2011;64 (1):9–12.

[111] M. N. M. Salleh, M. Ishak, L. H. Shah & S. R. A. Idris, The effect of ER4043 and ER5356 filler metal on welded Al 7075 by metal inert gas welding, WIT Transactions on The Built Environment, 2016, Vol 166, 213-224.

[112] Caceres C H, Davidson C J, Griffiths J R. The deformation and fracture behaviour of an Al-Si-Mg casting alloy [J]. Materials Science and Engineering A, 1995, 197: 171-179.

[113] Luijendijk, T, Welding of Dissimilar Aluminium Alloys, Journal of Materials Processing Technology 103 (1), 29-35, 2000.

[114] Taira S, Tanaka K, Yamazaki T (1978) A method of x-ray microbeam measurement of local stress and its application to fatigue crack growth problems. J Soc Mater Sci Jpn 27(294):251–256.

[115] C. Yeni ,S.Sayer, M. Pakdil , Comparison of mechanical and microstructural behaviour of TIG, MIG and Friction Stir welded 7075 Aluminium Alloy, Kovove Mater. 47 (2009), 341–347.

[116] N. S. Rossini, M. Dassisti, K. Y. Benyounis and A. G. Olabi. 2012. Methods of measuring residual stresses in components. Materials and Design. 35: 572-588.

[117] James M. N. 2010. Residual stress influences in mechanical engineering. In: XVIII Congreso Nacional de Ingeniería Mecánica. pp. 1-13.

[118] Yang Y. P., Babu S. S., Kikel J. M. and Brust F. W. 2011. Investigation of weld crack mitigation techniques with advanced numerical modeling and experiment-Summary. In: Hot Cracking Phenomena in Welds III. J. Lippold, T. Böllinghaus and C. E. Cross (Eds.). pp. 353-365.

[119] D. J. Buchanan and R. John. 2014. Residual stress redistribution in shot peened samples subject to mechanical loading. Materials Science & Engineering: A. 615: 70-78.

[120] Good SH and Brown IM, the nucleation of cavities by plastic deformation, Acta mater **27** 1-15 (1979).

[121] Tszeng TC, Interfacial stresses and void nucleation in discontinuously reinforced composites, J Eng Mater Technol. 2000;122: 86-92.

[122] Smith, William F.; Hashemi, Javad (2006), Foundations of Materials Science and Engineering (4th ed.), McGraw-Hill, ISBN 978-0-07-295358-9.

[123] W. Xu, J. Liu, G. Luan, C. Dong, Temperature evolution, microstructure and mechanical properties of friction stir welded thick 2219-O aluminum alloy joints, Materials & Design, 30 (2009) 1886-1893.

[124] Jia,Yonggui Qin, Yiwen Ou, Kehong Wang, Jizi Liu, The Influence of Microstructural Heterogeneity on Mechanical Properties of Friction Stir Welded Joints of T6-Treated Al-Zn-Mg Alloy 7A52Yang, Metals 2018, 8(7), 527.

[125] Mahadzir Ishak, Nur Fakhriah Mohd Noordin, Luqman Hakim Ahmad Shah, Feasibility study on joining dissimilar aluminum alloys aa6061 and aa7075 by tungsten inert gas (TIG), Jurnal Teknologi (Sciences & Engineering) 75:7 (2015) 79–84.

[126] Peel M, Steuwer A, et al. Microstructure, mechanical properties and residual stresses as a function of welding speed in aluminium AA5083 friction stir welds. Acta Materialia. 2003;51:4791-4801.Jitender Kundu and Hari Singh 2018 Adv in Mater Proc Technol **4** 183.

[127] Arbegast WJ. Modeling Friction Stir Joining as a Metalworking Process, Miner, Metals Mater Soci.2003:313-330.

[128] Patel VV, Badheka V, Kumar A. Influence of Friction Stir Processed Parameters on Superplasticity of Al-Zn-Mg-Cu Alloy. Mater Manuf Proce.2016; 31:1573-1582.

[129] S. Kou, Welding Metallurgy, second ed., John Willy & Sons, New York, 2003.

[130] Tang W, X. Guo, J. C. McClure and L. E. Murr, Heat Input and Temperature Distribution in Friction Stir Welding, J. Mater. Process. Manuf. Sci **7** 163-172 (1998).

[131] Senthil KT, Balasubramanian V, Sanavullah MY. Influences of pulsed current tungsten inert gas welding parameters on the tensile properties of AA 6061 aluminium alloy. Mater and Des.2007;28: 2080-2092.

[132] Mohammadzadeh Jamalian H, Farahani M, et al. Study on the effects of friction stir welding process parameters on the microstructure and mechanical properties of 5086-H34 aluminum welded joints. Int J Adv Manuf Technol.2016;83:611–621.

[133] Kasman Ş, Yenier Z. Analyzing dissimilar friction stir welding of AA5754/AA7075. Inter J Adv Manuf Tech.2014; 70:145-156.

[134] Liu G, Xin R, Li J, Liu D, Liu Q, Fracture localisation in retreating side of friction stir welded magnesium alloy, Sci Tech Weld Join 378-384 (2015).

[135] Shanavas, S., & DHAS, J. E. R. (2017). Parametric optimization of friction stir welding parameters of marine grade aluminium alloy using response surface methodology. Transactions of Nonferrous Metals Society of China, 27(11), 2334-2344. 13.

[136] Lakshminarayanan, A. K., & Balasubramanian, V. (2009). Comparison of RSM with ANN in predicting tensile strength of friction stir welded AA7039 aluminium alloy joints. Transactions of Nonferrous Metals Society of China, 19(1), 9-18. 14.

[137] Rajakumar, S., & Balasubramanian, V. (2012). Establishing relationships between mechanical properties of aluminium alloys and optimised friction stir welding process parameters. Materials & Design, 40, 17-35.

[138] Koilraj M, Sundareswaran V, Vijayan S, Rao SRK. Friction stir welding of dissimilar aluminum alloys AA2219 to AA5083 – Optimization of process parameters using Taguchi technique. Mater Des 2012;42:1–7,

[139] Silva AAMd, Arruti E, Janeiro G, Aldanondo E, Alvarez P, Echeverria A. Material flow and mechanical behaviour of dissimilar AA2024-T3 and AA7075-T6 aluminium alloys friction stir welds. Mater Des 2011;32:2021–7.

[140] Strombeck AV, Santos JFD, Torster F, Laureano P, Kocak M. Fracture toughness behaviour of FSW joints on aluminum alloys. In: Proceedings of the first international symposium on friction stir welding; 1999.

[141] Liu HJ, Fujii H, Maeda M, Nogi K. Heterogeneity of mechanical properties of friction stir welded joints of 1050-H24 aluminum alloy. Mater Sci Lett 2003;22:441–4.

[142] Sato YS, Kokawa H. Distribution of tensile property and microstructure in friction stir weld of 6063 aluminum. Metall Mater Trans 2001;32A(12): 3023–31.

[143] Hakan Aydın, Ali Bayram, Agah Uguz , Kemal Sertan Akay, Tensile properties of friction stir welded joints of 2024 aluminum alloys in different heat-treated-state, Materials and Design 30 (2009) 2211–2221.

[144] D. Radaj. Welding residual stresses and distortion: Calculation and measurement. DVS Verlag (January 2003). ISBN 3 87155 791

[145] M. Adak, N. R. Mandal. Pseudolinear equivalent constant rigidity concept for analyzing welding residual deformation. Applied Mathematical Modelling, 33(4): pp. 2096–2108 (April 2009). doi:10.1016/j.apm.2008.05.024.

[146] Liu FJ, Fu L, Chen HY (2017) Microstructures and mechanical properties of thin plate aluminum alloy joint prepared by high rotational speed friction stir welding. Acta Metall Sin 53(3):1651– 1658.

[147] M. Felix Xavier Muthu and V. Jayabalan (2016), "Effect of pin profile and process 15 parameters on microstructure and mechanical properties of friction stir welded Al-Cu 16 joints," Trans. Nonferrous Met. Soc. China (English Ed., vol. 26, no. 4, pp. 984–993.

[148] Yupeng Li, Daqian Sun, Wenbiao Gong, Effect of Tool Rotational Speed on the Microstructure and Mechanical Properties of Bobbin Tool Friction Stir Welded 6082-T6 Aluminum Alloy, Metals 2019, 9(8), 894.

[149] SM Handbook, volume 12: fractography. ASM International Materials Park (1987) 55.

[150] Akbar Heidarzadeh, Reza Vatankhah Barenji, Mohsen Esmaily, Atabak Rahimzadeh Ilkhichi, Tensile Properties of Friction Stir Welds of AA 7020 Aluminum Alloy, Trans Indian Inst Met (2015) 68(5):757–767.

[151] Yeong-Maw Hwang, Zong-Wei Kang, Yuang-Cherng Chiou, Hung-Hsiou Hsu, Experimental study on temperature distributions within the workpiece during friction stir welding of aluminum alloys, International Journal of Machine Tools & Manufacture 48 (2008) 778–787.

[152] Yaduwanshi D K, Bag S, Pal S. Numerical modeling and experimental investigation on plasma-assisted hybrid friction stir welding of dissimilar materials [J]. Materials & Design, 2016, 92: 166−183.

[153] Nandan R, Roy G G, Debroy T. Numerical simulation of three-dimensional heat transfer and plastic flow during friction stir welding [J]. Metallurgical and Materials Transactions A, 2006, 37(4): 1247−1259.

[154] L Shi, C S Wu, M A Chen, Numerical analysis of heat transfer and material flow in reverse dual-rotation friction stir welding, Proceedings of the 1st

International Joint Symposium on Joining and Welding, Osaka, Japan, 6–8 November 2013.

[155] Midling OT, Oosterkamp LD, Bersaas J. Friction stir welding aluminium process and applications. In: Proceedings of the seventh international conference on joints in aluminium, INALCO98; 1998.

[156] Backlund J, Norlin A, Andersson A. Friction stir welding-weld properties and manufacturing techniques. In: Proceedings of the seventh international conference on joints in aluminium, INALCO98; 1998.

[157] Hirata T, Oguri T, Hagino H, Tanaka T, Chung SW, Takigawa Y, et al. Influence of friction stir welding parameters on grain size and formability in 5083 aluminum alloy. Mater Sci Eng, A 2007; A456 (1–2):344–9.

[158] Simar A, Brechet Y, Meester B, de Denquin A, Gallais C, Pardoen T. Integrated modeling of friction stir welding of 6xxx series Al alloys: process, microstructure and properties. Progr Mater Sci 2012;57:95–183.

[159] Dinaharan I, Murugan N, Parameswaran S. Developing an empirical relationship to predict the influence of process parameters on tensile strength of friction stir welded AA6061/0–10 wt% ZrB2 in situ composite. Trans Indian Inst Met 2012;65(2):159–70.

[160] Ma ZY, Sharma SR, Mishra RS. Microstructural modification of as-cast Al–Si–Mg alloy by friction stir processing. Metall Mat Trans A 2006;37:3323–36.

[161] Azimzadegan T, Serajzadeh S. An Investigation into microstructures and mechanical properties of AA7075-T6 during friction stir welding at relatively high rotational speeds [J]. Journal of Materials Engineering Performance, 2010, 19(9): 1256−1263.

[162] Horton KR. Micro-hardness, strength and strain field characterization of self-reacting friction stir and plug welds of dissimilar aluminum alloys [dissertation]. Tuscaloosa: the University of Alabama; 2011.

[163] Mao Y, Ke L, Liu F, Huang C, Chen Y, Liu Q. Effect of welding parameters on microstructure and mechanical properties of friction stir welded joints of 2060 aluminum lithium alloy. Int J Adv Manuf Technol 2015;81:1419–31.

[164] Pandey C, Mahapatrab M M, Kumar P, Saini N, J.G, Study on effect of double austenitization treatment on fracture morphology tensile tested nuclear grade P92 steel, Engg Fail Analy **96** 158-167 (2018).